

Controlling Si(111) and Si(100) surfaces for subsequent GaP heteroepitaxy in CVD ambient

Dissertation

zur Erlangung des akademischen Grades
doctor rerum naturalium (Dr. rer. nat.)

eingereicht in der Fakultät für Mathematik und
Naturwissenschaften
Technische Universität Ilmenau

von M. Sc. Agnieszka Paszuk
geboren am 19.04.1987, Wrocław

Tag der wissenschaftlichen Aussprache: 01.06.2017

Gutachter:

1. Univ.-Prof. Dr. rer. nat. habil. Thomas Hannappel
2. Prof. Dr. rer. nat. habil. Gerhard Gobsch
3. Prof. dr hab. inż. Regina Paszkiewicz

Die Arbeit wurde angefertigt im Rahmen der Thüringer Landesgraduiertenschule für Photovoltaik **PhotoGrad** an der TU Ilmenau.

Zusammenfassung

Höhere Photovoltaik-Konversionswirkungsgrade und niedrigere Produktionskosten würden einen höheren Anteil erneuerbarer Energie ermöglichen. Die Integration von III-V-Unterzellen auf einem kostengünstigen aktiven Si-Substrat hat das Potential, Mehrfach-Solarzellen mit einem hohen Konversionswirkungsgrad zu ermöglichen. Das Wachstum von III-V-Materialien mit niedriger Defektdichte auf Si ist schwierig aufgrund der unterschiedlichen Kristallstrukturen. Dank der geringen Gitterfehlانpassung kann eine GaP Nukleationsschicht, die auf dem Si Substrat aufgewachsen wird, den Übergang von Si zu anderen III-V Materialien erleichtern. Solche pseudomorphen GaP/Si-Quasisubstrate ermöglichen die anschließende Integration planarer oder Nanodraht (ND)-basierter III-V-Strukturen. Die planaren Strukturen werden für gewöhnlich in [100]-Orientierung gewachsen, wohingegen ND-Strukturen bevorzugt entlang der [111]-Richtung wachsen.

Die vorliegende Arbeit untersucht die Präparation der Si Unterzelle und der pseudomorphen GaP/Si Quasisubstrate mittels metallorganischer chemischer Gasphasenabscheidung (MOCVD). Für die Herstellung eines p-n-Übergangs im Si wird die Diffusion der Gruppe-V-Elemente P und As in Si(100) und Si(111)-Substrate und ihre Auswirkung auf die Si-Oberflächenstruktur und das anschließende GaP Wachstum analysiert. Dabei wird eine präzise Kontrolle der Si-Oberfläche benötigt, um geringe Defektdichten in den nachfolgend gewachsenen Schichten zu ermöglichen: Im Falle der Si(100) Oberfläche verursachen Einfachstufen beim heteroepitaktischen Wachstum von III-V-Schichten die Entstehung von Antiphasendomänen, wohingegen bei Si(111)-Substraten die Kontrolle der Polarität der GaP-Schichten entscheidend ist, um das senkrechte Wachstum von ND zu erreichen. MOCVD-Wachstumsprozesse sind sehr komplex aufgrund der Anwesenheit von metallorganischen Ausgangsstoffen, des Prozessgases (H_2), welches einen starken Einfluss auf die Stufenformation des Si hat, und wegen des allgegenwärtigen Wechselspiels zwischen energetischen und kinetischen Prozessen. Um die Präparation der Si-Oberfläche kontrollieren zu können, ist eine *in situ* Kontrolle unabdingbar. Hierzu verwenden wir *in situ* Reflexions-Anisotropie-Spektroskopie (RAS) und korrelieren Signale, welche an entscheidenden Prozessschritten auftreten, mit Ultrahochvakuum (UHV)-basierten Oberflächenempfindlichen Methoden.

Beide Si-Oberflächen wechselwirken stark mit dem H_2 -Prozessgas, was während der Oberflächenpräparation zu einer Terminierung der Oberflächen mit Monohydrid führt. Der Kollektor in Si(100) und Si(111) wird durch Tempern in entweder tert-Butylphosphin- oder tert-Butylarsin (TBAs)-Atmosphäre gebildet, welches zu einer Diffusion von P oder As in Si führt. Nach der Kollektor-Bildung weisen *in situ* RA Spektren auf eine ungeordnete Si-Oberfläche hin. Die starke Wechselwirkung von P und As mit Si-Oberflächen verursacht eine Aufräumung der Si-Oberfläche. Weiteres Tempern in H_2 ist notwendig, um für die GaP Nukleation wieder eine glatte Oberfläche (epiready) zu generieren. Tempern in As-Umgebung führt zu einer As-Oberflächenterminierung des Si(111). Zudem wurden Unterschiede in der Si(111)-Stufenkonfiguration zwischen einer Fehlorientierung der Wafer in [112]-Richtung und [112]-Richtung gefunden, die sich auch auf die anschließend gewachsene GaP Nukleationsschichten auswirken: Diese ist glatter auf Si(111) $[\bar{1}\bar{1}2]$ und GaP Nuklei erstrecken sich entlang der Si(111):As Stufenkanten, während auf Si(111) $[11\bar{2}]$ die Nuklei zufällig verteilt sind. Das GaP-Wachstum auf H-terminierten Si(111)-Oberflächen führt, unabhängig von Nukleationsprozess, zu einer A-Typ Polarität. Um GaP(111) mit B-Typ-Polarität zu erzielen, was für vertikales III-V ND-Wachstum notwendig ist, ist eine Modifizierung der Si-Oberfläche nötig. Durch eine gezielte Terminierung der Si-Oberfläche mit As oder H_2 lässt sich die Polarität des GaP-Films kontrollieren. Im Falle von Si(100) 6° kann mittels *in situ* RAS die Dimer-Ausrichtung der Majoritätsdomäne auf der Oberfläche in Abhängigkeit der As-Quelle (As_x oder TBAs) und der Abkühlprozedur kontrolliert werden. Dies erlaubt die gezielte Einstellung der Untergitterausrichtung der nachfolgend gewachsenen, eindomänigen GaP/Si(100)-Schicht. Somit können sowohl für planare als auch für ND-basierte photovoltaische Mehrfachabsorber-Strukturen geeignete GaP/Si Quasisubstrate mit wohldefinierten Grenzflächen und einem p-n-Übergang im Si kontrolliert in der MOCVD präpariert werden.

Abstract

A higher share of renewable energy would largely benefit from increased photovoltaic conversion efficiencies and lower production costs. The integration of III-V sub-cells with a cheap active Si substrate has the potential to achieve high-efficiency multi-junction solar cells. Growth of III-V materials with low defect density on Si is difficult because of the different crystal structure. GaP grown on Si can facilitate the transition between Si and III-V materials due to the small lattice mismatch. The pseudomorphic GaP/Si quasisubstrates can allow for subsequent integration of planar and nanowire (NW)-based III-V structures. The planar structures are commonly grown in [100] orientation, while the NWs grow preferably along [111] direction.

The present work studies the preparation of the Si bottom cell and pseudomorphic GaP/Si quasisubstrates by metalorganic chemical vapor phase deposition (MOCVD). For the preparation of the p-n junction in Si, the in-diffusion of group-V dopants (P and As) by precursor supply into Si(100) and Si(111) substrates is analyzed, as well as its impact on the atomic Si surface structure and on the subsequent GaP growth. Precise control over the involved interfaces is required in order to achieve low defect densities: The atomic step structure of Si(100) substrates is decisive to avoid antiphase disorder in the III-V epilayers. Likewise, the polarity of the GaP epilayer has to be controlled via the Si(111) surface preparation in order to achieve vertical NW growth. Growth processes in MOCVD ambient are highly complicated due to the presence of complex metalorganic sources, the process gas (H_2) which strongly affects step formation on Si, and the competition between energetic and kinetic processes. Therefore, to achieve control over the Si surface preparation, *in situ* control is inevitable. To this end, we apply *in situ* reflection anisotropy spectroscopy (RAS) and correlate signals obtained at crucial steps of the process with ultra-high vacuum-based (UHV) surface sensitive methods.

Both Si surfaces strongly interact with the H_2 process gas, which leads to monohydride termination of the surfaces during preparation. The collector in Si(100) and in Si(111) can be formed by annealing in either tertiarybutylphosphine or tertiarybutylarsine (TBAs) ambient, which leads to P or As in-diffusion into the Si. After collector formation, *in situ* RA spectra indicate disordered surfaces due to the strong interaction of P and As with the Si substrate. Additional annealing in H_2 is necessary to recover a smooth surface suitable for GaP nucleation. Annealing in As ambient, leads to a Si(111) surface termination by As. Moreover, we found that the Si(111) step structure is different for Si with offcut in $[\bar{1}\bar{1}2]$ and $[11\bar{2}]$ direction, which influences the morphology of subsequently grown GaP nucleation layers: The GaP nucleation layer is smoother on Si(111) $[\bar{1}\bar{1}2]$ and GaP nuclei elongate the Si(111):As steps, whereas on Si(111) $[11\bar{2}]$, the nuclei are randomly distributed. GaP grown on H-terminated Si(111) surfaces, independently of the nucleation procedure, leads to GaP with A-type polarity. To achieve GaP(111) with B-type polarity, which is required for vertical III-V NW growth, we developed a specific procedure involving pre-termination of Si(111) substrate with As. Thereby, the polarity of GaP epilayers grown on Si(111) can be controlled by the termination of the Si surface. In case of Si(100) 6° , we apply *in situ* RAS to control the prevalence of the majority domain on the surface in dependence of the As source (background As_x or TBAs) and cooling procedure. This allows to control the sublattice orientation of subsequently grown, single domain GaP/Si(100) epilayer. GaP/Si quasisubstrates with well-defined interface and a p-n junction within Si, which are suitable for either planar or NW-based photovoltaic multi-junction structures, can thus be prepared in a controllable manner in MOCVD ambient.

Preface

This research is focused on studying the influences of the MOCVD process parameters and ambient on the atomic surface structure of Si(111) and Si(100) substrates. For this purpose, *in situ* reflectance anisotropy spectroscopy (RAS) is applied in combination with ultra-high vacuum surface sensitive methods. The aim of this work is to achieve control over the preparation of GaP/Si(100) and GaP/Si(111) quasi-substrates (extended by a p-n junction within Si) for the integration of planar and NW-based III-V structures. The research regarding Si(111) is novel, and part of the results were obtained with the support of Matthias Steidl and Dr. Weihong Zhao. The results regarding Si(100) surface preparation in CVD arsenic ambient are a continuation of research conducted by Dr. Sebastian Brückner and Dr. Oliver Supplie.

The work is divided in 10 chapters; the empirical results are laid out in the chapters: **6, 7, 8** and **9**. At the end of each of them a short summary is given, which presents the main findings.

The structure of the work is as follows:

1. **Introduction** outlines the motivation for this research, explains the challenges and presents the research and experimental approaches.
2. **Theoretical background** introduces important theoretical context for this research.
3. **Experimental background** describes the main experimental techniques used.
4. **State of the art: *in situ* study of III-V/Si surfaces in CVD ambient** summarizes previous research by our group when applying *in situ* RAS on Si(100) in the CVD ambient. These results are fundamental for further studies concerning this surface. In addition, the chapter shortly summarizes results obtained by other research groups regarding RAS of Si(111).
5. **Sample preparation** clarifies the process followed to prepare the samples.
6. **Si(111) in CVD ambient** details Si(111) surfaces in hydrogen and arsenic ambient.
7. **GaP/Si(111)** focuses on controlling the GaP polarity on Si(111), and preparation of quasi-substrates for vertical NWs growth.

8. **GaP/Si(100)** centers on the Si(100) surface in arsenic ambient, and control over the sublattice orientation of subsequently grown GaP.
9. **In-diffusion of phosphorus and arsenic into Si(111) and Si(100)** contains the first results of P and As in-diffusion into the Si, and shows an active p-n junction.
10. **Conclusion** summarizes the main results and gives an outlook to future studies.

This work was supervised by Prof. Dr. T. Hannappel at Technische Universität (TU) Ilmenau, Germany. The experiments presented at the beginning of this work were done at Helmholtz-Zentrum Berlin für Materialien und Energie (HZB). The subsequent experimental research was conducted at TU Ilmenau after transferring of the laboratory and research staff.

This work is a part of the German Federal Ministry of Education and Research (BMBF) projects: “Nanostrukturierte III-V/Si Solarzellen” (03SF0404A) and “Hocheffiziente III-V Mehrfachsolarzellen auf Silicium” (03SF0525B). The work was mostly financed by a scholarship from the Thüringer Landesgraduiertenschule für Photovoltaik (PhotoGrad).

Contributions

(a) journal articles:

- A. Paszuk, O. Supplie, M. Nandy, S. Brückner, A. Dobrich, P. Kleinschmidt, B. Kim, Y. Nakano, M. Sugiyama, and T. Hannappel, “*Double-layer Stepped Arsenic-modified Si(100) Surfaces Prepared in As-rich CVD ambient*,” Applied Surface Science, under review, 2018.
- A. Paszuk, O. Supplie, B. Kim, S. Brückner, M. Nadny, A. Heinisch, P. Kleinschmidt, Y. Nakano, M. Sugiyama, and T. Hannappel, “*GaAsP/Si tandem solar cells: In situ study on GaP/Si:As virtual substrate preparation*,” Solar Energy Materials and Solar Cells, vol. 180, p. 343, 2018.
- A. Paszuk, A. Dobrich, C. Koppka, S. Brückner, M. Duda, P. Kleinschmidt, O. Supplie, and T. Hannappel, “*In situ preparation of Si p-n junctions and subsequent surface preparation for III-V heteroepitaxy in MOCVD ambient*,” Journal of Crystal Growth, vol. 464, p. 14, 2017.
- A. Paszuk, S. Brückner, M. Steidl, W. Zhao, A. Dobrich, O. Supplie, P. Kleinschmidt, W. Prost, and T. Hannappel, “*Controlling the polarity of metalorganic vapor phase epitaxy-grown GaP on Si(111) for subsequent III-V nanowire growth*,” Applied Physics Letters, vol. 106, p. 231601, 2015.
- C. Koppka, A. Paszuk, M. Steidl, O. Supplie, P. Kleinschmidt, and T. Hannappel, “*Suppression of rotational twin formation in GaP/Si(111) quasi-substrates for III-V nanowire growth*,” Crystal Growth & Design, vol. 16, p. 6208, 2016.
- O. Skibitzki, A. Paszuk, F. Hatami, P. Zaumseil, Y. Yamamoto, M. Andreas Schubert, A. Trampert, B. Tillack, W. Ted Masselink, T. Hannappel, and T. Schroeder, “*Lattice-engineered $Si_{1-x}Ge_x$ -buffer on Si(001) for GaP integration*,” Journal of Applied Physics, vol. 115, p. 103501, 2014.
- B. Kim, K. Toprasertpong, A. Paszuk, O. Supplie, Y. Nakano, T. Hannappel, and M. Sugiyama, “*GaAsP/Si tandem solar cells: Realistic prediction of efficiency gain by applying strain-balanced multiple quantum wells*,” Solar Energy Materials and Solar Cells, vol. 180, p. 303, 2018.

- W. Zhao, M. Steidl, A. Paszuk, S. Brückner, A. Dobrich, O. Supplie, P. Kleinschmidt, and T. Hannappel, “*Analysis of the Si(111) surface prepared in chemical vapor ambient for subsequent III-V heteroepitaxy*,” Applied Surface Science, vol. 392, p. 1043, 2017.
- O. Supplie, M. M. May, P. Kleinschmidt, A. Nägelein, A. Paszuk, S. Brückner, and T. Hannappel, “*In situ controlled heteroepitaxy of single-domain GaP on As-modified Si(100)*,” APL Materials, vol. 3, p. 126110, 2015.
- O. Supplie, O. Romanyuk, C. Koppka, M. Steidl, A. Nägelein, A. Paszuk, L. Winterfeld, A. Dobrich, P. Kleinschmidt, E. Runge, and T. Hannappel, “*Metalorganic Vapor Phase Epitaxy of III/V-on-Silicon: Experiment and Theory*,” Progress in Crystal Growth and Characterization of Materials, accepted, 2018.

(b) conference papers:

- O. Skibitzki, A. Paszuk, F. Hatami, P. Zaumseil, Y. Yamamoto, M. A. Schubert, A. Trampert, B. Tillack, W. T. Masselink, T. Hannappel, and T. Schroeder, “*Lattice-engineered $Si_{1-x}Ge_x$ -buffer on Si(001) for GaP integration*,” 7th International Silicon-Germanium Technology & Device Meeting (ISTDM), p. 21, Singapore, Singapore, 2014.
- M. Steidl, A. Paszuk, W. Zhao, S. Brückner, A. Dobrich, O. Supplie, J. Luczak, P. Kleinschmidt, H. Döscher, and T. Hannappel, “*MOVPE-preparation of Si(111) surfaces for III–V nanowire growth*,” 2013 International Conference on Indium Phosphide and Related Materials (IPRM), p. 1, Kobe, Japan, 2013.

(c) selected conference contributions:

- A. Paszuk, O. Supplie, S. Brückner, M. M. May, A. Dobrich, A. Nägelein, B. Kim, Y. Nakano, M. Sugiyama, P. Kleinschmidt and T. Hannappel, “*Optical in-situ control over dimer orientation on Si(100) surfaces in arsenic ambient*,” poster, 17th European Workshop on Metalorganic Vapour Phase Epitaxy, Grenoble, France, 2017. *Awarded the best student poster contribution.*
- A. Paszuk, O. Supplie, S. Brückner, M. M. May, A. Nägelein, B. Kim, T. Watanabe, Y. Nakano, M. Sugiyama, P. Kleinschmidt, and T. Hannappel, “*As-modified Si(100) surface preparation in a CVD ambient*,” talk, Compound Semiconductor Week, Berlin, Germany, 2017.

- A. Paszuk, M. Steidl, S. Brückner, O. Supplie, W. Zhao, A. Dobrich, P. Kleinschmidt, and T. Hannappel, “*Epitaxial growth in a CVD ambient for high efficiency solar cells*,” invited talk, “Summer School of Microelectronics of Łódź University of Technology”, Szklarska Poręba, Poland, 2016.
- A. Paszuk, O. Supplie, M. Duda, M. Steidl, C. Koppka, S. Brückner, A. Dobrich, P. Kleinschmidt, and T. Hannappel, “*Silicon p-n junctions prepared by group-V in-diffusion in CVD ambient*,” talk, 2016 Meeting, European Materials Research Society Spring Meeting, Lille, France, 2016.
- A. Paszuk, O. Supplie, M. M. May, M. Duda, A. Nägelein, A. Dobrich, P. Kleinschmidt, S. Brückner, and T. Hannappel, “*Single-domain GaP heteroepitaxy on Si(100) p-n junctions prepared by group-V in-diffusion in VPE ambient*,” talk, 12th International Conference on Concentrator Photovoltaic Systems, Freiburg, Germany, 2016.
- A. Paszuk, O. Supplie, M. Duda, A. Dobrich, P. Kleinschmidt, S. Brückner, and T. Hannappel, “*Silicon p-n junctions prepared by group-V in-diffusion in CVD ambient*,” talk, 80th Annual Meeting of the DPG Spring Meeting, Regensburg, Germany, 2016.
- A. Paszuk, M. Duda, S. Brückner, A. Dobrich, O. Supplie, M. Steidl, C. Koppka, P. Kleinschmidt, and T. Hannappel “*Silicon p-n junctions prepared by group-V in-diffusion in CVD ambient*,” talk, 30. DGKK Arbeitskreistreffen Epitaxie von III-V Halbleitern, Göttingen, Germany, 2015.
- A. Paszuk, M. Steidl, S. Brückner, A. Dobrich, O. Supplie, P. Kleinschmidt, and T. Hannappel, “*In-situ reflection anisotropy spectroscopy study of the MOCVD prepared Si(111) surface*,” talk, 79th Annual Meeting of the DPG Spring Meeting, Berlin, Germany, 2015.
- A. Paszuk, M. Steidl, W. Zhao, S. Brückner, A. Dobrich, O. Supplie, P. Kleinschmidt, and T. Hannappel, “*In-situ reflection anisotropy spectroscopy study of the MOCVD prepared Si(111) surface*,” talk, 29. DGKK Arbeitskreistreffen Epitaxie von III-V Halbleitern, Magdeburg, Germany, 2014.

Table of Contents

Zusammenfassung.....	III
Abstract	V
Preface.....	VII
Contributions.....	IX
1 Introduction.....	1
2 Theoretical background.....	4
2.1 Multi-junction solar cell	4
2.2 Solar cell parameters	9
2.3 In-diffusion into silicon.....	13
2.4 Si and GaP crystal structure and surface	15
2.4.1 Si and GaP crystal structure	15
2.4.2 Si(100) surface in hydrogen ambient	16
2.4.3 Si(111) surface in hydrogen ambient	19
2.4.4 GaP(100) surface in hydrogen ambient.....	22
2.4.5 GaP(111) surface in hydrogen ambient.....	23
2.4.6 Arsenic terminated Si(100) surface.....	23
2.4.7 Arsenic terminated Si(111) surface.....	24
2.5 Hydrogen coverage on Si(100)	25
2.6 Challenges in III-V/Si heteroepitaxy.....	26
2.6.1 Antiphase disorder	27
2.6.2 Rotational domains.....	28
3 Experimental background	29
3.1 Metalorganic chemical vapor deposition (MOCVD).....	29
3.2 MOCVD-to-UHV transfer system	33
3.3 Reflection anisotropy spectroscopy (RAS).....	34
3.4 X-ray photoelectron spectroscopy (XPS).....	39
3.5 Low energy electron diffraction (LEED)	42
3.6 Fourier-transform infrared spectroscopy (FTIR)	45
3.7 Scanning tunneling microscopy (STM)	46
3.8 Atomic force microscopy (AFM).....	46
3.9 Electrochemical capacitance voltage profiling (ECV).....	47
4 State of the art: <i>in situ</i> study of Si surfaces in CVD ambient.....	49
4.1 Si(100) surfaces in hydrogen ambient.....	49

4.1.1	<i>In situ</i> control of Si removal in H ₂ ambient.....	50
4.1.2	Anomalous double step formation.....	51
4.1.3	<i>In situ</i> controlled preparation of Si(100) 6° in H ₂ ambient.....	52
4.1.3.1	<i>In situ</i> deoxidation	52
4.1.3.2	Formation of A- and B-type domains.....	54
4.1.3.3	Kinetic vs. energetic domain in a step formation process	55
4.2	Si(111) in hydrogen ambient	56
5	Sample preparation.....	57
5.1	Wet Chemical Etching.....	57
5.2	Standard process of Si and GaP deoxidation and growth in MOCVD.....	57
5.3	Standard GaP(100) epitaxy	58
5.4	GaAs NWs growth	58
6	Si(111) in CVD ambient.....	59
6.1	Si(111) surfaces in hydrogen ambient.....	59
6.1.1	Chemical composition after oxide removal.....	59
6.1.2	Hydrogen termination.....	60
6.1.3	Surface reconstruction.....	61
6.1.4	Step structure of Si(111) with an offcut in $[11\bar{2}]$ and $[\bar{1}\bar{1}2]$ direction	62
6.1.5	Surface morphology	67
6.2	Si(111) arsenic terminated surface	70
6.2.1	Surface morphology of weak sample offcut.....	70
6.2.2	Step structure of Si(111) with an offcut in $[11\bar{2}]$ and $[\bar{1}\bar{1}2]$ direction	72
6.2.3	As termination	75
6.3	Summary of this chapter.....	78
7	GaP/Si(111).....	80
7.1	GaP(111) polarity	80
7.2	GaP(111) homoepitaxy.....	83
7.3	Control of GaP(111) polarity on Si(111).....	85
7.4	Impact of Si(111) substrate offcut on GaP nucleation	89
7.5	Summary of this chapter.....	91
8	GaP/Si(100).....	92
8.1	<i>In situ</i> control of dimer orientation on Si(100) surfaces in As ambient	93
8.1.1	As-modified Si(100) 2° surface and domain formation.....	93
8.1.2	As-modified Si(100) 6° surface and domain formation.....	96
8.1.3	As dimer orientation in dependence on process parameters.....	100

8.1.3.1	Formation of As modified Si (100) 6° B-type surface	101
8.1.3.2	Formation of As modified Si (100) 6° A-type surface	102
8.2	Summary of domain formation on As- modified Si(100) surfaces	107
8.3	GaP/Si(100):As	109
8.4	Si(100) surface after phosphorus exposure	113
8.5	Summary of this chapter	115
9	In-diffusion of phosphorus and arsenic into Si(111) and Si(100)	116
9.1	Collector formation under different CVD conditions	116
9.2	Surface morphology	120
9.3	Current-voltage characteristic	121
9.4	Summary of this chapter	122
10	Conclusion	123
	Bibliography.....	127
	Acknowledgements	141

1 Introduction

The world population is increasing as well as the demand for energy, which at present is mostly satisfied by burning fossil fuels. The currently predicted energy demand for the year 2050 exceeds 27 terawatts (TWs), which is more than double in comparison to 2001 (13.5 TW) [1,2]. The growth in consumption of fossil fuels leads to a higher emission of carbon dioxide (CO_2) into the atmosphere. Reduction of CO_2 can be achieved by substituting the energy generated from burning fossil fuels by energy from renewable sources. One possibility for this is to use solar energy. The average energy that reaches the Earth's surface (irradiance) is around 1.37 kW/m^2 , from which, about 30 % is scattered and about 19 % is absorbed by the atmosphere and clouds [3]. Nevertheless, the theoretical potential of solar power is more than enough to cover the entire global energy consumption. However, there are important problems that photovoltaic (PV) as a renewable energy source has to face are cost reduction, storage of produced energy and improvement of solar cell (SC) efficiency. According to Swanson's Law, the price of solar PV modules tends to drop 20 % for every doubling of the production capacity of the solar industry [4]. Prices for Si solar cells decreased from \$76.67 per watt (W) in 1977 to \$0.26 per W in 2016¹. However, despite its falling prices, the theoretical maximum efficiency of a single junction Si solar cell cannot exceed 30 % (at one sun) according to the so-called Shockley-Queisser-Limit (SQL) [5].

Nonetheless, the Shockley-Queisser limit of a single-bandgap solar cell can be exceeded by stacking solar cells with different bandgaps on top of each other in so-called multi-junction solar cells (MJSC) [6]. III-V semiconductors are ideally suited for growth of multi-junction solar cells due to their superior optoelectronic properties and the tunability of bandgaps and lattice constant in a wide range by choice of composition [7]. Currently, the most efficient MJSCs reached 46 % conversion efficiency [8]. Metalorganic chemical vapor deposition (MOCVD) (also known as MOVPE - metalorganic vapor phase epitaxy) presents the established preparation technique for large-scale and high-quality III-V semiconductor growth [9]. However, the high cost of the (MOCVD) production process due to the expensive III-V precursors and wafers is the main reason for intense research efforts towards III-V integration on Si substrates. Si represents the cheapest available semiconductor substrate material, compared to III-V or Ge wafers. Si substrates exhibit attractive material properties [10] and benefits from mature manufacturing and technology, due to its scientific and technological relevance. III-V integration on Si microelectronics promises not only high-efficiency MJ solar cells, but also a new

¹ based on average sales price of crystalline silicon solar cells from EnergyTrend.com, from August 2016. The price 0.26 \$/W refers to monocrystalline silicon solar cells with efficiency between 19.6 ~ 19.8%.

generation of high performance optoelectronic devices, which attracts science since the 1980s [11]. In particular, Si exhibits a bandgap which is close to optimum for the bottom cell in tandem SC configurations [12]. There are two common approaches for III-V integration on Si substrates, in dependence on the Si substrate orientation: (i) planar III-V layer structures are grown on Si(100), (ii) III-V nanowires (NWs) are grown vertically on Si(111). The planar approach is well established on Ge or other III-V substrates, and might benefit from transfer of established layer structures and approved SC architectures to Si. However, the large lattice mismatch between Si and the mature GaAs- or InP-based MJSC structure presents a big challenge. In the case of heteroepitaxial III-V NW growth on Si, lattice matching is less critical due to the small diameter of the NWs, which enhances better stress accommodation [13]. This opens a wide choice of materials for III-V NWs. III-V NWs on Si present a further cost reduction compared to planar III-V film growth due to higher growth rates, and lower material consumption [14]. A common method to grow NWs is by vapor-liquid-solid (VLS), from a gold (Au) catalyst in the form of a nanoscale droplet [15]. For both the planar and the NW approach, using a pseudomorphically grown gallium phosphide (GaP) buffer on Si presents a promising strategy towards low-defect III-V/Si integration. Due to the small lattice mismatch of GaP to Si (only 0.37 % at room temperature), thin layers which serve as a transition layer from group IV substrate to III-V material can be grown without relaxation. GaP/Si quasi-substrates may also serve as growth template to prevent unintentional doping from the Si substrate into the NWs [16], and to overcome the problem of the strong Au-Si chemical interaction [17]. However, GaP/Si heteroepitaxy faces many challenges, such as growth of polar on non-polar material [11,18]. Polarity control of GaP on Si(111) is crucial since vertical growth of NWs requires GaP with a B-type polarity, i.e. the $\bar{1}\bar{1}\bar{1}$ crystal face [19]. In the case of Si(100), double-layer steps with a single-domain Si surface structure are indispensable to avoid antiphase domains. Structural defects in the III-V layers may act as recombination centers, which reduce drastically the carrier lifetime and thereby efficiency of an optoelectronic device [18]. Therefore, precise control over the interface and surface formation is crucial during the heteroepitaxy on Si [11].

With regard to Si as bottom cell in MJSCs, an *in situ* preparation of the Si p-n junction in MOCVD ambient prior to subsequent GaP nucleation could enable a single growth process for the entire tandem device. To prepare active Si substrates, precise control of group-V in-diffusion is highly important, but it has been little studied so far. For subsequent GaP heteroepitaxy, the influence of the precursor on Si surface and step formation is decisive. While heteroepitaxial growth of GaP on Si(100) substrates is well-established [20–25] in ‘clean’ hydrogen ambient, it is less intensively studied in presence of group-V precursors and residuals. Little is also known about GaP heteroepitaxy on Si(111), which might significantly differ from the heteroepitaxial growth on Si(100).

The aim of this work is to achieve control over the preparation of GaP/Si(100) and GaP/Si(111) quasi-substrates for integration of planar and NW-based III-V structures.

This also includes the extension of Si substrate by a p-n junction to serve as an active sub-cell in an III-V/Si tandem absorber structure. The research is focused on studying the influences of the MOCVD process parameters and ambient on the atomic surface structure of Si(111) and Si(100) substrates, and on the heteroepitaxial growth of GaP/Si(111). The main goals of this work are:

- to understand the Si(111) surface preparation in H₂ ambient with respect to deoxidation and interaction of hydrogen with the surface,
- to reveal the influence of arsenic exposure on the Si(111) surface structure,
- to control the polarity of the GaP epilayer on Si(111),
- to study vicinal Si(100) surface and step formation in As ambient,
- to control collector formation in Si and surface morphology after exposure to phosphorus or arsenic,
- to study GaP nucleation on Si terminated with arsenic and
- to form the Si p-n junction *in situ* and subsequently grow GaP.

In this work, all samples were prepared by MOCVD applying hydrogen (H₂) as process gas. The growth process is highly complex due to the presence of a process gas, which strongly affects surface reactions, complex metalorganic sources and their chemical reactions, as well as competition between energetic and kinetic processes. Additionally, III-V residuals in the reactor from previous processes can influence the surface preparation or epitaxial growth. Direct control of the process by UHV based surface sensitive techniques is impossible due to the high pressure (from 50 to 950 mbar) in the reactor. To overcome this problem, reflection anisotropy spectroscopy (RAS) can be applied as optical surface sensitive *in situ* method [26]. However, this technique does not provide direct information about the surface state. Therefore, *in situ* RA spectra obtained in this work are correlated with results from ultra-high vacuum (UHV) surface science techniques. A dedicated transfer system enables contamination-free transfer of the MOCVD-prepared surfaces to UHV [27]. Chemical analysis and surface reconstruction are investigated by x-ray photoelectron spectroscopy (XPS) and low energy electron diffraction (LEED), respectively. The hydrogen termination of the silicon surfaces is investigated using attenuated total reflectance Fourier transform infrared spectroscopy (ATR-FTIR). The surface morphology was analyzed with atomic resolution by scanning tunneling microscopy (STM) as well as *ex situ* on nanometer scale by atomic force microscopy (AFM). Doping profiles were measured by electrochemical capacitance voltage profiling (ECV-Profiling). This broad spectrum of complimentary techniques enables a detailed understanding of the complex growth mechanisms and control of Si(111) and Si(100) surfaces for subsequent GaP heteroepitaxy at the atomic scale.

2 Theoretical background

In the following chapter, the theoretical background of multi-junction solar cells, which is the main motivation for GaP/Si quasi-substrates, is discussed. Further, basic solar cell parameters and crystal lattice of group-IV and -III-V are introduced. The main differences between Si(100) and Si(111) surfaces structures are shown, as well the interaction of Si and GaP (both (100) and (111)) surfaces with hydrogen. Finally, the main challenges in III-V/Si heteroepitaxy are described.

2.1 Multi-junction solar cell

The first PV effect was observed in 1839 by Alexandre-Edmond Becquerel. He generated electricity by illuminating an electrode (platinum or silver coated with silver chloride or silver bromide) with different types of light, including sunlight [28]. The next significant PV discovery was an observation of the photoconductive effect in selenium by Adams and Day in 1877, which was the first PV effect in a solid state [29]. In April 1954, Bell Labs demonstrated the first silicon solar cell with 6 % efficiency. Today's single junction solar cells based on crystalline Si can exceed 25 % efficiency (Panasonic HIT, rear junction) [30], which is very close to the theoretical maximal limit of around 30 % [5]. The efficiency of the solar cells strongly depends on the probability that a photon with an energy higher than the bandgap of the semiconductor ($h\nu > E_g$, - ν is the frequency and h is the Planck's constant), absorbed into the bulk will produce a hole – electron pair. Therefore, the bandgap of the semiconductor material determines what part of the solar spectrum can be converted. Photons with energy less than the bandgap are not absorbed (transmission losses). Photons with energy equal to the bandgap are ideally converted. Photons with energy higher than the bandgap are lost as a conversion of carrier kinetic energy to heat by phonon emission (thermalization losses). An average energy of an electron after thermalization can be given by $E_g + 3kT/2$, where k is the Boltzmann's constant and T is the temperature. In addition, there are extraction losses related to the balance between collecting carriers at a high electrical potential and collecting those carriers before they recombine. Figure 2.1 shows all losses mentioned above for the silicon solar cell solar and global spectrum at air mass 1.5 (AM1.5g).

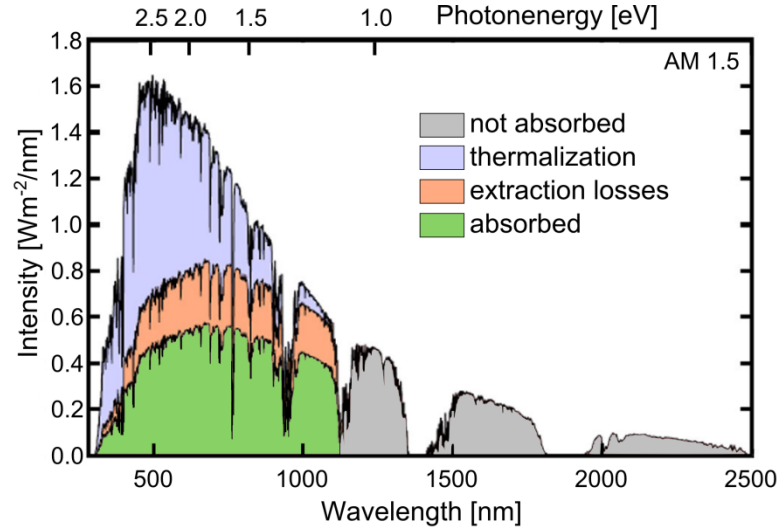


Fig. 2.1: Losses for a single-junction silicon solar cell (bandgap = 1.12 eV)².

Reduction of thermalization and spectrum losses in the solar cell can be realized by a serial connection of multiple absorbers with different bandgap energies - so-called multijunction solar cells (MJSC). For this purpose, III-V compound semiconductors are applied due to the possibility of tuning their bandgap and lattice constant by varying their elemental composition, e.g. according to Vegard's law (see Fig. 2.2) [7]. Moreover, they exhibit excellent optoelectronic properties, such as high carrier mobilities.

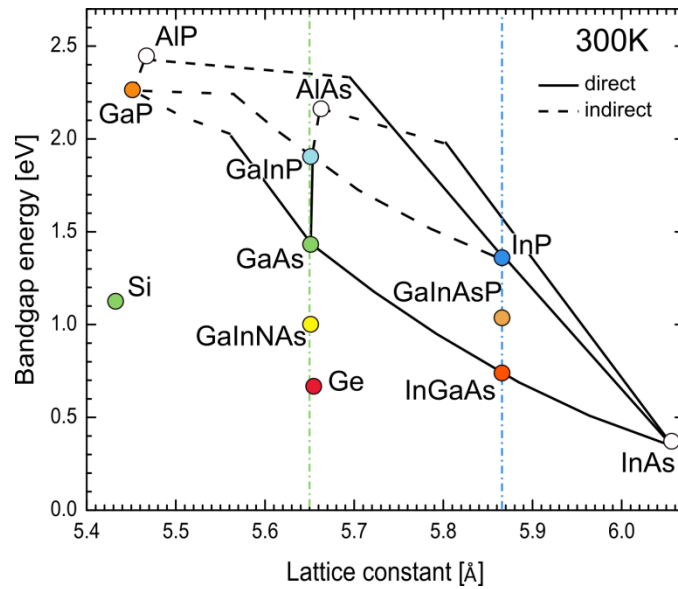


Fig. 2.2: Relation between bandgap and lattice constant of binary, ternary, quaternary III-V compounds, and Si and Ge. Direct and indirect bandgaps are indicated by the style of the line and symbol. The green and blue dashed line are indicating lattice constants of GaAs and InP, respectively. The diagram is based on data from Vurgaftman *et al.* [31].

² Based on a reference AM 1.5 spectrum available on <http://rredc.nrel.gov/solar/spectra/am1.5/>, NREL

Theoretically, an ideal 2-junction (tandem) solar cell can reach 42 % efficiency, a 3-junction cell - 49 % and an infinity-layer cell - 68 % (86 % under concentrated sunlight) [6,12] or according to Bremner *et al.* [32] even 46 %, 52 %, 56 % for 2- 3- and 4- junction solar cell, respectively, under unconcentrated AM1.5 spectrum. A good candidate for a substrate in MJSCs is a binary compound GaAs. Its bandgap 1.42 eV corresponds to the maximum theoretical efficiency limit for the AM 1.5 solar spectrum [5]. Tandem combination of InGaP as a top cell (20 % efficiency as a single junction solar cell [33]) with GaAs as a bottom cell, with a lattice constant 5.64 Å and the bandgap energy of 1.86 eV and 1.42 eV, respectively, exhibits a theoretical conversion efficiency of 34 %, under one sun AM1.5 [34]. This solar cell structure already exceeded 30 % efficiency (under one sun AM1.5) [35]. Figure 2.3 shows a solar spectrum AM 1.5 divided in four regions defined by materials with a different bandgap: InGaP, GaAs, GaInNAs, Ge. The gaps in the spectrum at around 900 nm, 1100 nm, 1400 nm, 1900 nm, etc. are due to the absorption in the atmosphere mainly by CO₂ and H₂O.

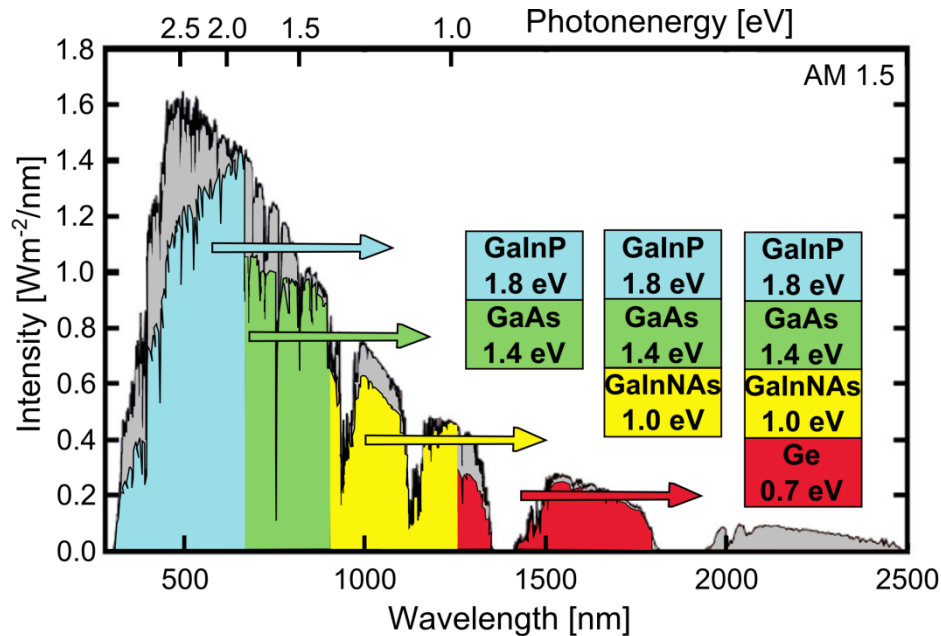


Fig. 2.3: AM 1.5 solar spectrum, divided in four different absorption regions - an example of a multijunction solar cell: semiconductors with different bandgaps convert different ranges of the solar spectrum, thereby thermalization and spectral losses are reduced. The graph shows the evolution of multijunction solar cell structures from the existing GaInP/GaAs 2-junction device to 3- and 4- junction devices by incorporation of an III-V material with 1 eV bandgap energy, as future generation solar cells. Theoretical efficiencies are idealized (practical efficiencies can be expected to be decreased to ~80 %) and given for the AM0 (for space application) and AM1.5D 500 suns (based on [36]).

The cost of the III-V solar cells is elevated due to the expensive III-V precursors and wafers, one could reduce the costs by applying cheaper germanium (Ge) as a substrate. The big advantage of Ge is its close lattice constant to GaAs (<0.1 % of lattice mismatch at room temperature). It can serve e.g. as a substrate for a tandem (InGaP/GaAs) or triple

junction solar cells: InGaP/GaAs/Ge [37]. State of the art GaInP/GaInAs/Ge triple junction solar cells exceed 40 % efficiency (AM1.5D at 240 suns) [38]. Higher cell efficiencies can be achieved by extending the triple junction to a four-junction cell (4J) by ideally adding a material with a bandgap of 1.0 eV. There are two possible materials with the 1.0 eV bandgap: InGaAsP with a lattice constant that could match InP - 5.868 Å or InGaAsN with a lattice constant of 5.65 Å, matching GaAs. 4J solar cell can be obtained by a combination of InGaP/GaAs/InGaAsN/Ge (see Fig. 2.2 and Fig. 2.3), with a theoretical efficiency of 41 % under one sun AM0 (spectrum in the space) [36,39]. Although the InGaAsN is a promising candidate, its minority carrier diffusion length is very short, leading to a low quantum efficiency and limiting the current in a 4J device [40]. An alternative solution to achieve a 4J device is realized by wafer bonding of two tandem solar cells based on two different lattice constants, or by spectrum-splitting by applying diffractive optics to simultaneously split and concentrate the incident light into several energy ranges for lateral multijunction solar cells. A quadruple solar cell, in which the bottom cell is based on the InP lattice: GaInAsP/InGaAs and the top cell on the GaAs lattice: GaAs/InGaP. A device of this structure already exceeds 44 % efficiency under 297 suns AM1.5D (see Fig. 2.2). High material and production costs of III-V MJSC limit their use in space application or in concentrated photovoltaics (CPV), where high efficiency is crucial. The increase of the solar concentration factor in CPVs allows to reduce the area of the solar cell (material reduction) and to increase efficiency. Calculated current values for CPV power plants are from 0.08 / kWh to 0.15 / kWh € [41]. Further improvements of cell efficiencies can lead to a significant reduction of the system costs. Therefore, reduction of defects in the crystal layer is crucial.

Significant price reduction of MJSC can be achieved by applying silicon as a substrate. Silicon is the cheapest crystalline semiconductor substrate available, it is abundant, mechanically stable and its fabrication process is very well established. Moreover, the Si bandgap (1.12 eV) is close to the theoretical maximum efficiency for a single-junction solar cell, based on the Shockley-Queisser limit [5], and its bandgap is a perfect candidate for a high efficiency tandem device. Figure 2.4 shows a theoretical maximum efficiency for a tandem device in dependence of bandgap energies for the top and bottom cell [42]. A tandem solar cell with a Si substrate combined with a material of a bandgap around 1.73 eV can exceed 45 % efficiency. However, the lattice constant of Si (Fig. 2.2) is 5.43 Å, which is much smaller than the lattice constants of binary, ternary or quaternary III-V materials, typically used for MJSCs. This high lattice mismatch makes it difficult to directly substitute Ge or GaAs substrates by Si in MJSC. Further challenges in the growth of III-V materials on Si are thermal expansion coefficient, which can lead to cracks in the film during cooling down from the growth temperature and polarity control of III-V materials on Si or unintentional doping from both materials. One possibility to overcome these problems is to fabricate a tandem device through a wafer-bonding based of Si p-n junction with a top cell based on a different lattice constant. As an example a GaInP/Si dual junction solar cell (trough bonding) can exceed 30 % efficiency [43].

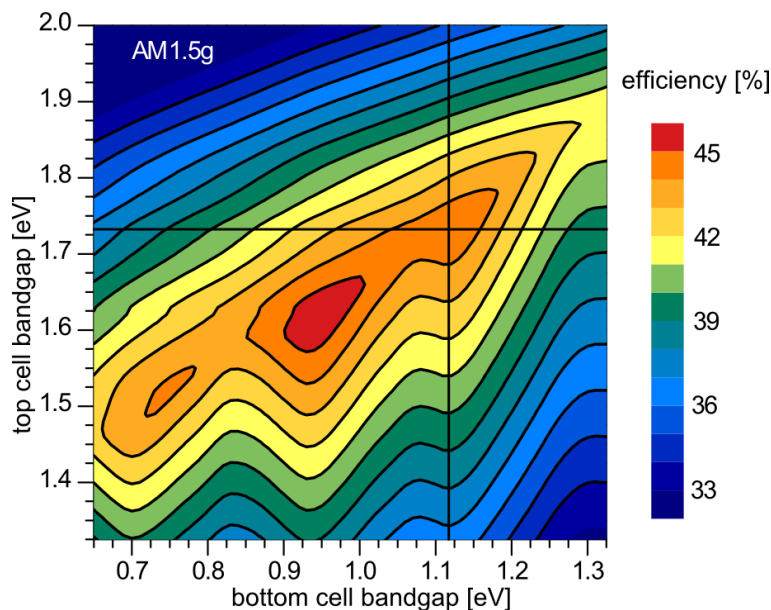


Fig. 2.4: Theoretical maximum efficiency for a tandem device in dependence of bandgap energies for the top and bottom cells, in the current matched detailed balance limit for solar AM1.5g irradiation at room temperature. The maximum efficiency for a two junction exceeds 46 % for the top cell with bandgap ~ 1.60 eV and the bottom cell with bandgap ~ 0.95 eV. Solar cell with Si (bandgap 1.12 eV) as a bottom cell in combination with a top absorber with a bandgap 1.73 eV can exceed 45 % efficiency. Figure after [42].

GaP represents a III-V material which exhibits a closest to Si lattice constant - 5.45 Å. Heteroepitaxial, defect free GaP growth on Si is very well established [20–25]. The high bandgap of GaP (2.26 eV) limits this material to application as a top junction cell. Alternatively GaP could serve as a window layer in Si SC [44], a collector in combination with Si absorber [45,46] or as a buffer layer for other III-V compounds, e.g. GaAsP solar cell [47–49]. Further possibilities to apply Si as a substrate for MJSCs is through application of a GaAs graded buffer layer [50]. As mentioned above, a 2-junction tandem cell based on materials with 1.72 eV and 1.12 eV bandgap has the theoretical potential to achieve maximum efficiency. By varying the lattice-matched composition of $\text{GaN}_x\text{P}_{1-x}\text{As}_y$ it is possible to achieve direct bandgaps in the range of 1.5 eV to 2.0 eV [51–53]. Moreover, Si as a substrate in combination with a top absorber between 1.6 and 1.8 eV has optimum photon energy to generate sufficient energy to electrolyze water in order to produce hydrogen and oxygen [52–54].

Motivation of this work is to prepare GaP/Si quasi-substrates with an active silicon bottom cell, which could serve as quasi-substrates for NWs growth (in case of Si(111)) or for further III-V growth (in case of Si(100)). However, growth of III-V materials in MOCVD hydrogen ambient requires precise control over the Si surface (more in chapter 4) and control of additional residuals in the reactor e.g. arsenic (more in subchapter 8.1).

2.2 Solar cell parameters

A solar cell is based on a semiconductor p-n junction formed by joining a p-type to an n-type semiconducting layers. The p-n junction serves as a charge separating contact to separate holes and electrons efficiently after generation. After photon absorption, the energy is given to the electron in the valence band and the electron "excites" into the conduction band where it is free to move within the semiconductor. The carriers are collected by metal contacts at the front and back of the cell. The top region in the solar cell is called collector and serves as a semipermeable membrane for electrons, i.e. an electron collector [55] (which in literature often is referred to as emitter). The bottom region is referred to as a base (or interchangeably absorber). The base of the cell is thicker and lighter doped than the collector, and absorbs most of the incident light. The cell design discussed in this thesis (see chapter 9) is based on a p-type absorber which corresponds to the lower doped (boron) Si substrate, and a highly doped (phosphorus or arsenic) n^+ -type layer on top, which is grown and doped in a MOCVD reactor.

In case where there is no external current, a p-n junction is in equilibrium between carrier generation, recombination, diffusion and drift in the presence of the electric field in the depletion region. The depletion region (region with no mobile charge carriers) is formed by a diffusion of electrons from the region of high electron concentration (n-type side of the junction) into the region of low electron concentration (p-type side of the junction). Despite the presence of the electric field, which creates a barrier to the diffusion of carriers across the electric field, some carriers still cross the junction by diffusion. This carrier becomes a majority carrier and its travel distance (before it recombines) is limited by its diffusion length. The current caused by the diffusion of carriers across the junction is called diffusion current and it is balanced by the equal and opposite drift current (minority carriers crossing the depletion region due to the electric field). Without illumination, the solar cell has the same electrical characteristics as a diode. The diode equation gives an expression for the current through a diode as a function of voltage:

$$I = I_0 \left(e^{\frac{qV}{nk_B T}} - 1 \right), \quad (1)$$

where: I_0 is dark saturation current, increases as the recombination in the cell or temperature increases, q is electron charge (1.6×10^{-19} coulomb), V is the voltage applied to the cell, n is ideality factor (a number between 1 and 2 which typically increases as the current decreases), k_B is the Boltzmann constant, and T is the absolute temperature. Illumination of a cell merely adds to the normal 'dark' currents in the diode so that the diode law becomes:

$$I = I_0 \left(e^{\frac{qV}{nk_B T}} - 1 \right) - I_L, \quad (2)$$

where I_L is light generated current. Figure 2.5 shows the reversed I-V curve of the cell (output curve is in the first quadrant), and is represented by:

$$I = I_L - I_0 \left(e^{\frac{qV}{nk_B T}} - 1 \right). \quad (3)$$

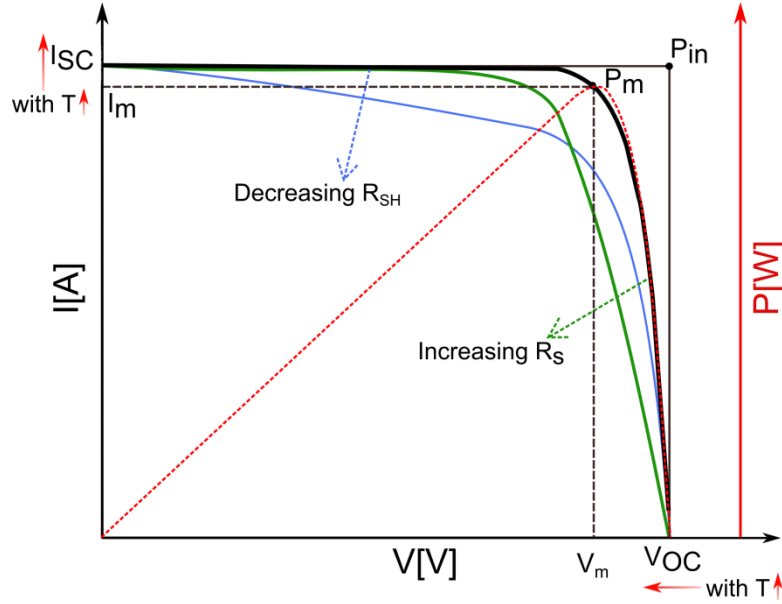


Fig. 2.5: The I-V characteristic of an ideal solar cell. I_{SC} – short circuit current, V_{OC} open circuit voltage, V_m and I_m maximum voltage and current. The area marked by a gray dashed rectangle is equal to the maximum power (point P_m). The red dotted line indicates power produced by the cell. Point P_{in} indicates input energy from the Sun. The effect of series (R_s) and shunt (R_{SH}) resistance on the I-V characteristic is indicated by green and blue color, respectively. Impact of temperature (T) on I_{SC} and V_{OC} are indicated by the red arrow: with increasing T the I_{SC} increases slightly and V_{OC} decreases linearly (diagram after [56]).

The two limiting parameters used to characterize the output of solar cells for given irradiance, operating temperature and area are [5]:

- 1) short circuit current (I_{sc}) - the maximum current, at zero voltage. Ideally, if $V = 0$, $I_{sc} = I_L$. I_{sc} is directly proportional to the available sunlight.
- 2) open circuit voltage (V_{OC}) - the maximum voltage, at zero current. The value of V_{oc} increases logarithmically with increased sunlight and is given by:

$$V_{OC} = \frac{nk_B T}{q} \ln\left(1 + \frac{I_L}{I_0}\right) \approx \frac{nk_B T}{q} \ln \frac{I_L}{I_0}. \quad (4)$$

The maximal power (P_{MP}) of the cell is produced at a voltage V_m and current I_m (see Fig. 2.5). The relation between maximal power of the cell and maximum power of an ideal cell is given by fill factor FF:

$$FF = \frac{V_m I_m}{V_{OC} I_{SC}} = \frac{P_{MP}}{V_{OC} I_{SC}}. \quad (5)$$

Efficiency is defined as the ratio of energy output from the solar cell to input energy from the Sun P_{in} :

$$\eta = \frac{P_{MP}}{P_{in}} = \frac{V_m I_m}{P_{in}} = \frac{V_{OC} I_{SC} FF}{P_{in}}. \quad (6)$$

In reality, each solar cell has additional resistances - a series resistance (R_S) and/or shunt resistance (R_{SH}) which reduce the efficiency. R_S is caused by an additional resistance between the metal contacts and the cell and the movement of current through the collector. It mainly affects the fill factor. R_{SH} is caused mainly by defects in the solar cell, causing power losses by providing an alternate current path for the light-generated current. The effect on the I-V characteristic from the both resistances is shown on Fig. 2.5 In the presence of both series and shunt resistances, the I-V curve of the solar cell is given by:

$$I = I_L - I_0 \left(e^{\frac{q(V+IR_S)}{nk_B T}} - \frac{V+IR_S}{R_{SH}} \right). \quad (7)$$

The ideality factor (n) describes how close the cell behaves as an ideal charge separating contact where no recombination occurs within the depletion region. At high voltages recombination in the device is dominated by the surface and bulk regions ($n=1$). At low voltages recombination in the junction dominates and an ideality factor approaches two ($n=2$). The I-V characteristic can be expressed by a two diode model (see Fig. 2.6):

$$I = I_L - I_{01} \left(e^{\frac{qV}{k_B T}} - 1 \right) - I_{02} \left(e^{\frac{qV}{2k_B T}} - 1 \right), \quad (8)$$

where the second part of the equation represents diffusion current, and the last part by recombination current. All in total, the current flowing through the cell can be expressed by:

$$I = I_L - I_{01} \left(e^{\frac{q(V+IR_S)}{k_B T}} - 1 \right) - I_{02} \left(e^{\frac{q(V+IR_S)}{2k_B T}} - 1 \right) - \frac{V+IR_S}{R_{SH}}. \quad (9)$$

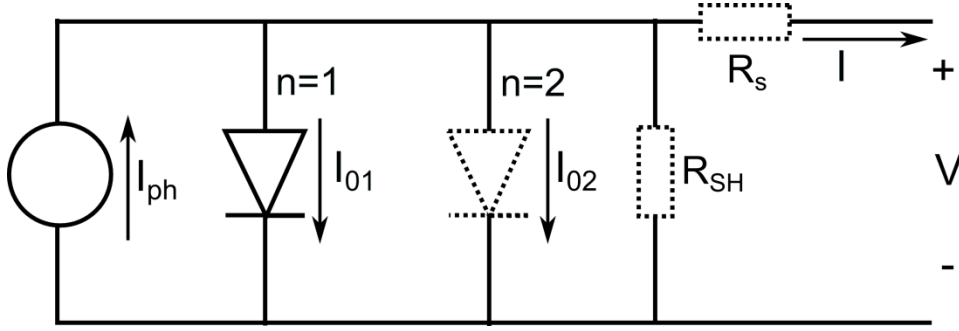


Fig. 2.6: A circuit of an ideal solar cell (full line) and real solar cell (components drawn by a dotted line), after [56].

Saturation currents I_{01} and I_{02} are caused by diffusion of minority carriers from the neutral regions to the depletion region and in approximation are determined by intrinsic carrier concentration.

Additionally temperature has an impact on solar cell performance. Increasing T causes an increase of dark current and V_{OC} is decreasing linearly [57]:

$$\frac{dV_{OC}}{dT} = \frac{1}{q} \frac{dE_g}{dT} - \frac{1}{T} \left(\frac{E_g}{q} - V_{OC} \right). \quad (10)$$

Solar cells with higher values of V_{OC} suffer smaller reductions in voltage with increasing temperature. The amount of photogenerated current (I_{ph}) increases slightly with rising temperatures because of an increase in the number of thermally generated carriers in the cell. For crystalline silicon the change of the current is around 0.065 % / °C and in V_{OC} around 0.50 % / °C and since the change in voltage is much stronger than the change in current, the total effect on efficiency tends to be similar to that on voltage, expressed by equation 12. The change in the temperature on the solar cell is indicated on Fig. 2.5.

Furthermore, changing the light concentration can increase efficiency of the solar cell. The light intensity on a solar cell is called the number of suns, where 1 sun corresponds to standard illumination at AM1.5. The V_{OC} and η can be expressed by equations:

$$\eta^{xsuns} = \frac{V_{OC}^{xsuns} I_{SC}^{xsuns} FF^{xsuns}}{P_{in}^{xsuns}} = \frac{V_{OC}^{xsuns} x I_{SC}^{1sun} FF^{xsuns}}{x P_{in}^{1sun}} = \frac{V_{OC}^{xsuns} I_{SC}^{1sun} FF^{xsuns}}{P_{in}^{1sun}}, \quad (11)$$

$$V_{OC}^{xsuns} = \frac{nk_B T}{q} \ln\left(\frac{x I_{ph}}{I_0}\right) = \frac{nk_B T}{q} \left[\ln\left(\frac{I_{ph}}{I_0}\right) + \ln x \right] = V_{OC}^{1sun} + \frac{nk_B T}{q} \ln x, \text{ therefore} \quad (12)$$

$$\eta^{xsuns} = \eta^{1sun} \frac{FF^{xsuns}}{FF^{1sun}} \left(1 + \frac{\frac{nk_B T}{q}}{V_{OC}^{1sun}} \ln x \right), \quad (13)$$

where X is the concentration of sun light (number of suns).

Additional parameters describing the solar cell are internal and external quantum efficiency. External quantum efficiency (EQE) is the ratio of electrons collected as photocurrent, per second to photons incident, and includes the effect of optical losses such as transmission and reflection. Internal quantum efficiency (QE) is defined by electrons collected as photocurrent, per second to photons absorbed, per second.

2.3 In-diffusion into silicon

Dopants in silicon can be divided into donors and acceptors. The donor (or the acceptor) impurity atoms have more (less) valence electrons than the semiconductor material, thus an n-type (p-type) region can be formed. If arsenic (As) or phosphorus (P) atoms are added to intrinsic silicon, four of their five valence electrons will bond with four neighboring Si atoms, but the fifth valence electron will remain free. This fifth electron of the impurity atom can become a negative charge carrier, as a very small amount of energy is required to detach this electron from its atom (ionization). In case of boron (B), which has only three valence electrons, the impurity will create an excess hole in the Si. The impurity atoms are ionized if they either donated or accepted an electron. The ionization of the impurities is dependent on the thermal energy and the position of the impurity level within the energy bandgap [58]. The ionization energy for P and As in Si, measured from the valence band edge are 45 meV and 54 meV, respectively [10]. Impurity atoms may occupy either substitutional or interstitial positions in the Si lattice [59]. The atoms occupy the substitutional position when the dopant atoms can contribute free electrons or holes. During high temperature processes the impurity is redistributed (due to random thermal motion) into Si – diffusion process. Figure 2.7 depicts three different mechanisms by which the impurity diffusion may occur: (a) vacancy, (b) interstitial or a (c) combination of both. Vacancy diffusion mechanism (Fig. 2.7 (a)) involves an interchange of places by the dopant atom and a neighboring vacancy (a presence of vacancy is required). Interstitial diffusion (Fig. 2.7 (b)) occurs when an interstitial atom jumps to another interstitial position [59]. Interstitialcy diffusion Fig. 2.7 (c)) results from silicon self-interstitials displacing substitutional impurities to an interstitial position. The impurity then might substitute Si lattice atom and move it to self-interstitial position. Arsenic and phosphorus are believed to diffuse into silicon through a vacancy mechanism with an interstitialcy component; boron on the other hand is assumed to diffuse exclusively by a vacancy mechanism [59–62]. At high concentration above $>10^{20}$ ($>10^{19}$), arsenic (phosphorus) atoms might be electrically inactive due to a cluster formation. One possible electrically inactive form is a formation of a cluster of four As atoms with a vacancy, which leaves no free electron. In order for atoms to jump from one position to another, atoms need energy to break bonds with neighbors, and to cause the necessary lattice distortions during jump.

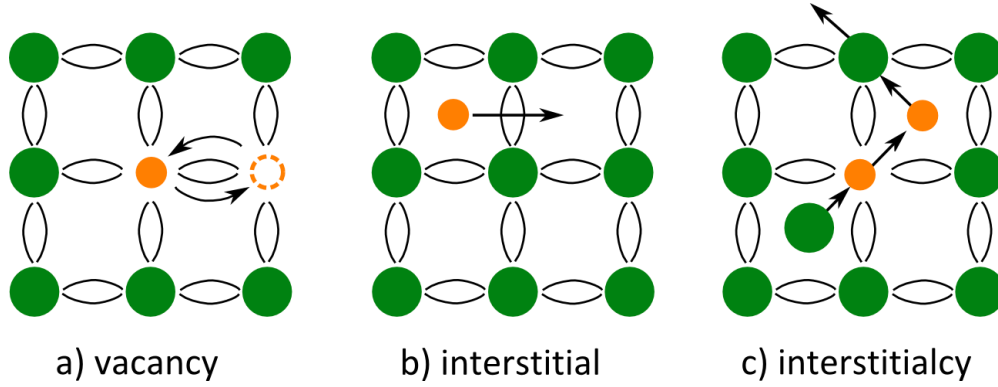


Fig. 2.7: Impurity diffusion mechanisms: (a) vacancy, (b) interstitial, (c) interstitialcy. The green circles and the small orange circles represent Si and impurity atoms, respectively (Fig. after [59]).

The probability of an atom to jump from one position to the next one increases exponentially with increasing temperature [59]. Fick's first law states that regions with a large concentration gradient diffuse more rapidly than regions with a small concentration gradient. The flux of atoms diffusing from high concentration to low concentration is proportional to the material's diffusivity coefficient and diffusion gradient. Fick's second law describes the changes of the concentration profile in dependence of time. The diffusion coefficient is the measure of mobility of diffusing species. The diffusion coefficient (D) is dependent on the temperature and can be described by Arrhenius equation:

$$D = D_0 \cdot \exp\left(\frac{-E_A}{k_B \cdot T}\right), \quad (14)$$

where D_0 is the maximum diffusion coefficient [m^2 / s], E_A is the activation energy of diffusion [eV / atom] (energy required to jump from one site to the next one), k_B is the Boltzmann constant and T is the absolute temperature [K]. The Boltzmann constant can be used interchangeably with the gas constant ($R = k_B \cdot N_0$, where N_0 is the Avogadro's number). If the Boltzmann constant is changed for the gas constant, the E_A is expressed per mole instead of per atom. The diffusion coefficient of phosphorus is greater than of arsenic [59].

In this work, in order to in-diffuse the dopant into Si, the Si substrate was annealed under a constant flow of a precursor tertiarybutylarsine or tertiarybutylphosphine (TBAs or TBP). In this case, the dopant source can be considered as an infinite source. The impurity concentration can be calculated from the equation:

$$N(x, t) = N_0 \cdot \operatorname{erfc}\left(\frac{x}{2\sqrt{Dt}}\right), \quad (15)$$

where: $N(x, t)$ – function of impurity concentration [mol / m^3], N_0 – impurity concentration at surface [mol / m^3], x – deepness [m], t – time [s], D – diffusion

coefficient [m^2 / s]. The *erfc* is the complementary error function. In this case, the doping concentration depends on the diffusion coefficient and time (assuming the same material and same conditions) and for arsenic the impurity concentration is expected to be lower than for phosphorus.

2.4 Si and GaP crystal structure and surface

The atomic structure of Si regarding steps and surface reconstruction is highly important for subsequent defect free III-V heteroepitaxy. This subchapter focuses on the (100) and (111) surfaces of silicon and gallium phosphide. The crystal structure, surface reconstruction, hydrogen and group-V termination are discussed.

2.4.1 Si and GaP crystal structure

Si crystallizes in a diamond structure, which equals two face-centered cubic (FCC) sublattices shifted by $(\frac{1}{4}, \frac{1}{4}, \frac{1}{4})$ (see Fig. 2.8 (a)). Each atom is connected to its four nearest neighbors by four tetrahedral (covalent) bonds that differ in spatial orientation of the two sublattices. In contrast, III-V semiconductors exhibit a zincblende structure (Fig. 2.8 (b)), where the two sublattices are occupied by different atomic species. Accordingly, the symmetry in the zincblende structure is reduced compared to the diamond structure. In the crystal lattice in Fig. 2.8 (a) and (b) the red rectangular and grey triangular are indicated (100) and (111) planes, respectively. The (100) surface cut would lead to two dangling bonds per Si atom, whereas cut of (111) plane, one dangling bond.

Growth of III-V material on single-domain silicon can lead to problems during heteroepitaxy, which are discussed in detail in the following subchapter 2.7.

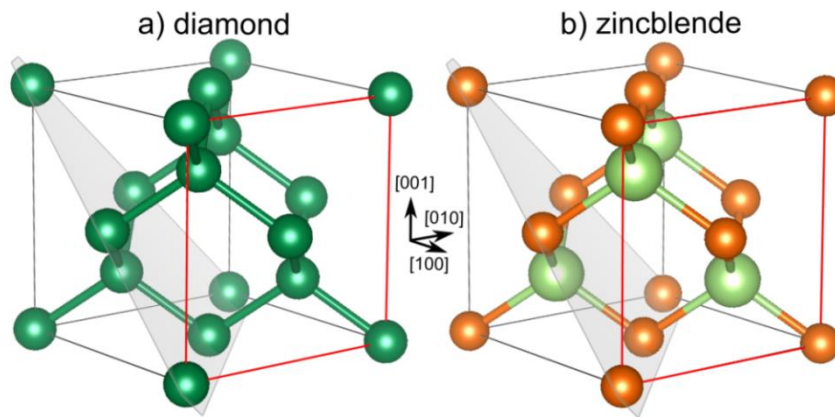


Fig. 2.8: (a) diamond and (b) lattice crystal structure. Red rectangular and grey triangular is indicating the (100) and (111) plane, respectively. Figure was done using the software VESTA [63].

2.4.2 Si(100) surface in hydrogen ambient

Clean surface

In 1959, Schlier and Farnsworth [64] first, observed a (2×1) surface reconstruction on Si(001) in UHV by applying LEED. In this reconstruction, atoms on the surface are separated by 3.84 \AA , which is more than the Si-Si bond length in the bulk (2.35 \AA). In order to reduce the number of broken bonds and to minimize the surface energy, the atoms rearrange and two neighboring surface atoms move towards each other to bond and form parallel rows of dimerized atoms along $\langle 110 \rangle$ directions. The formation of dimers decreases the density of dangling bonds by two. Due to the surface dimerization the subsurface distortion extends up to 4-5 layers into the bulk [65]. There are two possible dimer models: symmetric and asymmetric. In the symmetric dimer model, the atoms in the pair have the same height above the surface. In the asymmetric, also called buckled dimer model, the dimers are buckled where atoms in the pair have different height above the surface plane. On Si(100) with (2×1) surface reconstruction the surface energy for the symmetric and the asymmetric dimer reconstructions are 2.74 eV/dimer and 2.59 eV/dimer , respectively. Figure 2.9 shows dimerization of Si(100) for ideal (1×1) and (2×1) surface reconstruction. The upper row represents the top view, and the lower row the side view.

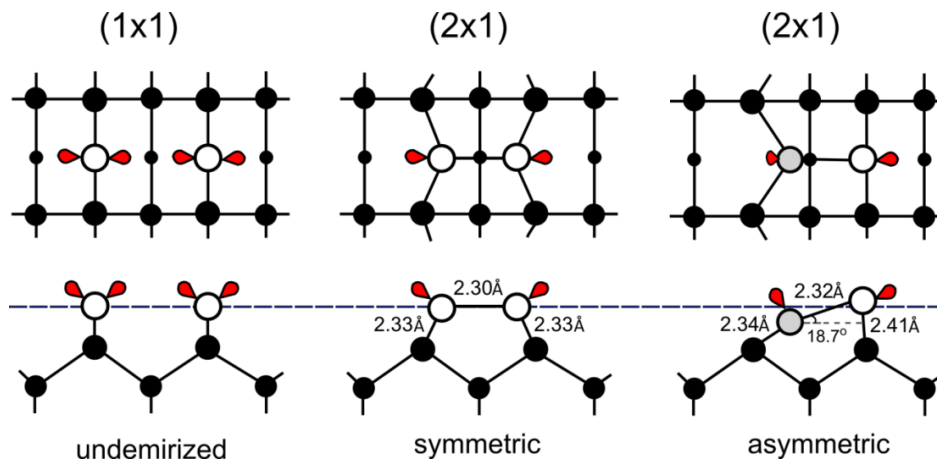


Fig. 2.9: Dimerization of Si(100), Top view (upper row) and side view (bottom row) of non-reconstructed surface (1×1) and reconstructed surface (2×1) with symmetric and asymmetric ([66]dimers (after [67,68])). White and gray surface atoms indicate downward buckled dimer atom, subsurface and bulk atoms are black. The bond length and the angle of the buckled dimer structure indicates a difference between symmetric and asymmetric dimers. If neighboring dimer rows buckle in the opposite direction, the $p(2\times 2)$ or $c(4\times 2)$ surface reconstructions are formed.

For (2×1) surface reconstruction two cases are shown, symmetric dimers and asymmetric (buckled) dimers with the lower surface energy. Asymmetric dimers are more favorable on higher periodicities as $p(2\times 2)$ or $c(4\times 2)$. The buckled dimers have the lowest energy when arranged in a $c(4\times 2)$ array. The formation of an asymmetric dimer leads to a

significant amount of mechanical stress at the surface. This surface stress can be partially released if the dimers are buckled in alternating form, which reduces the surface energy. Different orders of arrangements of these buckled dimers result in the $p(2\times 2)$ or $c(4\times 2)$ reconstructions. These are the most stable reconstructions on the Si(001) surface.

Hydrogen interaction with silicon surface

Exposure of the silicon surface in UHV at elevated temperature, to atomic hydrogen (produced by predissociation of H_2) leads to hydrogen passivation. The Si dangling bonds easily interact with H-1s orbital and rehybridize, forming covalent Si-H bonds. Depending on the temperature and the chemical potential of hydrogen three surface reconstructions are possible: monohydride (2×1), dihydride (1×1) and mixed (3×1) phase [69]. In the monohydride phase H atoms saturate the remaining dangling bonds of the Si dimers suppressing interaction between them and forming only symmetric dimer bonds. H coverage (desorption / adsorption rate) depends on the partial pressure of H_2 and on substrate temperature [70]. Moreover, H changes the atomic structure of the steps which can affect the Si(100) surface step and domain structure [71]. In 1987 Chadi [72] presented a model where steps can be labeled according to their height: either single- (S) or double-layer (D) and to the dimer orientation on the terrace-perpendicular (A-type) or parallel (B-type) to the step edge. Figure 2.10 depicts four possible steps arrangements based on this model: S_A (top left) and S_B (top right), as well as D_A (bottom left) and D_B (bottom right). The atomic structures of S_B , D_A , and D_B steps exhibits rebounded edge atoms - the second-layer edge atoms are bonded with the lower terrace atoms. On A-type terraces the dimers are perpendicular to the [011] direction and correspond to a (1×2) surface reconstruction (B-type surface corresponds to (2×1) surface reconstruction). In the case of both A- and B- type single-layer steps the dimer orientation is rotated by 90° for every lower terrace, inducing a two-domain surface. In case of double-layer steps the dimers retain their orientation on each step resulting in a single-domain surface. The S_B -type step edge exhibits two possible configurations, a rebonded and a non-rebonded S_B step. Since the rebonded S_B step features less dangling bonds, it is energetically favored over the non-rebonded S_B step. The single-layer step S_A has lowest formation energy because it is the only step, which does not lead to large strains or to extra dangling bonds. According to Chadi [72] for Si(001) with 5.4° offcut the D_A step requires the most energy to form after the S_B and the D_B , while the S_A step has the lowest formation energy. Single-layer steps are more commonly seen on normal offcut Si(001) substrates, while double-layer steps are more favorable on tilted surfaces [72]. This model was confirmed by Griffith *et al.* [73] on Si(001) substrates with a 2° or 4° offcut in $[1\bar{1}0]$ direction after sputtering by argon (Ar) and annealing at $\sim 900^\circ\text{C}$ in UHV. By STM they confirmed alternating A-type and B-type single steps with many kinks on the 2° surface, and straight and evenly spaced D_B steps on the 4° . Laracuate & Whitman [71] based on STM scans of Si(100) prepared in UHV, proposed a model in which, for substrates with an offcut lower than 7.3° towards [011] direction, S_A and S_B steps are more probable over D_B .

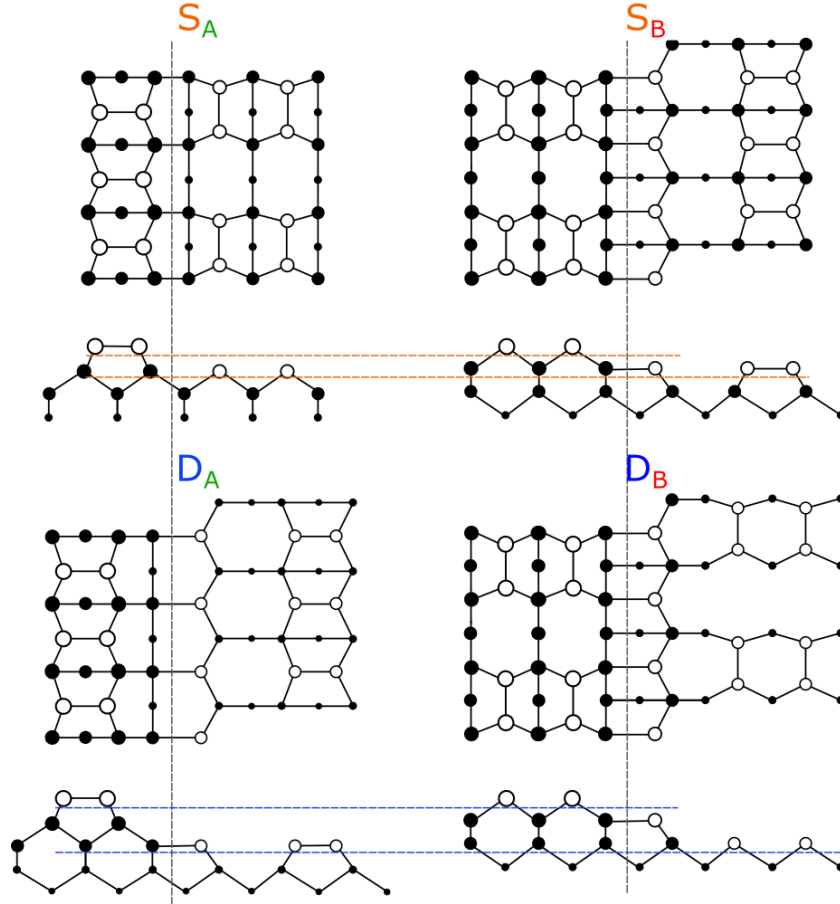


Fig. 2.10: Four possible atomic structures and steps arrangements for Si(100) with a (2×1) surface reconstruction: S_A (top left) and S_B (top right), as well as D_A (bottom left) and D_B (bottom right). In the case of S_B , D_A , and D_B steps edge atoms are rebounded - the second layer edge atoms are bonded with the lower terrace atoms. On A-type terraces the dimers are perpendicular to the $[011]$ direction and correspond to (1×2) surface reconstruction (in case of B-type surface exhibit (2×1) surface reconstruction). In the case of both A- and B-type single-layer steps the dimer orientation is rotated by 90° for every lower terrace, inducing a two-domain surface. In the case of double-layer steps the dimers retain their orientation on each step resulting in single-domain surface. White atoms indicate top most atoms, passivated by monohydride. Black atoms indicate atoms in the lattice (figure after [72]).

A Si(100) surface with 2° offcut, prepared in (MO)CVD ambient by Kitahara and Ueda [74] by annealing in H_2 revealed mostly retreat S_A steps, when measured by STM. For Si(001) with a 0.1° offcut in $[110]$ direction double-layer steps were observed [22] as in case of Si(001) with 0.12° offcut in $[1\bar{1}0]$ direction, where double-layer steps were found to dominate on the surface [75]. In both cases, the preparation included homoepitaxial buffer growth and subsequent high-temperature annealing in H_2 .

Step formation and hydrogen termination on Si(100) substrates with 0.1° , 2° and 6° offcut in $[011]$ was intensively studied by our group. Annealing for 30 min in H_2 ambient ensures a surface free of oxide and other contamination [76]. FTIR analysis revealed monohydride termination of the surface [77]. Depending on process conditions (more

precisely, the cooling procedure) a Si surface with either energetically unfavorable D_A or D_B steps can be prepared [78]. During the surface preparation, there is a competition between the kinetically driven D_A and the energetically governed D_B step formation mechanisms. The Si(100) surface preparation in MOCVD ambient is discussed in more detail in chapter 4.1.

2.4.3 Si(111) surface in hydrogen ambient

Surface reconstruction

The interaction of the Si(100) surface with the H_2 ambient has a great impact on the atomic surface structure, as described above. In contrast, the preparation of Si(111) and its interaction with common CVD-related species such as atomic or molecular hydrogen, has been studied almost exclusively in UHV.

In UHV, adsorption of hydrogen on Si(111) has been found only for H atoms, whereas molecular hydrogen was found not to react directly with the Si(111) surface [79,80]. At elevated temperatures (above 350 °C) atomic hydrogen passivates the Si(111) surface and forms mono-, di- and trihydrides on the surface, which leads to a (1×1) surface reconstruction as confirmed by LEED [79] or STM [81]. Moreover, exposure to atomic hydrogen leads to a roughening of the Si(111) surface due to etching by forming SiH_4 products [79,80]. Wet chemical etching in HF leads to well-ordered Si(111) surfaces, but microscopically rough, with monohydride on the terraces and coupled monohydride, di- and tri-hydride on the steps, as proved by FTIR [82,83].

Steps structure

There are two principal direction of offcut for the Si(111) surface: $\langle \bar{1}\bar{1}2 \rangle$ and $\langle 11\bar{2} \rangle$. Figure 2.11 exhibits a side view of the Si(111) lattice structure with highlighted directions in $[\bar{1}\bar{1}2]$ and $[11\bar{2}]$. The long dashed lines indicate Si (001), (113) and (110) surfaces. Excluding any reconstruction and assuming straight steps, in the first case, an atom on the step possesses two back bonds to other Si atoms, in the second case three (see the inset in Fig. 2.11, bonds to the silicon are highlighted in a yellow color). This results in two free dangling bonds for a Si atom on the $\langle \bar{1}\bar{1}2 \rangle$ steps edges and only one free dangling bond for a Si atom on the $\langle 11\bar{2} \rangle$ steps edges. In consequence, less energy is required to remove an atom from $\langle \bar{1}\bar{1}2 \rangle$ steps than from $\langle 11\bar{2} \rangle$ steps. In the same process conditions, the $\langle \bar{1}\bar{1}2 \rangle$ steps should be less stable than the $\langle 11\bar{2} \rangle$ steps, which might result in a different step structure for both directions. The diamond lattice shows a 3-fold symmetry along the $[111]$ direction. This means that the crystal will have the same properties with a rotation of 120°. As shown on Fig. 2.12 steps in direction $[\bar{1}2\bar{1}]$ and $[2\bar{1}\bar{1}]$ have the same properties as steps in $[\bar{1}\bar{1}2]$ direction. In analogy, the steps in $[11\bar{2}]$ direction have the same properties as every direction rotated by 120°. Si atoms on the step edges in $[\bar{1}2\bar{1}]$, $[2\bar{1}\bar{1}]$ and $[\bar{1}\bar{1}2]$ direction can have either vertical or horizontal

dangling bonds (see Fig. 2.12). In contrast, the Si atoms on the step edges in $[11\bar{2}]$, $[1\bar{2}1]$ and $[\bar{2}11]$ direction possess only one dangling bond.

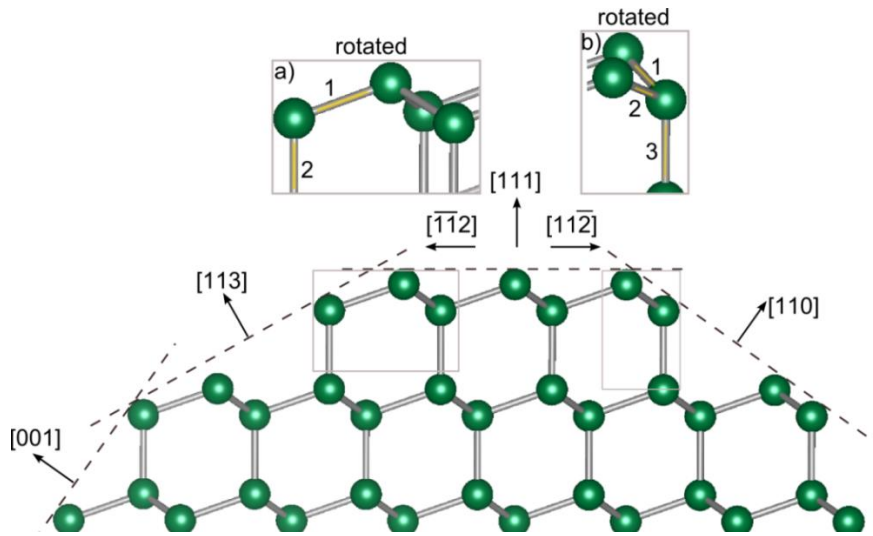


Fig. 2.11: Side view of the Si(111) lattice structure with highlighted terraces of $[001]$, $[113]$, $[111]$ and $[110]$ orientations. Insets (a) and (b) show a rotated steps in $[\bar{1}\bar{1}2]$ and $[11\bar{2}]$ direction, the yellow color highlights the number of back bonds of the Si atom to the step. Figure was done using the software VESTA [63].

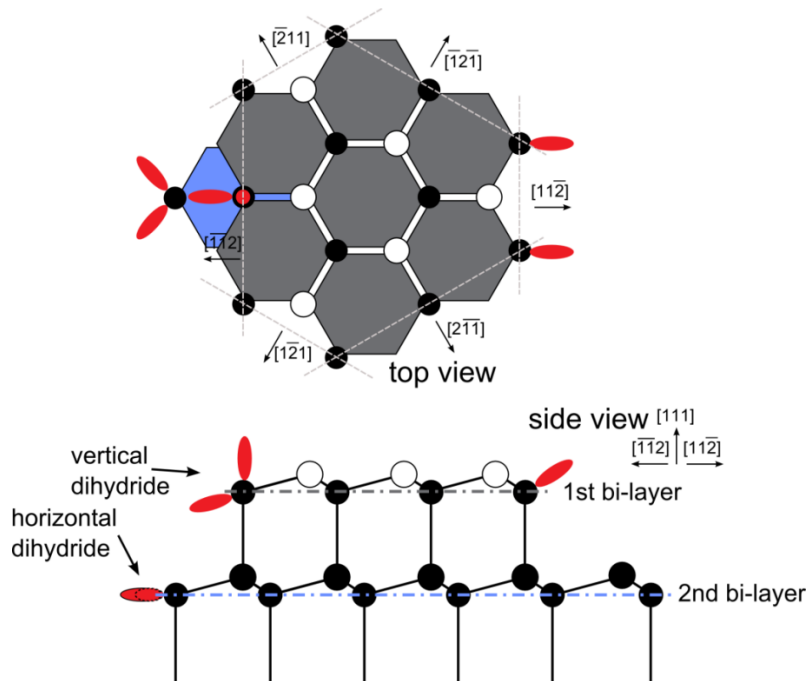


Fig. 2.12: Top view and side view of Si(111) crystal lattice. White atoms indicate the top most Si atoms possessing one dangling bond. Steps in direction $[\bar{1}\bar{1}2]$ possess two dangling bonds (red oval) either horizontal or vertical, same as the steps in $[\bar{1}2\bar{1}]$ and $[\bar{2}\bar{1}\bar{1}]$ direction. Steps in $[11\bar{2}]$ direction (or in $[1\bar{2}1]$ and $[\bar{2}11]$ direction) possess only one dangling bond and in consequence are more stable.

HF dip of Si(111) leads to unreconstructed surfaces with an ideal monohydride termination. This has been confirmed by (1×1) LEED pattern [84] or Si-H bonds on the surface detected by multiple-internal-reflection infrared-absorption difference spectrum [85]. Burrows *et al.* [82] were the first to show by IR spectra of HF-treated Si(111) that the surface is covered by not only monohydride but also di- and tri-hydride suggesting that the surface is microscopically rough.

This work was extended by Chabal *et al.* [86] confirming a microscopically rough surface with a regular array of double-layer steps (after HF treatment). By multiple internal infrared reflection spectroscopy he confirmed a monohydride termination at the Si surface, coupled monohydride at the steps and possible dihydride at the steps with an additional interaction of the trihydride.

Higashi *et al.* [87] or [88] have shown that the surface of Si(111) after wet chemical etching is much more atomically flat and extremely stable towards contamination by increasing the pH of HF solution by adding an NH_4F (buffered HF solution).

P. van der Putte *et al.* [89] observed a different surface morphology after etching in HCL for Si substrate with different misorientation. Si substrates with an offcut in two directions $[\bar{1}\bar{1}2]$ and $[11\bar{2}]$, were investigated applying IR absorption spectroscopy by Jakob and Chabal [90]. They showed that after wet chemical etching substrates with an offcut in $[\bar{1}\bar{1}2]$ direction exhibit IR absorbance at different frequencies, depending on the pH of the solution. The substrates which were etched in a solution with a pH = 6.6 (for three minutes) show absorption bands corresponding to a monohydride and dihydride species. For the substrates etched in a solution with a higher pH = 7.8 (for seven minutes) the modes attributed to the dihydride type of steps were not detected in the IR spectrum, indicating that only monohydride species are present on the surface. The results imply a transformation of straight $[\bar{1}\bar{1}2]$ dihydride steps into a stable monohydride zig-zag chain of ideal $[11\bar{2}]$ steps with an angle of $60^\circ / 120^\circ$ to the original step edges [91]. In consequence, multiple steps predominate over single bilayer steps and thereby the surface roughness is increased. Substrates with an offcut in the opposite direction, regardless of the etching process, exhibited absorption bands in the IR spectrum corresponding only to the monohydride species. Atoms on the steps possess only one dangling bond and therefore, the steps are more stable and it leads to the formation of straight steps. These results were later confirmed by Pietsch *et al.* [92] by STM scans and LEED measurements which revealed the different behavior of the steps on the atomic scale.

Flidr *et al.* [93] describes the kinetics of the steps after etching in NH_4F solution (for 15 min). This solution removes silicon through two steps: first the oxidation and second the etching step. After the first step the surface is unreconstructed and H-terminated [87]. Samples with an offcut in the $[\bar{1}\bar{1}2]$ direction on STM scans showed that approximately 2/3 of steps are orientated in a $[11\bar{2}]$ direction. In addition, Kinetic Monte Carlo

simulations of Si(111) surfaces show that the dihydride terminated steps are at least 20 times more reactive than monohydride-terminated steps.

Despite extensive research on the reaction of the Si surface with atomic hydrogen, little is known about the interaction between the Si surface with molecular hydrogen. However, it was indicated that the molecular hydrogen does not cause a direct etching reaction with Si(111) surface [80] and its direct adsorption on the surface is more than six orders of magnitude lower than the adsorption of the atomic hydrogen [79]. Adsorption of molecular hydrogen at nearly atmospheric pressure can differ, and will be described in the following chapters.

2.4.4 GaP(100) surface in hydrogen ambient

In MOCVD ambient the GaP(100) surface typically exhibits either (2×4) mixed dimer surface reconstruction when prepared in Ga-rich conditions [94], or the (2×2)/c(4×2) hydrogen stabilized P-rich surface [95,96], when prepared in P-rich ambient. The following section focuses on the P-rich GaP(100) surface, since that surface is prepared after GaP(100) heteroepitaxy on Si(100) substrates (subchapter 8.3). In H₂ ambient, this surface can be prepared after deoxidation of GaP(100) wafers or homoepitaxial growth in P-rich ambient.

According to Hahn *et al.* [94], at this P-rich surface, the top layer is terminated by two, oppositely directed buckled phosphorus dimers, each stabilized by a hydrogen atom which saturates one of the dangling bonds of the dimer (see Fig. 2.13) [96,97]. The buckled dimers are aligned in zig-zag chains along the [011] direction. This (2×2) surface reconstruction is highly ordered, however, if in adjacent rows a phase shift of the periodicity of half unit cell takes place, a c(4×2) reconstruction develops (see Fig. 2.13 (a)). In the LEED pattern from this surface, the P-dimers cause spots at half order along the dimer axis parallel to [0 $\bar{1}$ 1] direction [94,98], in consequence the LEED pattern reflects (2×1)-like surface reconstruction.

The GaP(100) P-rich surface prepared in MOCVD exhibits a characteristic RA spectrum [96]. Figure 2.13 (b) compares experimental data from *Ref.* [96] measured at low temperature with spectrum calculated by density functional theory in the local-density approximation (DFT-LDA) from Hahn *et al.* [94]. The P-rich GaP(100) RA spectrum (measured at the low temperature of 20 Kelvin) exhibits a characteristic sharp minimum (P₁) and maximum (P₂) peak at 2.6 and 3.7 eV, respectively. Despite lower intensity of the calculated spectrum and differences in the line shape in comparison to the measured one, the spectrum exhibits the main characteristics – minimum at around 2.6 eV and maximum at around 3.7 eV. The origin of the P₁ peak is attributed mainly to transitions between surface P lone pairs of electrons and empty surface resonances [94]. The origin of the P₂ peak is assigned to a surface modified bulk E₁ transition [101].

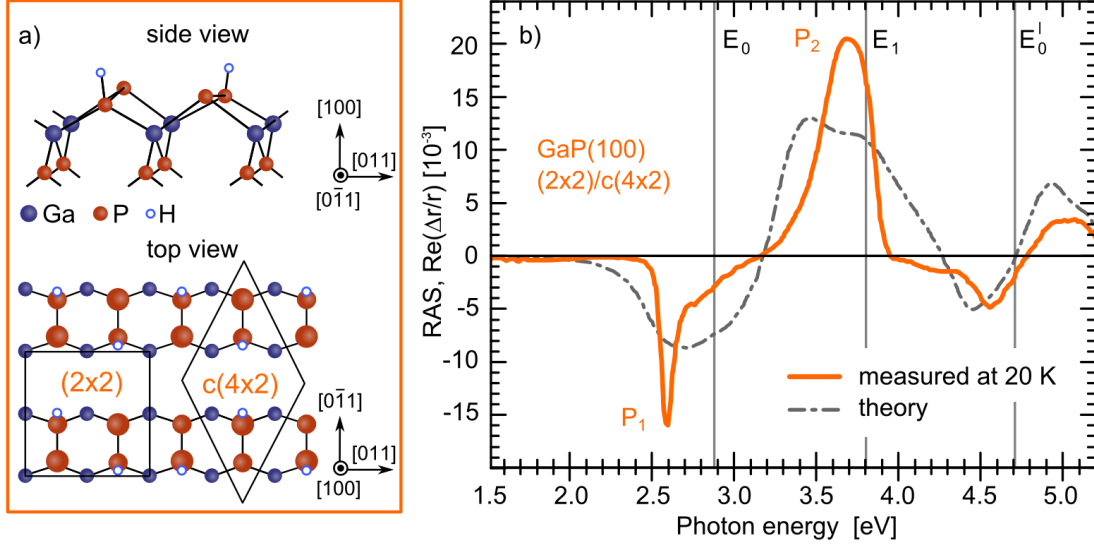


Fig. 2.13: (a) P-rich GaP(100) - (2×2)/c(4×2) surface reconstruction (in H₂ ambient) – top: side view, bottom: top view, the black rectangular and rhombus indicate the unit cells. (b) RA spectrum of GaP(100) P-rich surface – measured at 20K from Ref. [98] (orange line) and calculated from Ref. [94] (gray, dash-dotted line). Grey vertical lines indicate the interband transition energies of GaP at 20 K [99] (figure after [100]).

2.4.5 GaP(111) surface in hydrogen ambient

In the case of the GaP(111) B-type surface, various studies have reported a threefold (1×1) LEED pattern [102–104]. However, van Bommel *et al.* [105] observed a more complicated LEED pattern, which was confirmed by Hattori *et al.* [106], and further analyzed by STM. Hattori *et al.* [106] showed that the surface consists of six equivalent reconstruction domains containing two reconstruction units. Their modeling of the LEED pattern based on this proposed reconstruction provided good agreement with the experimental LEED data.

For GaP(111) A-type polarity (Ga-rich) a sharp and stable (2×2) LEED pattern was observed after bombarding the sample with Ar ions and annealing above 550°C [107]. This structure is vacancy-stabilized, with one quarter of the surface Ga atoms missing. The orbitals on the remaining surface Ga atoms rehybridize into sp² orbitals, while those in the nearest-neighbor p atoms rehybridize into s²p³ orbitals. This model was confirmed by STM scans [108]. There is very little known about GaP(111) surfaces in a CVD ambient, but these are discussed in chapter 8.

2.4.6 Arsenic terminated Si(100) surface

Exposure of a deoxidized Si(100) surface to As strongly affects surface morphology and dimer orientation [109]. The Si(100) interaction was well described in UHV conditions. It was shown that in UHV As₄ strongly impacts the atomic order at clean Si(100)

surfaces. The interaction of As with vicinal Si surfaces is complicated by the competition between kinetic and energetic effects [109]. The addition of arsenic to the single-domain surface results in a coverage of a single monolayer of As-As dimers and depending on process preparation the As atoms can either be added to the Si surface or substitute Si atoms. Controlling process parameters (As_4 flux and temperature) either Si:As A-type, (1×2) or Si:As B-type, (2×1) can be prepared. The lowest-energy structure is Si:As B-type, because this orientation requires no rearrangement of the underlying substrate and it is most likely the one determined by kinetic limits [72,110,111], but in many circumstances, the kinetically limited Si:As A-type structure was found. The Si:As surface preparation consequently can influence a lattice orientation of subsequent III-V heteroepitaxial film [109]. Moreover, STM images have shown qualitative differences in the step edge smoothness between the Si:As A and B- type cases, suggesting that the crystal quality of III-V films grown on these templates may differ. In MOCVD it was shown that arsine (AsH_3) and TBAs were found to etch Si(100) surfaces [98,112]. To enhance the surface smoothness after exposure to TBAs, an additional heating under hydrogen flow to 900°C was applied, followed by immediate cooling down. LEED measurements confirm a $(2 \times 1)/(1 \times 2)$ surface without a preferential domain - equal distribution of the different domains. In contrast, recently it was shown [113] that annealing under AsH_3 forms A-type dimer orientation on the surface, (1×2) surface reconstruction.

2.4.7 Arsenic terminated Si(111) surface

In UHV, Olmstead *et al.* [114] found that the strong reconstruction of the Si(111) (7×7) surface is removed upon exposure to As_4 molecular beam at 350°C . By LEED and XPS they confirmed a model in which a monolayer of As atoms replaces the outermost Si layer leading to a well order surface with (1×1) reconstruction. Three arsenic orbitals are taking part in bonding to Si and the two remaining valence electrons in a nonbonding "lone-pair" state. This surface is extremely stable with respect to either thermal annealing or contamination. The absence of unsaturated bonding orbitals on the Si(111):As surface greatly reduces the susceptibility of the surface to adsorption of either additional As or contaminants such as oxygen. The excess arsenic is bound to the surface only weakly, and can be removed by annealing at 200°C . The authors in *Ref.* [114] suggest that this surface strongly affects the first stage for GaAs growth, in which Ga is predicted to bound to arsenic. Patel *et al.* [115] confirmed that As termination of Si(111) determines the crystal polarity of subsequently grown GaAs, which turns out to be the (111) (B-type polarity). An additional intermixing between Si and GaAs interface is energetically favorable [116]. Step structure of Si(111) under As deposition was investigated by Ohno *et al.*, [117] on Si with an offcut toward $[\bar{2}11]$ and $[2\bar{1}\bar{1}]$. In both cases they observed double layer height steps and the LEED pattern exhibited spot splitting along offcuts direction. Antons *et al.* [118] compared *ab initio* calculations for the structures and energies of the $[11\bar{2}]$ and $[\bar{1}\bar{1}2]$ oriented step edges on Si(111) after exposure to As in

UHV. The STM images showed triangular and hexagonal islands terminated by steps with $[11\bar{2}]$ and/or $[\bar{1}\bar{1}2]$ orientation. The islands showed the same (1×1) surface reconstruction as the terraces and its height was equal to Si(111) double layer. For both step orientations, an incorporation of additional As atoms at the terrace edge that replace the exposed Si atoms in the second layer yields the lowest energy. Despite extensive research in UHV ambient very little is known about Si(111):As surface in MOCVD.

2.5 Hydrogen coverage on Si(100)

Hydrogen termination of the Si(100) surface depends strongly on H_2 pressure and substrate temperature. Komeda and Kumagai [70] described a model for the hydrogen coverage (θ) of Si(100) surfaces during annealing in H_2 based on STM observations in UHV. Hydrogen coverage is a function of pressure and substrate temperature, and is determined by the balance between the hydrogen adsorption and desorption rate at the Si surface. The change of the hydrogen coverage with time $\theta(t)$ can be written as:

$$\frac{d\theta(t)}{dt} = R_{\text{ads}} - R_{\text{des}}, \quad (16)$$

where R_{ads} and R_{des} correspond to the adsorption and desorption rate, respectively.

The hydrogen coverage was calculated in *Ref.* [66] in dependence of the substrate temperature for different H_2 pressures from 0.1 to 1000 mbar [119], based on calculated R_{ads} [120] and R_{des} [70]. The calculation was done assuming equilibrium conditions regarding surface and gas phase temperature ($T_s = T_g$) as well as regarding hydrogen coverage ($t \rightarrow \infty$). Figure 2.14 shows calculated hydrogen coverage on Si(100), the 0 ML and 1 ML refer to a clean and a monohydride terminated surface, respectively. From the plot, a strong dependence of the hydrogen pressure and the hydrogen adsorption and desorption is visible. With lower pressure the H_2 coverage decreases. The Si deoxidation and subsequent domain formation requires temperatures of 1000 °C and 700 – 900 °C, respectively. Typically the Si deoxidation step is carried out at 950 mbar and the domain preparation in dependence of the procedure at 950 mbar or 50 mbar. Subsequent III-V nucleation is carried out usually at reduced pressure at low temperature (420 °C). From the plot (Fig. 2.14), the complete hydrogen coverage of the Si(100) surface is estimated to be below 630 °C, about 95 % coverage at 800 °C and about 25 % at 1000 °C for nearly atmospheric pressure of hydrogen. For increasing annealing temperature, desorption eventually outbalances adsorption of hydrogen, but partial hydrogen coverage is predicted far beyond 1100 °C [66,119]. For lower H_2 pressures the transition from clean to hydrogen covered surface shifts to lower temperatures. The model agrees well with the *in situ* RAS results during cooling from 1000 °C to 600 °C in 950 mbar H_2 ambient, that were published in [78].

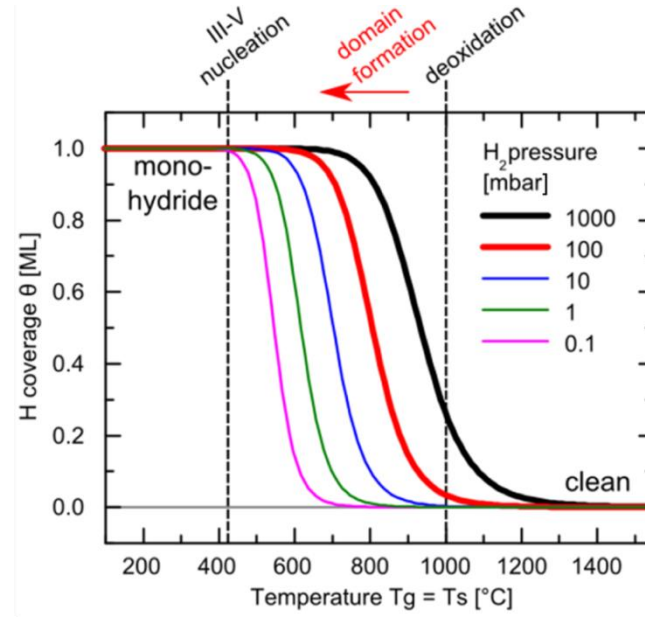


Fig. 2.14: H coverage in dependence of temperature for different H_2 pressures, taken from [66,119].

2.6 Challenges in III-V/Si heteroepitaxy

The main challenge of defect free, III-V heteroepitaxy on Si is related to the polarity of the III-V material. The III-V compounds which crystallize in the cubic or zinc-blende structure have crystallographic polarity resulting in two types of surfaces: one terminated with group-III element (A-type polarity) and one terminated with group-V element (B-type polarity), as shown on Fig. 2.15 (a) and (b) for the case of GaP(111).

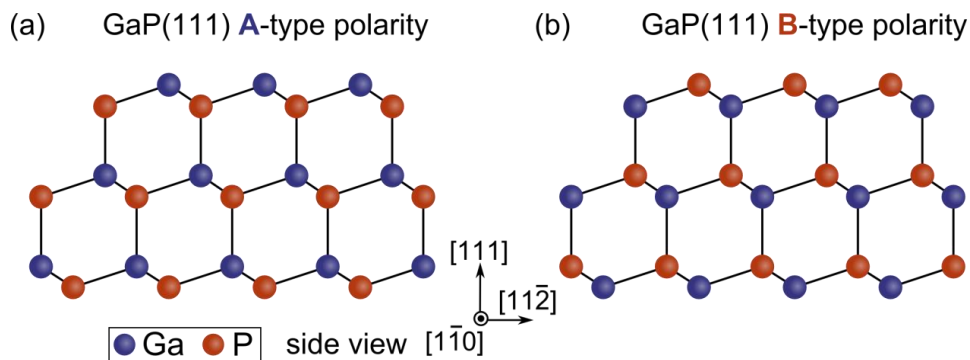


Fig. 2.15: side view of GaP(111) lattice, two possible surfaces terminations: (a) terminated with Ga (A-type polarity) (b) terminated with P (B-type polarity).

Control over the heterointerface allows to avoid problems in charge neutrality or defects: anti-phase domains or rotational domains in case of growth on Si(100) or Si(111), respectively.

2.6.1 Antiphase disorder

In a crystal without antiphase disorder the sublattice allocation is the same throughout the crystal [11]. The crystal lattice can be distorted by interface between domains with opposite sublattice allocation, which forms a two-dimensional structural defect called an antiphase boundary (APB). Such APBs can be expected to form when III-V material is grown on Si or Ge (100)-oriented substrate. The domains themselves are called antiphase domains (APDs). Figure 2.16. exhibits GaP grown on Si(100) with APB. The defect is caused by homopolar bonds between Ga–Ga or P–P atoms. Any real (100)-oriented substrate surface exhibits steps. At any step with only one atomic layer high (or odd number), the GaP sublattice is rotated by 90° in respect to the neighboring step. This is caused, as shown on Fig. 2.16, due to the first atomic layer bonded to the Si topmost atoms, which is P, independently of the step (see yellow ovals). Such bonds can caused electrically charged defects [11]. If two APBs on the $\{111\}$ lattice planes cross each other as indicated in Fig. 2.16 they can annihilate [75]. One approach to avoid APBs is to apply a substrate with a different crystallographic orientation on which APBs do not form, e.g. a substrate with (211) orientation [11]. The other approach is to enforce self-annihilation of all APD, however this excludes a thin film growth [75]. Another approach is to prepare the Si(100) with double-layer steps (even). At step edges of even numbered atomic height, the GaP bilayer can grow with one single domain (see the blue oval).

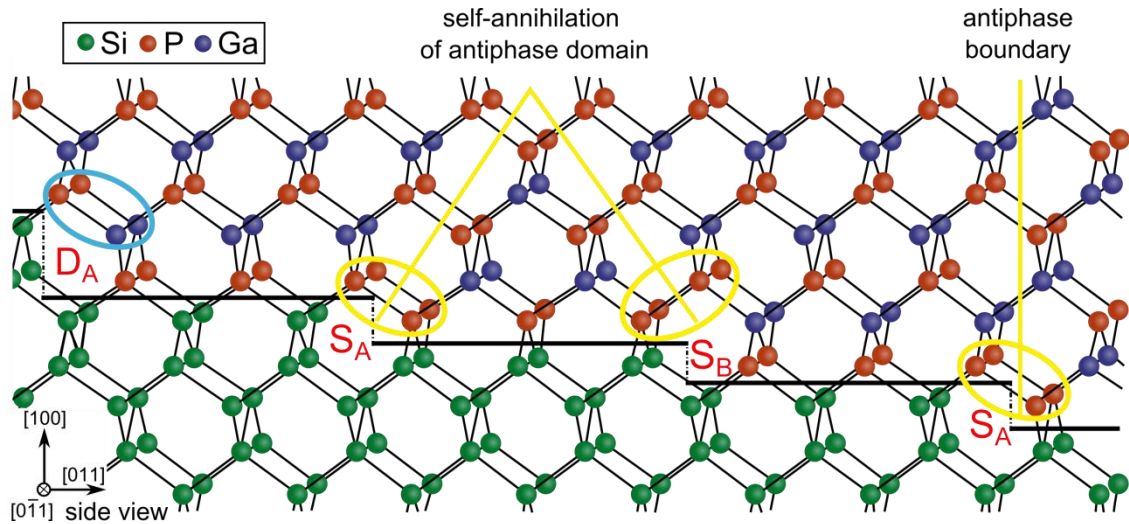


Fig. 2.16: Sketch of the APB formation in the $\{111\}$ and $\{110\}$ lattice planes of the GaP structure due to the presence of mono-layer steps on the Si surface. Antiphase boundaries are marked with yellow lines and may annihilate, after [100].

Si(100) double-layer steps surface preparation and *in situ* control in hydrogen-based MOCVD ambient are discussed in chapter 4.1.2.

2.6.2 Rotational domains

During III-V buffer nucleation on (111) oriented substrates, so called rotational twin domains (RTDs) can be formed, which results in twin boundaries defects. RTDs can be rotated by 60° around the $[111]$ axis. Figure 2.17 exhibits a “reflection twin” domain, the crystal lattice is rotated by 180° . In the reflection twin, the crystal lattice is mirror symmetric to the normal domain (ND). The red and green arrows point the difference in the crystal structure in the first III-V buffer mono-layer. RTD and ND domains cannot make the bond without strain, as shown in Fig. 2.17, which leads to a planar defect, influencing electrical properties of the semiconductor.

RTD are found to form during the initial stage of III-V buffer growth, precisely by the islands coalescence during the nucleation growth [121,122]. Nucleation time and temperature have a high impact on the RD to ND ratio in the film [121,123,124]. RTD can be observed using e.g. cross-sectional high-resolution transmission electron microscopy (HRTEM) [125,126], AFM [127] or SEM [122], and quantified by X-ray diffraction (XRD) [127].

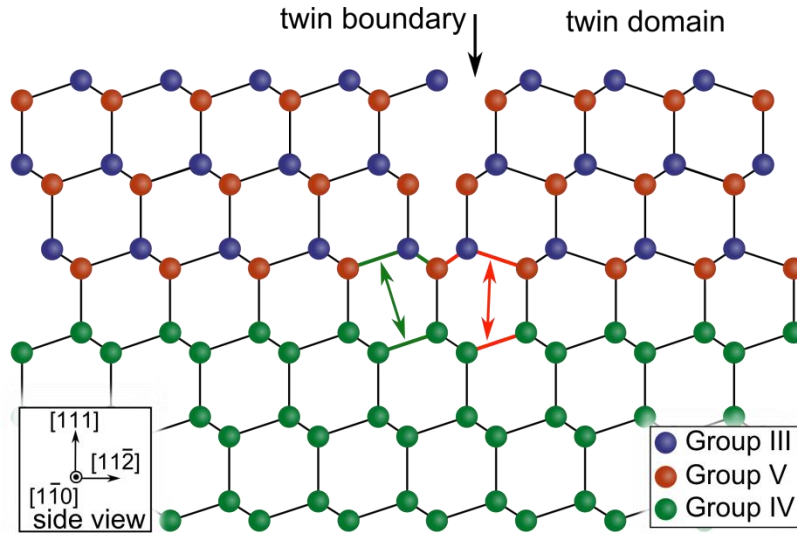


Fig. 2.17: A schematic illustration of rotational twin domain (RTD) in III-V buffer on Si (111) substrate. The domain is rotated by 180° around the $[111]$ axis. The crystal orientation of the RTD domain on the right hand side is “mirror like” to the crystal orientation of the Si substrate and the domain of left hand side.

3 Experimental background

In this chapter, the experimental methods applied in this work are described, with a focus on metalorganic chemical vapor deposition (MOCVD) and reflection anisotropy spectroscopy (RAS).

3.1 Metalorganic chemical vapor deposition (MOCVD)

Metalorganic chemical vapor deposition (MOCVD) also called metalorganic vapor phase epitaxy (MOVPE) or organometallic vapor-phase epitaxy (OMVPE) is a method for an epitaxial growth on semiconductor wafers applying organic or inorganic molecules or metalorganics as sources. The major attractions of MOCVD are the suitability for large-scale production applications, the ability to produce nearly atomically abrupt interfaces and the high purity of grown materials [9]. The growth is carried out in a quartz reactor in flowing e.g. H_2 or nitrogen (N_2) at atmospheric or low pressure (>5 mbar). The substrate typically is heated to temperatures above $400^\circ C$. The metalorganics precursors are transported to the growth zone by a carrier gas, where they decompose by thermal activation and surface chemistry. The growth processes in a MOCVD environment are highly complex; the process gas strongly interacts with the semiconductor surface. Moreover, the growth process depends on many parameters such as substrate temperature, reactor pressure, molar fractions of the precursors, their cracking efficiency and total gas flow. There is a strong competition between energetically and kinetically driven processes. In addition, the influence of residues from earlier deposited material has to be considered. Moreover, the presence of a process gas complicates analysis of the surface by standard UHV-based surface science tools.

In principle, the growth process involves the gas phase reactions [9]: pyrolysis of a precursor, transport to surface, adsorption of precursor, surface diffusion, re-desorption of precursor and incorporation to the substrate or epilayer: the atom can incorporate at energetically favorable places such as steps or kink sites, or attach to another atom to form a nuclei [128]. In the next step, the surface reaction products can desorb (by-products) and are transported into the gas flow region away from the deposition zone towards the reactor outlet.

The process can be subdivided by thermodynamic and kinetic components. Thermodynamics describes the driving force for all processes: reaching thermodynamic equilibrium, which is the point of lowest free energy for the system and involves

competition between surface and interface energies [9]. Usually thermodynamic equilibrium is never reached, since the processes occur too fast. The kinetics involve chemical reactions in the gas phase, on the substrate surface, chemisorption and desorption. In general, there are two models of epitaxial growth regarding kinetics [129]:

- 1) Layer-by-layer growth: in this mode, diffusion of the atom takes place first, then nucleation and then growth. This mode is usually at low temperature and high flux, and on a substrate with low step density.
- 2) Step-flow growth: here, the atom is sticking to step and the growth is through step flow. The growth mode is usually at high temperature, low flux and high step density.

Regarding thermodynamics in general there are three epitaxial growth models [129]:

- 1) Frank-van der Merwe mode: layer-by-layer growth (2D). In the case when the formation of the interface between layer and substrate (γ_i) and the surface of the film (γ_f) has a lower energy than the substrate (γ_s), the film will cover the substrate completely:

$$\gamma_s \geq \gamma_f + \gamma_i \quad (17)$$

- 2) Vollmer-Weber mode: island growth. If it is energetically more favorable to expose more substrate surface than to form the interface and surfaces island will form on the substrate.

$$\gamma_s < \gamma_f + \gamma_i \quad (18)$$

- 3) Stranski-Krastnov mode: layer-by-layer growth followed by island growth. Beyond a critical thickness, the mode changes from initial Frank-van der Merwe mode to Vollmer-Weber mode.

The deposition rate depends on the rate that precursor species impinge on a surface. The molecular flux per unit area J (molecules $\text{m}^{-2}\text{s}^{-1}$) is expressed by the Knudsen equation [130]:

$$J = \frac{N_A P}{\sqrt{2\pi M R T}}, \quad (19)$$

where N_A is Avogadro's number ($6.0221 \cdot 10^{23}$ / mol), P is the total gas pressure, M is the molar mass, R is the ideal gas constant (8.3145 J / mol·K), and T is the temperature in Kelvin.

Depending on the temperature, the growth rates may be divided into three regimes (based on Arrhenius equation) limited by: kinetics, thermodynamics and mass transport. At lower growth temperatures, the growth rate is controlled by the kinetics of chemical reactions occurring either in the gas-phase or on the substrate surface. The film growth rate increases exponentially with substrate temperature. At intermediate temperatures, the growth rate is controlled by mass transport of reagents through the boundary layer to the growth surface and is not much temperature dependent. Increasing temperature results in increased atoms desorption, which limits the growth and the growth rate decreases (thermodynamically limited growth).

All samples were prepared in either AIXTRON AIX200 system in Helmholtz-Zentrum Berlin (which later moved to TU Ilmenau) or in AIXTRON AIX200 double reactor system in Ilmenau, using equivalent horizontal reactor system. Both systems are extended by MOCVD-to-UHV-transfer and modified by an optical viewport at the reactor to enable optical *in situ* monitoring during the processes (see the two following subchapters).

The applied precursors at this work are: silane (SiH_4), triethylgallium (TEGa), tertiarybutylarsine (TBAs) and tertiarybutylphosphine (TBP), Fig. 3.1, (a), (b), (c), (d), respectively. The energy of the metal-carbon bond in the precursor determines the stability of the molecule against decomposition.

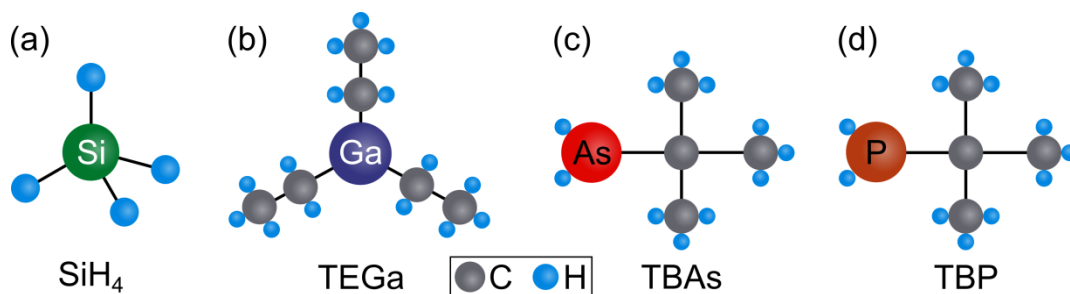


Fig. 3.1: Schematic diagrams of precursor molecules used in this work: (a) SiH_4 , (b) TEGa, (c) TBAs, (d) TBP. The small blue and medium size grey circles represent hydrogen and carbon atoms, respectively.

Figure 3.2 shows a schematic drawing of the MOCVD setup. The reactor itself consists of an outer quartz-tube (reactor tube) and an inner quartz-tube (liner). The samples are mounted on a specially designed molybdenum sample carriers placed in adapted graphite susceptor. The susceptor is heated up by six infrared halogen lamps (1600 Watt / lamp), which enables to reach temperatures above 1000 °C. Temperatures given in this work are measured with a thermocouple in the susceptor. To separate different material systems we use different susceptors and carriers. In addition, the liner may be cleaned in nitrohydrochloric acid (aqua regia). Transport of the metal-organics to the growth zone is achieved by bubbling a carrier gas (at this work purified H_2) through the liquid sources that are held in temperature-controlled bubblers.

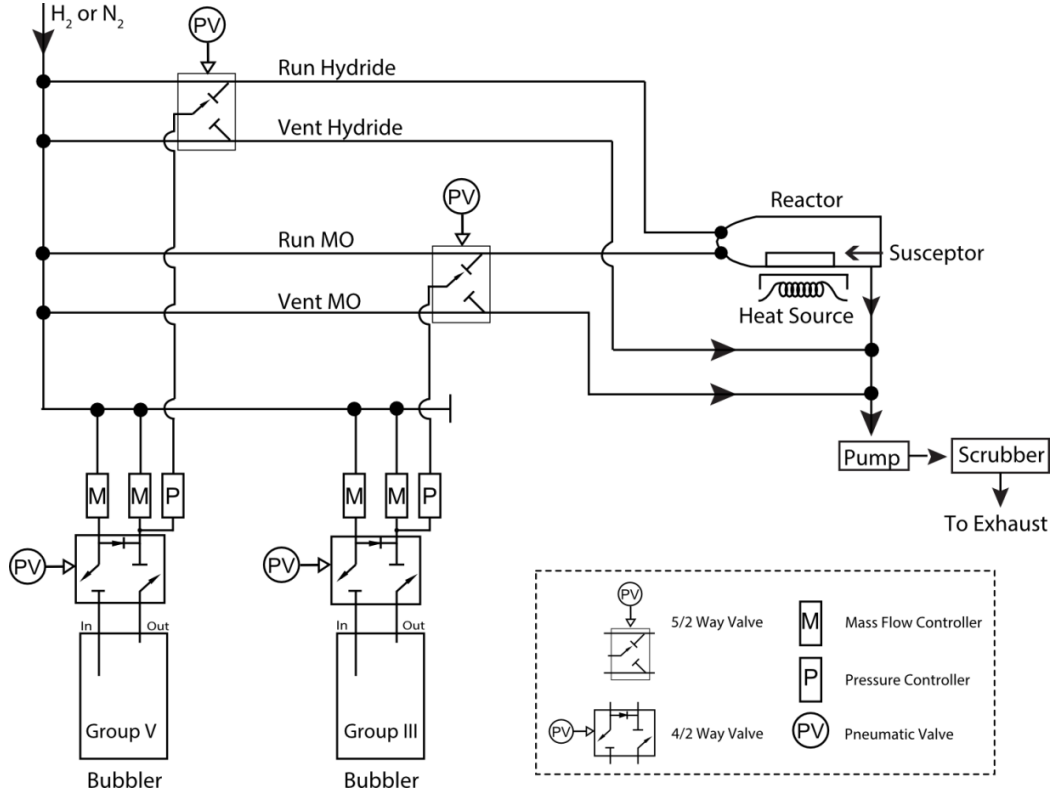


Fig. 3.2: Schematic drawing of the MOCVD setup. The precursor source is stored in a temperature-controlled bubbler and transported (separate lines for group-III and group-V precursors) by a carrier gas to the reactor.

The precursors are transported by carrier gas into the reactor in two different lines in order to separate group-V and group-III precursors to avoid pre-reactions (see Fig. 3.2). By a pneumatic 5/2 way valve, the precursor carrier gas can be directed either to the reactor or to the exhaust. Mass flow controllers (MFC) adjust the carrier gas and source flow into the reactor. The source flow (q_{source}) from the bubblers is set by the pressure MFC which controls the pressure in the bubbler ($p_{bubbler}$) by the incoming and outgoing carrier gas. The “push” MFC stabilizes the flow into the reactor. The partial pressure p_p of a precursor in the reactor is given by:

$$p_p = \frac{q_{source}}{q_{total}} \cdot \frac{p_{vapor} \cdot p_{reactor}}{p_{bubbler} - p_{vapor}} \quad (20)$$

where: q_{total} is the flow of all gases into the reactor, $p_{reactor}$ is the total pressure in the reactor and p_{vapor} is the vapor pressure of the precursor in the bubbler. The p_{vapor} can be calculated by the Antoine equation:

$$p_{vapor} = 1.33322 \text{ mbar} \cdot 10^{A-B/T_a} \quad (21)$$

Where T is the bubbler temperature and A and B are precursor-specific constants.

3.2 MOCVD-to-UHV transfer system

The presence of a process gas in the MOCVD reactor limits the access to the UHV-based surface science analysis. Light based techniques such as RAS are one possibility to investigate the sample preparation in MOCVD ambient (more details in subchapter 3.3). However, RA spectra do not provide direct information about the surface state; the spectra are very complex and difficult to understand. Our approach therefore is to correlate RA spectra from a characteristic surface obtained with *in situ* monitoring during the process with surface science tools, by applying a dedicated transfer system [27]. A mobile UHV shuttle gives us access to UHV-based surface science techniques, in particular to scanning tunneling microscopy (STM), photoelectron spectroscopy (PES), low energy electron diffraction (LEED) and Fourier-transform infrared spectroscopy (FTIR). The samples are mounted on a specially designed molybdenum sample carriers, which enable transfer into UHV environment. The sample carriers are fitted to an adapted susceptor. Figure 3.3 depicts a simplified sketch of the UHV setup.

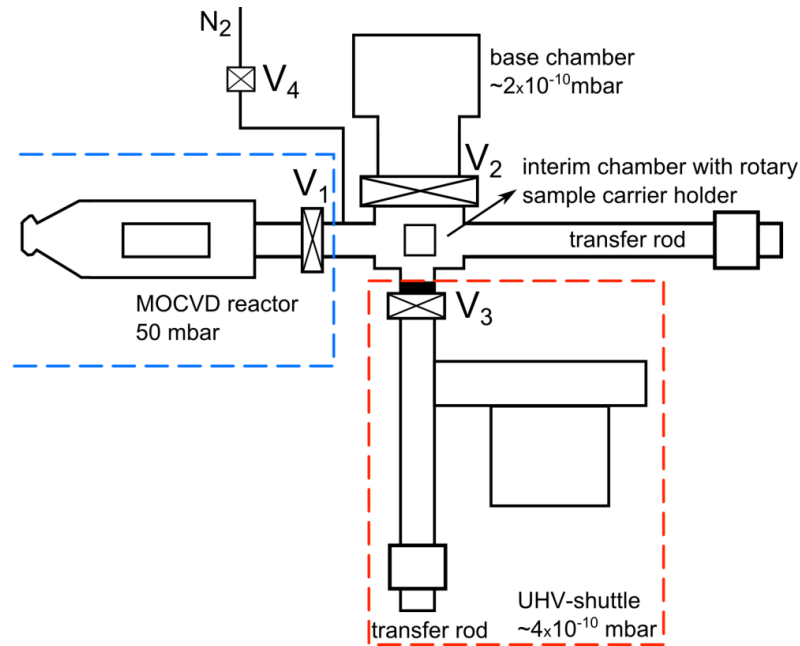


Fig. 3.3: Simplified schematic sketch (top view) of the MOCVD to UHV transfer system. Red rectangular indicates mobile part of the UHV shuttle and $V_1 - V_4$ indicate valves, after [27].

The MOCVD reactor is connected to an interim chamber through a pneumatic valve (V_1). The interim chamber contains a transfer rod and a sample holder, and is connected through a pneumatic valve (V_2) to the base chamber. We load the sample or attach the UHV shuttle when the interim chamber is flooded with N₂ (V_4) (V_1 is open, V_4 is closed). The sample is transferred from the MOCVD reactor by the transfer rod to the interim chamber in the N₂ ambient at 0 mbar pressure. Subsequently, after a few minutes, the sample is transferred to the UHV-shuttle at pressure below $5 \cdot 10^{-10}$ mbar (through valve V_3).

3.3 Reflection anisotropy spectroscopy (RAS)

Reflectance anisotropy spectroscopy (RAS), also known as reflectance difference spectroscopy (RDS), is a non-destructive, *in situ*, surface sensitive method applicable in different environments, such as UHV or MOCVD. It is based on the interaction of polarized electromagnetic radiation with the surface (and bulk) of the probed sample and subsequent analysis of the difference in the reflectance for the light polarized along two orthogonal axes in the surface plane. The reflected light contains rich information on the anisotropy of the measured semiconductor, such as surface reconstruction, interface bonds or doping induced internal electric fields. The method was first introduced in 1980s by Aspens *et al.* [131] to study the optical properties of the cubic semiconductors silicon and germanium.

The RAS signal

The RAS measures the difference in reflection (Δr) between the anisotropic complex Fresnel amplitude reflection coefficient (r) along two orthogonal crystallographic directions x and y in the surface plane in near normal incidence geometry, normalized to the total intensity of reflected light,

$$\frac{\Delta r}{r} = 2 \frac{r_{[x]} - r_{[y]}}{r_{[x]} + r_{[y]}}, \quad (22)$$

and it contains a real (Re) and an imaginary part (Im):

$$\frac{\Delta r}{r} = Re\left(\frac{\Delta r}{r}\right) + iIm\left(\frac{\Delta r}{r}\right). \quad (23)$$

The RAS signal can be correlated with the dielectric function of the material. For a surface layer of thickness $d \ll \lambda$ (λ = wavelength of the light) the RAS can be expressed by [26]:

$$\frac{\Delta r}{r} = - \frac{4\pi i}{\lambda} \frac{d\Delta\hat{\epsilon}_s}{(\Delta\hat{\epsilon}_b - 1)}. \quad (24)$$

Where, d is the thickness of the anisotropic surface layer, $\Delta\hat{\epsilon}_s$ is the anisotropy of the complex surface dielectric function ($\Delta\hat{\epsilon}_s = \epsilon[x] - \epsilon[y]$) and $\Delta\hat{\epsilon}_b$ is the bulk dielectric function. Expression $d \cdot \Delta\hat{\epsilon}_s$ defines the surface dielectric anisotropy (SDA) and enables to correlate the RAS signal to dielectric function of the surface layer.

Origin of surface optical anisotropies

Reflection anisotropies can, for example, originate from [132,133]:

- (i) the dielectric function of the semiconductor bulk.

(ii) the surface dielectric anisotropy (SDA) - caused by directed surface dipoles, which might originate from the local dimer arrangement.

(iii) field effects as in the case of highly doped III-V and II-VI semiconductors.

The contribution of interband transitions is strictly correlated with the dielectric function, which describes the optical properties of a semiconductor (such as refractive index n or extinction coefficient k). The real part of the dielectric function is related to polarization and anomalous dispersion, while the imaginary part is associated with absorption properties of the medium [134]. For semiconductors the main contributions in the imaginary part of the dielectric function is correlated with interband critical points [135] (valence band and conduction band have a similar slope). Figure 3.4 (a) shows the real and imaginary part of the dielectric function for Si [136], which are correlated with the critical points in Si on Fig. 3.4 (b) [137]. Similar behavior occurs in germanium and in common III-V semiconductors. The lowest absorption edge of Si corresponds to indirect transitions from the highest valence band at Γ point to the lowest conduction band near X direction and is marked as E_g in Fig. 3.4 (b). Three direct transitions, at critical points are marked as E'_0 , E_1 and E_2 [135]. E'_0 takes place in case of the lowest direct energy gap at Γ point of the BZ. E_1 takes place in case of parallel bands in the Λ direction. The higher interband transitions, E_2 are in case of flat bands along X direction. E'_0 , E_1 and E_2 equals to 3.32, 3.4 and 4.27 eV up to 350 K [134,135], respectively.

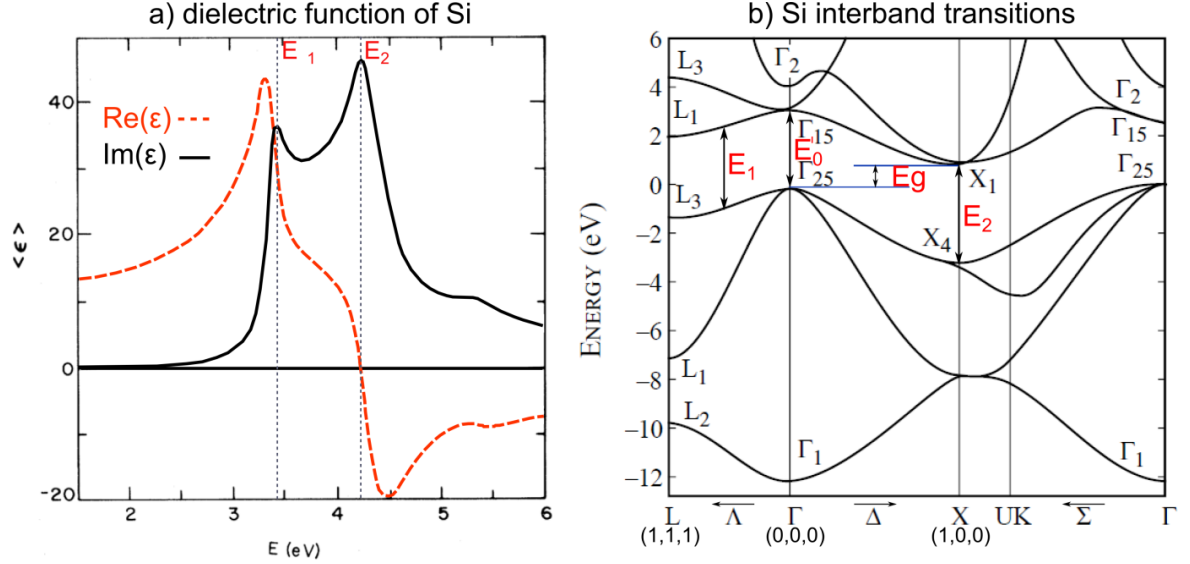


Fig. 3.4 (a) Imaginary (solid) and real (dashed) part of the dielectric function of Si (after [136]), (b) interband transitions in Si, with marked critical points corresponding to the maxima in the Im part of dielectric function (after [137]).

Direct interpretation of the RAS signal is not straightforward, especially when the RAS signal contains contributions from the bulk and the surface. To facilitate interpretation of the RA spectra, they can be compared with theoretical calculations. Such calculations might include the identified local-field effects, surface reconstruction or bulk optical

transitions [138], and can be performed by *ab initio* calculations based on density functional theory (DFT) or density functional theory in the local-density approximation (DFT-LDA) [139].

In this work, RAS is used to understand interactions of precursors with semiconductor surfaces in dependence of process parameters in MOCVD. To understand the RAS signals from the investigated surfaces and to identify individual contributions in the obtained RA spectra, we correlate them with results from UHV-based surface sensitive methods, such as XPS, LEED, FTIR and STM. The RA spectra presented in this work mainly reflect the dimer arrangement on the surface and electronic transitions from the valence band states to the states in the conduction band caused by photon absorption in case of (100) surfaces, and to the step arrangement in case of (111) surfaces.

The RAS setup

In this work, we employed a RA spectrometer from the company Laytec (EpiRAS 200), based on development by Aspnes *et al.* [140] and depicted schematically in figure 3.5 (more details in: [141]).

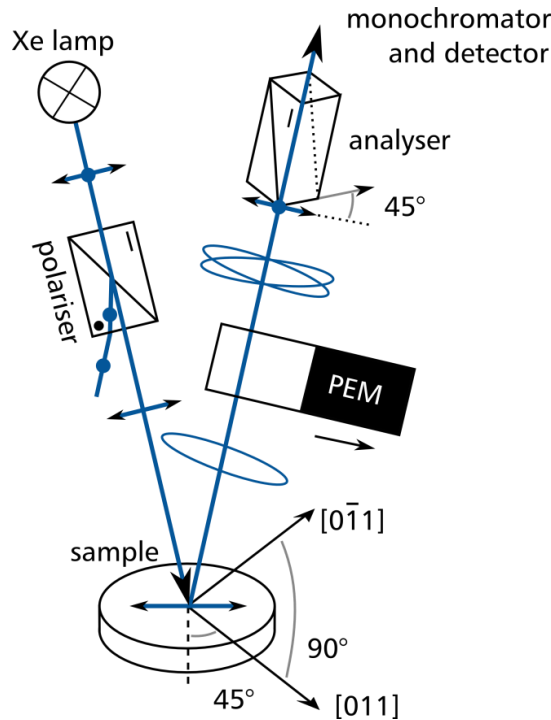


Fig. 3.5: The RAS setup showing the path of the light beam. The setup in this work is based on Refs. [140,141]. Figure taken from [119].

The RAS setup is placed on top of the MOCVD reactor therefore an incoming light beam passes through additional optics to focus the light beam through a lenses on the sample. This optical window is an additional optical element in the light path and might influence the measurement e.g. introduce an additional phase shifts due to windows strain. The light of a Xenon-arc-lamp (spectral range: 1.5 to 5.3 eV (~225 nm - ~837 nm)) is linearly

polarized by a polarizing Rochon prism, and focused on the sample. In our set up, the sample is adjusted so that the polarization of the incident beam is in the sample plane and the RAS signal measured in this work is defined as:

$$\frac{\Delta r}{r} = 2 \frac{r_{[0\bar{1}1]} - r_{[011]}}{r_{[0\bar{1}1]} + r_{[011]}}. \quad (25)$$

The reflected beam is elliptically polarized and passes through a photoelastic modulator (PEM), where it is phase modulated.

The RAS signal is determined by normalizing the alternating current (AC) components ($I_{1\omega}$ and $I_{2\omega}$) of the detector output to the respective direct current (DC) I_0 [140]. In an analyzing prism, the phase modulation of the light signal is converted in an intensity modulation. The light is detected in a Si photo-diode in combination with a grating-monochromator. The measured modulated signal is processed in the connected electronics, which includes a lock-in amplifier for analysis of the small RAS signals in the range of $\pm 5 \cdot 10^{-3}$. The signal consist of two components: a large DC component I representing the isotropic reflectance r and a very small AC component ΔI representing the anisotropy. Figure 3.6 depicts the optical path of the RAS set up. The RAS optics are mounted on the roof of the MOCVD reactor, which requires additional intermediate optics (a lens for focusing the light).

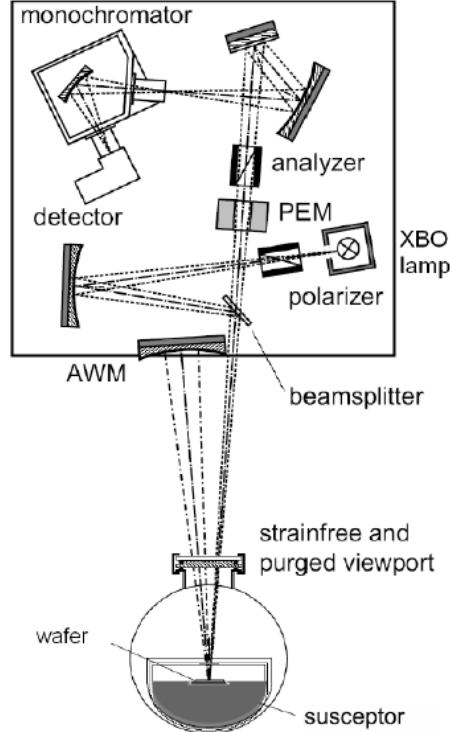


Fig. 3.6: Optical path of RAS (EpiRAS-200) applied in this work (note that intermediate optic are not shown here). Taken from [141].

An anti-wobble mirror (AWM) compensates tilt and directs the reflected light on the reversed path as the incoming light. Here, the beam is reflected twice on the sample. The optics are protected by a metal shield and constantly cooled by a fan. In addition the IR lamps from the heating system are shielded. The optical viewport at the reactor tube is strain-free and purged.

RAS measurements

The EpiRAS 200 system can be operated in three different modes:

- (i) the spectroscopic mode, which measures one single RA spectrum,
- (ii) the time resolved mode, where the change of dr/r is measured at a fixed energy in dependence of time,
- (iii) the colorplot mode, where RA spectra are measured continuously and can be presented in a color-coded graph.

Most RA spectra in this work are measured in the range from 1.5 eV to 5 eV with 10 or 20 meV steps. The spectroscopic mode is used to benchmark the signals with UHV-measurements and it is always taken at fixed temperature since RA is strongly temperature dependent (due to the T dependence of the involved optical transitions). Transient and colorplot modes enable observation of changes on the sample surface in dependence of the applied process parameters. In addition to the RAS signal, the U_{DC} signal is constantly measured, which reflects information about the reflectance R of the sample, where $R=|r|^2$. When the RA signal is measured in transient mode (at fixed energy), thickness and growth rate of the grown layer can be calculated if the refractive index n at growth temperature is known [132]. The reflection from the sample might not only contain the reflection from the grown layer but also, reflection from a layer beneath or a substrate, and therefore Fabry-Perot interference oscillations might occur. Based on the oscillation period (Tp) the growth rate (GR) can be calculated using an equation for Fabry-Perot interference oscillations:

$$GR = \frac{\lambda}{2*n*Tp}, \quad (26)$$

Baseline correction

The easiest approach to eliminate setup contribution to the RAS signal is to make an additional measurement of an isotropic sample (e.g. oxidized (amorphous) Si(100) or Si(111) with a low offcut degree) and simply subtract it from the measured spectra. The other method (without an isotropic sample) is to make two measurements of the sample, one with the sample rotated by 90°. The RAS signal of the sample changes sign when rotated by 90° because of the anisotropy axes are changed, but the contribution from the

setup itself is not changed. The last method is not always possible due to the fact that the sample would have to be taken out from the reactor and exposed to the air, which would cause oxidation of the sample. All RA spectra shown in this work are baseline corrected via the oxidized Si surface measured before starting the process.

3.4 X-ray photoelectron spectroscopy (XPS)

X-ray photoelectron spectroscopy (XPS) is a surface sensitive method to determine the elemental composition and the chemical state of solid surfaces and thin films. In this method x-ray photons are used to excite electrons from the core levels of the atoms of a solid into the vacuum. The analysis of the energy spectra of the electrons emitted from the sample provides information about the electronic structure, precisely the chemical state of the material. The process of photoemission is shown schematically in Fig. 3.7.

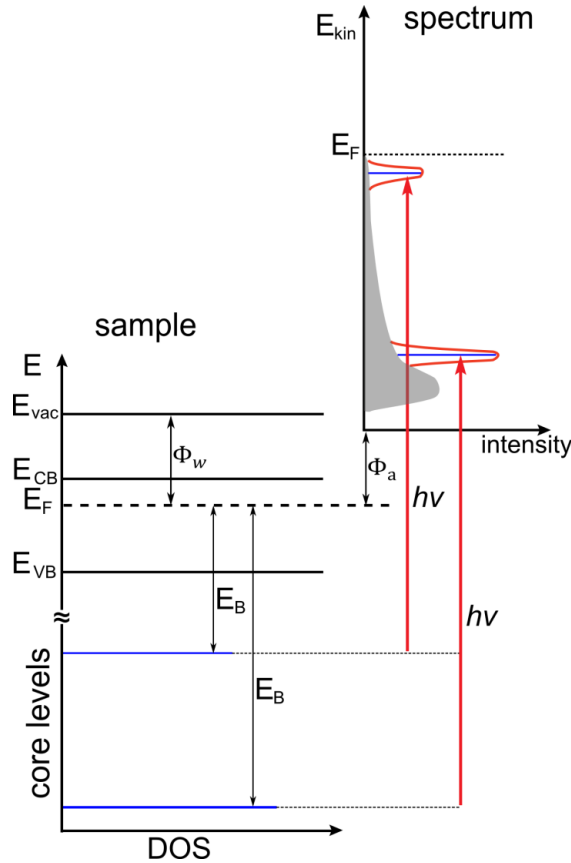


Fig. 3.7: Schematic of the photoemission process. Electrons with binding energy E_B can be excited above the vacuum level E_{vac} by photons with energy $h\nu > E_B + \Phi_w$. The photoelectron distribution (intensity) can be measured by an electron energy analyzer and in approximation is equal to $N(E_B)$, the occupied density of electronic states (DOS) in the sample. After [142].

When a solid surface is irradiated with x-ray photons an incident photon of energy $h\nu$ can be absorbed by an electron with binding energy (E_B) below the vacuum level. The entire photon energy is transferred to the electron, which is then excited above the vacuum level. As a result, this photoelectron is ejected into the vacuum with kinetic energy and can be detected by an electron energy analyzer. For a solid surface, the binding energy is conventionally measured with respect to the Fermi level rather than to the vacuum level (see Fig. 3.7). The kinetic energy is described by:

$$E_{kin} = h\nu - E_B - \Phi_w. \quad (27)$$

Here, the Φ_w is the work function of the material and represents the minimum energy required to remove an electron from the solid (e.g. an energy barrier that electrons need to overcome in order to escape from the surface into the vacuum). Usually the analyzer work function Φ_a is smaller than the sample work function Φ_w . Consequently, the kinetic energy of all electrons increases by $\Phi_w - \Phi_a$.

In consequence, the E_{kin} of the electron reaching the detector is equal to:

$$E_{kin} = h\nu - E_B - \Phi_a. \quad (28)$$

The work function is an adjustable instrumental correction factor that accounts for the few eV of kinetic energy given up by the photoelectron as it becomes absorbed by the instrument's detector. The binding energies of core levels are different for each chemical element, and no two elements share the same set of binding energies. The photoemission spectra can be considered as fingerprints of the emitting elements. The photoemission spectrum provides a distorted replica of the electronic structure, distorted e.g. by the occurrence of multi-electron processes and by the fact that the probability of a photon being absorbed is not the same for all electron states. The ejected electrons can originate from core levels or from the occupied portion of the valence band. In addition, in the spectrum, electrons which were scattered from a continuous background are visible (energy losses before escaping from the surface), so-called secondary electrons (gray field on Fig. 3.7) and secondary electrons excited in "cascade" processes. In the spectrum, additional lines stemming from Auger electrons are also visible. The binding energy of a particular core level changes in dependence on the different chemical bonds of the same atom. The according difference in energy is called chemical shift. Based on the chemical shift it can be determined how the atoms of the investigated material are bonded to any other atoms. XPS is highly surface sensitive, due to the strong interaction of electrons with matter. The latter entails that electrons travelling in a solid exhibit a very short inelastic mean free path (λ_e). It describes an average distance that an electron can travel through the material without energy losses by inelastic scattering. For electrons with kinetic energy in the range between 10 and 1300 eV, λ_e can vary between a few atomic layers, depending on the material and kinetic energy of the electron (between $\sim 4 \text{ \AA}$ and 30 \AA for Si [143]).

In this work, monochromated Al-K α 1 (1486.7 eV) was used as X-ray source (Specs Focus 500). Kinetic energies were filtered with a hemispherical analyzer (radius 100 mm) and detected with a channeltron (Specs Phoibos 100). At TU Ilmenau, a 1d delay-line detector was available (Specs 1D-DLD-43-100, Phoibos 150).

The measurements in this work were done at a 90° angle to the sample surface and to increase the surface sensitivity, at 30°. If electrons are collected at angles other than to the surface normal emission, information depth decreases by a factor of $\sin(\theta)$. Figure 3.8 depicts the two cases: (a) the electrons are collected at $\theta = 90^\circ$, (b) at $\theta = 30^\circ$ to the surface plane (0° or 60° with respect to the surface normal).

The electrons ejected by the photons of the x-ray source are focused by magnetic and electrostatic lenses to the entrance slit of the analyzer [144]. The electrostatic lenses apply a negative potential. Therefore, in addition the electrons entering the slit to the analyzer (to get between the two hemispheres) have to overcome this retarding voltage. A present voltage allows the passage of the electrons to the detector with fixed pass energy (E_{pass}). The E_{pass} has an influence on the resolution and the background noise. The highest contribution to the noise in the spectrum stems from electrons excited by secondary electrons which have low kinetic energy. In this work, the survey spectra were done at $E_{pass}=30$ eV, the spectra over a narrower energy region were done at reduced E_{pass} to obtain a high resolution.

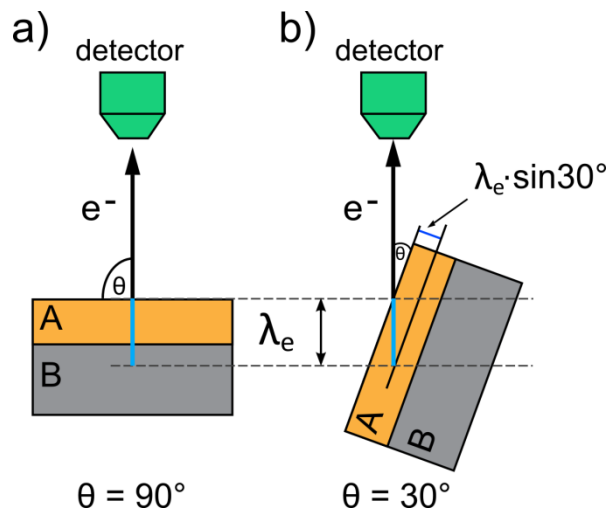


Fig. 3.8: Greater surface sensitivity XPS measurement is achieved by collecting electrons at an angle of 30° against the normal emission (b). In this case, the inelastic mean free path will decrease by factor of $\sin 30^\circ$ in comparison to the measurement at $\theta = 90^\circ$.

3.5 Low energy electron diffraction (LEED)

The low energy electron diffraction (LEED) is a principal technique for the determination of surface structures. The principle of LEED is depicted on Fig. 3.9. LEED operates by sending a beam of electrons from an electron gun to the surface of the sample. An electron gun consists of a heated cathode, from which electrons are emitted, anode, which accelerates electrons to energies between 20 – 1000 keV towards the lens system, and a Wehnelt cylinder. As the electrons collide with the surface of the sample, they can diffract in numerous directions depending on the surface crystallography. Once the electrons diffract, they head back towards three grids followed by a phosphor covered screen. The first grid is grounded and because of its negative potential serves as a shield, which protects the second grid. The second grid acts as filter by allowing only the electrons with higher energies to pass through. The lower energy electrons (scattered) are blocked out due to the fact that they disorder the image creating a clouded image. Once the electrons pass through the second grid, they come to third and final grid. This grid separates the previous negative grid from the phosphor screen, which carries a positive charge to accelerate the electrons to the phosphorus screen. As the electrons land on the phosphor screen, they create a phosphor glow. The intensity of the glow depends on the intensity of the electron.

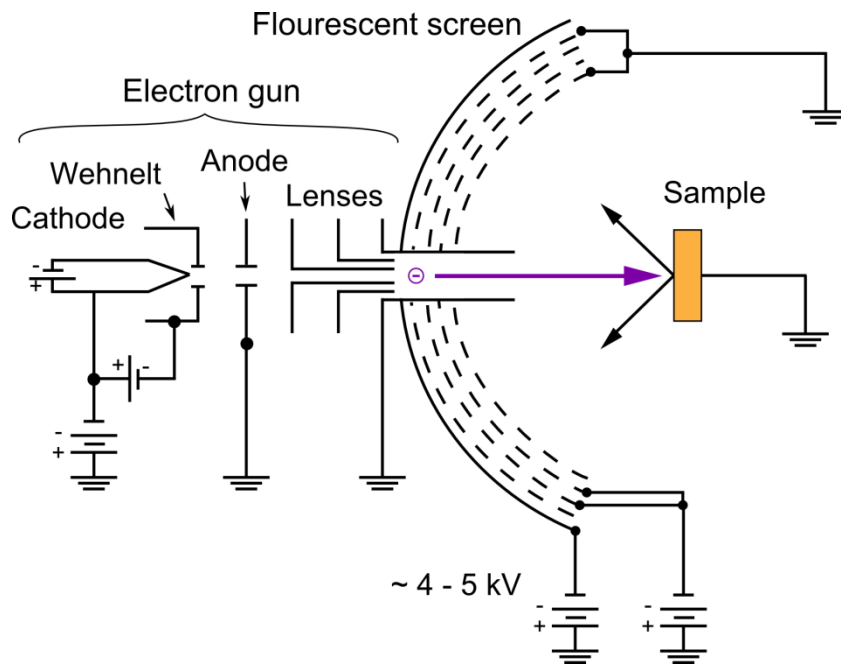


Fig. 3.9: Schematic drawing of the LEED setup (after [145]).

In order to realize measureable diffraction, the incoming wavelength should be in the same order as the periodicity of the atoms in a crystalline solid (a few Angstroms). The wavelength of the electrons is given by the de Broglie relation [145]:

$$\lambda = \frac{h}{m \cdot v} = \frac{h}{\sqrt{2 \cdot m_e \cdot E_{kin}}} , \lambda[\text{\AA}] = \sqrt{\frac{150}{E(\text{eV})}} \quad (29)$$

Where m is the mass of the electron, v is the velocity, E_{kin} is the kinetic energy of the incident electrons. The angle of diffraction of the wave-particle is governed by the Bragg equation. Constructive interference between two out-going waves only occurs if the path length difference between them is equal to an integral number of wavelengths. For this to occur, the Bragg equation must be satisfied (see Fig. 3.10):

$$d = a \cdot \sin(\theta) = n \cdot \lambda, \quad a \cdot \sin(\theta) = \frac{h}{\sqrt{2 \cdot m_e \cdot E_{kin}}} \quad (30)$$

A "path difference" (d) of the radiation that has to travel from the scattering centers (atoms) to a distant detector is illustrated by considering two "ray paths" such as the right-hand pair of green traces in the Fig. 3.10. The size of this path difference is $a \cdot \sin(\theta)$.

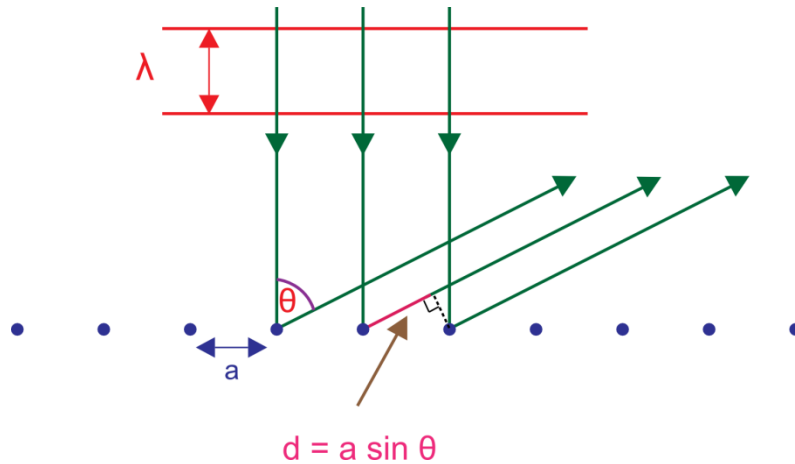


Fig. 3.10: Bragg's law: scattering at a solid corresponds to reflection at the lattice planes.

The $\sin(\theta)$ is proportional to $1/a$, which implies that a large atomic spacing will produce a small diffraction angle and a small atomic spacing will produce a large diffraction angle. The $\sin(\theta)$ is also proportional to $1/(eV)^{1/2}$, in consequence the size of the diffraction pattern will vary with incident wave-particle energy. The diffraction angle becomes smaller with increasing incident energy.

The diffraction pattern is not a direct representation of the real-space arrangement of the atoms in a solid or on a surface, but is directly related to the crystal reciprocal lattice by the Laue condition [145]:

$$\vec{k} - \vec{k}_0 = \vec{G} . \quad (31)$$

Here the \vec{k}_0 is the incidence wave vector, \vec{k} is the scattered wave vector and \vec{G} is the reciprocal lattice vector, and for the elastically scattered electrons $|\vec{k}| = |\vec{k}_0| = 2\pi/\lambda$. The diffraction can be represented graphically using the Ewald construction (see Fig. 3.11 (a)). The Ewald's sphere is centered on the origin of the incident wave vector with the radius $|\vec{k}_0|$ and illustrates the points of constructive interference formed by the incident and diffracted electron waves. The upper half of the sphere can be considered as the hemispherical fluorescent screen of the LEED apparatus as shown on Fig. 3.11 (a). Since the mean free path of electrons within a crystal is small and so only the first few atomic layers contribute to the diffraction, the diffraction elements perpendicular to the surface are omitted. Therefore, the lattice can be considered as a 2-dimensional series of rods extending from the surface lattice points. Figure 3.11 shows real space lattice and their reciprocal lattices, (b) and (c) for Si(100) and (d) for Si(111). A (1×2) surface reconstruction of Si(100) (Fig. 3.11 (c), open circles in the real-space lattice) causes additional half order diffraction spots along the dimer axis (Fig. 3.11 (c), white spots in the reciprocal lattice).

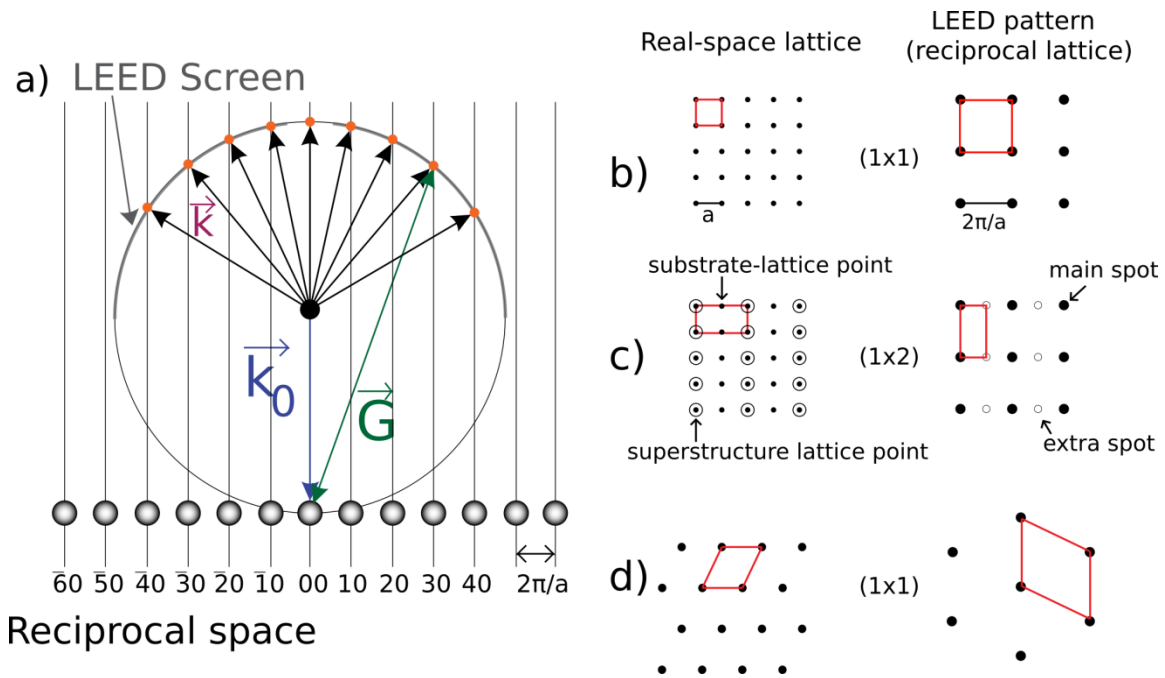


Fig. 3.11: (a) visualization of the Laue condition by the Ewald's sphere construction. The spots (rods) are numbered by their hkl value. Points where the rods cross the sphere coincide with the Laue condition. The (b), (c) and (d) are examples of real space lattice and their reciprocal lattices. In the real space, the superlattice points are shown by open circles. In the LEED patterns, the main spots are shown by black circles and the extra-spots (coming from the superlattice) are shown by small white points. The (b) (c) corresponds to (1×1) and (1×2) surface reconstruction of Si(100), respectively. The (d) corresponds to (1×1) surface reconstruction of Si(111) (after [145]).

In this work, a commercial LEED setup (Specs ErLEED 100-A) is used.

3.6 Fourier-transform infrared spectroscopy (FTIR)

Infrared spectroscopy is a technique based on the vibrations of the atoms of a molecule [146,147]. In the Fourier transform infrared spectroscopy (FTIR), IR radiation is passed through a sample. The sample molecules selectively absorb radiation of specific wavelengths which causes the change of dipole moment of sample molecules. In consequence, the vibrational energy levels of sample molecules transfer from ground state to excited state. The frequency of the absorption peak is determined by the vibrational energy gap. The measured spectrum reflects the absorption of infrared radiation by the sample versus wavelength. Each absorption band is unique for each molecular structure. Measuring each wavelength in a desired range would be a very slow process; however, this can be overcome by applying an interferometer allowing to perform a measurement in the order of seconds. An FTIR is typically based on a Michelson interferometer. The interferometer employs a beam splitter which divides the incoming infrared beam into two optical beams. One beam reflects from a flat mirror which is fixed in place. The other beam reflects from a flat movable mirror. Reflected beams recombine with each other at the beam splitter. Since the path that one beam travels is at a fixed length and the other is constantly changing as the movable mirror moves, the signal that exits the interferometer is the result of these two beams “interfering” with each other. The x-axis of the interferogram represents the optical path difference between two beams. Each individual spectral component contributes to this signal a single sinusoid with a frequency inversely proportional to its wavelength (the y-axis). A wavenumber represents the number of full waves of a particular wavelength per cm of length. The resulting signal has information about every infrared frequency which comes from the source, which means that all frequencies are being measured simultaneously. The signal is converted through the Fourier transformation algorithm. The FTIR resolution is limited by an inverse of the achievable optical path difference (in other words, step of the movable mirror).

Attenuated total reflection (ATR) uses a property of total internal reflection resulting in an evanescent wave [148–150]. A total internal reflection occurs when a propagating wave enters a medium boundary at an angle larger than a critical angle with respect to the normal to the surface. In this case, the angle of refraction is greater than the angle of reflection. This can only occur when the wave in a medium with a higher refractive index (n_1) reaches a boundary with a medium of lower refractive index (n_2). The number of reflections may be changed by varying the angle of incidence. A detector then collects the beam as it exits the crystal.

In this work, we used spectrometer (Bruker IFS 66v/s) in the surface sensitive ATR configuration. The FTIR system is extended by a UHV chamber, connected through a valve to an interim chamber, which allows to attach the UHV shuttle [151]. This extension enables contamination free sample transfer from the MOCVD reactor to the FTIR (see subchapter 3.2). The ultra-high vacuum in the main chamber prevents

interaction between the surface and contamination. As a detector, we used indium antimonite (InSb, range: $10\,000\text{ cm}^{-1}$ - 1850 cm^{-1}) or mercury cadmium telluride (MCT, HgCdTe, range: $10\,000\text{ cm}^{-1}$ - 590 cm^{-1}) detector. The data were evaluated using the software OPUS.

3.7 Scanning tunneling microscopy (STM)

In this work, we used scanning tunneling microscope (STM) to image the sample surface in an atomic resolution. The principle of this measurement is based on quantum tunneling. The metal, conductive sharp tip is positioned a few angstroms from the sample surface. A small voltage is applied between the probe tip and the surface, causing the electrons to tunnel through the vacuum, between the tip and the sample, causing a current. The probability of finding such tunneling electrons decreases exponentially as the distance from the surface increases. The position of sample and tip can be precisely controlled by piezoelectric elements. The changes in the surface height and density of states cause changes in the current. There are two possible measurements modes: (i) constant current mode – current generated between the tip and the surface is constant and the variation in z position of the tip is measured; (ii) constant height mode – the height of the tip is maintained constant and the current is measured which changes with respect to the tip position. For this work, a Specs Aarhus-150 STM was applied in UHV with electrochemically polished and *in vacuo* sputtered tungsten tips. Measurements were performed in constant current mode probing empty states. The STM measurements were performed by Dr. P. Kleinschmidt (HZB / TU Ilmenau), J. Luczak (HZB), A. Nägelein (TU Ilmenau) or X. Wen (TU Ilmenau).

3.8 Atomic force microscopy (AFM)

The surface morphology of the samples was measured by atomic force microscopy (AFM). The sample surface is scanned by a cantilever with a sharp tip (probe). The cantilever is typically from silicon or silicon nitride with a tip radius in the order of nanometers (the radius of the tip used in this work is $\sim 8\text{ nm}$). In this work the measurements were done in a tapping mode. The principle of the measurement is based on a probe maintained in close contact to a sample, in a constant oscillation at high amplitude. Changes in the surface morphology cause changes in the distance between the surface and the tip, meaning a change in the van-der-Waals forces between the tip and the sample, which leads to a change in the tip oscillation amplitude. The height is adjusted to maintain constant cantilever oscillation amplitude. The deflection is measured using a laser spot reflected from the top surface of the cantilever into an array of

photodiodes. The deviation of the tip allows to determine the impact of forces between the tip and the surface. The surface morphology is a reflection of the forces between the tip and the sample surface. The movement of the probe is controlled by a piezoelectric elements, due to which the probe can be moved very precisely in x, y and z directions. In this work, the AFM scans were done in HZB using a Park XE-100 AFM system and in TU Ilmenau using a Bruker Dimension V system, both with a damping stage. The AFM data were evaluated by the software WSxM 5.0 Develop 6.5 [152]. The surface roughness of the samples is given by a statistical measure, root mean square (RMS) [153].

3.9 Electrochemical capacitance voltage profiling (ECV)

Electrochemical capacitance voltage profiling (ECV-Profiling) is a destructive technique which can be applied for doping concentration measurement. It overcomes the restriction of the maximum accessible depth typical for conventional C-V profiling. The principle of this method is based on a wet-chemical etching and creation of a temporary Schottky contact on the surface after each step of etching [154]. A Schottky contact is a rectifying contact that occurs between a metal or electrolyte and a lightly doped semiconductor. The area of the Schottky contact is defined by a sealing ring (1 mm² or 10 mm²). To measure the semiconductor doping profile an electric current is applied. There are two modes of current supply: forward bias for p-type layers and reverse bias for n-type material. The applied voltage leads to a movement of carriers in the semiconductor and to formation a depletion zone which is free of the carriers. This movement causes the formation of an electrical field and is detected by equipment as the capacitance of the depletion region. The complete measurement process is controlled by a dedicated PC software. By applying an external voltage to the interface, the width of the depletion layer may be changed. If the border of the depletion layer in the semiconductor is assumed to be sharp and the semiconductor material is assumed to be homogeneous, the measured capacitance (C) depends on the applied voltage [154]. The $1 / C^2$ depends on the carrier concentration (N). This relation is described by the Mott Schottky equation:

$$\frac{1}{C^2} = \frac{-2}{e\epsilon_0\epsilon_R A^2 N} (V - V_{fb}). \quad (32)$$

Where: C is the measured capacitance, e - electron charge, ϵ_0 - vacuum dielectricity, ϵ_R - relative dielectricity of the semiconductor material (dielectric constant), A - measurement area, V – external voltage applied to the depletion zone, V_{fb} - flat band potential, N – carrier concentration in the semiconductor at the border of depletion zone. Thus, the carrier concentration (N) is inversely proportional to the slope of $1 / C^2$:

3 Experimental background

$$N = \frac{1}{e\epsilon_0\epsilon_R A^2} \frac{C^3}{\frac{dC}{dV}}. \quad (33)$$

In this work the free carrier concentration profiles were obtained by electrochemical capacitance voltage (ECV, WEP-CVP 21) profiling with NH_4HF_2 0.1m solution (applying forward bias for p-type layers and UV illumination for n-type layers).

4 State of the art: *in situ* study of Si surfaces in CVD ambient

This chapter summarizes previous work of our group regarding the Si(100) surface preparation for further, low defect III-V growth, in H₂ ambient (free of III-V residuals) employing *in situ* control of RAS. The key aspects of Si(100) surface preparation in dependence on the substrate offcut are shown. Understanding of H₂ interaction with Si(100) surface and the steps formation is necessary to prepare the Si surface in the ambient which contains in addition background residuals. Here, the *in situ* RAS is shown as a powerful surface sensitive tool during the Si(100) surface preparation. Finally, knowledge about Si(111) surfaces in H₂ ambient regarding *in situ* control based on research by other groups is shortly summarized.

4.1 Si(100) surfaces in hydrogen ambient

Typically, III-V/Si(100) MOCVD processes take place in the temperature and pressure range where strong interaction between surface and H₂ process gas influence the surface properties. Interaction between the Si surface and H₂ is fundamental to understand Si preparation in process gas ambient, which contains III-V residuals. Deoxidation of Si(100) surfaces takes place at 1000 °C, at this temperature the hydrogen coverage of the clean Si surface is estimated to be 25 % (at 950 mbar, see subchapter 2.5). However, during cooling down the H₂ coverage on the surface is estimated to be about 95 % at 800 °C and 100 % below 630 °C. Therefore, at this temperature range the interaction between hydrogen and Si(100) surface will have a strong impact on the domain and step formation on the surface. Steps on the Si(100) surface can be either of two-atomic (even) or one-atomic (odd) step height, respectively. Odd-atomic steps height causes the APD in the subsequently grown III–V buffer layer. Therefore, in order to avoid them, double-layer step formation of Si(100) is necessary (see subchapter 2.6.1). The step height is directly related to the domain formation on the Si(100) surface (see Fig. 2.10 in the subchapter 2.4.2): single-layer steps (odd) imply a (2×1)/(1×2) - two-domain surface whereas double-layer steps (even) imply single-domain surfaces. The dimer orientation on the upper terrace to the step edge can be either perpendicular (A-type) or parallel (B-type).

4.1.1 *In situ* control of Si removal in H₂ ambient

The RAS signal is sensitive to the surface reconstruction of monohydride-terminated Si(100) surfaces [78,155] and reflects the dimer orientation on the Si surface. Figure 4.1 (a) shows the RA spectra (taken at 50 °C) of monohydride terminated Si(100) 0.1° surfaces. Despite the opposite sign, the RA spectra have a characteristic peak at the E_1 interband transitions, a lower intensity peak close to the E_2 interband transitions, and a shoulder in between. It was shown that a strong negative peak at 3.4 eV in the RA spectrum of Si(100) surface reflects the A-type domain [78], therefore, the green (red) RA spectrum indicates the surface with majority of the A-type (B-type) domain. The RAS probes the normalized difference of the reflection of light polarized in two perpendicular directions in the surface plane at normal incidence. Therefore, the flip of the RAS sign corresponds to a rotation of the anisotropic structure by 90° (dimer orientation). Presence of two domains on the surfaces sums up and cancels the RAS signal. Therefore, the measured amplitude of the RAS signal reflects the domain ratio on the surface. Based on a comparison of the RAS signal amplitude at 3.4 eV of A-type domain surface (Fig. 4.1 red line) to RA spectra of [78] a domain ratio is about 75:25 with an A-type majority domain [156].

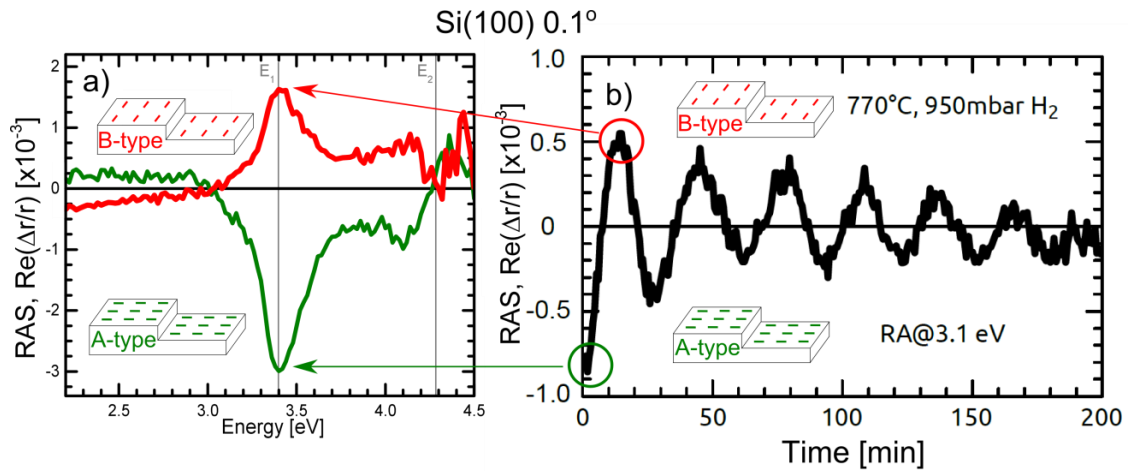


Fig. 4.1: (a) RA spectra of Si(100) 0.1° surface with A-type (green line) and the B-type (red line) domain taken at 50 °C. The inset shows the majority domain dimer orientation related to the step edges for the different domain types. (b) Transient *in situ* RA measured at 3.1 eV during annealing at 770 °C at 950 mbar in H₂. Green and red circle indicate the peaks in the RAS in Fig. (a) at energy 3.4 eV (shift in the energy is due to the temperature). At this temperature, formation of SiH_x species leads to vacancies on the surface causing Si layer by layer removal process. Observed sign flip of the RAS signal relates to the Si dimer orientation, which is rotated by 90° for every lower terrace. Figure taken from Ref. [156].

Figure 4.1 (b) shows *in situ* RAS fixed at energy at 3.1 eV at 770 °C (energy corresponds to characteristic peak at 3.4 eV at 50 °C, shifted due to the temperature) during annealing in H₂. The transient clearly shows an oscillation of the peak amplitude [156]. In the

beginning the surface exhibits the spectra of the monohydride-terminated Si(100) surface with a majority of A-type domain (the green circle corresponds to the peak minimum of the green RA spectrum in Fig. 4.1 (a)). During further annealing the change in the sign of the RAS peak around 3.1 eV corresponds to a switch of the majority amongst the two mutually perpendicular dimer orientations. After 190 min. the RAS signal cancels out completely, which corresponds to equal domain distribution on the surface. Change of the majority domain is due to removal of one mono-layer Si atoms from an A-type terrace, which results in a B-type terrace and vice versa. The decreasing amplitude during the oscillation indicates a reduction of the maximum prevalence for both majority domains [156]. Si vacancies nucleate during annealing in H₂ (Si etching processes is caused by formation of SiH_x species upon hydrogen desorption) and move anisotropic along the dimer rows. They coalesce to elongated vacancy islands oriented parallel to the dimer rows of the Si terrace with long single-atomic step edges [157–159]. Formation of elongated vacancy islands minimizes the surface energy compared to many small vacancies spread over the terraces. When these islands reach a certain size, continued Si removal may occur also on the next layer. This leads to Si layer-by-layer removal. Both surfaces can be prepared when the peak at 3.1 eV (Fig. 4.1) is reaching minimum/maximum (majority of A-type/B-type domain) and the sample is immediately cooled down (heater off) under immediate (limited by pump) pressure change from 950 to 50 mbar. The pressure change reduces the interaction of the Si surface and the H₂. The RAS amplitude of the B-type domain surface indicates a domain ratio of about 63:37 between majority and minority domain.

4.1.2 Anomalous double step formation

Formation of double layer steps was directly observed on Si(100) 2° offcut in [011] direction [78]. Figure 4.2 (a) shows an *in situ* RA transient at fixed energy at 3.1 eV during annealing in H₂ at 730 °C under 950 mbar. RAS signal (related to the dimer orientation on the surface) within the time, reaches minimum and does not change, indicating a finite change of the majority domains on the surface. Figure 4.2 (b) shows corresponding RA spectrum (Si(100) 2° surfaces was annealed at 730 °C in 950 mbar H₂ for 15 min) with a characteristic negative peak at the E₁ interband transitions, a lower intensity peak close to the E₂ interband transitions, and a shoulder in between. Quantification of the RAS amplitude results in a majority to minority domain ration of about 83:13 [78,155]. This RA spectrum corresponds to the surface with (1×2) reconstruction. Figure 4.2 (c) shows an STM scan of the surface, which confirms majority of A-type domain. On the edge of steps residues of the B-type domain terraces are visible.

As discussed above, a strong interaction between the Si surface and H₂ leads to vacancy generation on the terraces. On surfaces with a higher offcut the vacancies diffusion length is large compared to the terrace width. Vacancy diffusion is anisotropic and

preferably along dimer rows [159]. Here, in contrast to the Si(100) 0.1°, the vacancies annihilate preferentially on the B-type terraces due to the orientation of the step edges (at the end of the dimer rows) [160,161], which leads to retreat of B-type domain terraces and to the surface with majority of A-type domain. Si(100) 2° surface with a prevalence of B-type domain can be prepared at reduced pressure (50 mbar), which leads to weaker H₂ interaction with the surface resulting in reduced Si removal process. Diffusion of Si atoms still occurs leading to formation of an energetically favorable surface state [119].

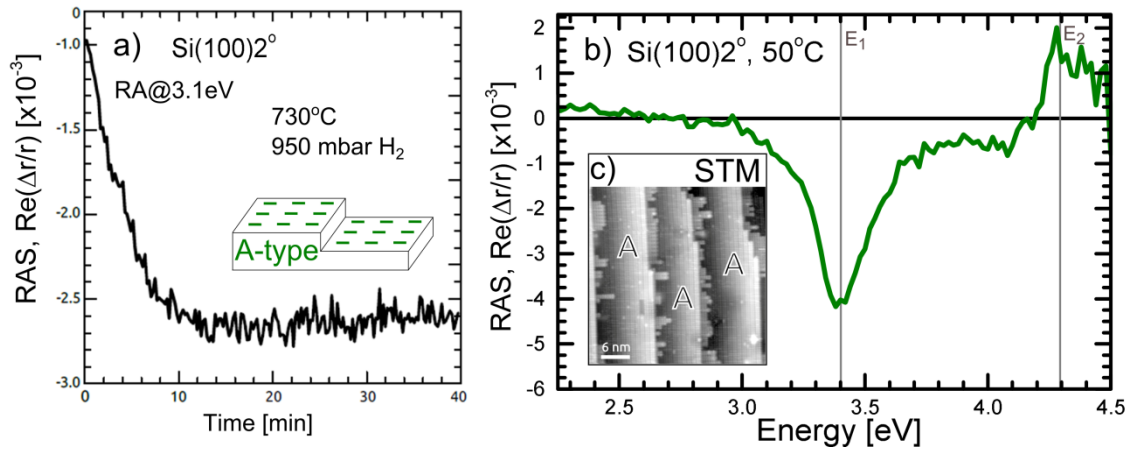


Fig. 4.2: (a) Transient *in situ* RA measured at 3.1 eV during annealing of Si(100) 2° offcut in [011] direction in 950 mbar at 730 °C. Over time Si vacancies diffuse anisotropic with a preference along the dimer rows and annihilate at the end of the dimer rows, which leads to retreat of the B-type terraces and majority of A-type domain on the surface. (b) shows RA spectrum of the A-type domain surface taken at 50 °C and (c) exhibits corresponding to the RA spectrum STM scan of the final surface. Based on data published in *Ref.* [78].

4.1.3 *In situ* controlled preparation of Si(100) 6° in H₂ ambient

This subchapter summarizes results regarding the Si(100) 6° surface. In contrast to Si(100) substrates with lower offcuts, the substrates with 6° offcut enables *in situ* control in all range of temperatures. Here, a short summary is provided concerning the clean Si surface, hydrogen termination and preferential dimer orientation after oxide removal and domain formation dependent on the H₂ pressure with an *in situ* RAS control. This knowledge is used when discussing the Si(100) 6° surface in As ambient (subchapter 8.1.2). Data presented in this subchapter have been published in *Ref.* [66].

4.1.3.1 *In situ* deoxidation

The inset in Fig. 4.3 shows *in situ* RAS data of vicinal Si(100) substrate with 6° offcut in [011] direction during annealing at 1000 °C [66,162]. Initially, the sample is covered by an oxide layer, which exhibits no RAS signal (Fig. 4.3 inset, black line). As shown in *Ref.* [66,162], during annealing in 950 mbar H₂ at 1000 °C, a RAS signal with a broad

minimum around 3.0 eV evolves. The final spectrum (Fig. 4.3 inset, thick red line) exhibits an additional shoulder at 3.4 eV and a small peak at 4.2 eV. The features of this RA spectrum match well the characteristic RAS signal of clean vicinal Si(100) [66,162,163]. This RA spectrum was assigned to the Si(100) surface partially terminated by H₂, precisely in this temperature range at 950 mbar to about 25 % [66,119,162,164] (see also subchapter 2.5).

Since *in situ* RAS of vicinal Si(100) 6° surface exhibits characteristic spectra which are different for the oxidized and clean or partly H-covered surface, it is possible to monitor the oxide removal process during the deoxidation at high temperature [66]. Figure 4.3 shows *in situ* RAS measurements during thermal annealing of Si(100) 6° substrates in H₂ at 950 °C (black line), 975 °C (red line), and 1000 °C (blue line) [66]. This range of temperatures enables complete removal of oxides from Si(100) surfaces [76]. The RAS transients are at fixed energy 3.0 eV, which corresponds to the position of the characteristic broad minimum in the RA spectrum of clean, vicinal Si(100) surfaces (see Fig. 4.3 inset, red line).

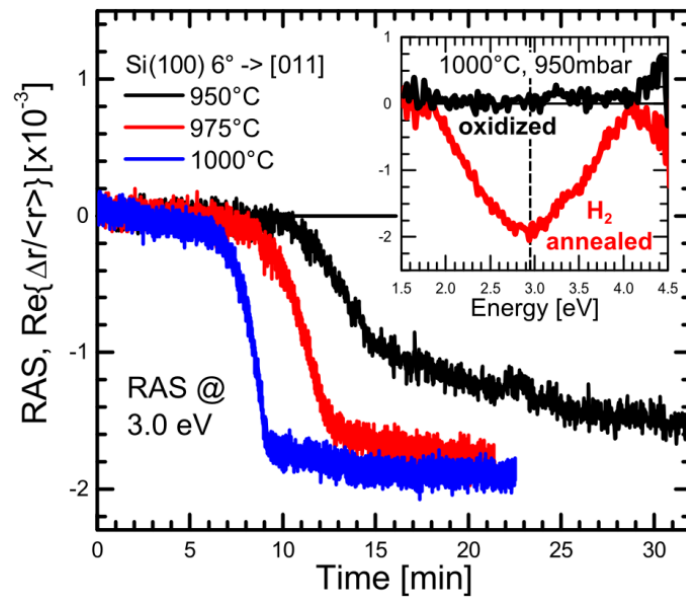


Fig. 4.3: Transient *in situ* RAS measurement at Si (100) 6° during annealing in 950 mbar, in H₂ at 950 °C, 975 °C, and 1000 °C. The transient at 3.0 eV monitors the transition from an oxidized surface to an oxide free surface with their characteristic spectra shown in the inset. The figure is taken from Ref. [66].

At the beginning of the deoxidation, the RAS signal is zero due to full coverage of the surface with an oxide layer (see Fig. 4.3 inset, black line). The drop of the signal in each measurement is correlated with the removal of the oxide layer and a partly clean Si(100) surface. The transients at 975 °C (red line) and 1000 °C (blue line) show a very abrupt drop, after around 13 min and 10 min, respectively, and faster saturation of the RAS signal compared to the deoxidation process at 950 °C. The signal saturation indicates complete oxide removal [66], confirmed by XPS measurements [76]. In the case of

sample annealed at 950 °C, the RAS transient does not show any signal change from the initial state until around 13 min. The slow change in the signal indicates a slow deoxidation, which is not complete until 30 min, when the signal is completely saturated. The RAS transients show a strong correlation between the time of the complete Si(100) 6° deoxidation and the annealing temperature. The higher the temperature, the faster the deoxidation processes. At 975 °C (red line) and 1000 °C (blue line), the transients are saturated already at 20 min, indicating that the Si(100) 6° surface is completely deoxidized.

4.1.3.2 Formation of A- and B-type domains

After oxide removal, the surface is terminated by hydrogen during cooling in H₂ due to the increasing H adsorption rate. As described in [119], the hydrogen strongly interacts with the Si surface at high pressure (950 mbar), which leads to formation of double layer steps with A-type majority domain on the terraces (kinetically driven process). During preparation under low H₂ pressure (50 mbar) the hydrogen interaction with the Si surface is reduced which results in energetically governed double-layer step formation with B-type majority domain.

Figure 4.4 shows RAS of Si(100) 6° surfaces from *Ref.* [66,119,162]. The sample cooled down in 950 mbar (green line) exhibits a spectrum which agrees with the characteristic RAS signal of a monohydride terminated Si(100) surface with a prevalence of the A-type domain indicated by the strong negative peak-like feature at 3.4 eV [78].

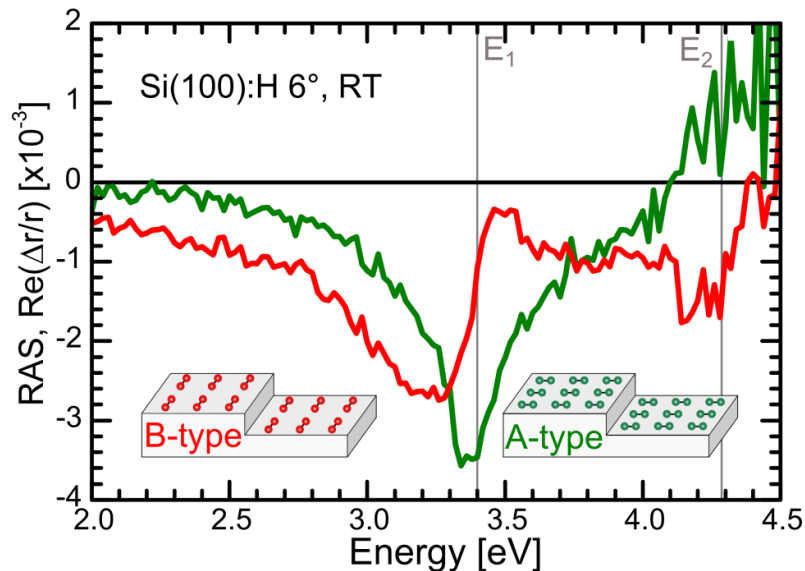


Fig. 4.4: RAS of Si(100) 6° surface prepared by slow cooling at 950 mbar H₂ (green line) and fast cooling at 50 mbar H₂ (red line) after our standard Si process. The spectra were measured at room temperature. Insets show dimer orientation on the surface in relation to the step edges. Figure after [66,119]. Gray vertical lines indicate the E₁ and E₂ interband transitions of Si [135] at room temperature.

From the amplitude of the RAS peak at 3.4 eV, which is sensitive to the dimer orientation on the surface, the domain ratio between the majority A-type to the minority B-type domain can be quantified to a ratio of 70:30 [66,155]. In contrast, the sample cooled down at 50 mbar (red line) exhibits the RAS signal with a characteristic “derivative”-like features at the transition band energies E_1 and E_2 at 3.4 and 4.27 eV, respectively [162]. The RAS signal agrees very well with spectra of monohydride terminated vicinal Si(100) surfaces with a B-type majority domain and D_B steps [163]. The majority domain orientation on the terraces of both surfaces were confirmed by LEED patterns and STM images [119].

In comparison to the RA spectra of Si(100) 0.1° (see Fig. 4.1) and 2° B-type domain [78,119], the RA spectrum of the Si(100) 6° B-type domain (Fig. 4.4 red line) does not exhibit a characteristic maximum at energy 3.4 eV. In the case of Si(100) 0.1° and 2° the change of majority domain on the terraces (from A-type to B-type surfaces) is represented by the opposite sign of the spectrum (see Fig. 4.1). In the case of the RA spectrum of B-type terraces on Si(100) 6° surface, domain ratio quantification cannot be obtained directly from the RA spectrum. The RA spectrum might reflect contribution not only from surface reconstruction (domain orientation) but also from steps on the surface [165]. However, the quantification of the domain ratio can be examined by FTIR in ATR, which was established in our group for Si(100) surfaces with lower offcuts [77,166]. FTIR measurements in ATR mode enable direct proof of the monohydride termination on the Si(100) samples as well as quantification of the domain distribution on the monohydride terminated Si(100) surfaces by polarization dependent measurements [167,168].

As shown in *Ref.* [66], ATR spectra of Si(100):H 6° B-type surface shows two major absorption peaks at 2098 cm^{-1} and 2086 cm^{-1} , which can be assigned to symmetric and antisymmetric stretch modes of coupled Si-H monohydrides, respectively [168–170]. The dipoles associated with the symmetric stretch mode are perpendicular to the surface and therefore only couple to p-polarized radiation, while the dipoles of the antisymmetric stretch mode are oriented within the surface plane and potentially couple to both polarizations [77]. Based on the ATR spectra, in *Ref.* [66] the majority to minority domain ratio was estimated by scaling the absorption signal of the s-polarized measurement (dimers oriented parallel to the plane of incidence) to the height of the p-polarized signal (dimers oriented perpendicular to the plane incidence) and was equal to 73:27. The FTIR measurements thus confirm that the B-type majority domain is more favorable for Si(100) 6° surfaces prepared under low H_2 pressure (50 mbar).

4.1.3.3 Kinetic vs. energetic domain in a step formation process

It is possible to control the prevalence for the A- or B-type domains (either kinetically or energetically governed surface formation) on vicinal Si(100) surfaces, by applying the

appropriate cooling procedure. RAS enables *in situ* control during the process and identification of the prevailing domain.

As shown above, preparation of substrates with high step density in H₂ ambient induces a strong competition between surface energetics (tendency for D_B steps) and kinetic processes (tendency for D_A step), which influence the step and domain formation. During preparation under high H₂ pressure (950 mbar) the hydrogen strongly interacts with the Si surface, which leads to Si removal and vacancy generation. The vacancy diffusion and annihilation at step edges leads to formation of double layer steps with A-type majority domain on the terraces – kinetically governed surface formation [78,119].

During preparation under low H₂ pressure (50 mbar) the hydrogen interaction with the Si surface is reduced. In consequence, the Si vacancies generation is also reduced. The diffusion of Si atoms leads to form energetically favorable double layer steps with B-type majority domain in accordance with theoretical studies [171,172] and studies in UHV [71].

4.2 Si(111) in hydrogen ambient

Since Si(111) after deoxidation in H₂-ambient results in (1×1) surface reconstruction (see chapter 6.3.3.) due to the surface isotropy, there is no expected RAS signal arising from the surface. However there is a RAS signal observed on Si(111) surfaces with an offcut which is step-induced. The first investigation of the optical anisotropy of H-terminated Si(111) surfaces was done by Yasuda *et al.* [173]. The Si(111) samples were cleaned by a standard RCA procedure, and afterwards etched in hydrogen fluoride for 30 sec. They observed two different RAS signals for surfaces of Si(111) with a offcut in $\langle 11\bar{2} \rangle$ and $\langle \bar{1}\bar{1}2 \rangle$ direction. RAS signal from Si(111) with an offcut in the $\langle 11\bar{2} \rangle$ direction exhibited two clear peaks at 3.45 eV and 4.25 eV, signed by the author as an electronic response from the bulk [136]. The RA spectrum line shape suggests that all response arise from (110) – like regions of the stepped (111) surfaces (Fig. 2.1 in subchapter 2.4.3). RA spectrum from Si(111) with an offcut in the $[\bar{1}\bar{1}2]$ direction was an approximately inverted version of the Si(111) with an offcut in the opposite direction. The authors suggested that the RAS signal must come from the modified step structure upon strong interaction between H and Si atoms on the steps. Si atoms on the $\langle \bar{1}\bar{1}2 \rangle$ step edges are bonded to other Si atoms by only two bonds, leaving two dangling bonds. In consequence, the steps are less stable than the $\langle 11\bar{2} \rangle$ steps and susceptible to roughening. Schmidt and Bernholc [91] explained this RAS signal as a response from newly formed $\langle 11\bar{2} \rangle$ steps: straight dihydride-terminated steps in $[\bar{1}\bar{1}2]$ direction transform to zigzag chains of monohydride terminated steps in $[1\bar{2}1]$ and $[\bar{2}11]$ direction.

5 Sample preparation

Here, sample preparation and standard MOCVD processes are described.

5.1 Wet Chemical Etching

The Si substrates were processed in the MOCVD reactor either covered by native oxides or by a thin oxide layer prepared by a wet-chemical pretreatment – RCA 1 + HF dip + RCA 2. Removal of organic contamination and metals was done by boiling the substrates for 10 min in a basic etch solution consisting of ammonium hydroxide (NH_4OH , 25 %), hydrogen peroxide (H_2O_2 , 30 %), and deionized (DI) water (H_2O) at the ratio of 1:1:6. Oxide removal for Si(100) was done by dipping in hydrogen fluoride (HF) mixed with DI water (1:4 ratio) solution for 10 s. In the case of Si(111) we used HF combined with ammonium fluoride (NH_4F) in ratio 1:7 – buffer oxide etching (BOE). Preparation of a well-defined thin oxide layer was done in a boiling acid solution of hydrochloric acid (HCl, 32 %), hydrogen peroxide (H_2O_2 , 30 %), and DI water at a ratio of 1:2:6 for 10 min. In between, the samples were rinsed in DI water for at least 5 min. The wet-chemical pretreatment ensured similar starting conditions for all samples.

5.2 Standard process of Si and GaP deoxidation and growth in MOCVD

In this study we use p- and n-type doped Si(111) substrates with normal orientation (0°), and with 3° and 6° offcut in $[\bar{1}\bar{1}2]$ or $[11\bar{2}]$ direction. In case of Si(100) we use p- or n-type doped substrates with 0.1° , 2° or 6° offcut towards $[011]$ direction. For Fourier-transform infrared spectroscopy (FTIR) we used an parallelepiped attenuated total reflectance (ATR) Si(111) crystal with 6° miss-orientation measuring $28.8 \times 10 \times 0.6 \text{ mm}^3$ with 45° bevels cut at the short edges in order to couple the infrared light in and out. The surface steps are parallel to the short edge of the crystal. All substrates were provided by the company CrysTec. For homoepitaxial growth of GaP we use GaP(111)A- and B-type polarity substrates (ITME) with a 0° offcut.

All samples were prepared in AIXTRON AIX200 MOCVD system (more details in subchapter 3.1). The temperature offset at the surface was estimated applying AlSi eutectics. The temperature offset for the horizontal reactor in the double-side system is:

at 950 mbar around 4 °C, at 100 mbar around 16 °C and at 50 mbar around 21 °C. For the one-side reactor the temperatures offsets are as follow: at 950 mbar 12 °C and at 100 mbar 22 °C. The temperature offset depends on the total H₂ flow in the reactor and on the design of the carrier. All temperatures given in this work refer to the temperature of the susceptor.

The “standard” Si MOCVD deoxidation process is carried out at 1000 °C for 30 min at 950 mbar H₂ pressure. For some samples, a Si buffer layer of 0.25 μm thickness was grown subsequently, at 950 °C and 200 mbar in 15 min by the use of SiH₄ (10 % in H₂). After buffer growth, the samples were annealed at 1000 °C and high H₂ pressures for 10 min. In case of Si(100) substrates with 2° offcut towards [011], to prepare well defined monohydride-terminated surface with a (1×2) surface reconstruction, samples were subsequently annealed at 730 °C, at 950 mbar (see subchapter 4.1.2).

GaP substrates were deoxidized by annealing at 650 °C for 15 min at 100 mbar under supply of TBP to prevent phosphorus desorption. Afterwards, the substrate was annealed at 420 °C for 10 min to remove any excess of P from the surface.

5.3 Standard GaP(100) epitaxy

To nucleate GaP pulses of TBP and TEGa (1s each with 1s pause in between) [174] were applied at low temperature in the range of 420 °C prior to GaP growth above 570 °C [175]. Both nucleation and growth are carried out at 100 mbar. The nucleation at low temperature leads to GaP epilayers free of islands, twin defects and stacking faults, as long as the Ga amount is low enough to avoid Ga droplets formation.

5.4 GaAs NWs growth

GaAs NWs were grown by the vapor-liquid-solid (VLS) method [15] in MOCVD ambient on GaP(111)A- and B-type polarity substrates, and as well on GaP/Si(111) quasi-substrates, and GaAs(111) B-type polarity substrates for a reference. The substrates were cleaned with boiling acetone and isopropanol prior to growth and gold particles were deposited from a colloidal gold solution with 100 nm diameter. The NWs were grown in a two-temperature growth mode procedure [176] for 1 min. at 450 °C and 8 min. at 400 °C without intentional doping [177]. The complete NW growth procedure on all the substrates was done by Matthias Steidl.

6 Si(111) in CVD ambient

This chapter focusses on Si(111) preparation in H₂ and As ambient. Initially we investigate the oxide removal, the surface chemical composition, hydrogen termination and the surface structure in the As-free ambient as a basis for the subsequent study. We show that despite isotropic Si(111) surface it is possible to benchmark characteristic RA spectra for the substrates with an offcut. Further, the Si(111) termination with As is analyzed in detail. We will discuss the different behavior of the steps on Si(111) depending on the offcut direction, which in turn will have an impact on subsequent GaP nucleation. Results regarding Si(111) 0° are the outcome of experimental collaboration with Matthias Steidl and Dr. Weihong Zhao and parts of this subchapter are published in Applied Surface Science, *Ref.* [178].

6.1 Si(111) surfaces in hydrogen ambient

Before we investigate the Si(111) As-terminated surface, we will focus on the deoxidation in the “clean” MOCVD system (free of III-V residuals). We examine if processing in H₂ ambient leads to the surface passivation by hydrogen. Subsequently, we investigate the Si(111) surface reconstruction and we look at the surface morphology.

6.1.1 Chemical composition after oxide removal

To deoxidize Si(111) samples we adapted the deoxidation parameters from the Si(100) (see subchapter 5.2) [76]. Figure 6.1 compares XPS spectra of Si(111) 0° surface before (black line) and after (blue line) annealing in H₂ ambient (deoxidation). Before annealing O 1s, C and SiO_x PE lines are clearly visible in the survey spectrum (black line). The O 1s PE line is at a binding energy of about 533 eV. This corresponds to a chemical shift of about 2.0 eV towards higher binding energies compared to the elemental O 1s PE line, which indicates silicon-oxygen bonding [179,180]. In agreement, an additional broad peak at about 103.9 eV and the contributions between 101.3 eV and 102.6 eV correspond to the Si 2p photoemission from the SiO₂ layer with different oxidation states of Si in the oxidized layer [181]. In contrast, we did not detect any contribution of oxygen or oxides in the XP spectra of the Si surface after annealing in H₂, neither in the O 1s nor in the Si 2p PE line. The splitting of the silicon PE line at 99.6 eV of around 0.59 eV correlates well with the separation of Si 2p_{3/2} and Si 2p_{1/2} due to spin orbit coupling [182]. The intensity of the Si 2p_{3/2} and Si 2p_{1/2} PE lines is greater in comparison to the samples

before the annealing. An asymmetric peak related to C 1s is visible at binding energy of 286 eV in the XP spectrum of the sample before annealing. This peak is shifted by 1.0 eV with respect to the PE line of elemental carbon at 285 eV (graphite) and contributions with a chemical shift of up to 5 eV are present. This indicates the presence of different carbon species, which are likely oxygen related [183]. In contrast, the absence of the C 1s peak after annealing confirms the removal of carbon related impurities.

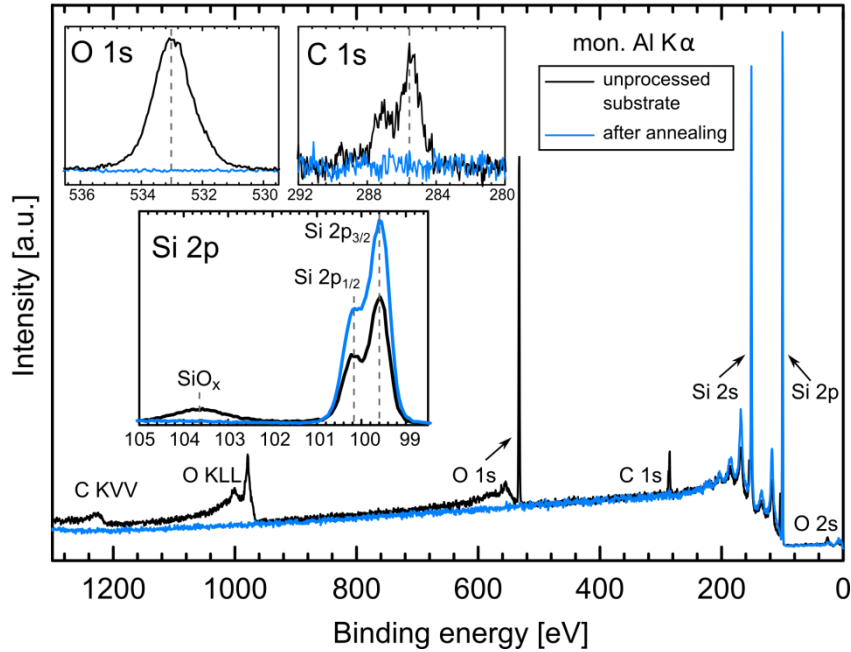


Fig. 6.1: XPS survey spectrum as well as O 1s (top left), C 1s (top right) and Si 2p (middle) photoemission lines. XPS spectra of Si(111) were measured under a photoelectron take-off angle of 90° of two samples: Si(111) surface before (black line spectrum) and after annealing in H₂ at 1000 °C for 30 minutes (blue line spectrum).

Carbon removal is decisive in order to avoid undesirable three-dimensional (3D) growth of subsequent epitaxial layers [184]. In comparison, carbon removal in UHV requires high temperatures above 1100 °C [185], which might promote undesirable diffusion processes of impurities and dopants. Our XPS results show that annealing for 30 min at 1000 °C is sufficient to remove oxides and other contaminations from the Si(111) surface within the detection limit of XPS. The XP spectra of Si(111) substrates with an offset do not differ and therefore are not shown here.

6.1.2 Hydrogen termination

Processing in H₂ MOCVD ambient could lead to a H-terminated Si(111) surface, as in analogy to our previous results regarding deoxidation of Si(100) in H₂ ambient [77]. The Si(111) sample after deoxidation was transferred in UHV to our FTIR set-up. Figure 6.2 shows surface sensitive FTIR measurements in ATR configuration employing light polarized perpendicular (s-pol) and parallel (p-pol) to the plane of incidence (see inset).

The p-pol spectrum (Fig. 6.2, orange line) shows a strong absorption band at 2083.5 cm^{-1} with a small shoulder at 2089.4 cm^{-1} , whereas no absorption lines are visible for s-polarized light within this range. Since the absorption line at 2083.5 cm^{-1} agrees well with the vibrational mode of silicon monohydride (Si-H) [90] and is absent for s-polarized light, we conclude that the hydrogen is bonded perpendicularly to the uppermost layer of Si atoms. The small shoulder at 2089.4 cm^{-1} can be attributed to the hydrides bonded to the Si atoms at the step edges [90,186] due to the crystal offcut. While continuous adsorption and desorption of H will occur at higher temperatures, the H-termination likely stabilizes during cooling, after the deoxidation step.

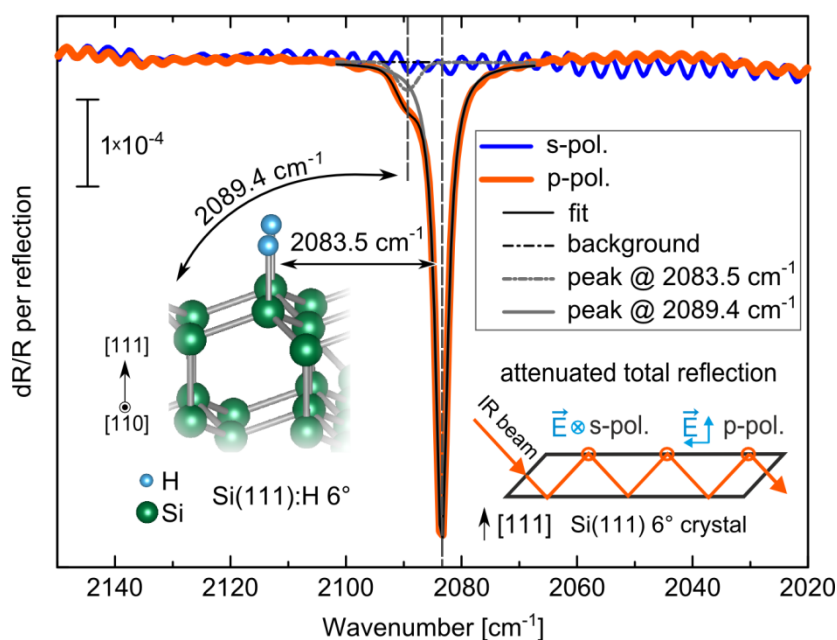


Fig. 6.2: Surface sensitive FTIR-spectra of MOCVD deoxidized Si(111) with 6° offcut: absorption at 2083.5 cm^{-1} is assigned to the Si-monohydride bonds at the terraces, and the small shoulder at 2089.4 cm^{-1} indicates hydrides bonded to the Si at the step edges.

6.1.3 Surface reconstruction

To investigate the surface reconstruction and atomic structure on Si(111) 0° surface after deoxidation we applied LEED and STM³. Figure 6.3 (a) shows the LEED pattern of the Si(111) surface (after deoxidation) measured at 150 eV acceleration voltage. The pattern exhibits first order spots (marked with black circles) with a clear 3-fold symmetry, which corresponds to a (1×1) surface reconstruction. This result confirms monohydride-terminated surface (hydrogen atom is bonded to the Si atoms on the terraces), detected by FTIR, which leads to non-reconstructed surface.

³ The STM measurement was done by Dr. Weihong Zhao.

The STM image in Fig. 6.3 (b) confirms very well ordered (1×1) reconstructed Si(111) 0° surface (here, shown a representative section of the surface). On the STM scan the Si atomic distance is equal to 3.8 Å which agrees with the Si(111), hydrogen terminated (1×1) reconstructed surface. The white rhombus indicates the unit cell.

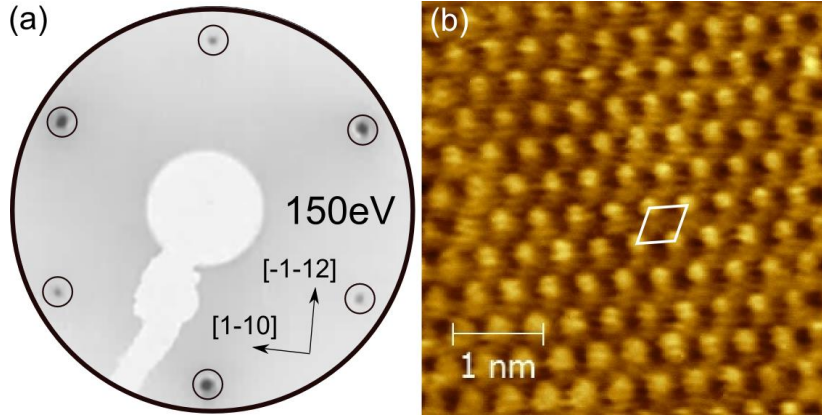


Fig. 6.3: (a) LEED pattern of Si(111) 0° surface after deoxidation in H₂ ambient, the first ordered spots confirm (1×1) surface reconstruction. (b) STM scan from the same surface, well ordered (1×1) reconstructed surface is visible (the white rhombus indicates the unit cell).

6.1.4 Step structure of Si(111) with an offcut in $[11\bar{2}]$ and $[\bar{1}12]$ direction

First we will look at the surface morphology of Si(111) with an offcut in $[11\bar{2}]$ direction after deoxidation. Si(111) samples with 0°, 3°, and 6° offcut were deoxidized (30 min, 950 mbar, 1000 °C) in hydrogen ambient. Figure 6.4 exhibits measured RAS of these surfaces at 50 °C.

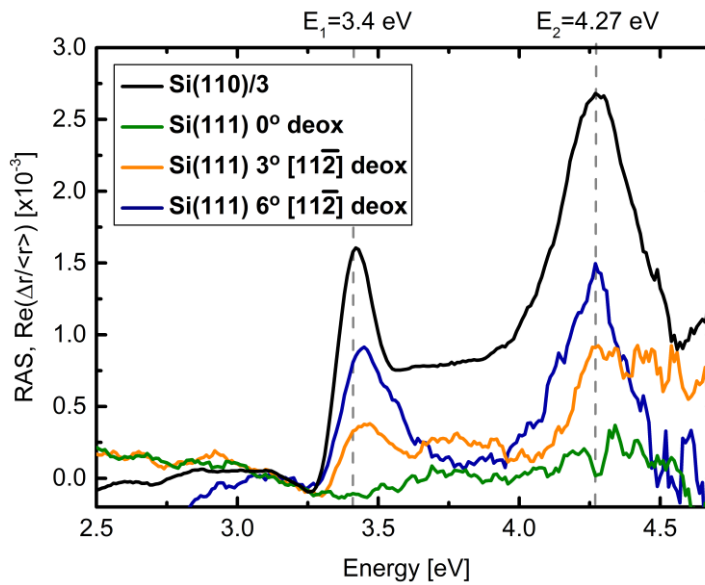


Fig. 6.4: Measured RA spectra (at 50 °C) of Si(111):H with offcut in $[11\bar{2}]$ direction. For comparison we show a RA spectrum from oxidized Si(100) sample (divided by factor of 3). RA spectra from Si(111) substrates with offcut exhibit two characteristic peaks at E_1 and E_2 transition band energy.

While there is no RAS signal from Si(111) 0° surface (green line), the RA spectra from Si(111) substrates with 3° (orange line) and 6° (blue line) offcut exhibit two characteristic peaks at E_1 and E_2 interband transitions [136]. For comparison we show a RA spectrum from oxidized Si(110) sample (Fig. 6.4 black line, the spectrum is divided by factor of 3). The Si(110) RA spectrum shows two maxima near the E_1 and E_2 critical points of the bulk band structure. The reflectance anisotropy spectroscopy of Si(110) mainly originates from the bulk (dielectric functions and refractive indices of the bulk and ambient phases) [131,187]. The oxidation layer, in addition creates an optical absorption band near 3 eV and enhances E_2 and derivative features [173]. The RAS line shape from Si(111) surfaces are very similar to the one from Si(110), and in addition, the intensity of the RAS signal increases with increasing offcut angle.

Since LEED measurements of Si(111) 3° , and 6° show the exact pattern as the Si(111) 0° sample, we exclude the possibility that the RA signal reflects a difference in a surface reconstruction. We conclude that the RA spectra arise from (110) regions (35.4° to (111) plane) of the stepped (111) surfaces (see Fig. 2.11 in subchapter 2.4.3) and in principle can be as small as a single bi-atomic step, in agreement with the literature [91,173,187]. We did not observe any differences in the RAS signals from samples after homoepitaxy and deoxidation or any influence of wet chemical etching prior to the MOCVD process (not shown here).

Figure 6.5 exhibits LEED patterns of Si(111) 3° $[11\bar{2}]$ after deoxidation (left hand side) and homoepitaxy (right hand side). In both cases, the LEED spots correspond to (1×1) surface reconstruction, they are sharp but despite the offcut of the sample there is no spot splitting visible, which on surfaces with an offcut indicates irregularly spaced terraces. When comparing the LEED pattern of the sample after homoepitaxy to the one after deoxidation, the spots are sharper and more pronounced, which could suggest a more ordered surface.

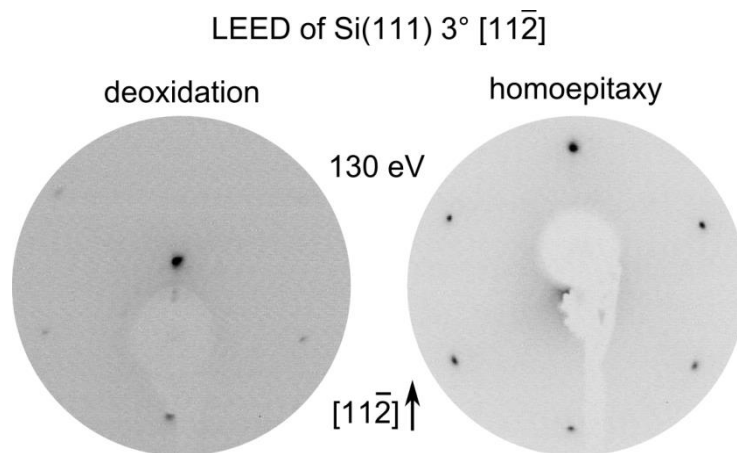


Fig. 6.5: LEED patterns of Si(111) 3° $[11\bar{2}]$ after deoxidation (left hand side) and homoepitaxy (right hand side). Both surfaces exhibit (1×1) surface reconstruction.

Since the RAS signals arise from (110)-like regions of bilayer steps on the Si(111) we assume straight steps on the surface. To investigate the Si(111) 3° $[1\bar{1}\bar{2}]$ surface in an atomic scale after deoxidation the sample was transferred to STM. The STM⁴ scan from this surface is shown in Fig. 6.6. Surprisingly, on the surface the steps are not only oriented in the offcut direction but there are also steps oriented 60° to the off cut direction. The terraces of the steps in both directions seem to be evenly spaced and the step edges are straight. Average terraces lengths, marked as (a) and (b) on the Fig. 6.6 are equal to 6 nm and 40 nm, respectively. The terrace width (a) is in agreements with the terrace width of the Si(111) sample with 3° offcut.

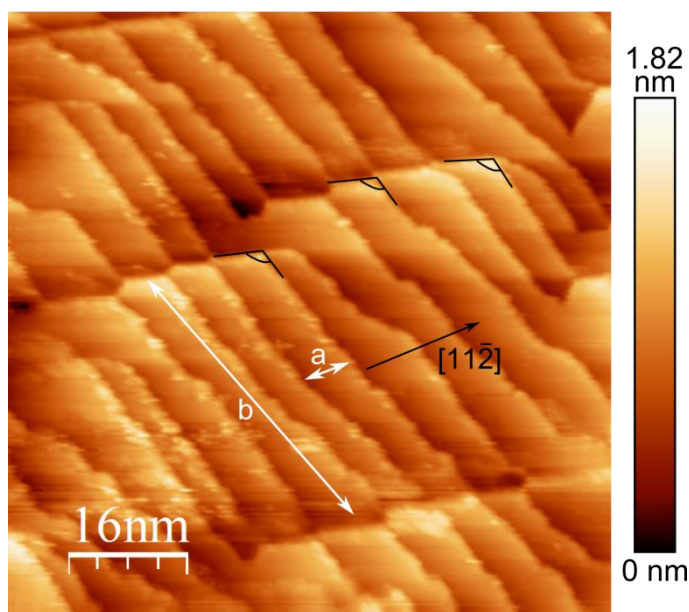


Fig. 6.6: STM scan of Si(111) 3° $[1\bar{1}\bar{2}]$ after deoxidation.

The terraces are spaced up to two bi-atomic layer height. The angle on the edge between the two terraces (Fig. 6.6, black lines) in average is equal to 120° . To explain the additional appearance of the terraces we measured the sample with XRD⁵, and found that on each wafer the offcut direction is not exactly oriented at 90° to the major flat, but possess an error equal to maximum 7° . Therefore, to accommodate the error in the offcut precision (the additional tilt) additional steps are formed. The STM scans revealed that any offset of the offcut angle would affect the step formation on the surface.

Now we will investigate the Si(111) $[\bar{1}\bar{1}\bar{2}]$ surface morphology after deoxidation and homoepitaxy. Si(111) substrates with 0° , 3° , and 6° offcut in $[\bar{1}\bar{1}\bar{2}]$ direction were deoxidized (30 min, 950 mbar, 1000°C) in hydrogen ambient. Figure 6.7 exhibits RAS (taken at 50°C) of the H_2 terminated surfaces. While there is no RAS signal from Si(111) 0° (green line), the RA spectra from Si(111) substrates with 3° (orange line), and 6° (blue line) offcut exhibit very similar spectra. In both, there are characteristic peaks around

⁴ The STM measurement was done by Dr. Weihong Zhao.

⁵ The XRD measurement was done by Christian Koppka.

3.3 eV and 3.55 eV and a minimum at around 3.8 eV. As in the case of Si(111) with offcuts in $[11\bar{2}]$ direction, the RAS signals from Si(111) $[\bar{1}\bar{1}2]$ surfaces increases with the offcut of the samples.

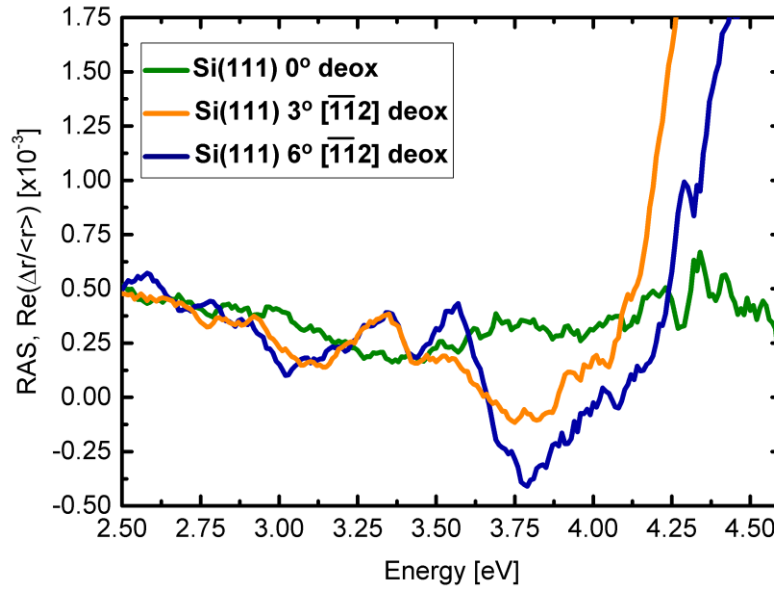


Fig. 6.7 Measured RAS (at 50 °C) of Si(111):H with offcut in $[11\bar{2}]$ direction.

Since the signal from Si(111) with offcut in direction $[11\bar{2}]$ arises from (110) planes we could expect that on samples with offcut in $[\bar{1}\bar{1}2]$ direction the RAS should arise from (113) or (001) planes [173,188], (see Fig. 2.11 in subchapter 2.4.3). However our signal is not comparable with the RAS signals from the (113) or (001) planes, [90,188]. The RA spectra shown on Fig. 6.7 are also not comparable with the RA spectrum shown by Yasuda *et al.* [173] of Si(111) $5^\circ [\bar{1}\bar{1}2]$ terminated by H after immersion in HF. The RAS signal in this *Ref.* reflects the modified step structure from unstable to stable zig-zags chains with monohydride step edges in $[\bar{2}11]$ and $[1\bar{2}1]$ direction (see Fig. 2.12 in subchapter 2.4.3). However, the spectra shown in Fig. 6.7 exhibit some similarities with RA spectrum calculated by density-functional theory in the local-density approximation (DFT-LDA) for Si(111) $24^\circ [\bar{1}\bar{1}2]$ surface [91]. Figure 6.8 shows calculated RA spectra for Si(111) $24^\circ [\bar{1}\bar{1}2]$ surface terminated by in-plane (green line) vertical dihydride [91] (the in-plane and vertical dihydrides are depicted on Fig. 2.12 in subchapter 2.4.3). The measured RA spectrum from Si(111) $6^\circ [\bar{1}\bar{1}2]$ substrate (Fig. 6.8 red line) is shifted by 0.1 eV towards higher energy to even the shift in energy of the calculated spectra due to difference in the temperature. After shifting the Si(111) $6^\circ [\bar{1}\bar{1}2]$ RA spectrum by 0.1 eV it is clear that the maxima at 3.35 eV and 3.56 eV and the shoulder up to 3.79 eV matches the calculated RA spectra. The measured RA spectrum shows more similarities to the calculated spectrum of Si(111) surface terminated by energetically preferred vertical dihydride structures on $\langle\bar{1}\bar{1}2\rangle$ steps. Remaining differences between two spectra might be caused by the Si(111) step structure modified after interaction with H_2 .

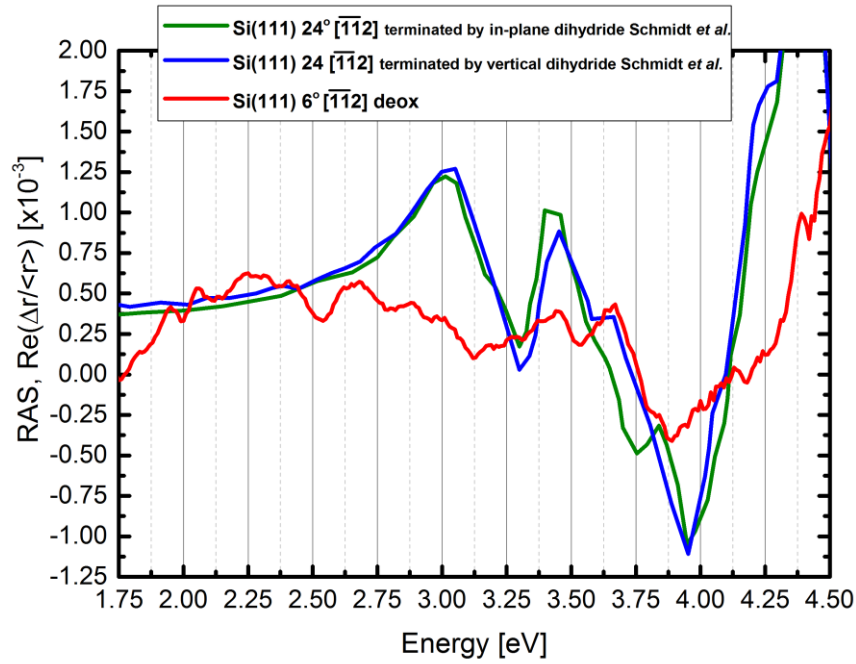


Fig. 6.8: Calculated RA spectra for Si(111) 24° $[\bar{1}\bar{1}2]$ surface terminated by in-plane (green line) and vertical dihydride. Spectra are taken from the *Ref.* [91] The measured RA spectrum from Si(111) 6° $[\bar{1}\bar{1}2]$ substrate (red line) is shifted by 0.1 eV (the shift is due to a difference in the temperature between the measured and calculated RA spectra).

Figure 6.9 exhibits LEED patterns of Si(111) 3° $[\bar{1}\bar{1}2]$ surfaces after deoxidation (left hand side) and homoepitaxy (right hand side). In both cases, the LEED pattern indicates the (1×1) surface reconstruction, the first order spots are sharp and spot splitting is visible which indicates regular terrace spacing. In the LEED pattern of the sample after homoepitaxy (right hand side) the spots seems to be brighter in comparison with the LEED pattern of the sample after deoxidation, which indicates a more ordered surface.

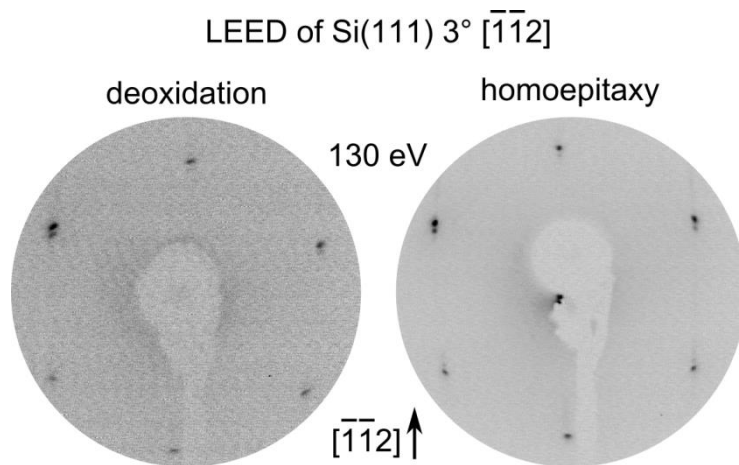


Fig. 6.9: LEED patterns of Si(111) 3° $[\bar{1}\bar{1}2]$ after deoxidation (left hand side) and homoepitaxy (right hand side). Both LEED patterns exhibit (1×1) surface reconstruction.

The Si(111) $[\bar{1}\bar{1}2]$ surface highly interacts with H_2 after etching in HF with a high pH. In a kinetic model (see subchapter 2.4.3) the etching of the surface occurs via attack of the corner atoms with dihydride termination (the Si atoms are bonded to two other Si atoms) causing a chain reaction resulting in the formation of perfect (111) regions with ideal monohydride termination (the Si atom is bonded to three other Si atoms). The orientation of these monohydride staircases is at an angle of $60^\circ / 120^\circ$ to the original step edges [90,91,173] (see Fig 2.12 in subchapter 2.4.3). To investigate the step structure on the Si(111) $[\bar{1}\bar{1}2]$ surface we carried out an STM measurement⁶ on a deoxidized surface (Fig. 6.10).

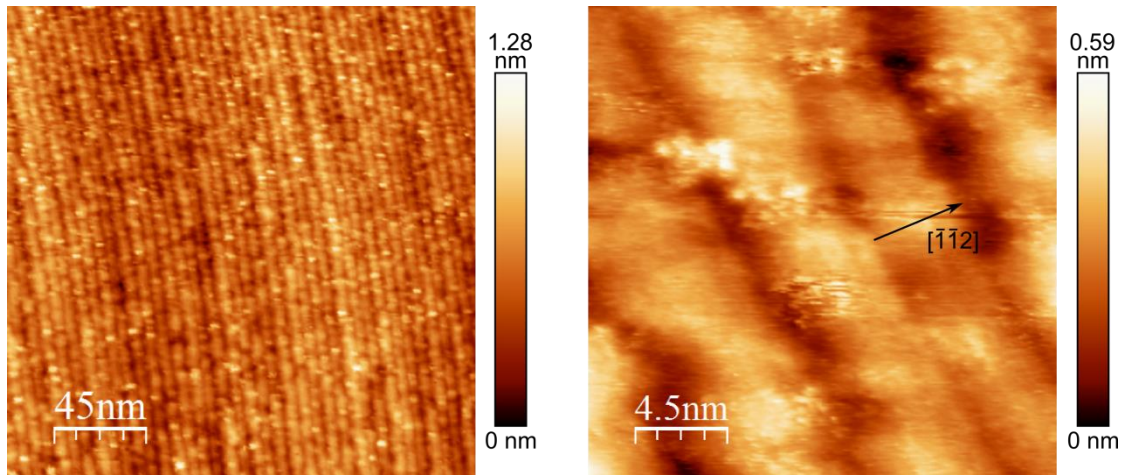


Fig. 6.10: STM scans of Si(111) $3^\circ [\bar{1}\bar{1}2]$ after deoxidation.

From the STM scans we observe that the steps are ordered with evenly spaced terraces and no step bunching is visible. The average terrace length on the STM scans is around 60 \AA , which agrees very well with the one calculated for Si(111) with 3° offcut (59.91 \AA). However, we were not able to achieve an atomic resolution; therefore, the atomic step structure cannot be concluded.

6.1.5 Surface morphology

In this subsection, we will focus on the surface morphology of differently prepared Si(111) samples, employing AFM. First, we will investigate the difference in surface morphology between the samples after deoxidation and homoepitaxy. In addition, as a comparison, we will investigate if wet chemical etching prior to deoxidation and homoepitaxial buffer layer have an impact on the surface morphology. For this purpose we have chosen Si(111) 0° . Secondly, we will discuss surface morphology of Si(111) substrates with 3° and 6° offcut.

⁶ The STM scans were done by Andreas Nägelein and Xin Wen.

Figure 6.11 shows AFM scans of Si(111) 0° surfaces after deoxidation and after deoxidation and homoepitaxy with and without prior wet chemical etching⁷. Figure 6.11 (a) shows AFM scan of Si(111) surface after the deoxidation process (see subchapter 5.2) without wet-chemical etching. On the surface, a step bunching is clearly visible, mostly of around 3 bilayers, which forms hillocks. The RMS roughness of this sample is 0.46 nm. Growth of a homoepitaxial buffer layer subsequent to the (thermal) deoxidation in case of Si(100) was shown to ensure defect-free and double-layer stepped substrate surfaces [189]. This common routine improves the surface morphology by reducing the surface roughness and provides a well-defined starting point for subsequent heteroepitaxy. Figure 6.11 (b) shows the AFM scan of the Si(111) surface after growth of a homoepitaxial buffer layer (see subchapter 5.2).

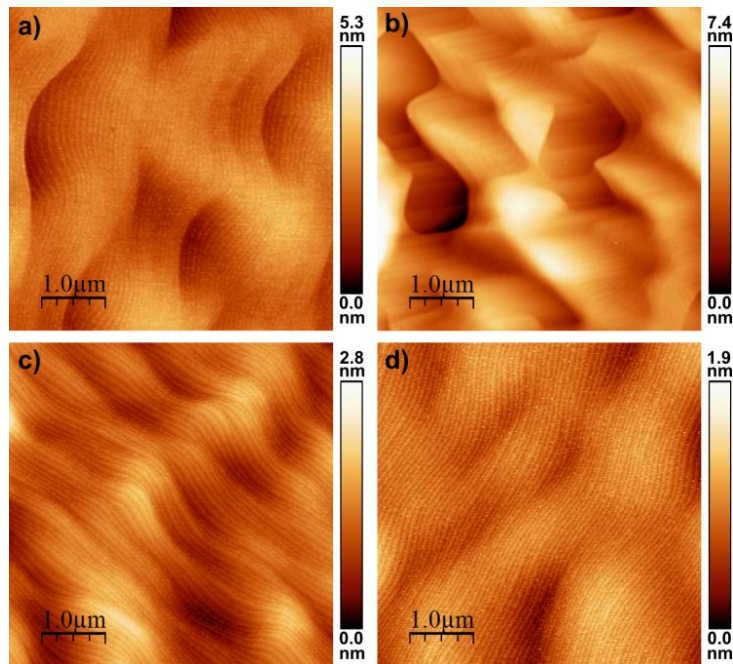


Fig. 6.11: Surface morphology of differently prepared Si(111): (a) only annealed (RMS = 0.46 nm); (b) annealed and growth of a homoepitaxial layer (RMS = 0.98 nm); (c) after wet-chemical treatment and annealing (RMS = 0.36 nm); (d) after wet chemical treatment, annealing and homoepitaxy (RMS = 0.20 nm).

In contrast to the surface after homoepitaxy (a), we observe on the surface the formation of a hill-and-valley structure with steep cliffs of up to 20 bilayers. The RMS surface roughness in this case is almost up to 1.0 nm. Figure 6.11 (c) images the Si surface morphology of Si(111) substrates after wet-chemical etching prior the thermal deoxidation. The surface roughness in this case is 0.36 nm, we observe a smooth surface with evenly distributed terraces and smooth wave-like shape step edges with a height of

⁷ Here, the wet chemical etching procedure was performed in HZB and was modified as follow: after dip in HF and rising with DI water the samples were dipped in 40% ammonium fluoride (NH_4F) to form atomically smooth, evenly spaced, monohydride-terminated terraces [232]. To reduce the formation of triangular etched pits on the surface, the NH_4F solution was bubbled through by nitrogen to remove oxygen [241].

one bilayer. It is clearly visible that the prior wet chemical etching treatment reduces surface roughness in comparison to the Si surface after thermal deoxidation without wet chemical pretreatment (a). Subsequent homoepitaxial buffer growth on the wet chemically pretreated Si(111) sample further reduced the surface roughness (Fig. 11 (d)). The AFM image shows a smooth surface with evenly spaced terraces. The wave-like shape of the step edges is decreased in comparison to the sample (c). The surface roughness in this case is reduced to 0.20 nm. It is known that in UHV (in the temperature range of 500 °C - 600 °C), the presence of (atomic) hydrogen during Si growth on Si(111) causes a change from layer-by-layer growth to a faceting of the layer [190]. Under CVD conditions, during Si(111) homoepitaxy, hydrogen flux causes formation of three-dimensional Si triangular “pyramids” [191]. Studies at atmospheric pressure in hydrogen ambient showed a transition from polycrystalline to monocrystalline growth with SiH₄ between 950 °C and 1000 °C [192], which was attributed to a change in hydrogen coverage. Theoretical calculations by Giling *et al.* [193] support this conclusion as they predict a hydrogen coverage of around 22 % at 1000 °C and 30 % at 950 °C (1 atm). However, it is unlikely that our surface roughens during the Si growth due to the presence of hydrogen, as samples which were wet chemically treated before annealing are smooth (Fig. 6.11 (d)). In principle, impurities and disordered Si surface can also cause roughening during homoepitaxial growth [184,194,195]. Dip of Si samples in NH₄F leads to Si etching by several nanometers (and possible contamination) and reduces the roughness of the Si surface after homoepitaxy.

We also carried out AFM measurements on Si(111) 3° and 6° with an offcut in $[\bar{1}\bar{1}2]$ and $[11\bar{2}]$ direction. The samples were wet chemically etched (to improve the surface morphology) prior the CVD process. The average RMS roughness from all the surfaces is summarized in the Table 6.12.

RMS of			
Si(111) 3° $[\bar{1}\bar{1}2]$		Si(111) 3° $[11\bar{2}]$	
deox	homoepitaxy	deox	homoepitaxy
0.29 nm	0.28 nm	0.67 nm	0.40 nm
Si(111) 6° $[\bar{1}\bar{1}2]$		Si(111) 6° $[11\bar{2}]$	
deox	homoepitaxy	deox	homoepitaxy
0.54 nm	0.49 nm	0.96 nm	0.77 nm

Tab. 6.12: RMS roughness of Si(111) 3° and 6° with an offcut in $[\bar{1}\bar{1}2]$ and $[11\bar{2}]$ direction after deoxidation and homoepitaxy.

In contrast to Si(111) 0° , the surface morphology between samples after deoxidation and homoepitaxy did not differ significantly (based on AFM scans, not shown here). The surface morphology of all the samples decreased after homoepitaxy and additional step bunching on the surface is visible. However, we did not observe any difference in the step structure (due to limited AFM resolution). In case of Si(111) with offcut in $[11\bar{2}]$ direction the surface roughness is almost twice higher when compared to the surface roughness of Si $[\bar{1}\bar{1}2]$. The difference in the surface roughness between Si(111) 3° $[\bar{1}\bar{1}2]$ and $[11\bar{2}]$ can result from a different behavior of the steps after interaction with H_2 .

6.2 Si(111) arsenic terminated surface

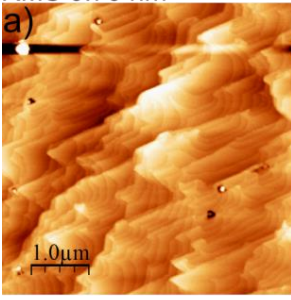
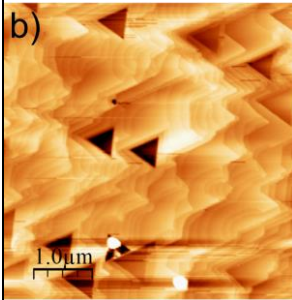
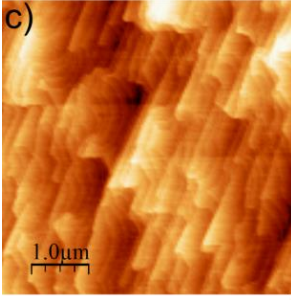
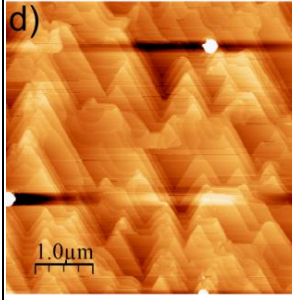
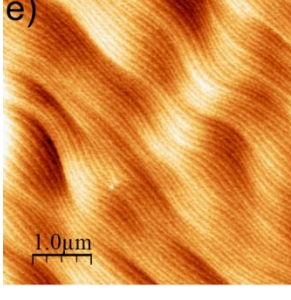
In this subchapter we will focus on Si(111) terminated with As. We will discuss the influence of background As on the surface structure and influence of TBAs on the step structure. Similarly to the previous chapter we apply RAS to benchmark Si(111) offcut surfaces.

6.2.1 Surface morphology of weak sample offcut

To investigate the influence of As on the Si(111) surface structure we did a series of experiments with different parameters of annealing in TBAs ambient at 950 mbar. Here, we employ Si(111) 0° and the process parameters that result in the smoothest surface morphology are transferred later to the Si(111) substrates with an offcut. All samples were first deoxidized and secondly a homoepitaxial buffer layer was grown. The experiments were done on wet chemically etched⁷ and not etched samples. The samples were annealed at 670°C under the TBAs source with a partial pressure equal to 2.74^{-1} mbar (molar flow = 9.13^{-5} mol/min). Selected AFM scans of the surfaces are shown in the Tab. 6.13. On selected samples we carried out XPS measurements which confirmed the presence of As on the Si(111) surface. On all the samples, the AFM scans show steps equal to the height of bi-atomic layer.

Samples (a) and (b), wet chemically etched and not etched respectively, after annealing in TBAs were annealed in H_2 (and unavoidable background As_4) at 850°C . On the not etched sample a strong pattern of triangles (Tab. 6.13 (b)) is visible. These triangular holes extend up to 11 bi-atomic layers. This triangular shape defect results from the fact that each Si atom on the inner step edges in the triangle has only one dangling bond. This configuration is energetically favored and consequently all three inner edges are stable. If on the Si surface (terrace) a defect site is present, which means that a Si atom with one dangling bond is removed and exposes a Si atom with two dangling bonds (either horizontal or vertical, see Fig. 2.12, subchapter 2.4.3) a chain reaction of removal of all

Si atoms with two dangling bonds starts. Si atoms with two dangling bonds are unstable, and form an energetically unfavorable configuration [92]. This removal process continues until only Si atoms with one dangling bond remain. The remaining monohydride edges are stable and form a triangle-like shape. The steps edges on both samples (a) and (b) are not straight, but modified and ragged. Arsenic might substitute the Si atoms on the step edges but also As (or its hydrides) might “attack” the Si on the step edges and remove the Si atom, which could lead to a chain reaction of removal of the neighbor Si atoms, which leads to a rough shape of step edges.

parameters	etched	not etched
420 °C, TBAs open 670 °C 10 min, TBAs close 850 °C 8 min 420 °C	RMS 0.70 nm 	RMS 0.97 nm 
420 °C, TBAs open, 670 °C, 10 min 420 °C, TBAS close	RMS 0.71 nm 	RMS 0.97 nm 
670 °C, TBAs open, 670 °C 10 min, 420 °C, TBAs close, 420 °C, 10 min	RMS 0.26 nm 	

Tab. 6.13: AFM scans of Si(111) samples after different arsenic treatment.

Tab. 6.13 (c) and (d) shows AFM scans of samples with the same sample preparation as (a) and (b) but without additional annealing in H₂. On both samples, steps with a height of bi-atomic layer are visible. In addition, on the not etched sample triangular etched shapes are visible reaching up to 6 bi-atomic layers. The surface roughness and the morphology of the samples (c) and (d) is very comparable to (a) and (b) samples, however, the steps edges seem to be less ragged than in the case of samples (a) and (b).

Therefore, we conclude that background As is highly interacting with the Si(111) surface at high temperatures (here 850 °C). Samples annealed under higher As partial pressure (1.37 mbar which is equal to $4.57 \cdot 10^{-4}$ mol / min), or at lower temperature of 420 °C, or at 670 °C but for a longer period of time (not shown here) also revealed similar surface morphology, on which the steps exposed a zig-zag like shape. On all surfaces, step-bunching up to 6 bi-atomic layers was observed. Furthermore, clear steps of the height of bi-atomic layer were visible.

Based on the results we can conclude that independently from the process parameters the surface morphologies of Si(111) are very similar. Also, we did not observe any changes in the Si(111):As surface morphology when we omitted homoepitaxial buffer layer growth (not shown here). However, surface morphology of the sample shown in Tab. 6.13 (e) is significantly different from the other samples. This sample was processed in a “clean” susceptor (we exclude As in the reactor or on the susceptor). As was the case with the other sample, the sample was deoxidized and subsequently annealed in TBAs at 670 °C (here the homoepitaxial buffer layer growth was omitted). Surprisingly, the terraces are atomically flat and ordered, the step edges are smooth without a zig-zag structure. The surface RMS roughness is equal to 0.3 nm, which is comparable to the Si(111) 0° samples processed in As free ambient. Based on this result, we conclude that the critical point at which the Si(111) surface is interacting mostly with As (etched by As) is not during the annealing under TBAs source, but during the deoxidation step e.g. annealing at 1000 °C. From the AFM scans above we can conclude that the homoepitaxial buffer does not improve the surface morphology, nor does the time of annealing in TBAs. The surface is already affected at high temperature after deoxidation process by the background As_x.

6.2.2 Step structure of Si(111) with an offcut in $[11\bar{2}]$ and $[\bar{1}\bar{1}2]$ direction

First we will look at the RA spectra from the Si(111) $[11\bar{2}]$ surfaces after deoxidation in arsenic ambient and subsequent termination by As. We chose Si(111) with a 6° degree offcut due to the fact that a stronger RAS signal can be obtained from this surface. Figure 6.14 exhibits RA spectra of Si(111):As with a 6° offcut in $[11\bar{2}]$ direction after deoxidation (30 min, 950 mbar, 1000 °C, orange line) and additional annealing under TBAs for 3 min at 670 °C (red line). As a reference, the black RA spectrum corresponds to Si(111) substrate with the same offcut, but deoxidized in As-free MOCVD reactor, which results in hydrogen terminated surface. The RA spectra from deoxidized Si(111) surface in As ambient (orange line) exhibit two characteristic peaks at E_1 and E_2 transition band energy as in a case of hydrogen terminated surface (black line). The RA spectrum of the sample, which was annealed 3 min at 670 °C in TBAs (the red line) is

similar to the RA spectrum of the reference sample (deoxidized in As-free reactor), but is distorted. The two maxima are shifted by around 0.05 eV towards higher energy and two shoulders (one between 3.5 eV and 4.0 eV, and the second between 4.0 eV and 4.3 eV) are significantly shifted towards higher energy by around 0.3 eV. In addition, the amplitude of the peak around 3.5 eV is significantly higher, when compared to reference RA spectrum. Nevertheless, two peaks are visible around 3.4 eV and 4.3 eV, which could indicate that the RAS signal originate from the steps in $[110]$ direction (see Fig. 6.4). The changes between the RA spectrum from the As-terminated surface (red line) and the surface after deoxidation (orange line) might indicate changes in the step arrangement.

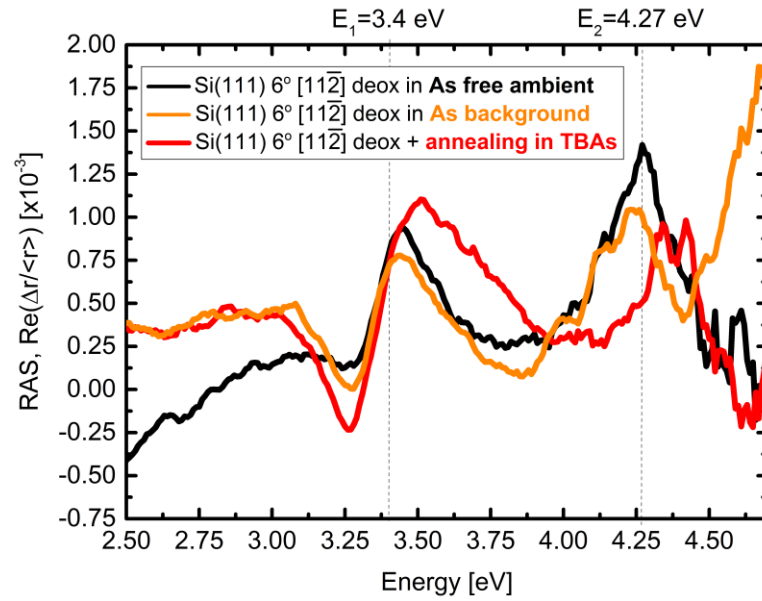


Fig. 6.14: RAS of Si(111):As surfaces with 6° offcut in $[11\bar{2}]$ direction (measured at 50°C). For comparison a RAS from oxidized Si(111):H 6° surface is shown. The RA spectra exhibit two characteristic peaks at E_1 and E_2 transition band energy.

Now we will compare the RA spectra from Si(111) 6° $[\bar{1}\bar{1}2]$ surface after deoxidation in arsenic ambient and termination by As. Figure 6.15 exhibits measured RAS of the Si(111) 6° $[\bar{1}\bar{1}2]$ surface after deoxidation (orange line) and after As termination (red line). For a comparison, the RA spectrum from Si(111):H is shown (black line). In contrast to Si(111) with offcut in $[11\bar{2}]$ direction, here the spectrum already differs after deoxidation when compared to H-terminated surface. The RA spectrum from deoxidized surface in As ambient (orange line) shows a clear visible minimum at 3.3 eV and a small minimum at energy around 4.25 eV. Since RAS signal can contain contribution from the hydrogen bounded at the step edges (see Fig. 6.8.), change in RAS features between sample deoxidized in As ambient and As-free ambient, could indicate that the As atoms substitute Si atoms at the step edges, to which no hydrogen is bounded. After arsenic termination (red line), the amplitude of the minimum at energy 3.3 eV is higher and in addition a second minimum at 4.25 eV is observed. The change in the RA spectrum indicates changes in the surface morphology after deoxidation and As termination.

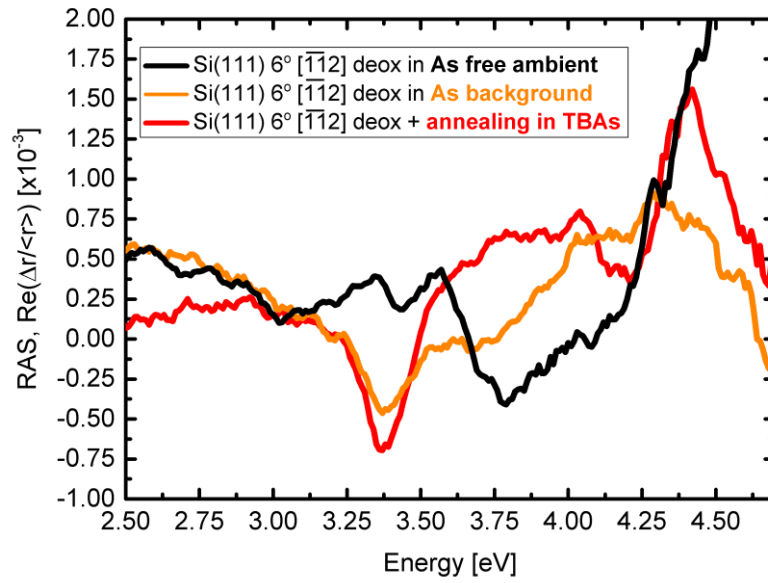


Fig. 6.15: RAS (measured at 50 °C) Si(111):As surfaces with 6° offcut in $[\bar{1}\bar{1}2]$ direction. For comparison we show a RAS from oxidized Si(111):H 6° surface.

The surface morphology after As termination was investigated by AFM. Figure 6.16 shows AFM scans of Si(111):As and Si(111):H surfaces with 3° offcut in $[\bar{1}\bar{1}2]$ (top row) and $[11\bar{2}]$ (bottom row) direction after deoxidation in “clean” ambient (left), deoxidation in As ambient (middle) and after As termination (right).

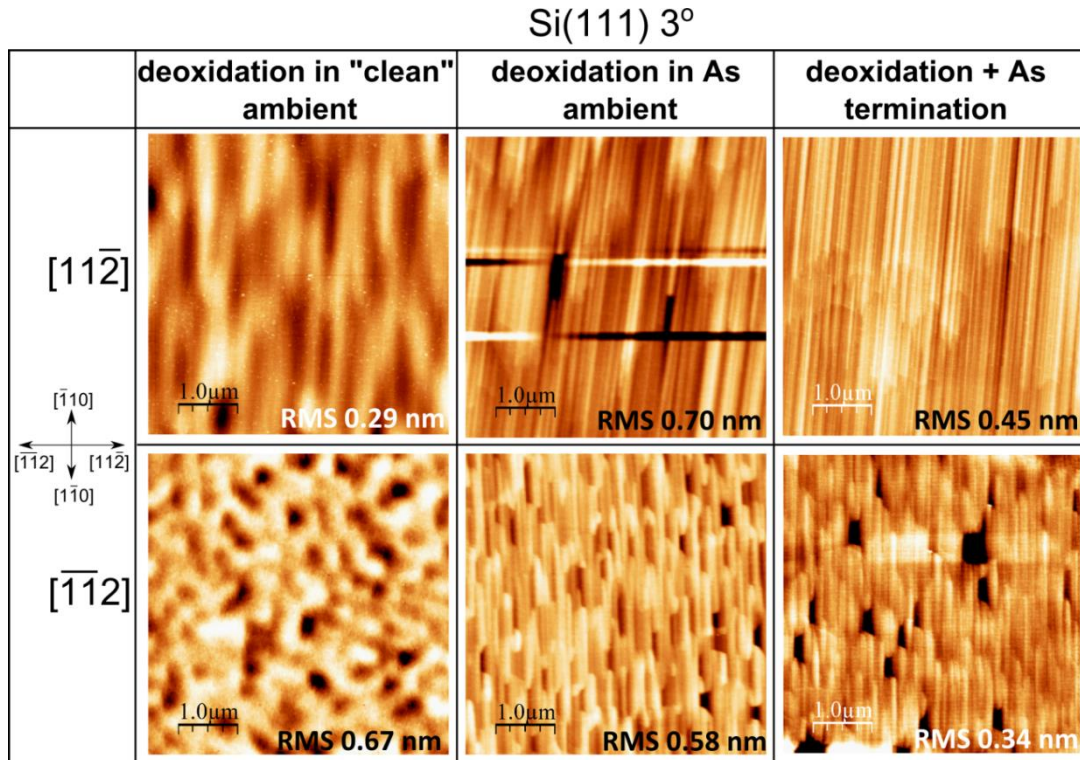


Fig. 6.16: AFM scans of Si(111):As Si(111):H surfaces with 3° offcut in $[\bar{1}\bar{1}2]$ and $[11\bar{2}]$ direction.

AFM scans show a strong difference in surface morphology between the samples deoxidized in H_2 and As ambient. During the deoxidation in As ambient, the background As interacts with the Si(111) surface, which leads to a change in the surface morphology and step roughening. The surface morphology depends on the direction of the substrate offcut. AFM scans of Si(111):As 3° $[\bar{1}\bar{1}2]$ show large terraces towards $[1\bar{1}0]$ direction and small terraces towards the offcut direction. Additional steps are compensating a $\sim 7^\circ$ offset of the precision of the offcut direction (see Fig. 6.16, top, right hand side). In case of Si(111):As 3° $[11\bar{2}]$ we observe step bunching towards the offcut direction and long terraces towards $[1\bar{1}0]$ direction. However, to understand the As interaction with Si(111) surfaces and to investigate the surface and step edges structure in atomic scale after As termination, additional STM measurements have to be carried out.

6.2.3 As termination

To investigate if the As termination of the Si surface was complete, we performed FTIR measurements in ATR configuration. The Si(111) was deoxidized and subsequently the As termination of the Si(111) surface was achieved by annealing the substrates for 10 min at 670°C under TBAs source flow. Afterwards, the samples were cooled down to 420°C and annealed for 10 min without TBAs stabilization in order to remove excess TBAs fragments from the surface. Figure 6.17 (a) shows FTIR spectra of Si after deoxidation in As-free reactor (blue spectrum line) and after As termination (red spectrum line). After Si deoxidation in As free ambient, a strong absorption band at 2083.5 cm^{-1} is visible (see also subchapter 6.1.2), which corresponds to the stretch mode of Si-H present on the Si surface. As previously described the Si-H bonds are perpendicular to the surface and H is bonded as monohydride to the uppermost layer of Si atoms on the substrate terraces. Additionally, a shoulder at 2089.4 cm^{-1} is visible, which is probably due to Si-H bonds at step edges. In case of the spectrum of Si(111):As (Fig. 6.17 (a) red line) no absorption at frequencies corresponding to Si-H was detected, which indicates that the Si surface is completely covered by As. The incorporation of additional As atoms at the terrace edge, which replaces the exposed Si atoms in the second layer yields the lowest energy configuration for Si(111) with offcut in $[\bar{1}\bar{1}2]$ or $[11\bar{2}]$ direction [118]. Therefore, we conclude that As atoms are replacing the Si atoms at the step edges. The LEED measurements confirmed a (1×1) surface reconstruction (Fig. 6.17 (b)) [114]. To investigate how stable are the As-Si bonds we performed an additional experiment. After measuring FTIR and LEED the sample was transported back to the MOCVD reactor and annealed at 670°C for 10 min in the process gas ambient. Afterwards the sample was transferred in UHV back to the FTIR. The orange spectrum in Fig. 6.17 (a) exhibits a small peak at frequency 2090.0 cm^{-1} , which probably corresponds to the hydride on the steps. No signal from bonds between the Si and monohydride is visible, which indicates that the temperature of 670°C is too low to break the Si-As bonds on the surface. As a matter of comparison, to remove arsenic from Si(111) surface in UHV temperatures above 700°C are required [114]. The peak at

2090.0 cm^{-1} is stronger for the sample terminated with As, and shifted by 0.6 cm^{-1} towards higher energy, when compared with the Si surface terminated with H_2 , which can be caused by the fact that the intensity of the FTIR signal is not normalized, by step bunching or by changes in the step structure. The peak is visible only in the p-polarized measurement, which means that the hydrides on the steps must be in-plane. This surface also exhibits (1×1) surface reconstruction, which was confirmed by LEED measurement.

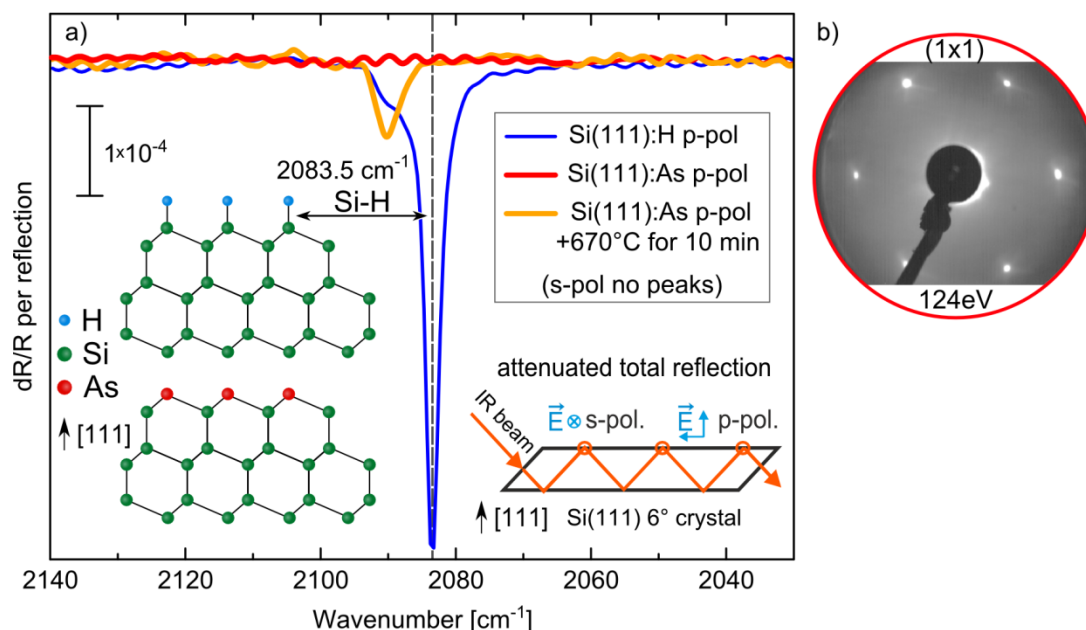


Fig. 6.17: (a) FTIR spectra of: Si(111):H (blue line), complete As-termination of Si(111) (red line) and incomplete As-termination of (111) (orange line). The strong absorption band at 2083.5 cm^{-1} corresponds to monohydride on the Si(111) terraces. All surfaces exhibit (1×1) surface reconstruction. (b) LEED pattern of Si(111):As.

The presence of As on the Si(111) surface was confirmed by XPS measurements. Si(111) 3° p-type $[\bar{1}\bar{1}2]$ and n-type $[11\bar{2}]$ samples were deoxidized and subsequently terminated with As by annealing at 670°C for 3 min ⁸ in TBAs. Figure 6.18 exhibits XPS measurements (taken at $E_{\text{pass}} = 20\text{ eV}$) of Si 2p and As 3d photoemission (PE) lines of those two surfaces. The blue line corresponds to the XPS measurement and black line corresponds to the fitting. The measurements were taken at angles of 90° and 30° against the normal emission (see subchapter 3.4). The black line in the Si 2p (As 3d) PE lines is the result of a fit to the data of two spin-orbit pairs of equal width, with spin-orbit splitting equal to 0.60 eV (0.69 eV) and the statistical intensity ratio equal to 2:1 (3:2). In the Si 2p peak for both Si(111) surfaces an additional component is fitted which stems from Si-As bonds (orange dash-dot line). The relative contribution in the Si 2p PE line of Si-As component (Fig. 6.18, orange dash-dot line) increases when the photoelectron takeoff angle (with respect to surface plane) is varied from 90° to 30° . This confirms that

⁸ By analysis of the XPS data (not shown here) we found that the Si(111) should be completely terminated by As already after 3 min of annealing in TBAs at 670°C .

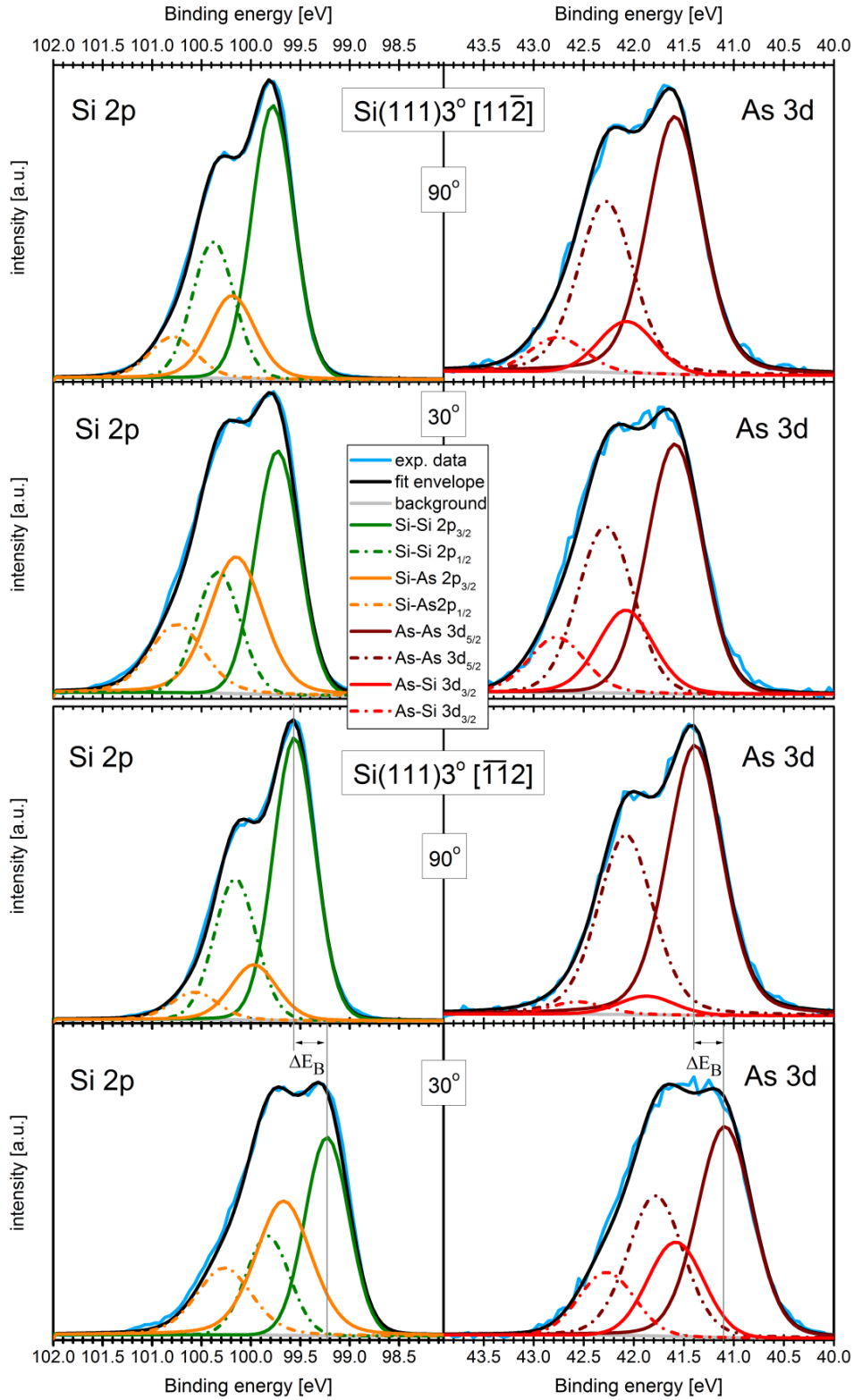


Fig. 6.18: XPS data (blue lines) of Si 2p and As 3d PE lines of Si(111) 3°:As with an offset in $\bar{1}\bar{1}\bar{2}$ and $[11\bar{2}]$ direction, measured at 90° and at 30° photoelectron takeoff angle. The fit envelope (black line) and its components Si-Si (green line), As-Si (orange line), As-As (red line) are indicated. Monochromated Al K α excitation was used and binding energy is given with respect to the Fermi level ($E_{\text{pass}} = 20$ eV).

this component (orange dash-dot line) is near the surface, while the other component (green line) arises from the bulk Si atoms. A chemical shift of the Si-As component towards higher binding energy (E_B) by $0.41 \text{ eV} \pm 0.2 \text{ eV}$ confirms the Si-As bonds [114]. We did not detect any contaminant, such as O, C, or Ga, which implies that the chemically shifted component is due to the Si bonding to As. In analogy, in the As 3d peak for both Si(111) 3° surfaces an additional component is fitted which, also stems from Si-As bonds (orange dashed-dot line) and its contribution is increased with the surface sensitive measurement. The Si-As component in the As 3d peak is shifted by $0.41 \text{ eV} \pm 0.2 \text{ eV}$ to higher E_B from the Si-Si component, confirming the Si-As bonds. The Si 2p and As 3d PE lines of Si(111) 3° $[11\bar{2}]$ surface (measured at 90°) are shifted towards higher E_B of around $0.22 \pm 0.2 \text{ eV}$ in comparison to the PE line of Si(111) 3° $[\bar{1}\bar{1}2]$. This shift is caused by a shift in the Fermi level arising from different types of doping in the Si(111) substrate (see Fig. 3.7). Moreover, in case of the Si(111) 3° $[\bar{1}\bar{1}2]$ XPS data show a significant shift in position of all components at the surface sensitive measurement to a lower E_B ($0.32 \text{ eV} \pm 0.2 \text{ eV}$ and $0.30 \text{ eV} \pm 0.2 \text{ eV}$ for the Si 2p and As 3d peaks, respectively). The shift E_B to lower energy indicates band bending upward near the surface. This change might be caused by electrical potential difference at the interface induced by arsenic. In case of n-type Si(111) 3° $[11\bar{2}]$ there is no visible shift in the E_B at surface sensitive measurement (or is within the XPS limit), indicating a flat band.

A quantitative comparison of the As to the Si amount on both surfaces was done by comparison of intensity ratios of Si 2p to As 3d peak or of Si-Si to As-As component in the Si 2p PE line. Measurement at the 90° takeoff angle reveals a higher As amount on the Si(111) 3° $[11\bar{2}]$ sample. However, measurement at the 30° takeoff angle reveals a higher As amount on the Si(111) 3° $[\bar{1}\bar{1}2]$ sample. While measurement at the 90° takeoff angle indicates the As amount in the volume, the surface sensitive measurement indicates the As amount close to the surface. Excluding difference in in-diffusion of As into Si(111) between the two surfaces, from the XPS measurement it is clear that there is more As on the Si(111) 3° $[\bar{1}\bar{1}2]$ surface. Difference in the As coverage between the two surfaces might have an origin in a difference in the steps structure. If we would assume a transformation from straight steps into a zig-zag-like steps on the Si(111) $[\bar{1}\bar{1}2]$ surface [90,118,173,196], and straight steps on the Si(111) $[11\bar{2}]$ surface, the Si(111) $[\bar{1}\bar{1}2]$ surface should result in higher As coverage.

6.3 Summary of this chapter

XPS analysis showed that high-temperature annealing at 1000°C for 30 min at a H_2 pressure of 950 mbar reliably removes oxides and carbon from the Si(111) surface. FTIR measurements confirm that the interaction between hydrogen and the Si(111) surface leads to hydride termination. In particular, we found monohydride bonds on the terraces,

which agree with the well-ordered (1×1) surface reconstruction observed by LEED and STM. Wet chemical pretreatment of the Si substrates strongly affects the surface morphology of the surface as well as of the subsequent homoepitaxy.

While there is no RAS signal from the Si(111) 0° surface, which results from the isotropic surface, we did observe RA spectra from Si(111) surfaces with an offcut. The RA spectra in the case of Si(111) with offcut in $[11\bar{2}]$ direction arise from (110)-planes at the steps. In the case of Si(111) with offcut in $[\bar{1}\bar{1}2]$ the exact origin of the RAS is unclear and additional STM measurements resolved in an atomic resolution would be necessary to benchmark the RAS signal to the step structure.

Annealing in arsenic ambient leads to As-terminated Si(111) surface, which was confirmed by XPS and FTIR measurements. The LEED pattern from the Si(111):As surface confirms a (1×1) surface reconstruction. Significant change in the RAS signal of Si(111) with offcut in $[\bar{1}\bar{1}2]$ direction after As termination indicates a change in the step structure on the surface. The lack of this change in the RAS signal for the opposite direction indicates that this surface is stable against As etching.

7 GaP/Si(111)

This chapter focuses on GaP growth on Si(111). First, we show a non-destructive method to determine the GaP(111) polarity. Before heteroepitaxial growth, GaP(111) homoepitaxy is investigated. Secondly, we show how to control GaP polarity on Si(111), which is necessary to obtain vertical growth of NWs on GaP/Si(111). Finally, we underscore the influence of the Si(111):As surface structure on the GaP nucleation. Parts of the experiments were done in cooperation with Matthias Steidl and Dr. Weihong Zhao. All SEM scans and nanowire growth experiments presented in this chapter were done by Matthias Steidl. Part of this work is published in *Applied Physics Letters*, *Ref.* [197].

7.1 GaP(111) polarity

To benchmark the heteroepitaxial GaP layers to the known polarity of GaP(111) substrates, we carried out LEED measurements and NW growth experiments on GaP(111)A and GaP(111)B substrates. GaAs NWs were grown on GaP(111) substrates by the VLS method (see sub-section 5.4). Both substrates were measured by scanning electron microscope (SEM). Figure 7.1 shows the SEM scans of GaAs NWS on (a) GaP(111)A- and (b) GaP(111)B-type.

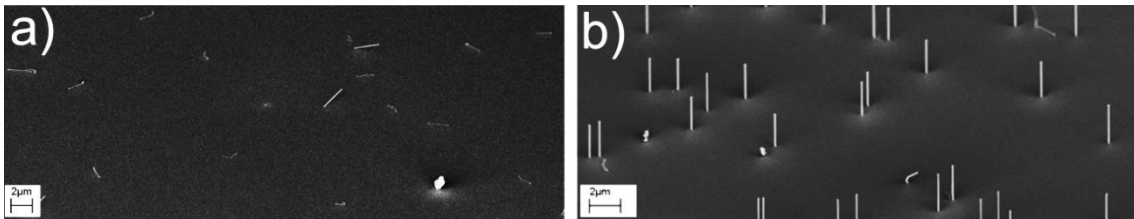


Fig. 7.1: The SEM scans of GaAs NWs on (a) GaP(111)A and (b) GaP(111)B. The NW growth on sample (a) is suppressed, while on the sample (b) most of the NWs are vertical to the substrate.

Only on the GaP(111)B substrate we obtained straight, vertical NW growth with a yield of around 90 %. The NWs exhibited an almost circular cross-section with pronounced {110}-facets, which are commonly observed for nanowires grown on (111)B surfaces with hexagonal shape (not shown here) [198,199]. On GaP(111)A substrates most of the NWs grew along the surface and were kinked. For comparison, we also carried out NW growth experiments on GaAs(111)B, and in this case, we also obtained straight, vertical NW growth with a yield of 95 %. This behavior is attributed to differences in the

surface free energy depending on surface orientation: i.e. growth on GaP(111)B succeeds, while the higher energy associated with the [111] direction prevents NW growth on GaP(111)A [19,200,201]. Hence, in our case it is crucial for subsequent NW growth to obtain heteroepitaxially grown GaP buffers with B polarity.

Deoxidized (see subchapter 5.2 for details) GaP(111) wafers with A- and B- type polarity were measured by AFM. Figure 7.2 (a) and (b) exhibits AFM scans of surfaces of GaP(111) with A- and B-type polarity, respectively. There is no visible difference in the surface morphology between both surfaces. The RMS roughness on both GaP(111) surfaces is around 0.15 nm. Another method to distinguish between the GaP(111) Ga-rich and P-rich face is the application of wet chemical etching on the wafers [100]. GaP(111) wafers with A- and B-type polarity were dipped in $\text{HCl}:\text{HN}_2\text{O}_3:\text{H}_2\text{O}$ (3:1:4) solution for two minutes. Figure 7.2 exhibits AFM scans of GaP(111) with A-polarity (c) and B-polarity (d) after the etching procedure. The surface morphology of two wafers is significantly different and the surface roughness is: 0.15 nm and 4.5 nm for GaP(111) with A- and B-type polarity respectively. GaP(111) A- and B- type surfaces, differ in the number of free bonds per surface atom. In GaP(111)A, the group-III atoms on the surface have no free bonds because all of them are used to bond to the crystal lattice. In GaP(111)B, on the other hand, the group-V surface atoms have two free bonds per atom as only three of them are used to bond to the crystal lattice.

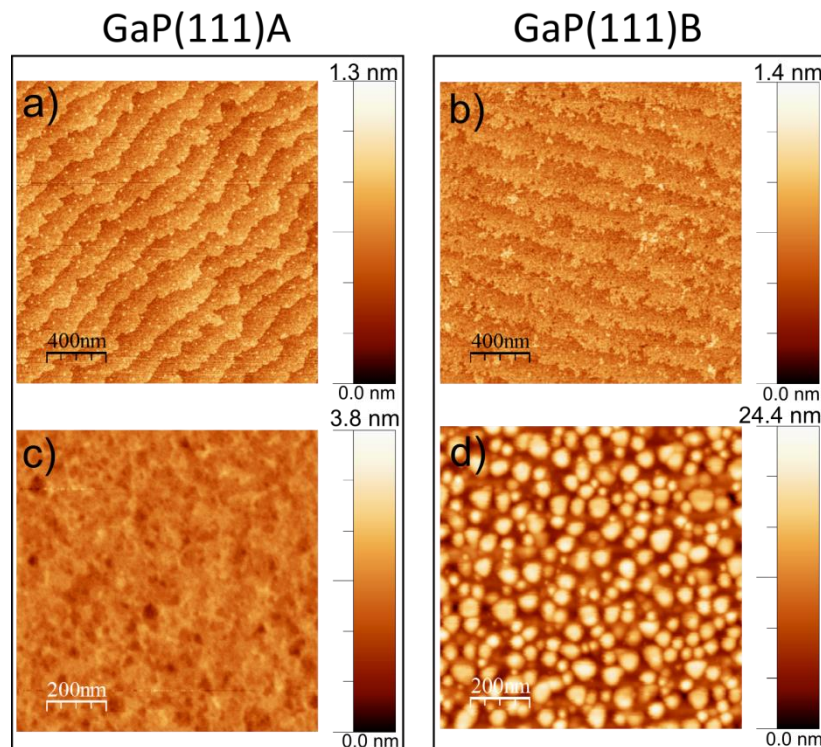


Fig. 7.2: AFM scans of GaP(111) morphology after (a) and (b) deoxidation in hydrogen ambient and (c) and (d) wet-chemical etching.

Therefore, the two surfaces possess different physical and chemical properties. The difference in morphology after wet chemical etching can be explained by the different

chemical reactivity of the group-III and the group-V atoms with the etching solution. On B-type polarity surface atoms are more reactive than on A-type, when electrophilic agents are involved. Therefore, atomic hydrogen reacts with the B-face atoms.

Another, non-destructive approach to distinguish between the two polarities is to apply LEED. LEED measurements will give direct information about the surface reconstruction of GaP(111)A- and B-type surfaces after preparing the surface in the H₂ ambient. Correlation of polarity with the surface reconstruction can serve as a benchmark of the heteroepitaxial GaP on Si(111).

We applied LEED to the GaP(111)A and GaP(111)B surfaces after deoxidation or with additional, homoepitaxially grown GaP buffer. Figure 7.3 (e) and (f) show the LEED diffraction patterns of GaP(111) A- and B-type wafers prepared in MOCVD by deoxidation only (see experimental). Substrates with A-type and B-type polarity exhibit different diffraction patterns, both with a threefold symmetry. The LEED pattern of GaP(111)A (Fig. 7.3 (e)) exhibits half-order spots (marked with a black circle) indicating a (2×2) surface reconstruction. For GaP(111)B we observed only first order spots in the corresponding LEED pattern (Fig. 7.3 (f)).

Comparing these results with the UHV-prepared GaP(111) surfaces from literature, we find agreement in the LEED pattern for the A-type material: GaP(111)A prepared in UHV also exhibits a (2×2) surface reconstruction when analyzed by LEED [105]. Xu *et al.* [107] compared this surface reconstruction to the well understood (2×2) surface reconstruction of GaAs(111)A [202]. For this surface reconstruction a model was proposed and confirmed by analysis of LEED intensity-energy curves [203] and by total-energy calculations, where one quarter of the group-III constituent at the surface is removed (see top view of the surface reconstruction in Fig. 7.3 (c)) [204]. The group-III atoms that remain on the surface rehybridize from sp³ to sp² orbitals. The group-V atoms in the layer below are pushed sideways and outwards, producing σ -type and Π -type bonds. The (2×2) symmetry of our GaP(111)A LEED pattern may correspond to the same surface reconstruction, although in our case, the remaining group-III atoms at the surface may not rehybridize, but instead may be saturated by hydrogen due to the presence of the hydrogen environment. In the case of the GaP(111)B surface, various studies have reported a (1×1) LEED pattern [102–104]. However, van Bommel *et al.* [105] observed a more complicated LEED pattern, which was confirmed by Hattori *et al.* [106], and further analyzed by STM. Hattori *et al.* [106] showed that the surface consists of six equivalent reconstruction domains containing two reconstruction units. Their modeling of the LEED pattern based on this proposed reconstruction provided good agreement with the experimental LEED data.

In our case, the LEED pattern of GaP(111)B shows first order diffraction spots only. However, this does not allow to draw unambiguous conclusions regarding the surface structure. The diffraction pattern could be due to a (1×1) surface reconstruction (Fig. 7.3 (d)), or instead due to insufficient quality of the surface preparation or a surface which

lacks short range order. However, the LEED pattern we obtained is clearly distinct from the one obtained in the case of the GaP(111)A surface. This allows to use the LEED results of the GaP(111) surfaces as a reference in order to distinguish the polarity of the heteroepitaxially grown GaP on Si(111). We correlate the (2×2) surface reconstruction with A-type polarity and the (1×1) surface with B-type material.

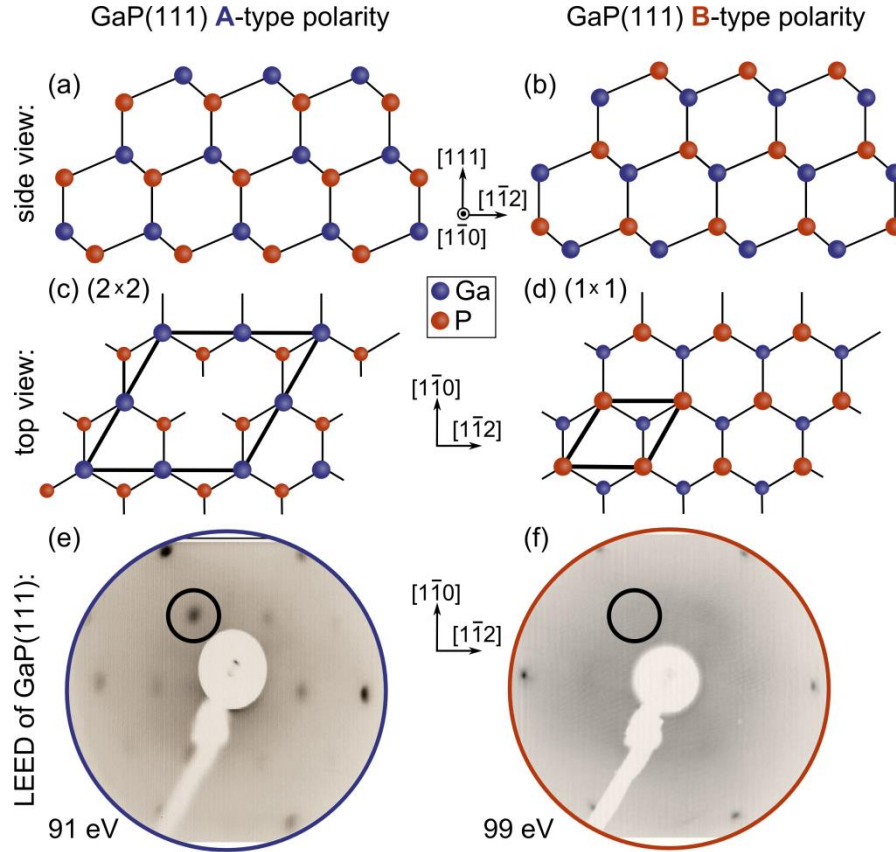


Fig. 7.3: Crystal lattice of GaP(111)A- and B-type polarity. (a) and (b) – side view, (c) and (d) top view. (e) and (f) corresponding LEED patterns of GaP(111) after deoxidation in hydrogen ambient.

7.2 GaP(111) homoepitaxy

To understand the heteroepitaxial GaP growth on Si(111) it is important to first investigate and characterize the homoepitaxy on GaP(111) in dependence on different process parameters. Since very little is known about the GaP(111) homoepitaxy, the study was done in an extensive range of parameters, precisely: growth temperature, reactor pressure, growth rate and V/III ratio. Since our interest is in a quasi-substrate suitable for vertical NWs growth, this research focused on homoepitaxy on GaP(111)B substrates and only a few results on GaP(111)A substrate as a reference are described.

To study the influence of V/III ratio and temperature on the growth of the GaP homoepitaxial buffer layer, two series of experiments were prepared. In the first series of experiments, we varied the V/III ratio from 13 to 1200 in 6 steps at a constant temperature of 620 °C. In order to increase the V/III ratio, we increased the P flow and decreased the Ga flow, the latter of which defines the GaP growth rate. In the second series of experiments, samples were prepared at constant V/III ratio of 13 and at different temperatures, ranging from 620 °C to 750 °C.

Figure 7.4 shows the surface morphology of 8 selected samples in dependence on V/III ratio (samples: (a), (b), (c) and (d)) and the growth temperature (samples: (e), (f), (g) and (h)). A clear change in surface RMS roughness is visible for all of the samples. In the case of the samples (a), (b) and (c), increased V/III ratio leads to decreased surface roughness. A low V/III ratio could result in the formation of lattice defects such as phosphorous vacancies. The surface morphology of sample (a) is very rough and a 3D structure is observed. Samples (b) and (c) have a very similar surface morphology and size of the grains on the surface are comparable. Further increase of V/III ratio does not decrease the surface roughness (sample (d)). Hence, the surface morphology of GaP strongly depends on the chosen V/III ratio and the growth rate.

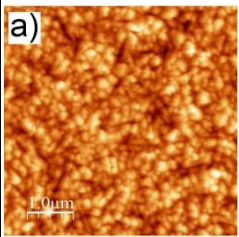
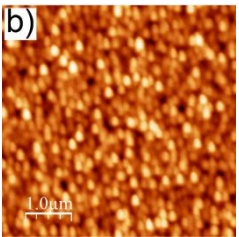
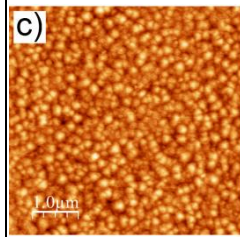
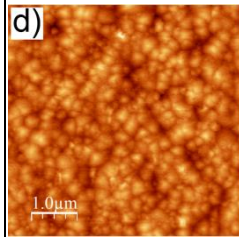
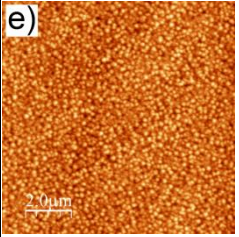
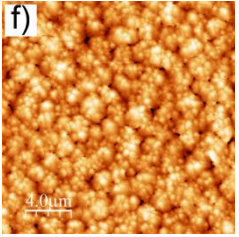
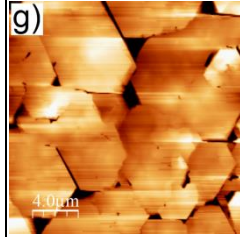
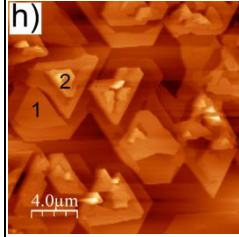
GaP(111)B homoepitaxy				
V/III	13	152	607	1200
Surface morphology				
RMS	7.58 nm	0.88 nm	0.26 nm	0.46 nm
Temp.	620 °C	700 °C	720 °C	750 °C
Surface morphology				
RMS	0.26 nm	0.65 nm	5.80 nm	10.10 nm

Fig. 7.4: AFM scans of GaP(111)B morphology after homoepitaxy in dependence on process parameters.

The second series of experiments shows a strong impact of the growth temperature on the surface structure (samples: (e), (f), (g) and (h)). We observed that with increasing temperature, the surface roughness also increases. At the higher temperature (samples (g)

and (h)) we observe 3D grains. On sample (h), the difference between the grains is up to 20 nm and the surface roughness on each “island” is up to 10 nm. Furthermore, this sample (h) the height of the islands is reaching up to 60 nm, there is a larger distance between them and rotational twins are clearly visible (marked with number 1 and 2).

Growth conditions with a high V/III ratio above 150 and medium growth temperatures between 600 °C and 700 °C provided the best results and were chosen for subsequent GaP-on-Si(111) growth.

To compare GaP(111)B homoepitaxy with the one on the A-type polarity wafer we carried-out an additional experiment of homoepitaxial growth. The buffer was grown at 620°C with a V/III ratio of 300. Figure 7.5 shows AFM scans of homoepitaxially grown GaP on GaP(111)A (a) and GaP(111)B (b) substrates. The morphology of GaP(111) with A-type polarity differs significantly from the morphology of GaP(111)B. The surface roughness of GaP(111)A is 7 times higher than that of GaP(111)B. GaP(111)B substrate possesses lower surface energy and should be more stable than GaP(111)A due to the lower number of dangling bonds. Therefore, we expect a lower growth rate on the GaP(111)B. As we see from Fig. 7.5, the same growth parameters for GaP(111)A- and B-type homoepitaxial growth result in a different surface morphology. Therefore, to obtain a flat surface morphology of GaP(111)A, the growth parameters would have to be studied separately.

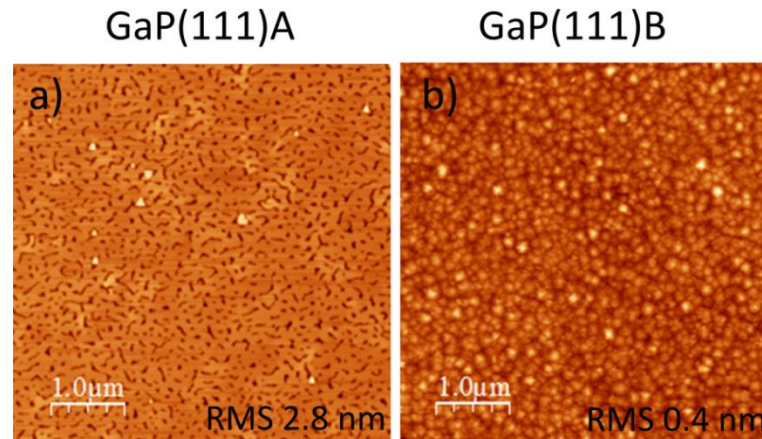


Fig. 7.5: AFM scans of GaP(111)B morphology after homoepitaxy in dependence on substrate orientation.

7.3 Control of GaP(111) polarity on Si(111)

Control over the polarity of epitaxial III-V buffer layers on Si(111) has been mainly studied for GaAs [115]. Patel *et al.* established that the termination of the Si(111) surface determines the crystal polarity of subsequently grown GaAs: GaAs layer growth on

Si(111) leads to GaAs with A-type polarity (Ga terminated surface), while GaAs grown on Si terminated with As possess inverted polarity, i.e. B-type (As-terminated surface). As replaces the top layer of Si creating one monolayer of As, which enforces subsequent growth proceeding with Ga [115]. No data has been reported to date on the polarity of GaP grown on Si(111).

B-type polarity buffer layers with high crystalline quality and with a flat surface are favorable for vertical NW growth [201]. To establish two-dimensional GaP buffer growth on Si(111), we carried-out two series of experiments investigating homoepitaxy on GaP(111)B substrates (see subchapter 7.2). As previously described, growth conditions with a high V/III ratio (above 150) and medium growth temperatures between 600 °C and 700 °C provided the best results (meaning no 3D growth and a smooth surface) and these were chosen for the subsequent GaP-on-Si(111) growth. Since high temperatures at the beginning of the nucleation are known to lead to island formation [205], we applied a two-step process where, after a low-temperature nucleation step at 420 °C and V/III ratio of 200, we raised the temperature for the subsequent growth to 660 °C and a V/III ratio of 400. Both nucleation and buffer growth were carried out for 30 min, at a pressure of 50 mbar. Applying this process we grew GaP layers on Si(111) substrates with 0° and 3° offcut in $[11\bar{2}]$ direction, which was previously deoxidized by our standard MOCVD process (see 5.2).

Figure 7.6 (a) shows the LEED pattern for GaP grown on Si(111)3°, which exhibits a clear (2×2) symmetry. Based on our benchmarking described above (see subchapter 7.1), we conclude that the GaP layer features A-type polarity. In a simplistic atomic model of the interface without intermixing of Si and III-Vs [206], one may conjecture that under the applied phosphorus-rich conditions, GaP growth starts with phosphorus which, followed by ideal layer-by-layer growth, should lead to a Ga-terminated surface (...Si-Si-P-Ga-P-...-P-Ga) [20]. In order to invert the GaP polarity we tried to start the growth with Ga, which could lead to B-type material if Ga bonds to the Si substrate without replacing the silicon. However, the resulting surface exhibited a (2×2) surface reconstruction, indicating A-type polarity. Longer pre-deposition of Ga on the Si(111) substrate leads to the formation of metallic Ga droplets on the Si surface [174,207]. Hence, we followed a different approach to obtain heteroepitaxial GaP(111)B, and instead applied an As treatment to the Si substrates prior to GaP growth, where As was intended to replace the topmost Si layer [114,208]. In the following, by layer-by-layer growth of GaP, Ga should bond to As, in analogy to the heteroepitaxial growth of GaAs on Si(111) [115]. This should then lead to GaP with B-type polarity (...Si-As-Ga-P-Ga-...-Ga-P). In order to terminate the Si(111) surface with As, the substrate was annealed for 10 min at 670 °C under tertiarybutylarsine (TBAs) source flow. Subsequently, the samples were cooled down to 420 °C and annealed for 10 min without TBAs stabilization in order to remove excess TBAs fragments from the surface. The surface morphology of As-terminated Si(111) surfaces are described in detail in subchapter 6.2. As-termination of the Si(111) surfaces occurs by the replacement of the topmost layer of substrate atoms with As atoms

[114] and the complete coverage by As was proven by FTIR measurements, described in subchapter 6.2.3. The LEED measurements confirmed a (1×1) surface reconstruction, as described in subchapter 6.2.3.

After terminating the Si(111) surface with As, a GaP buffer was grown with the growth parameters based on the GaP homoepitaxy experiments. X-ray diffraction (XRD) measurement⁹ yielded a GaP layer thickness of 80 nm (not shown here).

Figure 7.6 (b) shows the LEED pattern of heteroepitaxial GaP, grown on Si(111)3°, in which prior to GaP growth, the Si surface was terminated by As. The LEED measurement shows clear first order spots only. Since the LEED spots are bright and sharp and the background has low intensity for varied LEED voltages, we rule out atomic surface disorder as the cause of the (1×1) LEED pattern. However, we do not observe spot splitting in step direction indicating that we have a step structure which is not well-ordered. As the sample does not exhibit a (2×2) reconstruction, we conclude that the material grown in this manner differs from the heteroepitaxial GaP grown on Si with H-termination. Since there is no ambiguity regarding composition or crystallinity of the heteroepitaxial layer, the material must be GaP(111)B.

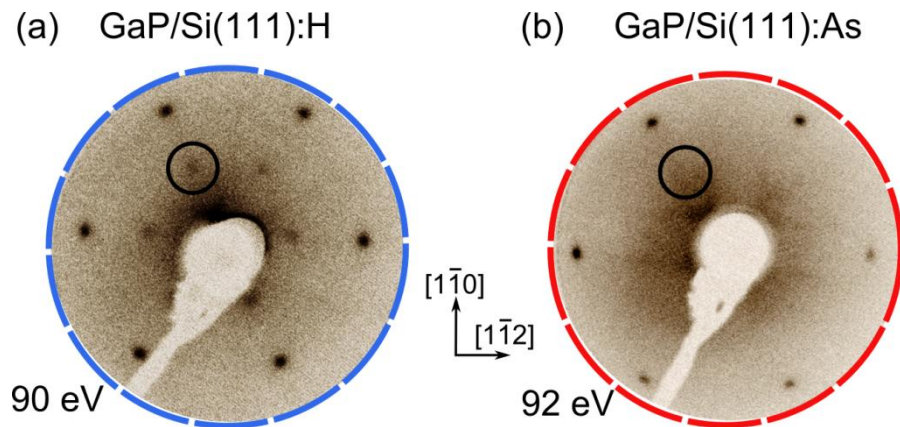


Fig. 7.6: The LEED pattern of GaP grown on Si(111) terminated with H (a) and As (b). Half order spots in the (a) indicate (2×2) surface reconstruction benchmarked previously to GaP(111) with A-type polarity. LEED pattern of GaP grown on As-terminated Si(111) surface exhibits (1×1) surface reconstruction, which corresponds to GaP(111)B-type polarity.

Further evidence that GaP grown on Si(111):As possess B-type polarity arises from growth of NWs on these substrates. Figure 7.7 shows an SEM image of vertical NWs grown on GaP(111)B/Si(111):As 3°. The NWs exhibit pronounced $\{110\}$ -facets, which confirms the B-type polarity of the substrate [199]. The percentage of vertical NWs on GaP/Si(111) quasi-substrates, depending on the substrate offcut, nucleation and growth time and temperature reach up to 80 % and 98 % for GaAs and GaP NWs respectively.

⁹ XRD measurement was done by Dr. Oliver Supplie.

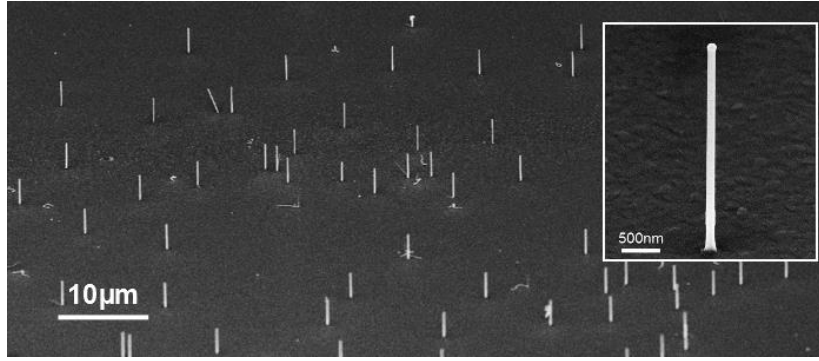


Fig. 7.7: SEM scan of NWs on GaP(111)B/Si(111) quasi-substrate.

Although GaP growth on Si(111):As leads to B-type polarity, one cannot assume an abrupt interface formation followed by ideal layer by layer growth. At the Si(111):As-GaP interface intermixing could occur. Northrup *et al.* [116] reported that for GaAs epitaxy on Si(111) the abrupt interface of ...SiAsGaAs is energetically very unfavorable leading to surface intermixing that results in a ...SiGaAsSiAs structure. This requires more than one monolayer of As, which in our case would have to be present prior to heteroepitaxy (which we cannot rule out, but would contradict *Ref.* [209]) since no additional As is offered during GaP growth. For GaP/Si(111) heterointerfaces grown at P-rich condition, the interface is predicted to be abrupt [206], but no calculations are available for our experimental situation where As is present at the interface.

Presence of rotational domains¹⁰ (the term is explained in the subchapter 2.6.2) in the heteroepitaxially grown GaP(111) film can be confirmed by LEED measurements. By choosing a beam energy that reflects the 3-fold symmetry of the FCC substrate, here GaP(111)B type (Fig. 7.8 (a)) or GaP(111)A-type (not shown here), we do see that after deoxidation the substrate reflects only one domain in the LEED pattern. If in the GaP(111) layer there was a present domain rotated by 120°, the LEED pattern should reflect that. Figure 7.8 (b) exhibits LEED patterns of GaP/Si(111):As measured at the same energies as a reference GaP(111) substrate after deoxidation. In contrast to the reference sample, the LEED pattern does not exhibit 3-fold symmetry (also in the case of GaP/Si(111):H), which indicates a presence of rotated lattice in the film.

¹⁰ The RD in the GaP/Si(111):As layers are studied by HR-XRD in detail by Christian Koppka in *Ref.* [210]. The suppression of the RD is obtained by different growth parameters of GaP nucleation layer in the MOCVD reactor, and by applying Si(111) substrate with different offcuts. Moreover, the amount of RD strongly affects the subsequent nanowire growth, typically leading to kinking and prohibiting vertical growth, which was investigated in detail by Matthias Steidl, and published in *Ref.* [242].

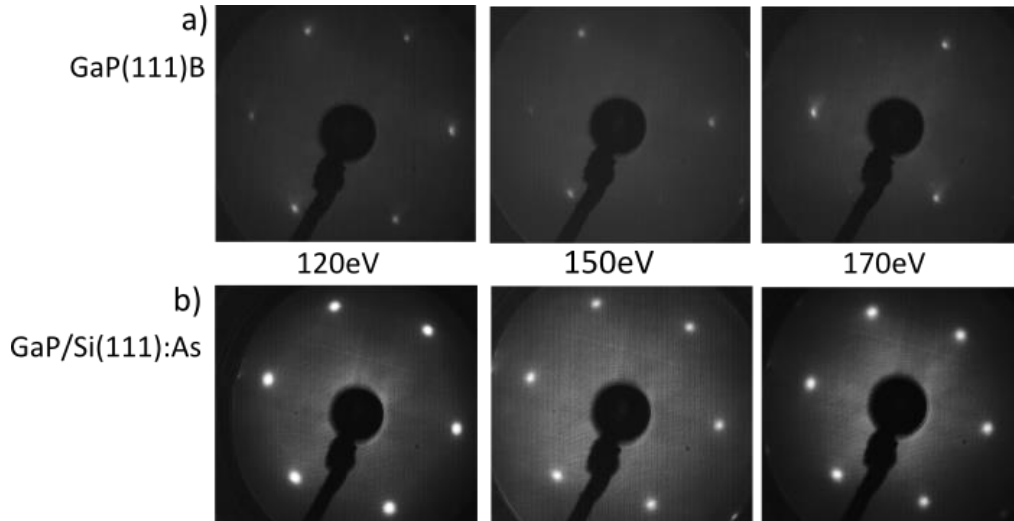


Fig. 7.8: The LEED patterns of (a) GaP(111)B wafer after deoxidation and (b) GaP/Si(111):As. LEED patterns for both surfaces clearly show (1×1) surface reconstruction, but in the case of GaP(111)B, LEED spots show a clearly visible threefold symmetry. In the case of heteroepitaxially grown GaP there is no threefold symmetry, caused by a RD in the epitaxially grown GaP layer.

7.4 Impact of Si(111) substrate offcut on GaP nucleation

In the subchapter 6.1.4 we show that As termination of Si(111) strongly influences the Si surface morphology, precisely the step structure, which differs in dependence on the substrate offcut direction. Therefore, different substrate morphologies of Si(111):As might influence the GaP nucleation. In the following, we give an outline of GaP nucleation layer on Si(111):As.

In one of a series of experiments, the Si(111) 3° substrates with a offcut in $[\bar{1}\bar{1}2]$ and $[11\bar{2}]$ direction were deoxidized and terminated by As. A GaP nucleation layer was grown at 480°C for 10 min with a high V/III ratio of 600. Figure 7.9 shows SEM scans (a) and (b) and AFM scans (c) and (d) of GaP grown on Si(111) with an offcut in $[\bar{1}\bar{1}2]$ and $[11\bar{2}]$ direction. Both SEM and AFM scans exhibit a different GaP(111) structure. While GaP nuclei on Si(111) 3° $[\bar{1}\bar{1}2]$ seem to be ordered in the stripes which follow the steps on the Si surface, on the Si(111) 3° $[11\bar{2}]$ the nuclei seem to be randomly distributed. The pattern of the GaP nuclei distribution on both types of Si substrates does not change in dependence on the growth temperature and V/III ratio (not shown here). Based on the AFM profile the GaP nucleation layer seems to have the same thickness. The RMS roughness is smaller for the GaP/Si(111) 3° $[11\bar{2}]$ surface. The different morphology of GaP nucleation layer is a consequence of the different step structure on

the Si substrates¹¹. In case that the atoms arrive far away from the step edge, they have a high probability to start a new nucleus or to agglomerate at an already existing cluster. In the case that atoms arrive close to the step edge, they are able to diffuse along the step edge until they hit other atoms. The more step edges and the smaller terraces on the Si(111):As surface, the less probability that the nuclei will start at the terrace. A RD is more energetically favorable to nucleate on the terraces, while it is energetically favorable that the nuclei are elongating the step edges e.g. follow the crystal lattice orientation. Therefore the amount of the RD in the GaP layer should decrease with the increasing density of the steps on the surface (details in *Ref.* [210]). Moreover, step edge nucleation enables formation of smaller critical nuclei, which should lead to smoother surfaces.

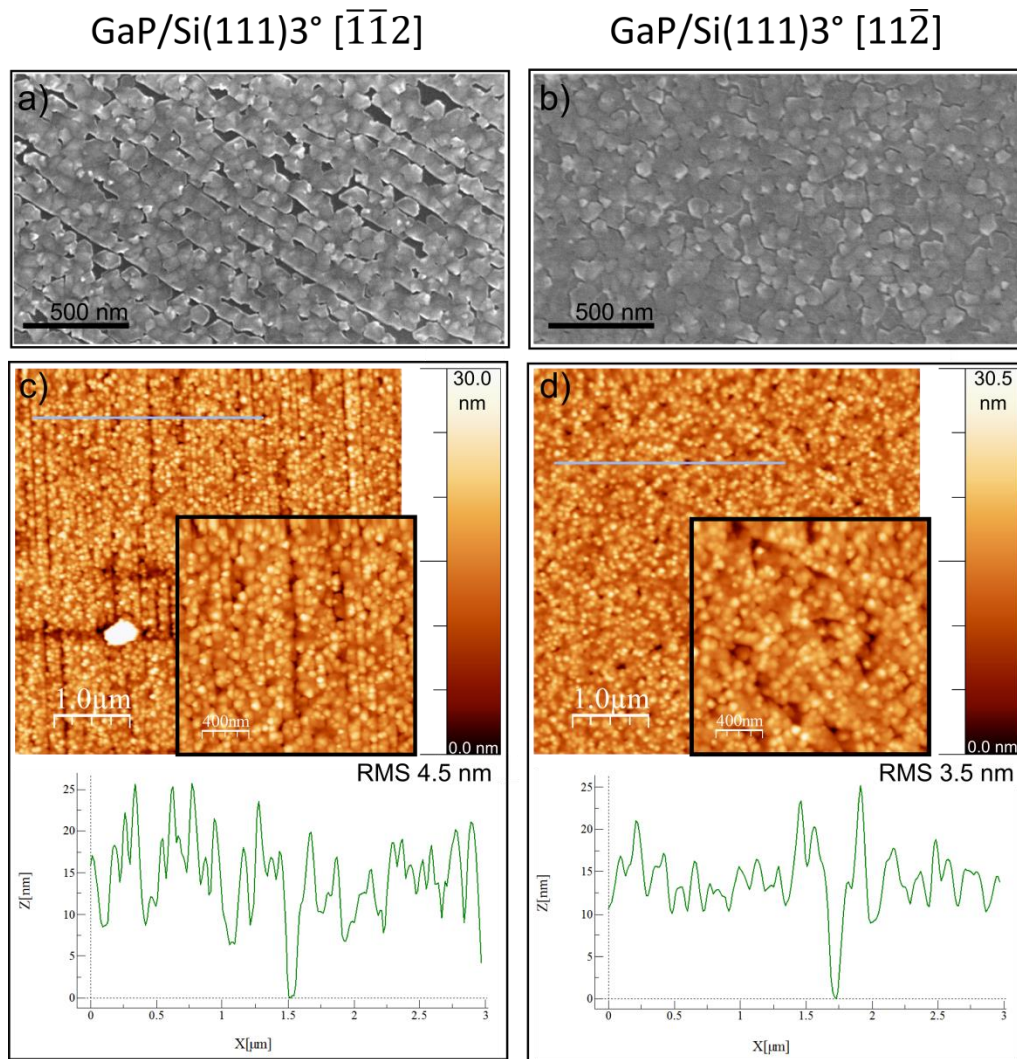


Fig. 7.9: SEM (a) and (b) and AFM (c) and (d) scans of GaP nucleation layer grown on Si(111)3° $[\bar{1}\bar{1}2]$ and Si(111)3° $[11\bar{2}]$, respectively.

¹¹ STM scans of As-terminated Si(111) 3° substrates with an offset in $[\bar{1}\bar{1}2]$ and $[11\bar{2}]$ direction are planned, in order to investigate in detail the step reconstruction and clarify the GaP nuclei distribution.

7.5 Summary of this chapter

We have shown that GaP(111) processed in H_2 ambient exhibits (2×2) and (1×1) surface reconstruction for A-type and B-type polarity, respectively. We used the different surface reconstruction of GaP(111)A- and B-type as a benchmark for GaP growth on Si(111). We have achieved control over the polarity of heteroepitaxially grown GaP layers on Si(111): the H-terminated Si(111) surface leads to GaP with A-type polarity, while GaP grown on the Si(111) surface terminated with As results in B-type polarity, enabling vertical GaAs NW growth on this type quasi-substrates. Theoretical and experimental investigations of the GaP/Si(111):As interface would be desirable in order to clarify the atomic structure of the interface with respect to the possibility of intermixing of the III-V material and the Si substrate. In addition, we showed that the morphology of the GaP nucleation layer strongly depends on the Si(111) offcut direction, precisely the Si(111) step structure after As termination.

8 GaP/Si(100)

This chapter focuses on Si(100) surface preparation after annealing in the presence of a group-V precursor, in particular either TBAs or TBP, for subsequent GaP growth. Exposure of the Si substrate to group-V precursors in order to form a p-n junction by in-diffusion may lead to surface disorder and roughening. However, to avoid defects in the GaP buffer, a single domain Si surface with double layer steps has to be prepared.

Arsenic is not only interesting as a dopant in the active silicon sub-cell but enables wider choice of III-V materials which are relevant for devices designed for PV and water splitting applications. By varying the lattice-matched stoichiometry of $\text{GaN}_x\text{P}_{1-x}\text{As}_y$ it is possible to achieve direct bandgaps in the range of 1.5 eV to 2.0 eV [51–53], which are ideally suited for top cells in combination with an active Si bottom-cell. Another approach is to apply a graded metamorphic $\text{GaAs}_{1-x}\text{P}_x$ buffer layer between the Si substrate and the GaAs or GaAsP top absorber [47,49,50]. Furthermore, As-termination of Si(100) was also found to prevent out-diffusion of Si in the GaP buffer layers [211]. From an applied point of view, it is also important to study the impact of As because As is mostly present in industry relevant MOCVD reactors.

Exposure of Si(100) to As (either in the form of background As_4 , TBAs or AsH_3) strongly affects the dimer orientation on the surface [109], the atomic configuration at the step edges [112] and the height of the steps [212]. In early studies of GaAs buffer growth on Si(100), it was found that GaAs nuclei nucleate at facets and at multi-height steps [213]. The surface structure of GaAs was shown to follow the Si-As structure, and can exhibit two domain directions depending on Si preparation [214]. The preparation of double-layer stepped Si(100) surfaces in an As ambient might differ from the one in H_2 ambient. Process temperature, source, and partial pressure of As are the key parameters for the Si(100):As surface preparation [209,214].

On the other hand, phosphorus in-diffusion into Si by annealing under phosphine supply in CVD ambient has been shown to be suitable to form a collector [49]. However, exposure of Si to PH_3 leads to a roughened, non-single-domain Si surface, which might cause APDs in the subsequent GaP buffer layer [215].

In this chapter, a suitable Si(100) preparation in As or P ambient for a subsequent low-defect GaP integration is studied. Initially, we focus on understanding the As- modified Si(100) 2° surface in comparison to well defended H-terminated Si(100) 2° surface. For this purpose, we employ *in situ* control by RAS with a combination of UHV-based surface sensitive methods. To understand in detail the interaction between the Si(100) surface and arsenic, either originating from TBAs source or background As_4 we chose Si(100) substrates with an offcut of 6° , which enables *in situ* control by RAS in the

temperature range relevant for the entire MOCVD process. We show that we are able to control the sublattice orientation of the subsequently grown GaP(100) epilayer, in dependence on the Si(100):As 6° surface preparation. Finally, we focus on the Si(100) surface reconstruction during annealing in TBP and its preparation for a subsequent GaP(100) growth. Part of this work regarding As-modified Si(100) 2° surface have been published in *Ref.* [216]. Results and discussion related to the formation of Si(100):As A- and B-type surface are currently under review in *Applied Surface Science*, *Ref.* [217]. Part describing Si(100) 2° surface preparation in P-rich MOCVD ambient was published in *Journal of Crystal Growth*, *Ref.* [218].

8.1 *In situ* control of dimer orientation on Si(100) surfaces in As ambient

Before discussing the vicinal Si(100) surfaces, we will briefly summarize our previous work on As-modified Si(100) surfaces with 2° offcut [100,216]. Since the atomic surface structure of the Si(100) substrates is strongly dependent on the preparation route, we employed *in situ* RAS for direct characterization of Si(100):As surfaces during MOCVD processing. In the second subsection, we employ substrates with a 6° offcut, where *in situ* control with RAS is possible over the entire range of temperatures relevant for Si processing. To correlate the surface properties with the observed RA spectra, we apply UHV-based methods. In particular, LEED enables to identify the surface reconstruction, STM allows to image the step structure and XPS is applied to confirm the presence of As on the Si surface. We also analyze the influence of the As source (TBAs or background As₄) on the atomic order at the Si surface.

8.1.1 As-modified Si(100) 2° surface and domain formation

In order to study the influence of As on the Si(100) 2° surface, we used well-defined reactor conditions free of III-V residuals other than As. Prior to processing, the reactor, susceptor and carrier were annealed in H₂ for 30 min at 1010 °C in order to further minimize surface contamination.

In previous research [98,112] it was found that annealing under TBAs or AsH₃ at high temperatures, above 800 °C etches the Si surface leading to roughening. An additional re-heating under H₂ (and unavoidable background As_x) at high temperature leads to re-arranging of the surface structure [98,112]. To avoid this surface roughening, the Si(100) 2° surfaces discussed here were first prepared according to the As-free standard preparation [78] and the monohydride-terminated (1×2) reconstructed Si(100) surface was obtained. Subsequently, the samples were annealed in the presence of TBAs ($p_{TBAs}=0.274$, molar flow = $9.13 \cdot 10^{-5}$ mol / min) in a temperature range between 420 °C -

670 °C. Subsequently, the sample was annealed at 850 °C under H_2 and in presence of the background arsenic deposited before. More details about Si(100):As 2° surface preparation are published in *Ref.* [100,216].

Figure 8.1 (a) compares the final RA spectrum (taken at 50 °C) of the As-modified Si(100) 2° surface [216] prepared as discussed above (orange line) with RAS from As-free, Si(100):H 2° surface (blue line). The Si(100):H 2° surface was prepared following the standard preparation (see chapter 4.1. or in *Ref.* [78]). The spectrum of As-modified Si(100) 2° exhibits a clear maximum at an energy around 3.7 eV, two minima at energies around 3.35 eV and 4.2 eV, and a wide peak with low intensity at energies around 2.5 eV – 2.9 eV. The minimum around 3.35 eV of the Si:As spectrum is shifted to lower energy in comparison to the minimum of Si:H.

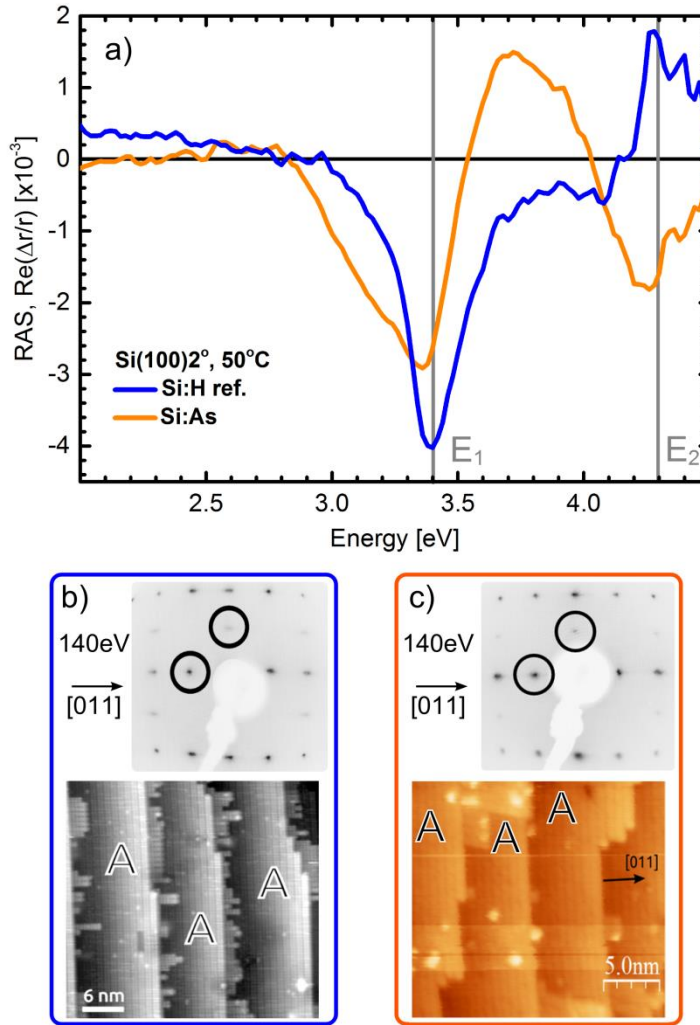


Fig. 8.1: (a): RAS of Si(100) 2° at 50 °C: surface terminated with H_2 (reference sample, blue line, taken from *Ref.* [78]) and surface terminated with As (orange line [216]). (b) and (c): top: LEED patterns of Si-H [78] and Si-As [216] surfaces, respectively (circles mark spots at half order); bottom: STM image (empty states) of Si-H (b), taken from *Ref.* [78] and Si-As (c), taken from *Ref.* [216]. Gray vertical lines indicate the E_1 and E_2 interband transitions of Si [135].

The RAS signal of the Si(100):As 2° surface agrees well with the RAS measurements from literature. Kipp *et al.* [219] reported RA spectra for UHV-prepared Si(001):As-(1×2) and Si(001):As-(2×1) samples with either 2.5° or 4° offcut. The experimental RA spectrum for Si(001):As-(1×2) showed two maxima at energy around 2.7 eV and 3.7 eV, and two minima at 3.15 eV and 4.15 eV, which agrees with the theoretically calculated spectrum for the same surface. They assigned the features to transitions between surface-perturbed bulk states and the transitions from the bonding to the antibonding As-As dimer states. However, the negative peak at around 3.15 eV (in our case at 3.35 eV) is very weak in the calculated spectrum, and its origin is not discussed. In *Ref.* [220], a negative peak close to 3.35 eV in the RA spectrum of (1×2) reconstructed Si(100):As surface, was assigned to Si–As bonds and As lone pairs, based on discrete dipole calculations. The line shapes of RD spectra of Si(100):As-(1×2) surface prepared after exposure to TBAs or AsH₃ [98,112,113] are almost identical with our Si(100):As 2° RA spectrum.

Figure 8.1 ((b), bottom) depicts an STM scan of Si(100):H 2° surface [78] which corresponds to the RA spectrum showed in the Fig. 8.1 (a). The step height equals to a double atomic layer step and the terraces reveal dimer rows parallel to the step edge – confirming D_A-type steps. The short stripes extending perpendicular from the step edges correspond to residual dimer rows of the B-type domain. Corresponding to this surface the LEED pattern (b) exhibits half order spots confirming a majority of A-type dimers on the surface (black circles). The minority of B-type dimers, visible in the LEED pattern and the STM image, was quantified based on FTIR measurements [77] and RAS signal [78] to cover 18 % of the surface.

The STM scan in Fig. 8.1 (c) reveals A-type dimer rows where both terrace width and step height correspond to a double-layer stepped surface. The maximum step height found on the surface was equal to four-layer steps; the most prominent were single-, double and triple-layer steps and step bunching was not observed [216]. The LEED pattern (Fig. 8.1 (c)) exhibits spots at half order along the offcut direction, which indicates that the majority of dimers is oriented with their axes perpendicular to the step edges. This is in accordance with the STM results. XPS quantification of the Si 2p peak shows a high contribution of a near-surface surface component, which is chemically shifted towards higher binding energies. Its high intensity compared to the lower intensity of the As 2p_{3/2} PE line indicates intermixing at the interface [216] rather than coverage of one As monolayer on top of Si. Given the previous, it remains unclear whether Si dimers, As dimers or Si–As heterodimers are present on the surface.

Based on the presented UHV analysis, we assign the RA spectrum of Si(100):As 2° (Fig. 8.1 (b), orange line) to double-layer steps with A-type dimer orientation on the surface [216]. The origin of the characteristic RAS peaks will be further discussed in the following subsection focusing on vicinal Si substrates.

8.1.2 As-modified Si(100) 6° surface and domain formation

In order to understand in exact terms the interaction of As with the Si surface we employed vicinal Si(100) substrate with a 6° offcut due to the possibility of *in situ* investigation during the entire Si preparation process, including high temperatures. Moreover, substrates with higher offcuts (>2.5°) are relevant for PV applications since they promote the formation of a double-stepped surface and encourage the annihilation of APDs (more details about double layer step formation in subchapter 4.1.2).

In this chapter, we will discuss *in situ* RA spectra of two different types of samples, where the As source was varied between the precursor TBAs (Si(100):As A-type) and background As₄ desorbing from the reactor parts (Si(100):As B-type). In contrast to Si(100) 2°, the reactor was free of III-V residuals except As, and there was no additional annealing in H₂ of the reactor before each process. Both samples were deoxidized at 1000 °C for around 20 min and cooled down. Cooling after thermal deoxidation is decisive for the actual surface formation: Si(100):As B-type was prepared by cooling down quickly (heater off) in presence of the background As_x. In this case, to ensure an indirect source of background arsenic from the reactor walls, the TBAs source was open while heating up the sample to the deoxidation temperature (where the Si surface is still oxidized), and closed before reaching 950 °C (around 4 min, $p_P = 1.09$ mbar). In contrast, Si(100):As A-type surface, (after deoxidation) was additionally annealed in TBAs ($p_P = 0.274$ mbar) at 850 °C for around one minute before the TBAs supply was closed and the sample was further annealed in H₂ (and background As) at 850 °C for around one minute before cooling to room temperature.

Figure 8.1 shows the RA spectra (left hand side) of Si(100):As B-type (red dashed line, As₄ only) and of Si(100):As A-type (green line, additionally annealed in TBAs) surfaces, which were measured at 50 °C, and the corresponding LEED patterns (on the right hand side, color frames correspond to colors of the RA spectra). The LEED pattern of the Si(100):As B-type surface shows spots at half-order with significantly stronger intensity in $[0\bar{1}1]$ direction than in $[011]$ direction (see red and green circle) indicating a preference for the (2×1) surface reconstruction domain - equivalent to the majority of dimers on the surface oriented parallel to the step edges (see upper red inset sketch in Fig. 8.1). In contrast, the LEED pattern of the Si(100):As A-type sample exhibits a clear preference for the (1×2) reconstruction, causing spots at half order in $[011]$ direction (see green circle). The dimers on the Si(100):As A-type surfaces are oriented perpendicular to the step edges (see green inset of Fig. 8.1). Both LEED patterns exhibits spot splitting along $[011]$ direction, which is more pronounced for the Si(100):As B-type surface, which indicates a more regular step structure. Both *in situ* RA spectra exhibit similar line shapes but opposite sign. In particular, for Si(100):As A-type (B-type) we observe a broad maximum (minimum) between 2.2 eV and 2.7 eV, a high intensity minimum (maximum) at around 3.4 eV (near the E_1 critical point energy of Si), a maximum (minimum) at ~3.7 eV and a minimum (maximum) at ~4.3 eV.

The similarity in the line shape becomes obvious when the sign of the spectrum of Si(100):As B-type is flipped (thin dash-dotted line). To match the intensity of the peak close to E_1 when comparing to Si(100):As A-type (green line), the flipped spectrum of Si(100):As B-type was additionally scaled by a factor of 1.32 (thin dash-dotted line). The line shapes of the spectra also matches the one from Si(100):As 2° (orange line), which was discussed in the previous section. In the RA spectrum of Si(100):As B-type, the peak around 3.4 eV is slightly shifted (0.05 eV) towards higher photon energies. The LEED pattern of that B-type surface indicates the presence of a small amount of minority domain on the surface, which is in line with the reduced intensity of the corresponding RA spectrum in comparison to the A-type surface. All spectral RA features flip when changing from the A-type to the B-type surface. However, the peaks scale differently: the shoulder of the peak at 3.4 eV of B-type surface is shifted towards higher photon energies in comparison to the A-type surface. In addition, the intensity of maximum at around 3.7 eV and minimum at around 4.3 eV is larger for the B-type surface when compared to the A-type surface.

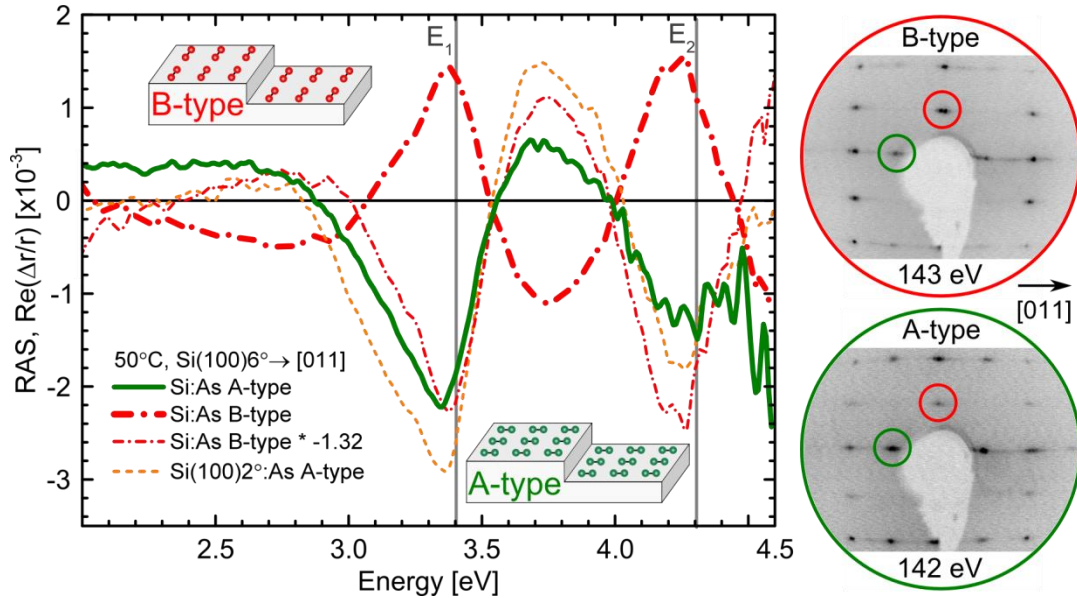


Fig. 8.1: Left side: RAS of Si(100):As 6° with predominant (2×1) (red) and (1×2) (green) surface reconstruction - dimers are oriented parallel (B-type domain) or perpendicular (A-type domain) to the step edges, respectively. The thin red dash-dot line depicts the flipped RA spectrum of Si(100):As 6° with predominant (2×1) reconstruction. For comparison, the orange line corresponds to the Si(100):As 2° modified surface. The insets illustrate the major As dimer orientation on the surface with respect to the step edges. Gray vertical lines indicate the E_1 and E_2 interband transitions of Si [135]. Right side: LEED patterns of measured RA spectra, green and red circles indicate half order spots from (1×2) and (2×1) surface reconstruction, respectively.

Kipp *et al.* [219] showed that annealing of the Si(100) surface in an As_4 flux in UHV either during heating up from room temperature to 600°C , or directly at 500°C , leads to an A-type or B-type surface, respectively, terminated by As-As dimers. RAS obtained from these surfaces exhibited opposite signs. It was concluded that the opposite sign of

the RA spectra is caused by the rotation by 90° of dimer orientation on the surface, and that the dimers dominate the spectral features. As mentioned in the chapter 8.1.1, the RA spectrum from the A-type surface is almost identical to the one shown in the *Ref.* [219]. In general, the RAS signal can have contributions not only from the terrace-related structure but also from the step structure [221]. As a matter of example, in the case of As-terminated Ge(100) 6° , the RA spectra of A- and B-type surfaces exhibit similar line shape also with an opposite sign [165]. Additional features, however, were observed beyond 3.0 eV which were explained by a different step structure observed by STM. The absence of additional features in our spectra indicate little contributions from the step edges, implying that the spectra are mostly terrace-related. Since the spectra of Si(100):As 6° A- and B-type surfaces depicted in Fig. 8.1 are significantly similar, we attribute the flip of the sign of the RA spectra to the change in the dimer orientation on the surface (as confirmed by LEED patterns). In addition, the RAS line shape of Si(100):As A-type surfaces with 2° (dashed orange line) and 6° (green solid line) offcut are very similar, which confirms that the RA signal is terrace related. However, it is not clear whether the RAS signal contains any information about As coverage or specific type of dimers present on the surface (As-As, Si-As or Si-Si dimers). Small differences of the RAS line shape between the Si(100):As 6° A- and B-type surface, in particular between 2.8 eV - 3.4 eV, and 3.5 eV - 4.0 eV, hint to different microscopic origins (e.g. difference in the step structure, dimers on the surface or As coverage), as it was suggested in *Ref.* [216] for the As-modified Si(100) 2° A-type surface.

In order to analyze the chemical state and As coverage, we performed XPS measurements on Si(100):As 6° A- and B-type samples. Figure 8.3 displays XPS measurements (blue line) and fitting (black line) of As $2p_{3/2}$ and Si 2p photoemission (PE) lines of the Si(100):As 6° A-type (green frame) and Si 2p PE of the B-type (red frame) surfaces. To vary the surface sensitivity, measurements were performed at photoelectron take-off angle equal to 90° and 30° against normal emission (see subchapter 3.4). The As $2p_{3/2}$ PE line on both samples confirms that As is present on the surface, however it is shifted towards lower binding energy (E_B), compared to the elemental As $2p_{3/2}$ PE line. In the As $2p_{3/2}$ peak, for both A- and B- type surfaces, an additional component is fitted (red dash-dot line). The fit of the Si 2p PE lines was performed with two spin-orbit pairs of equal width (spin-orbit splitting equal to 0.6 eV; $2p_{3/2}$ to $2p_{1/2}$ intensity ratio equal to 2:1, solid and dash-dot line). For both A- and B-type surfaces, the two spin-orbit pairs (green and orange lines) are chemically shifted to each other by 0.35 ± 0.2 eV. The relative contribution in the Si 2p PE line of the component shifted to the higher energy (Fig. 8.3, orange solid and dash-dot line) increases when the photoelectron takeoff angle (with respect to surface plane) is varied from 90° to 30° . The change of intensity ratio between both components indicates that the component shifted to the higher E_B (orange solid and dash-dot line) is closer to the surface, while the other component (green solid and dash-dot line) arises from bulk silicon atoms. We did not detect any contaminants, such as O, C, or Ga on the surface, which denotes that one of the contributions is chemically shifted

by incorporated As atoms. A chemical shift of the Si-As component towards higher E_B can indeed be explained by Si-As bonds [114].

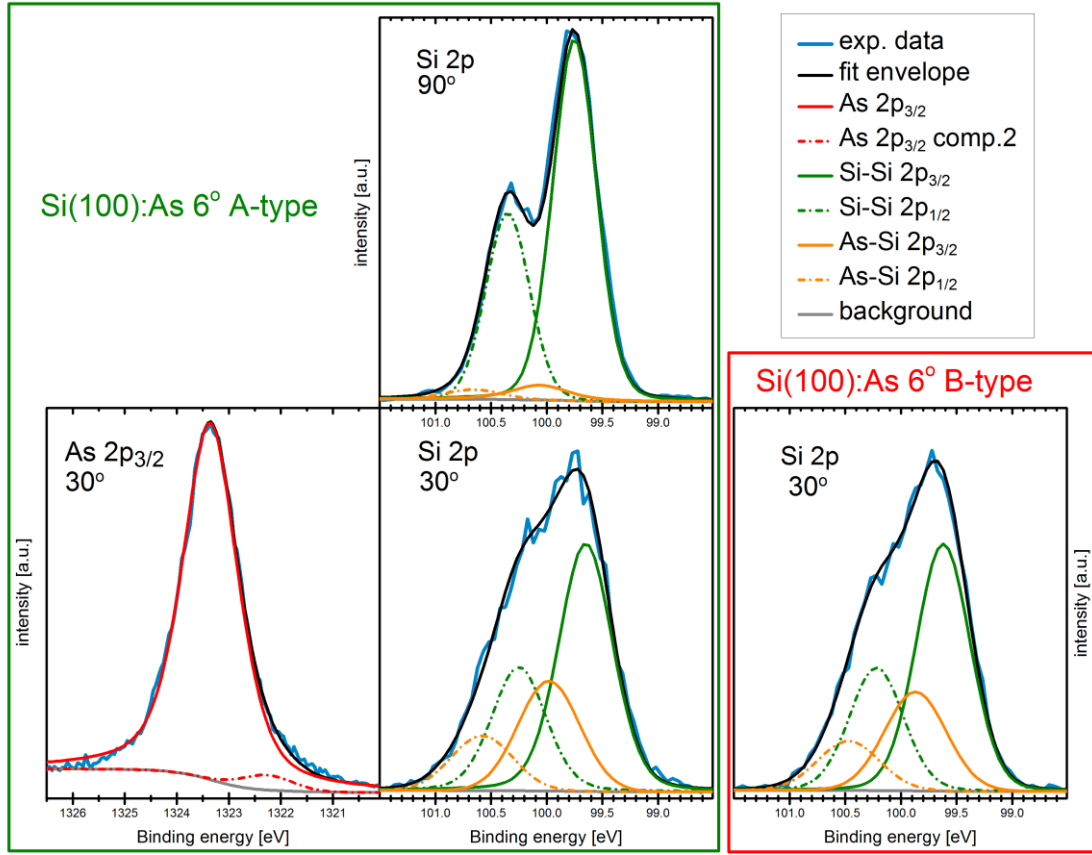


Fig. 8.3: XPS data (blue lines) of As $2p_{3/2}$ and Si $2p$ PE lines Si(100):As 6° A-type (green frame) surface, measured at 90° and at 30° photoelectron takeoff angle. The Si $2p$ PE lines of Si(100):As 6° B-type surface, measured at 30° photoelectron takeoff angle are in the red frame. The fit envelope (black line) and its components Si-Si (green line), As-Si (orange line), As $2p_{3/2}$ (red line) are indicated. Monochromated Al $K\alpha$ excitation was used and binding energy is given with respect to the Fermi level ($E_{\text{pass}} = 5$ eV).

Evaluation of Si $2p$ PE lines (measured at the 30° takeoff angle) from Si(100):As 6° A- and B-type surfaces, reveals that the intensity area of the component close to the surface (orange line), in comparison to the component stemming from the bulk (green line) is higher for the A-type sample. This indicates a higher As coverage (or more intermixing at the interface) on the A-type surface, also confirmed by the intensity ratio of As $2p_{3/2}$ PE line compared to the Si $2p$ PE line. In *Ref.* [216] the As coverage on Si(100):As 2° A-type surface was estimated to 0.75 ± 0.5 ML (under the assumption of a fractional coverage and an abrupt interface). However, a high intensity of the component close to the surface in the Si $2p$ PE line and the photoelectron escape depth equal to several nm indicated intermixing at the interface. In comparison to the Si(100):As 2° A-type surface from *Ref.* [216], the intensity ratio of that surface component (orange line) to the bulk component (green line) in the Si $2p$ PE line measured at 30° takeoff angle from

both samples measured here is smaller, which would indicate less intermixing in both samples. However, similar ratio of the intensity area of As $2p_{3/2}$ PE line to the component close to the surface in the Si $2p$ PE line between Si(100):As 2° from *Ref.* [216] and Si(100):As 6° B-type samples indicates intermixing. In the case of Si(100):As 6° A-type, the ratio of As $2p_{3/2}$ PE line to the component close to the surface in the Si $2p$ PE line in comparison to the Si(100):As 2° surface is almost twice higher. This indicates bigger amount of As in the sample, but less As intermixed with Si atoms.

In summary, it was demonstrated that both (1×2) and (2×1) reconstructed vicinal Si(100) surfaces can be prepared depending on the actual process conditions in the MOCVD ambient containing As. RAS enables *in situ* control over the As-modification of the Si surface, which will be applied in the following to study the influence of the processing parameters in detail.

8.1.3 As dimer orientation in dependence on process parameters

In this subchapter, *in situ* RAS was employed to accurately characterize the influence of process temperature and source of arsenic on the domain formation of vicinal Si(100) 6° during preparation in MOCVD ambient.

For As-free ambient, previous work revealed that the H_2 pressure strongly influences the interaction between the process gas (H_2) and the Si(100) surface: energetically governed D_B double-layer step formation is favored at low pressures, whereas increased interaction at high pressure is favorable for a kinetically driven D_A step formation (see subchapter 4.1 or *Ref.* [119]). All results shown here were obtained at a high reactor pressure of 950 mbar. These results concerning Si(100):As 6° surfaces are preliminary and triggered more detailed studies to be performed in future.

To investigate the domain formation mechanism on the Si(100) 6° surface and its correlation to the features in the RAS signal, we will focus on RA spectra taken at elevated temperatures. It is important to note that the features in RA spectra taken at low temperatures are sharper and shifted towards higher energy compared to features in spectra taken at elevated temperatures, which is due to the temperature dependence of the involved optical transitions and electron-phonon interactions [101]. In addition, higher temperatures induce strain in the optical components, which can lead to artificial shifts of the RA baseline. Therefore, interpretation of the line shape of the entire spectrum is more reliant than compared to single RA transients. Nonetheless, even though the interpretation of the RA spectra at elevated temperatures is more complex than at low temperatures, the changes in the higher temperatures RA spectra shown here are clear and distinguishable enough to allow unambiguous interpretation.

8.1.3.1 Formation of As modified Si (100) 6° B-type surface

Figure 8.4 shows *in situ* RAS measurements in color-coded representation performed on the Si (100):As 6° B-type surface during heating at 1000 °C (deoxidation temperature) in As₄ ambient, and subsequent cooling to 420 °C. Background As_x was indirectly supplied by the inner MOCVD reactor walls. The TBAs source ($p_p = 1.09$ mbar) was opened at 420 °C for about 4 min while heating up the sample to the deoxidation temperature. TBAs was closed before reaching 950 °C (where the Si surface is still oxidized). The RA spectra plotted below refer to the colored horizontal lines in the colorplot at different temperatures. The RAS transients on the right hand side correspond to the vertical lines at 3.2, 3.7 and 4.2 eV in the colorplot, and show the temperature-dependent development of the RAS signal over time. The time $t=0$ min signifies reaching 1000 °C. The sample is deoxidized after about 11 min at 1000 °C (as seen in Fig. 4.3 in subchapter 4.1.3). For the sake of simplicity and readability, the CP here is shown after the sample is deoxidized. During annealing at 1000 °C, the RA spectrum remains stable. This RA spectrum is similar to the one of clean vicinal Si(100) (see subchapter 4.1.3), this becomes clear when comparing, for example, the RA spectrum after 18 min (grey line) with that shown in Fig. 4.3 (subchapter 4.1.3) for As-free processing (inset, red line). Note that the elevated temperature causes a broader line shape with reduced amplitude.

The black dashed line indicates the beginning of the cooling down to 420 °C. From the color-coded graph and the transient spectra on the right side, we observe that the peaks at energies of 3.2, 3.7 and 4.2 eV start to develop right after the cooling down procedure starts. The RA spectrum of the final surface measured at 420 °C corresponds to that of Si(100):As B-type surface, discussed above.

Based on the peak evolution visible in the corresponding RA transients, we conclude that the formation of the As modified Si(100) B-type surface begins immediately upon cooling in presence of background arsenic. Right after the deoxidation, the clean Si surface at this temperature is covered by approximately 25 % of hydrogen and the step formation on the surface is mainly energetically driven (see subchapter 4.1.3), in consequence leading to B-type surface. Assuming this case in As ambient, in a simplified model of one As ML, which forms the As-modified B-type surface, the As dimer orientation implies that As replaced the top most Si atoms on the surface during the cooling procedure in background As. The lack of changes in the RA spectrum during further cooling down indicates that As detains the interaction between the Si surface and H₂, preventing the kinetically driven step formation observed in As-free ambient at 950 mbar (reduced Si vacancy formation and its annihilation at the end of the steps, causing retreading of B-type steps [66]). Furthermore, we observed a correlation between the amount of As₄ in the reactor and the amplitude of the RA spectrum: the surface cooled down in the ambient containing less background arsenic exhibited a RA spectrum with lower amplitude. A quantitative evaluation of this observation will be part of future studies.

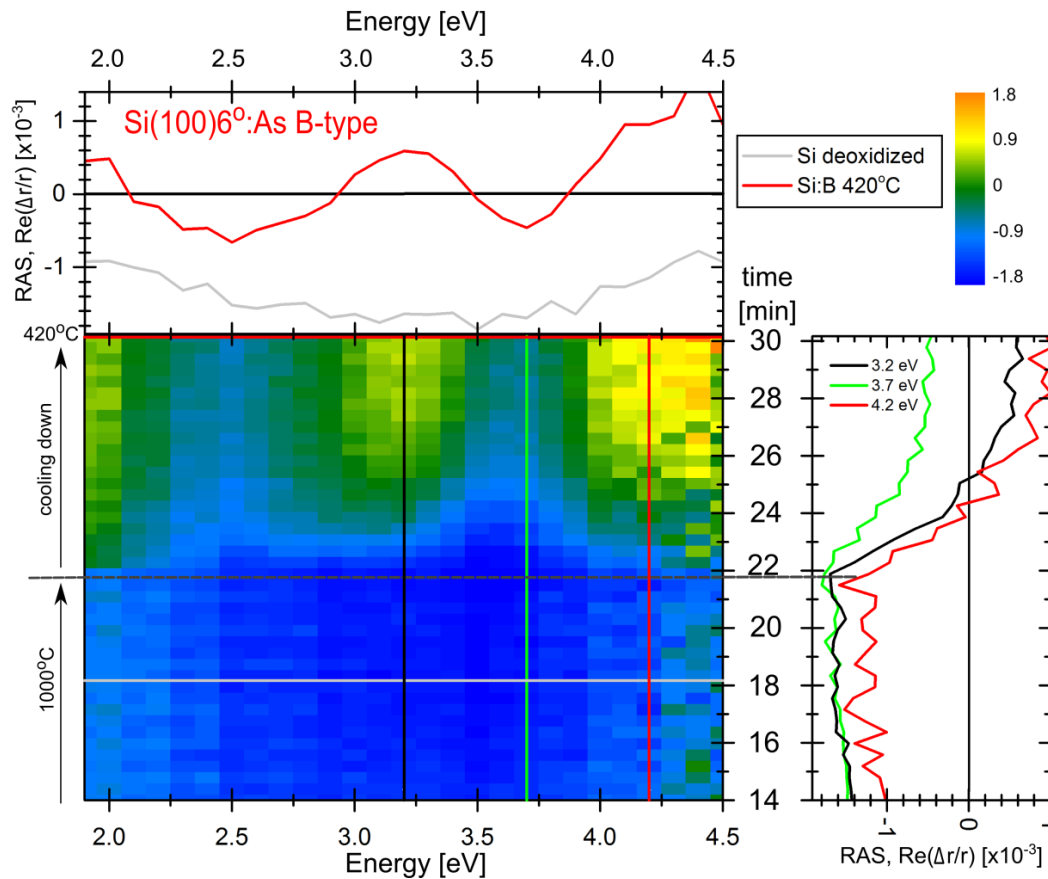


Fig. 8.4: Continuous *in situ* RAS measurements (~ 23 s per spectrum) in color-coded representation during heating at 1000°C (deoxidation) and subsequent cooling, both in presence of background As_4 . The time scale refers to time after reaching 1000°C . The RA spectra above the CP corresponds to the colored horizontal lines at different temperatures: clean (grey) and B-type Si:As surface (red). RA transients on the right display the temporal RA evolution at 3.2, 3.7 and 4.2 eV as indicated by the vertical lines. The CP is shown here 14 min after reaching the 1000°C , after the Si(100) surface is deoxidized.

8.1.3.2 Formation of As modified Si (100) 6° A-type surface

The preparation of Si(100):As 2° (1×2) surface involves a two-step preparation: annealing in TBAs and subsequent annealing at high temperatures without TBAs supply [100,216]. A sudden change in the RAS amplitude was observed when the sample was annealed to 850°C : at this temperature the amplitude of the RAS remained stable. We observed that after cooling down of the As modified Si(100) 6° surface from the deoxidation temperature to 420°C in the presence of TBAs, the RAS signal from this surface did not exhibit any characteristics from As modified Si(100) 6° A-type surface. In analogy to the preparation of As modified Si(100) 2° A-type surface, additional annealing without TBAs supply and exceeding 800°C was necessary to observe a development of the characteristic A-type RAS spectrum (described in subchapter 8.1.1 or 8.1.2, or in Ref. [100,216]).

Arsenic desorption from the Si(100) surface in UHV starts above 600 °C [109]. However, at 850 °C (950 mbar) the hydrogen coverage on the Si(100) surface decreases to around 80 % (see subchapter 2.5), which can facilitate As adsorption, Si replacement or interaction with other As species.

Figure 8.5 shows *in situ* RAS measurements in color-coded representation during deoxidation at 1000 °C in the As₄ ambient and subsequent annealing under TBAs supply. Here, the Si(100):As 6° A-type domain surface was formed at 850 °C, after deoxidation process and after switching on the TBAs source. The RA spectra plotted below refer to the colored horizontal lines in the colorplot at different temperatures. The RAS transient on the right hand side corresponds to the vertical lines at 3.0 eV in the colorplot and shows the temperature-dependent development of the RA. The horizontal grey line shows a clean Si(100) 6° surface.

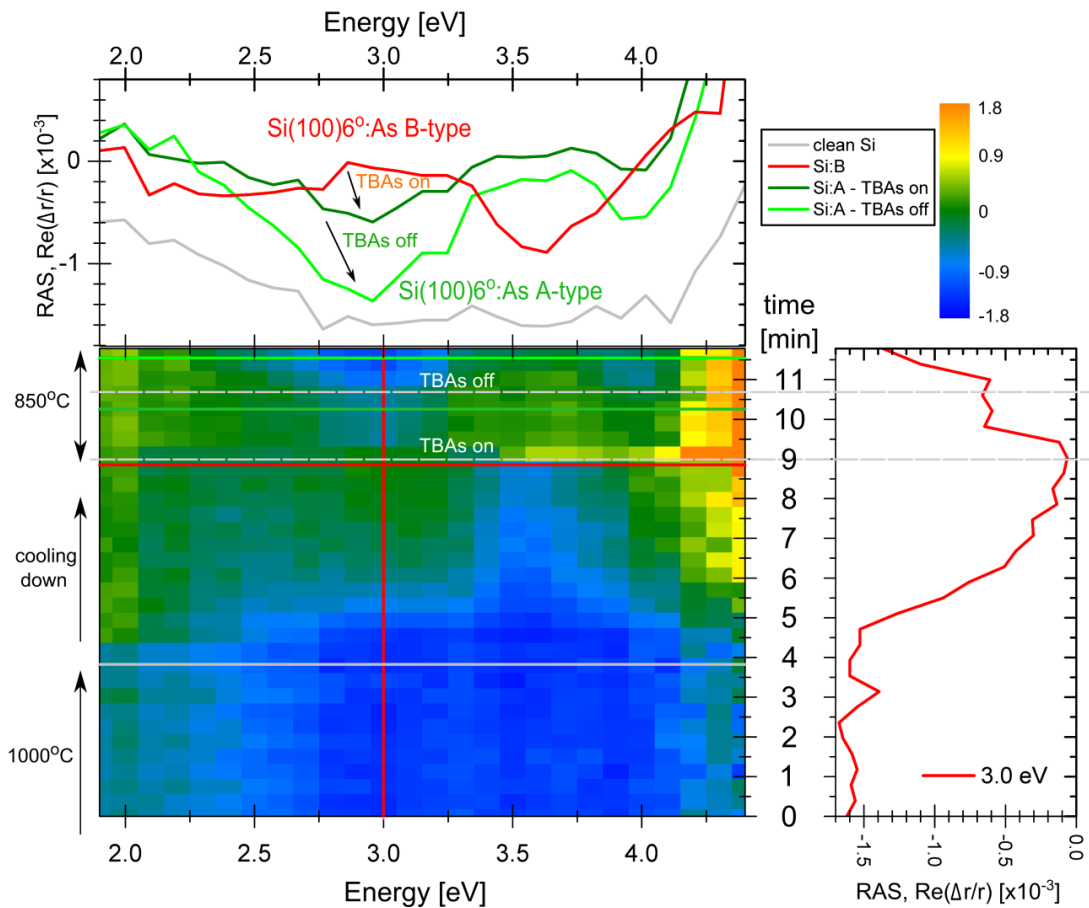


Fig. 8.5: Continuous *in situ* RAS measurements in CP representation (~23 s per spectrum) during 850 °C. The RA spectra above the CP correspond to the colored horizontal lines at different temperatures. The graph on the right side corresponds to the transient measurement at 3.0 eV. RA spectra shows the change of the majority domain on the surface from B-type (red line) to A-type (green line) when switching on the TBAs source at 850 °C.

The interpretation of the line shape of the entire spectrum is more reliant compared to single RA transients due to temperature induced artificial shifts of the RA baseline. From

the CP above we observe that the As modified Si(100) B-type surface starts forming directly after cooling in As₄ ambient step (as in Fig. 8.4). The red line spectrum taken at 850 °C (before the TBAs source was switched on) indicates that B-type domain is predominant at the surface. After switching on the TBAs source (grey dash line), we observe an almost immediate change in the RA spectrum. The line shape of the RA spectrum where TBAs was opened (green line) is very similar to the one from Si(100):As A-type surface shown in Fig. 8.1. Therefore, we assume that the A-type domain starts evolving directly upon offering TBAs. The RAS signal of A-type domain evolves further when TBAs is closed and the Si surface is annealed in the presence of H₂ and background As_x.

The change from B-type majority domain on the surface to A-type upon TBAs exposure is not clear. The process is very complex, since beside the strong interaction between the Si surface and H₂, the Si surface might interact with not only As but also TBAs fragments. At 850 °C and 950 mbar, the As desorption rate is higher than the absorption rate, which can facilitate interaction of the Si(100) surface with the H₂ or TBAs fragments. At this temperature, the H₂ coverage on the Si(100):H surface is higher than 80 % (for As-free ambient, see subchapter 2.5). In addition, TBAs decomposes to the species: AsH₃, AsH, As, AsH₂, and As₂ [222]¹². The ratio between AsH₃ and its sub-hydrides (AsH and AsH₂) to As is around 4:1 (at 530 °C - 610 °C, 50 mbar). In the case of Ge(100), annealing in AsH₃ ambient was found to rapidly etch the surface, in contrast to As₄ [165,223,224]. Considering a high ratio of As hydrides to As, we cannot exclude the possibility of a quick interaction between the Si surface and the radicals stemming from the TBAs decomposition, which could affect the atomic order on the surface. The increase of the amplitude of the RA spectrum, when TBAs is closed and the surface is annealed in H₂ and background As_x (Fig. 8.5 light green line), could result from desorption of TBAs fragments from the Si(100) surface.

To investigate if the RA spectrum contains any additional information about the amount of As on the Si(100) surface, we performed additional annealing steps in TBAs and background As₄ at two different temperatures with cooling to 420 °C to measure RAS at rather low T where the spectra features are sharper (Fig. 8.6). First, the A-type domain surface was prepared as described above (Fig. 8.5) and cooled down to 420 °C. In the next step, the sample was heated to 850 °C, and annealed first with and secondly without TBAs (about one minute each) and then cooled down to 420 °C to measure RAS (orange line). Subsequently, this annealing procedure was repeated on the identical sample at 670 °C, and again cooled to 420 °C (blue line). The process was controlled *in situ* with RAS and at each step the RAS signal from the surface was stable before going to the next step. As an additional reference, we show the RA spectrum of the A-type sample figure 8.2 (but here measured at 420 °C). The RA spectrum of the reference sample (green line)

¹² Based on mass spectrometry measurements of TBAs decomposition at 50 mbar, detected in the MOCVD reactor in HZB [222].

has a very similar shape and identical peak amplitude at 3.7 eV as the spectrum of the sample annealed in TBAs at 850 °C (orange line). However, a small difference in the RAS line shape and amplitude at energies below 2.9 eV is visible, which, could artificially originate in a shifted base line due to temperature. Nevertheless, we assume that the surfaces of the reference sample (green line) and the one annealed in TBAs at 850 °C (orange line) are similar, regarding the dimer orientation of the majority domains and possibly the As coverage.

After annealing in TBAs, the overall line shapes are similar, but the amplitudes are different: while the amplitude of the peak at 3.2 eV after annealing at both temperatures is comparable to the A-type reference, the annealing at 670 °C leads to an increased intensity of the peak at 3.7 eV. At 850 °C, the desorption rate of As from the Si surface is higher than at 670 °C, which indicates that the intensity of the peak at 3.7 eV relates to the amount of As present on the surface. The lack of change in amplitude of the peak at 3.2 eV hints to different microscopic origins of both peaks (e.g. difference in the step structure, dimers on the surface or As coverage), as it was suggested in *Ref.* [216] for the A-type Si(100) 2° surface.

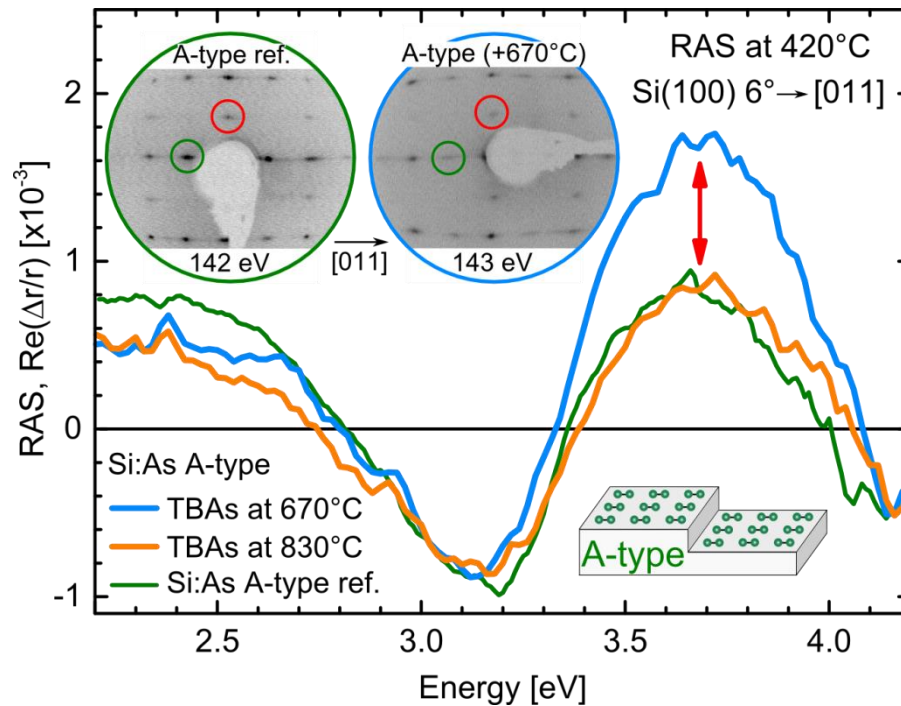


Fig. 8.6: RA spectra (taken at 420 °C) of Si(100):As 6° A-type. The samples differ in preparation, in particular an additional annealing in TBAs first at 850 °C (orange line) and secondly at 670 °C (blue line). As a reference sample we show the RA spectrum of the Si(100):As 6° A-type sample described in Fig. 8.2 (green line). The inset shows LEED patterns corresponding to the Si(100):As 6° A-type sample with an additional annealing in TBAs at 670 °C (blue frame) and the reference sample (green frame, also shown at Fig. 8.2). The second positive peak in the RA spectrum shows sensitivity to the As amount on the surface.

A higher As coverage for the sample annealed at 670 °C in comparison to the reference sample can be confirmed by XPS: Figure 8.7 shows XPS measurements (blue line) and fitting (black line) of As 2p_{3/2} and Si 2p PE lines of the Si(100):As 6° A-type surface with an additional annealing in TBAs at 670 °C (blue frame) compared to the Si 2p PE lines of the Si(100):As 6° A-type shown in Fig. 8.1 (green frame).

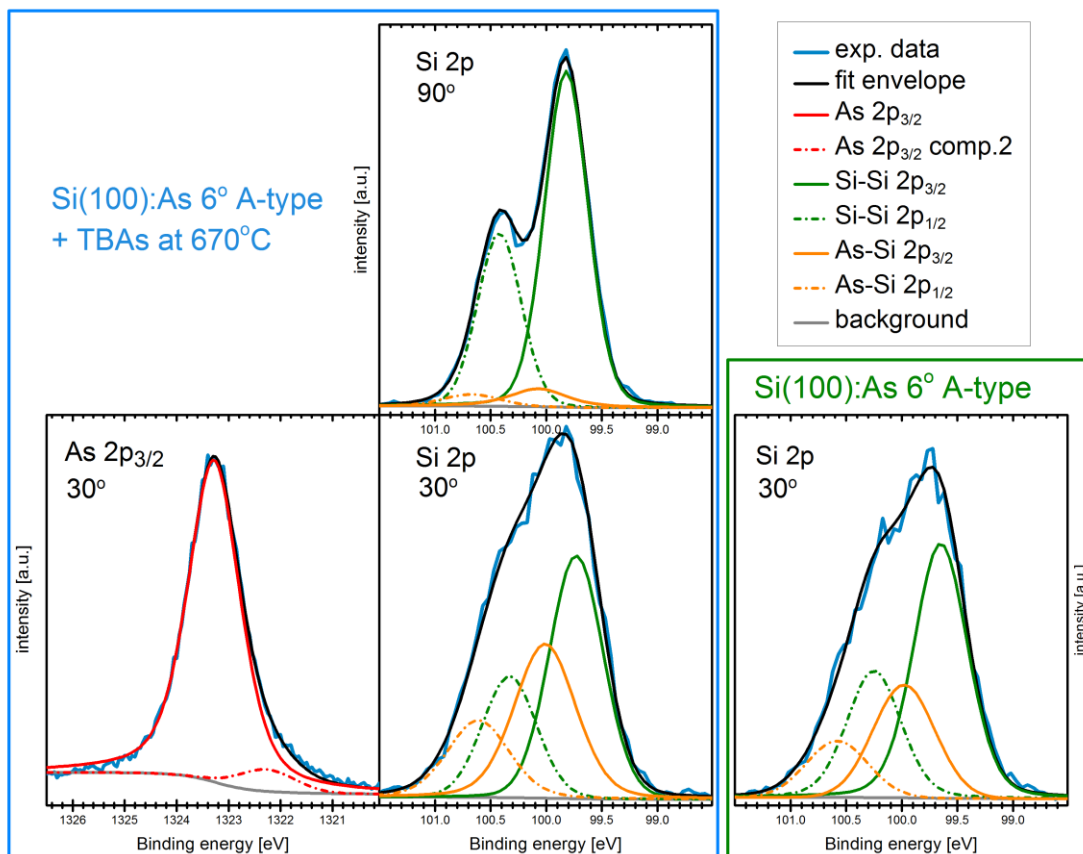


Fig. 8.7: XPS data (blue lines) of As 2p_{3/2} and Si 2p PE lines of Si(100):As 6° A-type annealed additionally in TBAs at 670 °C, measured at 90° and at 30° photoelectron takeoff angle. The fit envelope (black line) and its components Si-Si (green line), As-Si (orange line), As 2p_{3/2} and a second component (red and red dash-dotted line) are indicated. Monochromated Al K α excitation was used and binding energy is given with respect to the Fermi level ($E_{\text{pass}} = 5$ eV).

The intensity ratio of As 2p_{3/2} to Si 2p PE line is higher for the sample annealed at 670 °C in comparison to the reference sample. PE spectra were measured at an angle of 90° and 30° against normal emission (see subchapter 3.4). In the As 2p_{3/2} peak an additional component is fitted (red dash-dotted line). In the Si 2p PE lines two components are fitted: one stemming from the bulk (Si-Si bonds) and the second originating from the component close to the surface (Si-As bonds). The origin of both components was verified by comparing their intensity ratio between the surface sensitive measurement and the measurement at 90° takeoff angle. The data were fitted applying a model of spin-orbit splitting equal to 0.6 eV and 2p_{3/2} to 2p_{1/2} intensity ratio equal to 2:1. The Si-As component in both Si 2p peaks is shifted to a higher E_B by 0.35 ± 0.2 eV. As was the case

in previous XPS measurements (Fig. 8.2, subchapter 8.2.2) we did not detect any contaminant such as O, C or Ga on the surface, which implies that one of the contributions is chemically shifted by incorporated As atoms.

The LEED pattern of the sample, which was additionally annealed at 670 °C (Fig. 8.6 blue frame) exhibits rather balanced ratio between the (2×1) and (1×2) surface reconstruction (see red and green circles), the spots in the LEED pattern are not as pronounced as in the LEED pattern from the reference sample (annealed at 850 °C). This could indicate less ordered surface in comparison to the surface annealed at 850 °C. After exposure of the Si(100) surface to As, the sample must be annealed in H₂ and background As_x above 800°C. This LEED results confirm that the change of the RAS amplitude at 3.7 eV is rather correlated with As coverage on the sample and not only corresponds to the dimer orientation on the surface.

8.2 Summary of domain formation on As- modified Si(100) surfaces

On Si(100) surfaces with 0.1°, 2° and 6° offcut, the sensitivity of RAS to the dimer orientation either on monohydride terminated Si(100) surfaces (see subchapter 4.1), or arsenic modified surfaces, enables *in situ* control of interactions with hydrogen or arsenic. Moreover, on Si(100):As 6° surfaces, the sign of the RAS signals indicate present domain distribution on the surface – either majority of A- or B-type domain.

Figure 8.8 summarizes the RAS signals of the arsenic modified Si(100) surfaces for samples with 0.1°, 2° and 6° offcut. Preparation of Si(100):As 0.1° consisted of deoxidation and fast cooling down in As ambient at reduced pressure of 100 mbar in order to minimize interaction of the surface with H₂ and to prevent Si vacancy formation [217]. Presence of As on the Si(100) 0.1° surface was confirmed by XPS, and the majority of A-type domain on the surface was confirmed by LEED measurement (not shown here) [217]. Preparation of Si(100):As 2° and Si(100):As 6° is described in subchapters: 8.1.1 and 8.1.2, respectively.

The RAS of Si(100) surfaces with A-type majority domain with 0.1°, 2° and 6° offcut (Fig. 8.8) have a characteristic minimum at 3.4 eV, a maximum at around 3.7 eV and minimum at around 4.3 eV. All Si(100):As A-type surfaces exhibit almost identical characteristic RAS signals, independently of the offcut angle. Moreover, the amplitude of RAS consistently increases with lower offcut angle (lower step density), which would confirm that the RA signal is related with the terraces rather than with the steps. Which is in agreement with the flip of the RAS sign for the Si(100) 6° A- and B-type surface, which is caused by rotation of the dimers on the Si surface. The origin of the peaks is discussed in subchapter 8.1.1.

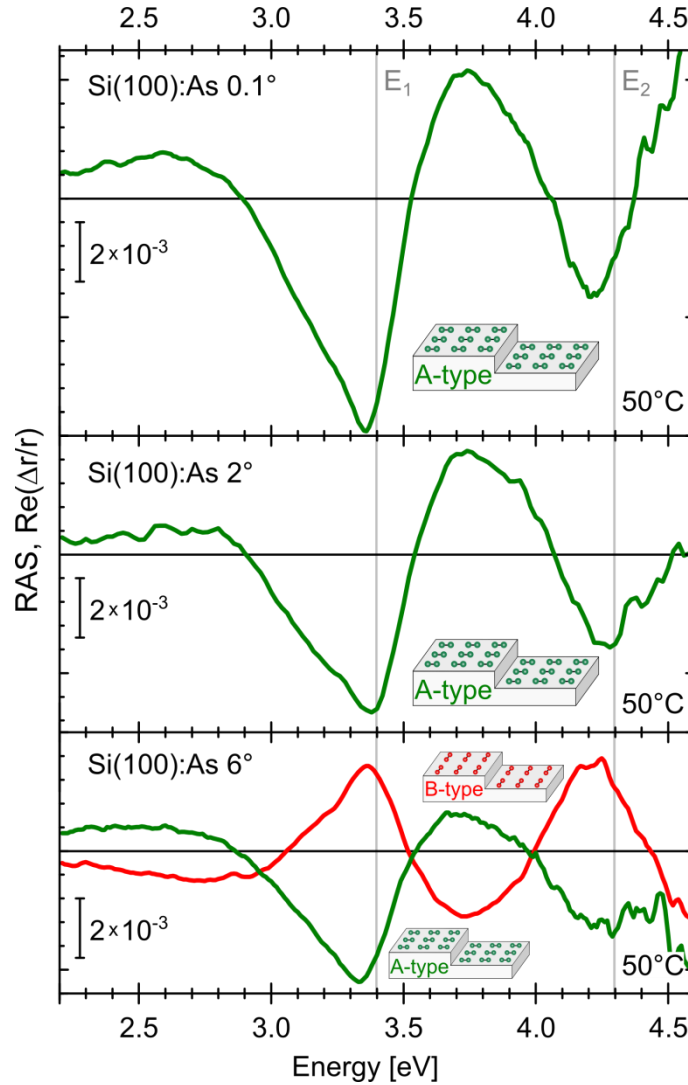


Fig. 8.8: RA spectra (taken at 50 °C) of Si(100):As surfaces with 0.1°, 2°, and 6° offcut in [011] direction. The green line spectra correspond to the majority of A-type dimers on the terraces and red to B-type (see insets). All RA spectra exhibit characteristic peak at 3.4 eV. The flip of the RAS signal in the case of Si(100):As 6° B-type surface, corresponds to a rotation of 90° of the majority dimers on the surface. Gray vertical lines indicate the E_1 and E_2 interband transitions of Si [135].

The *in situ* RAS experiments performed in this work revealed a significant influence of TBAs and background As_x on the domain structure on the Si(100) 6° surface, which also strongly depends on processing conditions. As in the case of Si(100) preparation in H_2 ambient, we are able to obtain *in situ* control over the domain formation on Si(100):As 6° surfaces in dependence of the source of arsenic. Precisely, cooling down in background As_x leads to Si(100):As 6° B-type surface (dimers are oriented parallel to the step edge), while additional annealing in TBAs (AsH_3) and background As_x at 850 °C leads to an A-type surface (dimers are oriented perpendicular to the step edge). We observed that the formation on the B-type majority domain on Si(100):As 6° surface starts after the deoxidation step, while cooling down. At temperatures above 900 °C, hydrogen desorption dominates over adsorption on the Si(100) surface. In this range of

temperatures, As adsorption to the Si(100) surface could be facilitated, either coming from the inner walls from the reactor or from the TBAs supply.

Further RAS measurements in combination with our UHV-based techniques are required to obtain a complete understanding of the Si(100):As surfaces. STM images with atomic resolution could for instance, give an insight into the difference in step formation after surface exposure to TBAs and As₄. ATR-FTIR measurements may provide further understanding whether Si-Si, As-As or Si-As dimers are present on the surface.

In summary, in As ambient we are able to prepare well-defined Si(100) surfaces with 0.1°, 2° and 6° offcut with an A-type majority domain. Additionally, by controlling the relevant process parameters we are able to prepare Si(100):As 6° with either A- or B-type majority domain on the surface, with an *in situ* RAS control. On both surfaces, LEED measurements confirm presence of only a small residual domain. The two well-defined As modified surfaces seem to be suitable for subsequent III-V nucleation and single-domain GaP heteroepitaxy, which will be discussed in the following.

8.3 GaP/Si(100):As

GaP nucleation on Si(100) for quasisubstrates is established in As-free MOCVD ambient [20–25,100]. In this subchapter, we will investigate GaP nucleation on As-modified, vicinal Si(100) surfaces. *In situ* RAS enables us to prepare a very well-defined Si(100):As 6° surface featuring either a majority of A-type or B-type domain on the terraces prior to GaP nucleation. Subsequently, we apply RAS to compare the GaP/Si:As interface formation and compare it with previous results of GaP grown on monohydride-terminated Si(100) [20,225,226].

Assuming an abrupt interface formation, the GaP sublattice orientation depends on the dimer orientation of the Si(100) substrate prior to nucleation [20]. P-rich prepared GaP surfaces (see subchapter 2.4.4) [20,95,227,228] grown in As-free ambient on Si(100):H 2° with A-type (B-type) majority domain prior to nucleation exhibit the B-type (A-type) majority domain of P-dimers on the surface [20]. The term GaP(100) A- and B- type here does not refer to the GaP crystal polarity as in the case of GaP(111), but it refers to the P-dimer orientation on the surface¹³, in analogy to the notation of Chadi defined for Si(100) [72] (see subchapter 2.4.2, Fig. 2.10). Such a rotation (by 90°) of the P-dimer at the P-rich GaP/Si(100) surface corresponds to a change in GaP sublattice orientation due to the zincblende structure. In a simplified abrupt interface model [20], the GaP

¹³ The P-dimer rows oriented parallel or perpendicular to the step edges correspond to (1×2)- or (2×1)-like surface reconstruction, respectively. The P-dimers on (2×2)/c(4×2) reconstructed GaP(100) are depicted on Fig. 2.13 (a), in subchapter 2.4.4.

sublattice orientation depends on whether Ga or P binds preferably to the Si surface. Accordingly, from the dimer orientations of (i) the Si dimers prior to nucleation and (ii) of the P dimers at the GaP/Si(100) surface it can be deduced whether Si-P or Si-Ga bonds are preferred at the buried heterointerface. In common P-rich conditions, Si-P were found to prevail [20,225]. GaP grown on As-modified Si(100) 2° A-type surfaces results in single-domain GaP epilayers with an inverted sublattice orientation compared to growth on monohydride-terminated Si(100) 2° [216]. XPS measurements indicate an intermixed Si:As interface where the actual stoichiometry could not yet be resolved [216].

Figure 8.9 shows RAS signals (measured at 50 °C) of heteroepitaxially grown GaP on Si(100):As 6° A-type (green line) and B-type (red dash-dotted line) surfaces. The RA spectrum of the GaP/Si(100):As 6° B-type surface is very similar to that of P-rich GaP(100) from *Ref.* [96], regarding both line shape and sign of the signal. The signal has a characteristic negative peak at 2.45 eV and a positive peak at about 3.6 eV, which both correspond to a B-type (2×2)/c(4×2) reconstructed P-rich GaP/Si(100) surface (see subchapter 2.4.4, Fig. 2.7) where buckled P-dimers are aligned (2×1)-like on the surface (see red inset in the graph, and model on the right hand side, red frame) [20,228].

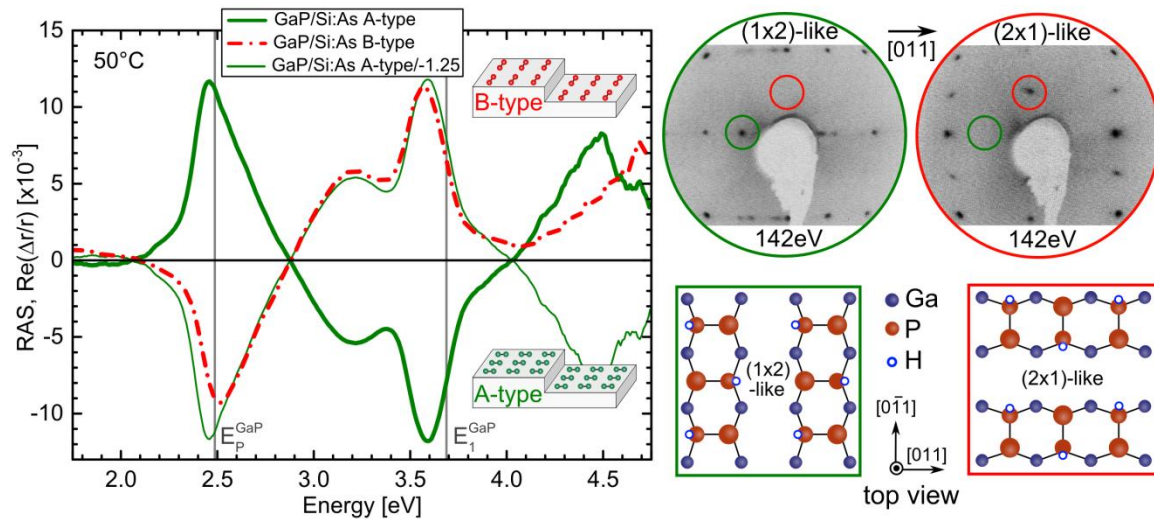


Fig. 8.9: RA spectra (measured at 50 °C) of P-rich, (2×2)/c(4×2) reconstructed GaP layers grown on Si(100):As 6° A-type (green line) and B-type (red dash-dot line). Grey vertical lines indicate energy of the P-rich reconstruction surface state (E_P^{GaP}) [229] and the interband transition of GaP (E_1^{GaP}) [99] at 50°C. LEED patterns (top) and model of the surface reconstruction (bottom) on the right hand side correspond to the RAS signals (color-coded).

The LEED pattern of GaP/Si(100):As 6° B-type (Fig. 8.9, right hand side, red frame) clearly shows spots at half order along $[0\bar{1}1]$, which corresponds to a majority of B-type P-dimers on the surface. Half order spots, which indicate A-type minority domain on the GaP(100) surface are not visible in the LEED pattern. Identical GaP growth conditions applied on a Si(100):As 6° A-type surface result in the GaP(100)-like RAS signal of opposite sign (Fig. 8.9, green line). Since a flipped sign of the RAS signal implies a rotation of majority dimer orientation on the surface, the signal corresponds to a

(2×2)/c(4×2) surface reconstruction where the P-dimers are aligned (1×2)-like on the surface (see green inset in the graph, and a model of right hand side, green frame). Correspondingly, the LEED pattern from this surface (Figure 8.9, right hand side, green frame) exhibits half order spots in [011] direction, which confirms the A-type majority domain on the surface. The green thin solid line in Fig. 8.9 corresponds to the flipped RA spectrum of the GaP/Si(100):As 6° A-type surface. The line shape of the spectrum matches the one from GaP/Si(100):As 6° B-type surface but the first minimum and second maximum have smaller intensities. The difference in the RAS spectra above 4 eV is affected artificially by the baseline correction.

LEED and RAS analyses clearly show that the orientation of the P dimers at the GaP/Si(100) surface depends on the dimer orientation on the Si(100):As substrate: GaP grown on Si:As A-type (B-type) results in A-type (B-type) polarity. This is the opposite relation as observed for GaP heteroepitaxy in As-free ambient [20]. This would be in line with Ga binding first on top of Si-As, assuming an abrupt interface. However, XPS results indicate more complex intermixed interface structures [216]. The atomic structure of the buried interface cannot be resolved here. We conclude that by controlling the Si(100):As 6° surface preparation, we are able to choose the prevailing GaP sublattice orientation with either A- or B-type dimers at the GaP/Si(100) surface.

In analogy to the domain quantification discussed above for Si(100):H surfaces, the amplitude of the RAS signals in Fig. 8.9 reflects the domain ratio at the GaP/Si(100):As surface: antiphase disorder would cause additional mutually perpendicular P-dimers on the surface and therefore decrease of the RAS signal [227]. The APD concentration in the heteroepitaxially grown GaP/Si(100) layer can be quantified by scaling the RA spectrum by a factor m to a single-domain reference GaP(100) substrate [227]. However, internal reflection at the buried heterointerface between Si and GaP of the transmitted light also contributes to the GaP/Si(100) RAS signal. For a precise APD quantification, the RA spectrum has to be corrected for the effect of the Fabry-Pérot-like oscillations [21,227]. These oscillations occur due to the optical path differences between the light reflected at the surface and the GaP/Si(100) interface. In a semi-empirical model, the GaP/Si(100) RAS signal is corrected by a so-called relative reflectance ($R_{rel.} = R_{GaP/Si}/R_{GaP}$) and normalized by the signal of the GaP(100) reference, which is exemplified in Fig. 8.10 for GaP grown both on A-type and B-type Si(100):As. Figure 8.10 (a) shows the $R_{rel.}$ for the GaP/Si(100):As 6° A-type (green line) and B-type (red line) samples. The Fabry-Pérot oscillations vanish at energies beyond the E_1 interband transition due to increasing absorption in the GaP epilayer. Figure 8.10 (b) shows the RAS signals for GaP/Si(100):As 6° A-type (green line) and B-type (red line) sample and the corresponding spectra corrected (multiplied) by R_{rel} (dash-dot lines). Figure 8.10 (c) compares these corrected spectra with a P-rich, (2×2)/c(4×2) reconstructed, homoepitaxially grown GaP(100) reference (blue line). Both surfaces were prepared identically. RAS signals from the heteroepitaxially grown GaP are scaled by a factor m to match the RA spectrum intensity of the GaP(100) reference sample. If the surface area of

$1/m$ contributes to the RAS signal, half of the remaining area is covered by APDs. The scaling factor of $m = 1.025$ and 1.16 indicate the APD concentration of only 1.2 % and 6.9 % at the GaP/Si(100):As 6° A-type and B-type surface, respectively. The amplitude of both signals indicates almost single-domain surfaces, implying self-annihilation of antiphase boundaries during GaP growth [230].

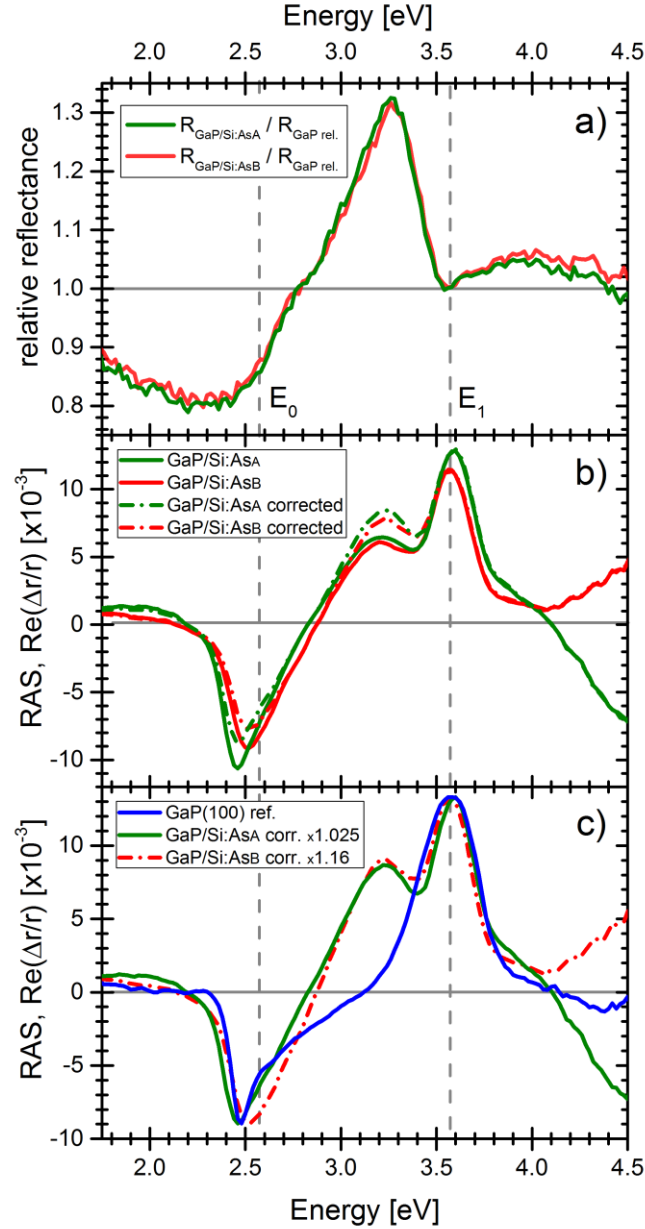


Fig. 8.10: Spectra of about 40 nm thick GaP epilayers grown on Si(100):As A-type and Si(100):As B-type substrates (measured at 50 °C): (a) relative reflectance spectra used for correction of the Fabry-Pérot oscillations. (b) The measured and the corrected RA spectra. (c) The corrected RA spectra scaled to the amplitude of an APD-free GaP(100) reference RA spectrum. All GaP(100) surfaces were prepared identically and are P-rich with a $(2\times 2)/c(4\times 2)$ surface reconstruction.

The shape of the corrected and scaled GaP/Si(100):As 6° RA spectra (Fig. 8.10 (c), green and red-dashed line) strongly agree with that of the homoepitaxial reference (Fig. 8.10 (c), blue line). However, differences are present in the line shape in the region between about 2.7 and 3.6 eV (Fig. 8.10 (c)). That difference in the area between corrected and reference spectra is likely due to dielectric anisotropies arising at the GaP/Si(100) buried heterointerface [100,113,225,227,231].

The almost identical line shapes of GaP/Si(100):As A- and B-type imply that both GaP layer thicknesses are comparable. The thickness of the GaP(100) epilayers is around 40 nm, when compared the RAS spectra to the one in *Ref.* [216]. Since both spectral line shapes are very equivalent, the anisotropy arising at the GaP/Si(100):As heterointerface might be also comparable. The RMS roughness, measured by atomic force microscopy is around 5.8 Å for both samples.

8.4 Si(100) surface after phosphorus exposure

With regard to *in situ* preparation of Si p-n junctions by group-V in-diffusion, which will be discussed in chapter 9, Si(100) surface preparation in phosphorus ambient will be studied in the following. It is known in literature that annealing of Si at high temperatures in presence of PH_3 causes P to in-diffuse into the silicon substrate creating a n-doped collector of the silicon sub-cell. However, this process also leads to significant roughening of the Si surface [232]. In the following subchapter, we will investigate the Si(100) surface after exposure to the P precursor TBP and the surface preparation for the subsequent GaP growth. For this, we apply *in situ* RAS to control Si(100) 2° surface morphology after exposure to TBP. We will correlate the RAS spectra with the results from the UHV-based surface sensitive methods.

The Si(100) 2° substrate was deoxidized and a homoepitaxial buffer layer was grown, according to the process described in section 5.2. After preparation of a double-layer A-type Si(100):H 2° surface, the samples were annealed under a TBP flow of 5.15×10^{-4} mol/min at 650°C at 950 mbar reactor pressure for 20 min. Subsequently, TBP was closed and the sample was slowly heated up to 830°C (heating rate of $\sim 22^\circ\text{C}/\text{min}$), where the Si(100) surface was annealed for one minute before being cooled to 730°C , which is the established temperature to prepare A-type double layers steps on Si(100) 2° surface in the “clean” MOCVD ambient [78].

Figure 8.11 (a) shows the RAS transient at 3.2 eV of Si(100) 2° during the process. Immediately after the TBP precursor is open, the characteristic minimum in the RA spectrum of the D_A surface (see Fig. 8.11 (b)) vanishes. During annealing in TBP the RAS spectrum does not show any anisotropy, indicating that the surface is either disordered or both (1×2) and (2×1) domains are equally distributed. The RAS signal does

not change when TBP is closed (at around $t=1200$ s) and further annealed at 650°C . At elevated temperature, the amplitude of the transient signal starts to increase which is likely due to P desorption from the surface. At 830°C the RAS signal remains constant and a further increase of the transient signal is observed at 730°C , where the monohydride-terminated, (1×2) reconstructed Si(100) 2° surface forms. Figure 8.11 (b) shows three RA spectra of the Si(100) 2° surface measured at 420°C : (i) before exposure to TBP (green line), (ii) after exposure to TBP (orange line), and (iii) after subsequent additional annealing in H_2 without TBP supply (blue line). Prior exposure to TBP, the RA spectrum (green line) indicates a monohydride-terminated Si surface with a prevalent (1×2) surface reconstruction [78].

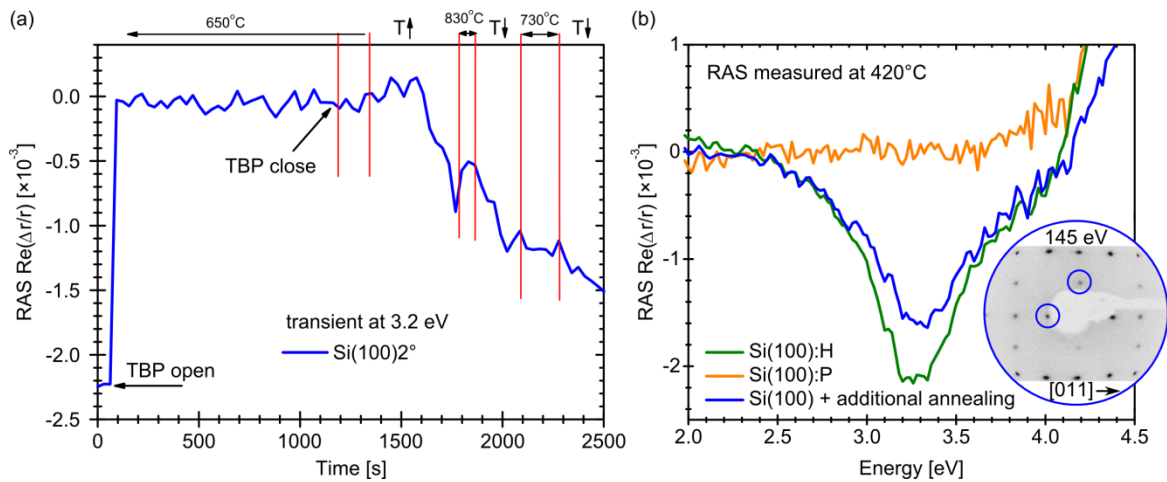


Fig. 8.11: (a) RA transient at 3.2 eV of Si(100) 2° during heating with and without TBP supply. (b) *In situ* RA spectra of monohydride terminated (green line), TBP annealed Si(100) with 2° offcut in [011] measured at 420°C (orange line) and after additional annealing in H_2 (blue line). The inset shows the LEED pattern from the Si(100) 2° surface after annealing in TBP and subsequently in H_2 ambient. The half order spots indicate a majority of A-type domain on the surface (see blue circles).

The RA spectrum after annealing in TBP (orange line) does not show the characteristic minimum at 3.4 eV, indicating either a disordered, not dimerized or a two-domain ($2\times 1/1\times 2$) surface with similar domain ratios. Additional annealing at high temperature in H_2 restores the (1×2) surface reconstruction, as evidenced by the emerging RAS fingerprint at 3.4 eV (blue line). The RA spectrum of the surface annealed in TBP and H_2 exhibits lower amplitude compared to the RA spectrum prior to TBP exposure, which indicates a larger amount of the B-type minority domain on the surface or remaining excess P. The LEED pattern from this surface (see inset in Fig. 8.11 (b)) exhibits spots at half order along [011] and $[0\bar{1}1]$ directions, which indicates A-type (1×2) and B-type (2×1) domains respectively, present on the Si(100) surface. However, a higher spot intensity along [011] direction indicates a majority of A-type domains with a residual amount of B-type (2×1) domains.

8.5 Summary of this chapter

The sensitivity of RAS to the dimer orientation of As-modified Si(100) surfaces enables *in situ* control of arsenic interaction with the Si surface. By benchmarking the RAS signals from Si(100) surfaces with UHV-surface sensitive methods we are able to prepare well-defined Si(100) surfaces with 0.1°, 2° and 6° offcut, which are suitable for subsequent low defect III-V epilayers. Annealing of Si(100) surfaces in As ambient leads to As incorporation into near-surface layers, as was confirmed by XPS measurements. As-modified Si(100) 0.1° surface is prepared by fast cooling down in background As_x at reduced pressure (100 mbar). The interaction between the Si(100) 2° surface and TBAs precursor leads to an A-type Si(100):As surface. In case of Si(100) 6° we can control prevalence of the majority domain on the surface in dependence of the As source and cooling procedure. Cooling down in background As_x leads to Si(100):As 6° B-type surface (dimers are oriented parallel to the step edge), while additional annealing in TBAs (AsH₃) and subsequent annealing in background As_x at 850 °C leads to an A-type surface (dimers are oriented perpendicular to the step edge). By controlling the dimer orientation on the As-modified Si(100) 6° we are able to control sublattice orientation of subsequently grown GaP(100).

Annealing in P-rich ambient of Si(100) surface leads to roughening and disorder of the surface. Therefore, (in an equivalent manner to As) an additional annealing in H₂ ambient at temperatures above 800 °C is necessary to re-order the surface reconstruction.

9 In-diffusion of phosphorus and arsenic into Si(111) and Si(100)

In this chapter we give an outline of our first experiments of P and As in-diffusion into homoepitaxial Si buffer layers. Parts of this chapter were published in Journal of Crystal Growth, *Ref.* [218].

9.1 Collector formation under different CVD conditions

Here, we used p-type Si(100) substrates with 2° offcut towards [011] direction and p-type Si(111) with 3° offcut towards $[\bar{1}\bar{1}2]$. After thermal deoxidation, a nominally intrinsic homoepitaxial Si buffer was grown (~ 200 nm) and the preferentially (1x2) reconstructed, monohydride-terminated Si(100) surface was prepared (for details see subchapter 5). The process was controlled *in situ* by RAS, and the Si(111) sample was prepared in the same process. The samples were annealed in TBP or TBAs, at 650°C and 670°C respectively, for group-V in-diffusion.

We investigated the in-diffusion in dependence of duration, precursor source and reactor pressure. Collectors in the Si sub-cell with a thickness less than $0.25\ \mu\text{m}$ and high doping level concentration ($> 5 \cdot 10^{18}\ \text{cm}^{-3}$) should ensure a high short circuit current density and open circuit voltage [233]. Figure 9.1 shows the free carrier concentration profiles measured by ECV (see subchapter 3.9) after P in-diffusion in Si(100) (a) and Si(111) (b) in dependence on process parameters. In general, we observe that annealing in TBP ambient creates a collector in the previously intrinsic Si buffer layer with doping concentrations as high as $10^{18} - 2.5 \cdot 10^{19}\ \text{cm}^{-3}$. The doping levels of all samples exhibit a flat plateau. The n-type region thickness is in the range between 120 nm to 450 nm in dependence on annealing time and reactor pressure. In comparison the collector thicknesses are greater in the case of Si(100) than in Si(111), except for the sample annealed for 10 min at 950 mbar with partial pressure ($p_{\text{TBP}} = 1.54$ mbar). In Si the (100) plane has a lower atomic packing density than the (111) plane, in consequence the mobility of dopant atoms is greater in [100] direction, resulting in thicker collector [234]. Longer annealing and lower reactor pressure increase the thickness of the collector. Reduction of the exposure time of the samples to TBP from 20 min (orange lines) to 10 min (blue lines) at a reactor pressure of 950 mbar (maintaining the same TBP-partial pressure, p_{TBP}) leads to reduced free carrier concentration levels, from $9 \cdot 10^{18}\ \text{cm}^{-3}$ to $1.5 \cdot 10^{18}\ \text{cm}^{-3}$ for Si(100) and from $2.5 \cdot 10^{19}\ \text{cm}^{-3}$ to $7 \cdot 10^{18}\ \text{cm}^{-3}$ for Si(100). In addition, in the case of Si(100) the longer annealing time of 20 min (orange line), leads to a larger

collector thickness of more than 250 nm as compared to that after 10 min of annealing (blue line) of 150 nm. In case of Si(100), the annealing in TBP at 950 mbar for 10 min at higher p_{TBP} (green line as compared to blue line) results in a higher free carrier concentration ($5 \cdot 10^{18} \text{ cm}^{-3}$ as compared to $1.5 \cdot 10^{18} \text{ cm}^{-3}$), while the collector thickness remains almost constant. This confirms that the collector thickness is limited by the exposure time to TBP and by the reactor pressure. The results are consistent considering molecular gas dynamics as the number of molecules impinging on a plane per unit area and time is proportional to the partial pressure of the precursor [130] (see subchapter 3.1, equation 19).

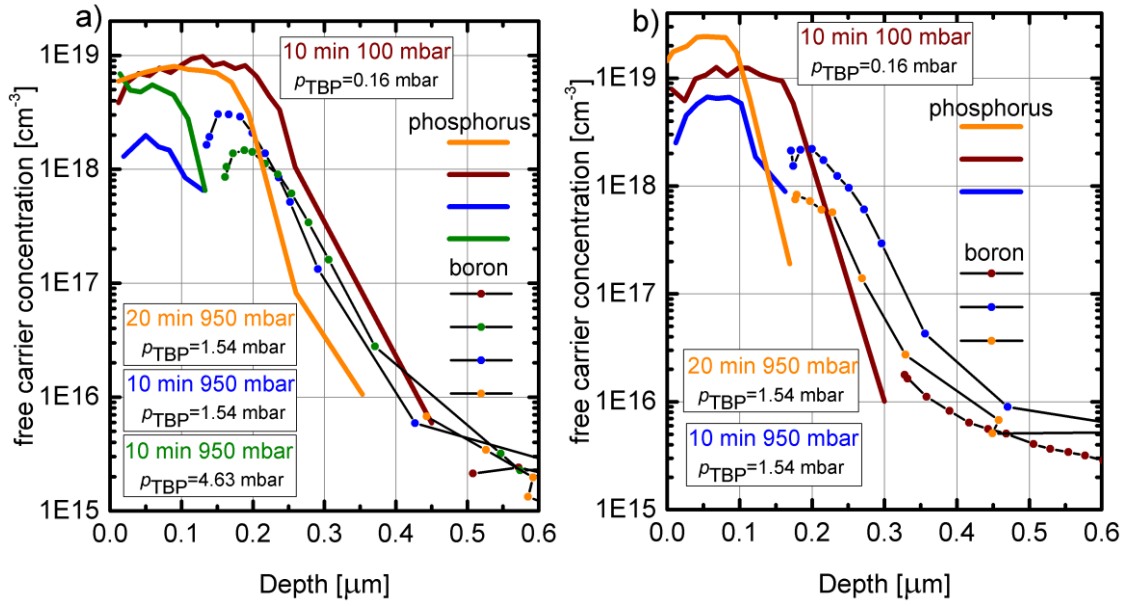


Fig. 9.1: Carrier concentrations in Si(100) (a) and Si(111) (b) after annealing in TBP under different process parameters.

Annealing in TBP at a reactor pressure of 100 mbar for 10 min (brown line) caused a higher free carrier concentration level as well as a larger collector thickness compared to an annealing procedure at 950 mbar for 20 min. Schofield *et al.* [235] found that P can substitute the top most Si atoms on the clean Si(100) surface. However, the authors observed that H on the Si(100) surface blocks the surface diffusion of P atoms and their incorporation into the Si(100) bulk material. Lower pressure or higher temperature in the CVD reactor can facilitate H-desorption and as a consequence P-adsorption to the surface up to temperatures where there is a disproportional P desorption from the Si surface. According to our estimations [66], the reduction of the pressure from 1000 mbar to 100 mbar at a temperature around 650 °C in a “clean” reactor does lead to a reduction of H coverage on the Si surface. This can explain the higher doping concentration and deeper collector region when P in-diffusion is performed at lower reactor pressures. For all samples, the level of the p-type doping concentration is observed to be higher near the collector than in the Si bulk. This can be caused by out-diffusion of boron from the substrate during the high temperature annealing step for thermal deoxidation. We confirmed identical behavior for Si samples that were only deoxidized thermally without

precursor supply and any further processing (not shown here). Moreover, the mobility of boron in Si is considered to be higher than that of phosphorus or arsenic due to its smaller atomic radius. It is important to note however, that the difference in the effective diffusion constants between B and P or As becomes less significant at high temperatures due to Si lattice vibration [234].

In analogy to P in-diffusion, Fig. 9.1 shows the doping concentration for Si(100) (a) and Si(111) (b) after annealing in TBAs at 670 °C for 20 min at 950 mbar H₂ pressure (red dash-dotted line), in comparison to the collectors formed by P in-diffusion (orange line, TBP open for 20 min at 650 °C and 950 mbar H₂ pressure). In both samples, the free carrier concentration of the n-type region formed by As in-diffusion is not significantly lower than the one formed by P in-diffusion, even though the TBAs partial pressure was less than half of the TBP partial pressure ($p_{\text{TBAAs}} = 0.64$ mbar versus $p_{\text{TBP}} = 1.54$ mbar). As in the case for the collectors doped by P, the free carrier concentration levels exhibit a plateau (Fig. 9.2, red line).

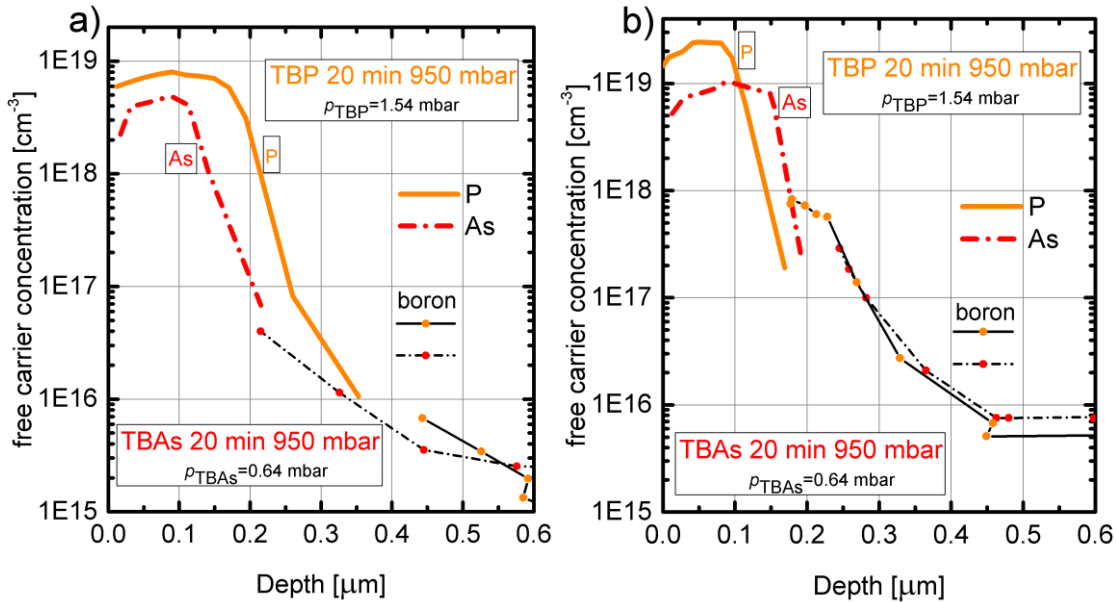


Fig. 9.2: Carrier concentrations in Si(100) (a) and Si(111) (b) after annealing in TBAs at 670 °C for 20 min, at 950 mbar (red line), in comparison to the samples annealed in TBP (orange line).

The *in situ* RA spectra from Si(100) surfaces after the collector formation step indicate a disordered Si surface (see chapter 8). Subsequent III-V growth would result in epilayers of poor crystal quality. Therefore, additional annealing in H₂ without precursor supply at 830 °C (P) and 850 °C (As, [216]) for around 2 min was applied to desorb excess atoms and precursor residuals from the surface and to obtain an atomically ordered surface during subsequent cooling. The process was controlled by *in situ* RAS and is described in detail in subchapter 8.4 for the case of annealing in TBP. Figure 9.3 compares the corresponding carrier concentration profiles (P-doped Si(100) and Si(111) collector, orange dashed line in (a) and (b), respectively, and As-doped Si(100) and Si(111)

collectors, red dashed line in (c) and (d), respectively). The levels of free carrier concentration of collectors formed by P or As in-diffusion in Si(100) (Figs. 9.3 (a) and (c)) after additional annealing is equal to the concentration levels before the annealing procedures and both profiles exhibit a rather flat plateau. The collector thickness after annealing in H_2 is thinner for the P-doped material (Fig. 9.3 (a)) and thicker for the As-doped collector (Fig. 9.3 (c)) compared to the corresponding thickness before annealing. In case of Si(111), the doping levels and collector thickness after additional annealing (dashed lines) are lower and thinner compared to the values before the annealing steps (solid lines).

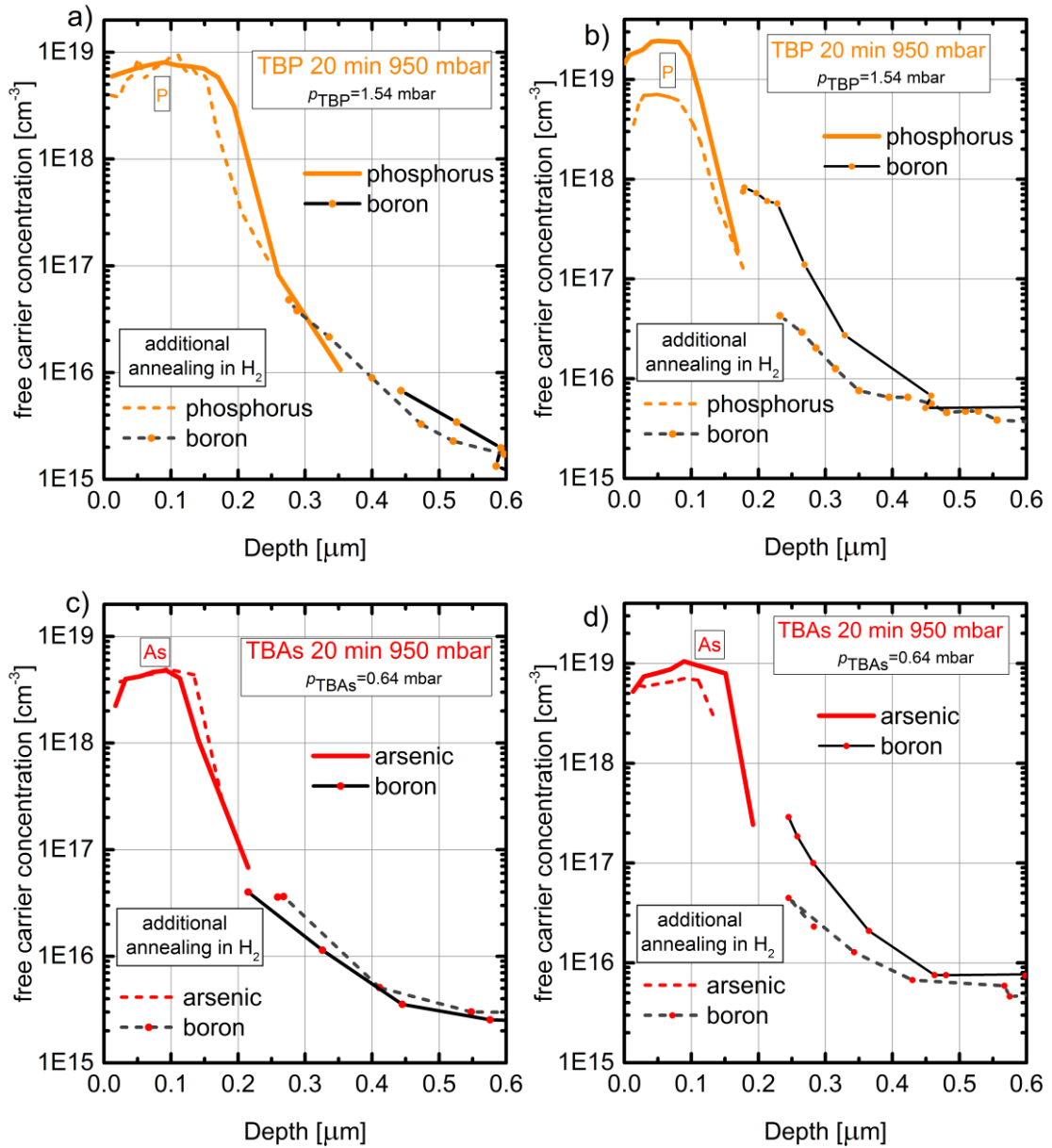


Figure 9.3: Carrier concentrations in Si(100) (a and c) and Si(111) (b and d). (a) and (b) – collector formed by P in-diffusion, (c) and (d) – collector formed by As in-diffusion. The dash-dotted line indicates collector after additional annealing in H_2 at 850 °C, without precursor supply.

An additional step of annealing under H_2 at high temperatures is known to redistribute dopants in the silicon film, which leads to a lower level of doping concentration and thus a deeper collector profile [236]. However, based on the doping profiles in Fig. 9.3 we can exclude this process for all samples except the As-doped collector in Si(100) (Fig. 9.3 (c)). The reduction of the doping concentration and the thickness of the collectors are probably caused by out-diffusion of the dopant.

It was shown in the literature that the free carrier concentration level profiles are very comparable with the doping level concentration obtained by secondary ion mass spectrometry (SIMS) measurements [46,236]. However, to understand the in-diffusion process it is very important to define the exact dopant concentration in the Si, and to exclude any other unintentional doping or contamination, which could influence the p-n junction performance.

9.2 Surface morphology

Morphologies of all surfaces before and after additional annealing in H_2 were measured by AFM. Figure 9.4 shows AFM images of Si(100) and Si(111) after annealing in TBP without (left hand side) and with (right hand side) additional annealing in H_2 .

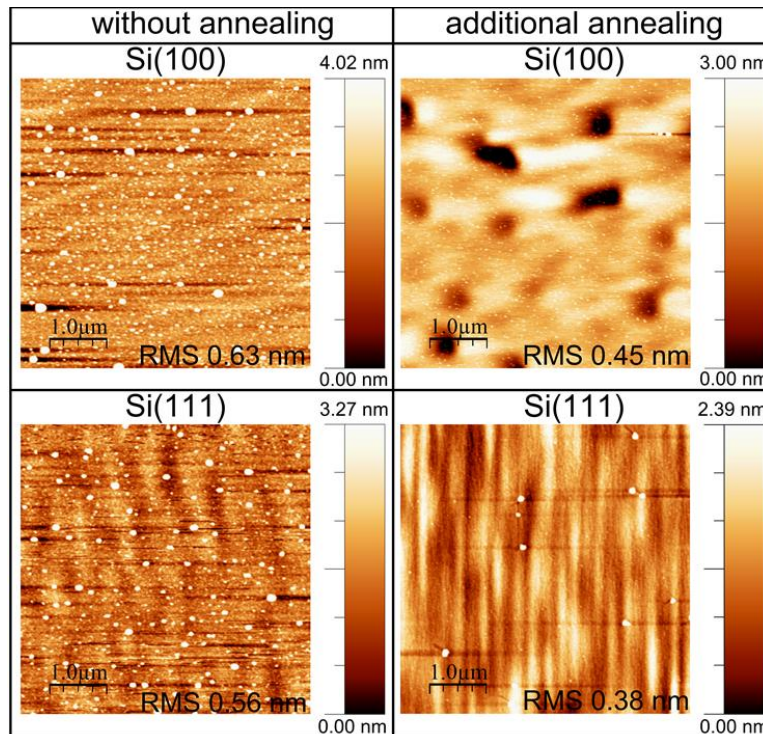


Fig. 9.4: AFM scans of Si surfaces after annealing in TBP (20 min 650 °C), without (left hand side) and with (right hand side) additional annealing in H_2 , without precursor supply for Si(100) (top row) and Si(111) (bottom row). White spots visible on all surfaces are P droplets, as indicated by EDX.

The white spots visible on the surface are found to be phosphorus as confirmed by EDX. On both surfaces, the amount of phosphorus before annealing is much higher than after annealing. The RMS roughness of both surfaces is lower after additional annealing in H_2 ambient. Similarly, the RMS roughness for both Si surfaces is decreased by subsequent annealing in H_2 after As in-diffusion (as given in Tab. 9.5), most prominently for Si(100). This already indicates a recovery of the surface morphology due to the annealing procedures in hydrogen, as will be confirmed by *in situ* measurements (subchapter 8.4 or Ref. [216,236]).

RMS [nm]	Si(111)		Si(100)	
	TBAs	TBP	TBAs	TBP
w/o additional annealing	0.68	0.80	1.05	0.66
additional annealing	0.45	0.39	0.28	0.50

Table 9.5: the RMS roughness for Si(111) and Si(100).

9.3 Current-voltage characteristic

To investigate the I-V characteristic on selected samples, we deposited back contacts from aluminum 100 nm (Al), and front contact from titanium 10 nm (Ti) and gold 100 nm (Au)¹⁴. Titanium forms a low-resistance ohmic contact to semiconductor surfaces and has excellent adherence [237], while gold has excellent bonding characteristics and resistance to corrosion. The exact dimensions of the contacts were adjusted to an average Si sample size and are shown on Fig. 9.6: (a) Ti/Au front contact, (b) Al back contact. To reduce the resistance of the contact, each side of the sample was annealed at 350 °C for one minute [238].

The current-voltage (I-V) measurements of solar cells were recorded with a Keithley 2400 Source Measure Unit using a solar simulator (Solar Light, XPS 400). The I-V characteristic was measured without any passivation or antireflection layer. The maximum efficiency was equal to 5.8 % and was obtained for Si(100) with collector formed by annealing in TBP for 20 min at 950 mbar. From the shape of all measured I-V characteristics, we conclude that we can have an impact from the series (R_S) and possibly from shunt resistance (R_{SH}). The series resistance is caused by an additional resistance between the metal contacts and the cell and the movement of current through the collector. Other annealing temperatures of the contacts must be tested. The shunt resistance indicates defects in the bulk.

¹⁴ The contacts were deposited by electron beam evaporation by Joachim Döll and Marek Duda at TU Ilmenau.

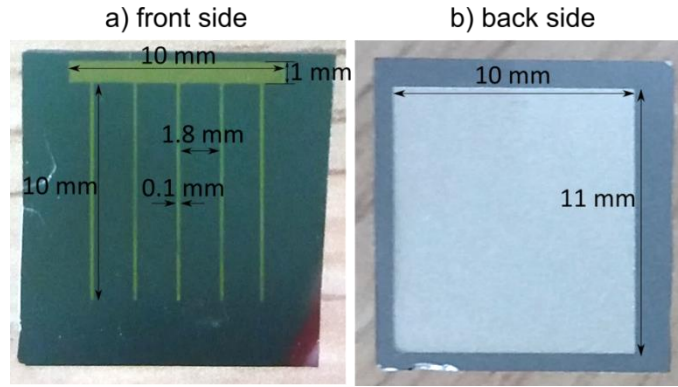


Fig. 9.6: (a) Ti/Au front and (b) Al back contact on the Si sample.

The influence of the R_s on the solar cell efficiency was confirmed by a Suns- V_{OC} measurement¹⁵ [239] on the Si(100) substrate with a collector formed by annealing in TBP for 20 min at 950 mbar. On this sample only back Al contact was deposited. In the Suns- V_{OC} measurement, the samples are illuminated by a slowly decaying flash lamp, while their open-circuit voltage (V_{OC}) is measured [239]. A sharp probe is utilized as a required crude contact to the doped region [239]. To obtain a pseudo-IV curve, the light intensity is associated with an implied current density [239,240]. The pseudo-IV curves from the Suns- V_{OC} method solely reflect the generation and recombination processes. Since there is no current flowing during a Suns- V_{OC} measurement, the series resistance of the cell does not affect the pseudo-JV curve [239,240]. The measured Si(100) sample showed 11.6 % efficiency ($I_{SC} = 28$ mA, $V_{OC} = 0.525$ V).

9.4 Summary of this chapter

We demonstrate the *in situ* MOCVD preparation of silicon p-n junctions by annealing of intrinsic homoepitaxial Si buffers grown on p-Si(100) and p-Si(111) in the presence of the group-V precursors TBP or TBAs. While the precursor source only affects the carrier concentration, the duration of the annealing and the reactor pressure strongly impact the collector thickness. Doping concentrations in the order of 10^{19} cm^{-3} with rather flat plateaus were achieved both for P and As in-diffusion. Annealing of the Si surface in the presence of the precursor results in a disordered surface. Subsequent annealing without precursor supply leads to atomically well-ordered, smooth Si(100) surfaces with prevailing (1x2) surface reconstruction, suitable for III-V nucleation while largely maintaining the previous doping levels. The I-V characteristic shows that the p-n junction is active, however further investigations must be done to improve the device performance.

¹⁵ The Suns- V_{OC} measurement was done at CiS Forschungsinstitut für Mikrosensorik GmbH in Erfurt by Dr. Kevin Lauer.

10 Conclusion

III-V integration on Si microelectronics promises not only high-efficiency multijunction solar cells but also a new generation of high performance optoelectronic devices. Silicon benefits from its mature technology and exhibits a bandgap which is close to optimum for the bottom cell in tandem solar absorber configurations. Research shown in this work focused on: (i) GaP heteroepitaxy to obtain virtual substrates suitable for the integration of planar or nanowire-based III-V structures in MOCVD ambient, (ii) the in-diffusion of dopants from group-V precursors (in particular TBP and TBAs) into Si(100) and Si(111) substrates in order to form an active Si bottom cell, and (iii) the impact of the in-diffusion process on the Si surface structure. This study shows the significance of the interface between Si and GaP and its impact on the polarity of GaP(111) and the sublattice orientation of GaP(100) epilayers.

Structural defects in the III-V layers, such as antiphase disorder in GaP/Si(100) or rotational twin domains in GaP/Si(111), may be induced at the buried heterointerface. They can drastically reduce the carrier lifetime in the final device structure and thereby the photovoltaic conversion efficiency. Therefore, precise control over the interface and surface formation is crucial during heteroepitaxy of GaP on Si. The Si(111) surface structure and Si(100) interaction with arsenic is well known, but is mostly limited to studies in UHV where no carrier gas is present. Growth processes in MOCVD environment are highly complex: the process gas strongly interacts with the semiconductor surface and the parameter space is huge (such as substrate temperature, reactor pressure, molar fractions of the precursors, their cracking efficiency and total gas flow). Moreover, residues from earlier deposited material might interact with the Si surface and there is a strong competition between energetically and kinetically driven processes. In addition, presence of a process gas in the MOCVD reactor limits the access to the UHV-based surface science analysis. To monitor and investigate the Si surface during such complex processing in CVD ambient, an *in situ* optical spectroscopy was applied. The unique possibility of transferring the MOCVD-prepared surfaces to UHV allows us to establish RA spectra of different Si surfaces by benchmarking the RAS signals to results from complementary UHV-based surface-sensitive methods.

The novelty of the performed research is the verification of the sensitivity of RAS to the dimer orientation on As-modified Si(100) and to the step structure on H- or As-terminated Si(111) surfaces. Further, the application of *in situ* RAS control enables to recover smooth epi-ready Si(100) surfaces after in-diffusion of P or As into Si. Finally, it is shown that the GaP(111) polarity and GaP(100) sublattice orientation can be controlled in dependence on surface preparation of Si(111) and Si(100), respectively. The following paragraphs conclude on these results, which were obtained in this work, in more detail.

Hydrogen- and arsenic-terminated Si(111) surfaces in CVD ambient were studied. The various XPS measurements confirmed that high-temperature annealing at 1000 °C for 30 min at a reactor pressure of 950 mbar in “clean” H₂ ambient reliably removes oxides and other contamination of the Si(111) surface (within the detection limit of XPS). FTIR measurements confirmed that the interaction between hydrogen and the Si(111) surface leads to hydride termination. In particular, it was found that monohydride bonds are on the terraces, which agrees with the well-ordered (1×1) surface reconstruction confirmed by LEED and STM scans. It was demonstrated that wet-chemical pretreatment of the Si substrates and subsequent homoepitaxy improves the surface morphology: the Si surface roughness is decreased, no step bunching is visible, and terraces are evenly spaced. While Si(111) 0° surfaces show no reflection anisotropy, Si(111) surfaces with well-defined offcut directions yield characteristic RA spectra. The observed RA spectra in the case of Si(111) with offcut in $[11\bar{2}]$ direction arise from (110)-planes from the steps, which is in agreement with the literature. In the case of Si(111) with offcut in $[\bar{1}\bar{1}2]$, the RAS line shape indicates contributions from dihydrides on the steps. However, the exact origin of the RA remains unclear and additional STM measurements are envisaged to benchmark the RAS signal to the step structure resolved with atomic resolution.

Annealing in TBAs leads to As-termination of the Si(111) surface, as evidenced by XPS and FTIR measurements. LEED patterns from the Si(111):As surface reveal a (1×1) surface reconstruction. RA spectra of Si(111) with offcut in $[\bar{1}\bar{1}2]$ direction obtained after deoxidation in As-ambient and also after As termination differ from the RA spectra of As-free surfaces. This characteristic change in the RA spectra indicates a change in the step structure on the surface, which is possibly caused by a reaction of As with the Si atoms situated at the step edges.

GaP(111) surfaces, which were processed in H₂ ambient, exhibit (2×2) and (1×1) surface reconstruction for A-type and B-type polarity, respectively. These different surface reconstructions were used as a benchmark for the polarity of GaP epilayers grown on Si(111). Further, the control over the polarity of heteroepitaxially grown GaP layers on Si(111) is shown: the H-terminated Si(111) surface leads to GaP with A-type polarity, while GaP grown on the Si(111) surface terminated with As results in B-type polarity. The latter one is required to enable vertical GaAs NW growth on GaP/Si(111) quasi-substrates. Theoretical and experimental investigations of the GaP/Si(111):As interface would be desirable in order to clarify the atomic structure of the interface with respect to the possibility of intermixing of the III-V material and the Si substrate. In addition, it is shown that the morphology of the GaP nucleation layer strongly depends on the Si(111) offcut direction, in particular on the Si(111) step structure after the As termination.

Regarding the Si(100) preparation in As ambient, it is demonstrated that the sensitivity of RAS to the dimer orientation of As-modified Si(100) surfaces enables *in situ* control over the interaction of As with the Si surface. This work showed preparation of well-defined Si(100) surfaces with 0.1°, 2° and 6° offcut, which are suitable for subsequent III-V epilayers with low defect density. Annealing of Si(100) surfaces in As ambient leads to

As incorporation into near-surface layers, as was confirmed by XPS measurements. As-modified Si(100) 0.1° surfaces were prepared by fast cooling in presence of background As_x species at reduced pressure (100 mbar). The interaction between the Si(100) 2° surface and the TBAs precursor leads to an A-type Si(100):As surface. In the case of Si(100) with 6° offcut, *in situ* RAS enabled control over the prevalence of the majority dimer orientation on the surface, which can be chosen in dependence of the As source and cooling procedure. Cooling in the presence of background As_x species leads to Si(100):As 6° B-type surfaces (where dimers are oriented parallel to the step edge), while additional annealing in TBAs and subsequent annealing in background As_x at 850 °C leads to an A-type surface (where dimers are oriented perpendicular to the step edge). The sublattice orientation of subsequently grown GaP epilayers can be controlled via the dimer orientation on the As-modified Si(100) 6° surface. Quantitative analysis of the RA spectra of the GaP/Si(100):As epilayers confirms almost single domain layers for both orientations.

This work investigated *in situ* P and As in-diffusion into silicon in dependence on (i) duration and temperature of the annealing step, (ii) the precursor source, (iii) reactor pressure and (iv) post diffusion annealing. Sufficiently high P and As doping levels with a wide plateau in the depth profile could be achieved. While the precursor source only affects the carrier concentration, the duration of the annealing and the reactor pressure strongly impact the thickness of the collector. Annealing of the Si surfaces in presence of the precursor results in surface roughening and a disordered surface. Subsequent annealing in H₂ without precursor supply reduces the roughness of the Si surfaces and the amount of excess phosphorus on the surface. The additional annealing step does not drastically reduce the collector doping level or the thickness. The I-V characteristic shows that the p-n junction is active, however further investigations must be performed to improve the device performance.

The work presented in this thesis opens the opportunity to establish MOCVD processing of planar and NW-based III-V solar cells on active Si bottom cells with well-defined heterointerfaces. For advanced NW-based devices, further research regarding the exact step structure on Si(111):As substrates is necessary to understand its impact on structural defects in the GaP(111) layers and subsequently grown NW structures. The *in situ* RAS investigations of the As-modified Si(100) surfaces provide a sound basis for further studies of the atomic interface structures relevant for planar photovoltaic devices. Future work will also focus on improvement of the ohmic contacts for the Si bottom cell and precise IV characterization of the Si p-n junctions in order to maximize the possible efficiency.

Bibliography

- [1] M. I. Hoffert, K. Caldeira, A. K. Jain, E. F. Haites, L. D. D. Harvey, S. D. Potter, M. E. Schlesinger, S. H. Schneider, R. G. Watts, T. M. L. Wigley, and D. J. Wuebbles, "Energy implications of future stabilization of atmospheric CO₂ content," *Lett. to Nat.*, vol. 395, no. October, p. 881, 1998.
- [2] N. Nakicenovic, J. Alcamo, G. Davis, B. de Vries, J. Fenhann, S. Gaffin, K. Gregory, A. Gruebler, T. Yong Jung, T. Kram, E. L. La Rovere, L. Michaelis, S. Mori, T. Morita, W. Pepper, H. Pitcher, L. Price, K. Riahi, A. Roehrl, H. H. Rogner, A. Sankovski, M. Schlesinger, P. Shukla, S. Smith, R. Swart, S. van Rooijen, N. Victor, and Z. Dadi, *Special report on Emissions Scenarios*. Cambridge University Press, 2000.
- [3] J. W. Wallace and P. V. Hobbs, *Atmospheric Science: An Introductory Survey*. Academic Press, San Diego, 1977.
- [4] G. Carr, "Sunny uplands: Alternative energy will no longer be alternative," *The Economist*, 2012.
- [5] W. Shockley and H. J. Queisser, "Detailed balance limit of efficiency of p-n junction solar cells," *J. Appl. Phys.*, vol. 32, no. 3, p. 510, 1961.
- [6] C. H. Henry, "Limiting efficiencies of ideal single and multiple energy gap terrestrial solar cells," *J. Appl. Phys.*, vol. 51, no. 8, p. 4494, 1980.
- [7] L. Vegard, "Die Konstitution der Mischkristalle und die Raumfüllung der Atome," *Zeitschrift für Phys.*, vol. 5, p. 17, 1921.
- [8] T. N. D. Tibbits, P. Beutel, M. Grave, C. Karcher, E. Oliva, G. Siefer, A. Wekkeli, M. Schachtner, F. Dimroth, A. W. Bett, R. Krause, M. Piccin, N. Blanc, M. Muñoz-Rico, C. Arena, E. Guiot, C. Charles-Alfred, C. Drazek, F. Janin, L. Farrugia, B. Hoarau, J. Wasselin, A. Tauzin, T. Signamarcheix, T. Hannappel, K. Schwarzburg, and A. Dobrich, "New efficiency frontiers with wafer-bonded multi-junction solar cells," *Proc. Eur. Photovolt. Sol. Energy Conf. Exhib.*, vol. 29, no. September, p. 1975, 2014.
- [9] G. B. Stringfellow, *Organometallic vapor-phase epitaxy: Theory and practice*. Academic Press, San Diego, 1989.
- [10] E.-K. Badih and L. N. Hutter, *Silicon Analog Components. Device Design, Process Integration, Characterization, and Reliability*. Springer-Verlag New York, 2015.
- [11] H. Kroemer, "Polar-on-nonpolar epitaxy," *J. Cryst. Growth*, vol. 81, p. 193, 1987.
- [12] A. De Vos, "Detailed balance limit of the efficiency of tandem solar cells," *J. Phys. D Appl. Phys.*, no. 13, p. 839, 1980.
- [13] M. W. Larsson, J. B. Wagner, M. Wallin, P. Håkansson, L. E. Fröberg, L. Samuelson, and L. R. Wallenberg, "Strain mapping in free-standing heterostructured wurtzite InAs/InP nanowires," *Nanotechnology*, vol. 18, no. 1, p. 015504, 2007.
- [14] M. Heurlin, M. H. Magnusson, D. Lindgren, M. Ek, L. R. Wallenberg, K. Deppert, and L. Samuelson, "Continuous gas-phase synthesis of nanowires with tunable properties," *Nature*, vol. 492, no. 7427, p. 90, 2012.
- [15] R. S. Wagner and W. C. Ellis, "Vapor-liquid-solid mechanism of single crystal growth," *Appl. Phys. Lett.*, vol. 4, no. 5, p. 89, 1964.
- [16] A. Suzuki, T. Mori, A. Fukuyama, T. Ikari, J.-H. Paek, and M. Yamaguchi, "Effect of silicon doping on the photoluminescence and photoreflectance spectra of catalyst-free

- molecular beam epitaxy–vapor liquid solid grown GaAs nanowires on (111)Si substrate,” *Jpn. J. Appl. Phys.*, vol. 50, no. 6, p. 06GH08, 2011.
- [17] E. Piscopiello, L. Tapfer, M. Antisari, P. Paiano, P. Prete, and N. Lovergine, “Formation of epitaxial gold nanoislands on (100) silicon,” *Phys. Rev. B*, vol. 78, no. 3, p. 035305, 2008.
 - [18] S. F. Fang, K. Adomi, S. Iyer, H. Morkoç, H. Zabel, C. Choi, and N. Otsuka, “Gallium arsenide and other compound semiconductors on silicon,” *J. Appl. Phys.*, vol. 68, no. 7, p. R31, 1990.
 - [19] E. I. Givargizov, “Fundamental aspects of VLS growth,” *J. Cryst. Growth*, vol. 31, p. 20, 1975.
 - [20] O. Supplie, S. Brückner, O. Romanyuk, H. Döscher, C. Höhn, M. M. May, P. Kleinschmidt, F. Grosse, and T. Hannappel, “Atomic scale analysis of the GaP/Si(100) heterointerface by in situ reflection anisotropy spectroscopy and ab initio density functional theory,” *Phys. Rev. B*, vol. 90, no. 23, p. 235301.1, 2014.
 - [21] H. Döscher, T. Hannappel, B. Kunert, A. Beyer, K. Volz, and W. Stolz, “In situ verification of single-domain III-V on Si(100) growth via metal-organic vapor phase epitaxy,” *Appl. Phys. Lett.*, vol. 93, no. 17, p. 172110, 2008.
 - [22] A. Beyer, J. Ohlmann, S. Liebich, H. Heim, G. Witte, W. Stolz, and K. Volz, “GaP heteroepitaxy on Si(001): Correlation of Si-surface structure, GaP growth conditions, and Si-III/V interface structure,” *J. Appl. Phys.*, vol. 111, no. 8, p. 083534, 2012.
 - [23] A. Beyer, I. Németh, S. Liebich, J. Ohlmann, W. Stolz, and K. Volz, “Influence of crystal polarity on crystal defects in GaP grown on exact Si (001),” *J. Appl. Phys.*, vol. 109, no. 8, p. 083529, 2011.
 - [24] H. Döscher, B. Kunert, A. Beyer, O. Supplie, K. Volz, W. Stolz, and T. Hannappel, “In situ antiphase domain quantification applied on heteroepitaxial GaP growth on Si(100),” *J. Vac. Sci. Technol. B Microelectron. Nanom. Struct.*, vol. 28, no. 4, p. C5H1, 2010.
 - [25] T. J. Grassman, J. A. Carlin, B. Galiana, L.-M. Yang, F. Yang, M. J. Mills, and S. A. Ringel, “Nucleation-related defect-free GaP/Si(100) heteroepitaxy via metal-organic chemical vapor deposition,” *Appl. Phys. Lett.*, vol. 102, no. 14, p. 142102, 2013.
 - [26] J. D. E. McIntyre and D. E. Aspens, “Differential reflection spectroscopy of very thin surface films,” *Surf. Sci.*, vol. 24, p. 417, 1971.
 - [27] T. Hannappel, S. Visbeck, L. Töben, and F. Willig, “Apparatus for investigating metalorganic chemical vapor deposition-grown semiconductors with ultrahigh-vacuum based techniques,” *Rev. Sci. Instrum.*, vol. 75, no. 5, p. 1297, 2004.
 - [28] A. E. Becquerel, “Recherches sur les effets de la radiation chimique de la lumiere solaire au moyen des courants electriques,” *Comptes Rendus L’Academie des Sci.*, no. 9, p. 145, 1839.
 - [29] W. G. Adams and R. E. Day, “The action of light on selenium,” *Proc. R. Soc. London*, vol. 25, p. 113, 1877.
 - [30] K. Masuko, M. Shigematsu, T. Hashiguchi, D. Fujishima, M. Kai, Y. Naoki, T. Yamaguchi, Y. Ichihashi, T. Mishima, N. Matsubara, T. Yamanishi, T. Takahama, M. Taguchi, E. Maruyama, and S. Okamoto, “Achievement of more than 25 % conversion heterojunction solar cell,” *IEEE J. photovoltaics*, vol. 4, no. 6, p. 1433, 2014.
 - [31] I. Vurgaftman, J. R. Meyer, and L. R. Ram-Mohan, “Band parameters for III–V compound semiconductors and their alloys,” *J. Appl. Phys.*, vol. 89, no. 11, p. 5815, 2001.
 - [32] S. P. Bremner, M. Y. Levy, and C. B. Honsberg, “Analysis of tandem solar cell efficiencies under AM1 .5G spectrum using a rapid flux calculation method,” *Prog. Photovoltaics Res. Appl.*, vol. 16, p. 225, 2008.

- [33] J. F. Geisz, M. A. Steiner, I. García, S. R. Kurtz, and D. J. Friedman, "Enhanced external radiative efficiency for 20.8% efficient single-junction GaInP solar cells," *Appl. Phys. Lett.*, vol. 103, no. 4, p. 041118, 2013.
- [34] P. P. Nayak, J. P. Dutta, and G. P. Mishra, "Efficient InGaP/GaAs DJ solar cell with double back surface field layer," *Eng. Sci. Technol. an Int. J.*, vol. 18, no. 3, p. 325, 2015.
- [35] T. Takamoto, E. Ikeda, H. Kurita, and M. Ohmori, "Over 30% efficient InGaP/GaAs tandem solar cells," *Appl. Phys. Lett.*, vol. 70, no. 3, p. 381, 1997.
- [36] D. J. Friedman, J. F. Geisz, S. R. Kurtz, and J. M. Olson, "1-eV GaInNAs solar cells for ultrahigh-efficiency multijunction devices," *2nd World Conf. Exhib. Photovolt. Sol. Energy Convers.*, no. July, p. 3, 1998.
- [37] W. E. McMahon, S. Kum, K. Emery, and M. S. Young, "Criteria for the design of GaInP/GaAs/Ge triple-junction cells to optimize their performance outdoors," *Photovolt. Spec. Conf. 2002. Conf. Rec. Twenty-Ninth IEEE*, p. 931, 2002.
- [38] R. R. King, D. C. Law, K. M. Edmondson, C. M. Fetzer, G. S. Kinsey, H. Yoon, R. A. Sherif, and N. H. Karam, "40% efficient metamorphic GaInP/GaInAs/Ge multijunction solar cells," *Appl. Phys. Lett.*, vol. 90, no. 18, p. 183516, 2007.
- [39] S. R. Kurtz, D. Myers, and J. M. Olson, "Projected performance of three- and four-junction devices using GaAs and GaInP," *26th IEEE Photovolt. Spec. Conf.*, no. September, p. 875, 1997.
- [40] J. F. Geisz, D. J. Friedman, J. M. Olson, S. R. Kurtz, and B. M. Keyes, "Photocurrent of 1 eV GaInNAs lattice-matched to GaAs," *J. Cryst. Growth*, vol. 195, p. 401, 1998.
- [41] C. Kost, J. N. Mayer, J. Thomsen, N. Hartmann, C. Senkpiel, S. Philipps, S. Nold, S. Lude, N. Saad, and T. Schlegel, "Levelized cost of electricity - renewable energy technologies," *report; Fraunhofer Inst. Sol. energy Syst. ISE*, 2013.
- [42] H. Döscher, O. Supplie, M. M. May, P. Sippel, C. Heine, A. G. Muñoz, R. Eichberger, H.-J. Lewerenz, and T. Hannappel, "Epitaxial III-V films and surfaces for photoelectrocatalysis," *Chemphyschem*, vol. 13, no. 12, p. 2899, 2012.
- [43] S. Essig, S. Ward, M. A. Steiner, D. J. Friedman, J. F. Geisz, P. Stradins, and D. L. Young, "Progress towards a 30% efficient GaInP/Si tandem solar cell," *Energy Procedia*, vol. 77, p. 464, 2015.
- [44] M. Feifel, T. Rachow, J. Benick, J. Ohlmann, S. Janz, M. Hermle, F. Dimroth, and D. Lackner, "Gallium Phosphide Window Layer for Silicon Solar Cells," *IEEE J. Photovoltaics*, vol. 6, no. 1, p. 384, 2016.
- [45] H. Wagner, T. Ohrdes, A. Dastgheib-Shirazi, B. Puthen-Vettil, D. König, and P. P. Altermatt, "A numerical simulation study of gallium-phosphide/silicon heterojunction passivated emitter and rear solar cells," *J. Appl. Phys.*, vol. 115, no. 4, p. 044508, 2014.
- [46] S. A. Ringel, J. A. Carlin, T. J. Grassman, B. Galiana, A. M. Carlin, C. Ratcliff, D. Chmielewski, L. Yang, M. J. Mills, A. Mansouri, S. P. Bremner, A. Ho-Baillie, X. Hao, H. Mehrvarz, G. Conibeer, and M. A. Green, "Ideal GaP/Si heterostructures grown by MOCVD: III-V/active-Si subcells, multijunctions, and MBE-to-MOCVD III-V/Si interface science," in *2013 IEEE 39th Photovoltaic Specialists Conference (PVSC)*, 2013, p. 3383.
- [47] J. R. Lang, J. Faucher, S. Tomasulo, K. Nay Yaung, and M. Larry Lee, "Comparison of GaAsP solar cells on GaP and GaP/Si," *Appl. Phys. Lett.*, vol. 103, no. 9, p. 092102.1, 2013.
- [48] E. E. Beck, A. E. Blakeslee, and T. A. Gessert, "Application of GaP/Si heteroepitaxy to cascade solar cells," *Sol. cells*, vol. 24, p. 205, 1988.
- [49] E. García-Tabarés, I. García, I. Rey-Stolle, C. Algora, and D. Martín, "Integration of III-V Materials on Silicon Substrates for Multi-junction Solar Cell Applications," *Proc. 8th*

- Spanish Conf. Electron Devices, CDE'2011*, p. 1, 2011.
- [50] R. K. Ahrenkiel, M. M. Al-Jassim, B. Keyes, D. Dunlavy, K. M. Jones, S. M. Veron, and T. M. Dixon, "Minority carrier lifetime of GaAs on silicon," *J. Electrochem. Soc.*, vol. 137, no. 3, p. 996, 1990.
 - [51] J. F. Geisz, J. M. Olson, D. J. Friedman, K. M. Jones, R. C. Reedy, and M. J. Romero, "Lattice-matched GaNPAs-on-silicon tandem solar cells," *Conf. Rec. Thirty-first IEEE Photovolt. Spec.*, vol. 31, p. 695, 2005.
 - [52] T. G. Deutsch, C. A. Koval, and J. A. Turner, "III-V nitride epilayers for photoelectrochemical water splitting: GaPN and GaAsPN," *J. Phys. Chem. B*, vol. 110, no. 50, p. 25297, 2006.
 - [53] S. Hu, C. Xiang, S. Haussener, A. D. Berger, and N. S. Lewis, "An analysis of the optimal band gaps of light absorbers in integrated tandem photoelectrochemical water-splitting systems," *Energy Environ. Sci.*, vol. 6, no. 10, p. 2984, 2013.
 - [54] O. Supplie, M. M. May, H. Stange, C. Höhn, H.-J. Lewerenz, and T. Hannappel, "Materials for light-induced water splitting: In situ controlled surface preparation of GaPN epilayers grown lattice-matched on Si(100)," *J. Appl. Phys.*, vol. 115, no. 11, p. 113509, 2014.
 - [55] P. Würfel, *Physics of solar cells: From basic principles to advanced concepts*. Wiley, 2005.
 - [56] T. Markvart and L. Castañer, *Practical Handbook of Photovoltaics*. Elsevier Advanced Technology, 2003.
 - [57] C. Hu and R. M. White, *Solar cells: from basic to advanced systems*. McGraw-Hill, 1983, 1983.
 - [58] S. Panda, "Chapter: Semiconductor fundamentals," in *Microelectronics and Optoelectronics Technology*, University Science Press (Imprint - Laxmi Publications), 2009.
 - [59] S. W. Jones, *Diffusion in silicon*. IC Knowledge LCC, 2008.
 - [60] L. Nanu and A. G. R. Evans, "Phosphorus diffusion in silicon during rapid thermal annealing," *Semicond. Sci. Technol.*, vol. 4, p. 711, 1989.
 - [61] M. Yoshida, "General theory of phosphorus and arsenic diffusions in silicon," *Jpn. J. Appl. Phys.*, vol. 19, no. 12, p. 2427, 1980.
 - [62] M. Yoshida, "Diffusion of group V impurity in silicon," *Jpn. J. Appl. Phys.*, vol. 10, no. 6, p. 702, 1971.
 - [63] K. Momma and F. Iyumi, "VESTA 3 for three-dimensional visualization of crystal, volumetric and morphology data," *J. Appl. Crystallogr.*, vol. 44, no. 6, p. 1272, 2011.
 - [64] R. E. Schlier and H. E. Farnsworth, "Structure and adsorption characteristics of clean surfaces of germanium and silicon," *J. Chem. Phys.*, vol. 30, no. 4, p. 917, 1959.
 - [65] J. A. Appelbaum, G. A. Baraff, and D. R. Hamann, "The Si (100) surface. III. Surface reconstruction," *Phys. Rev. B*, vol. 14, no. 2, p. 588, 1976.
 - [66] S. Brückner, O. Supplie, A. Dobrich, P. Kleinschmidt, and T. Hannappel, "Control over dimer orientations on vicinal Si(100) surfaces in hydrogen ambient: Kinetics vs. energetics," *Phys. Status Solidi*, vol. 255, no. 4, p. 1700493, 2017.
 - [67] J. Dąbrowski and H. J. Müssig, *Silicon Surfaces and Formation of Interfaces: Basic Science in the Industrial World*. World Scientific Publishing Co. Pte. Ltd., 2000.
 - [68] H. Over, J. Wasserfall, W. Ranke, C. Ambiatello, R. Sawitzki, D. Wolf, and W. Moritz, "Surface atomic geometry of Si(001)-(2×1): A low-energy electron-diffraction structure

- analysis," *Phys. Rev. B*, vol. 55, no. 7, p. 4731, 1997.
- [69] J. J. Boland, "Structure of the H-saturated Si(100) surface," *Phys. Rev. Lett.*, vol. 65, no. 26, p. 3325, 1990.
 - [70] T. Komeda and Y. Kumagai, "Si (001) surface variation with annealing in ambient H₂," *Phys. Rev. B*, vol. 58, no. 3, p. 1385, 1998.
 - [71] A. Laracuente and L. . Whitman, "Step structures and energies on monohydride-terminated vicinal Si(001) surfaces," *Surf. Sci.*, vol. 476, no. 3, p. L247, 2001.
 - [72] D. J. Chadi, "Stabilities of single-layer and bilayer steps on Si(001) surfaces," *Phys. Rev. Lett.*, vol. 59, no. 15, p. 1691, 1987.
 - [73] J. E. Griffith, G. P. Kochanski, J. A. Kubby, and P. E. Wierenga, "Steps on Si(001)," *J. Vac. Sci. Technol. A*, vol. 7, no. 3, p. 1914, 1989.
 - [74] K. Kitahara and O. Ueda, "Observation of atomic structure by scanning tunneling microscopy of vicinal Si(100) surface annealed in hydrogen gas," *Jpn. J. Appl. Phys.*, vol. 33, no. Part 2, No. 11B, p. L1571, 1994.
 - [75] B. Kunert, I. Németh, S. Reinhard, K. Volz, and W. Stolz, "Si (001) surface preparation for the antiphase domain free heteroepitaxial growth of GaP on Si substrate," *Thin Solid Films*, vol. 517, no. 1, p. 140, 2008.
 - [76] H. Döscher, S. Brückner, A. Dobrich, C. Höhn, P. Kleinschmidt, and T. Hannappel, "Surface preparation of Si(100) by thermal oxide removal in a chemical vapor environment," *J. Cryst. Growth*, vol. 315, no. 1, p. 10, 2011.
 - [77] A. Dobrich, P. Kleinschmidt, H. Döscher, and T. Hannappel, "Quantitative investigation of hydrogen bonds on Si(100) surfaces prepared by vapor phase epitaxy," *J. Vac. Sci. Technol. B Microelectron. Nanom. Struct.*, vol. 29, no. 4, p. 04D114, 2011.
 - [78] S. Brückner, H. Döscher, P. Kleinschmidt, O. Supplie, A. Dobrich, and T. Hannappel, "Anomalous double-layer step formation on Si(100) in hydrogen process ambient," *Phys. Rev. B*, vol. 86, no. 19, p. 195310.1, 2012.
 - [79] G. Schulze and M. Henzler, "Adsorption of atomic hydrogen on clean cleaved silicon (111)," *Surf. Sci.*, vol. 124, p. 336, 1983.
 - [80] J. Abrefah and D. R. Olander, "Reaction of atomic hydrogen with crystalline silicon," *Surf. Sci.*, vol. 209, p. 291, 1989.
 - [81] F. Owman and P. Mårtensson, "STM study of Si(111)1x1-H surfaces prepared by in situ hydrogen exposure," *Surface Science*, vol. 303, no. 3, p. L367, 1994.
 - [82] V. A. Burrows, Y. J. Chabal, G. S. Higashi, K. Raghavachari, and S. B. Christman, "Infrared spectroscopy of Si(111) surfaces after HF treatment: Hydrogen termination and surface morphology," *Appl. Phys. Lett.*, vol. 53, no. 11, p. 998, 1988.
 - [83] Y. J. Chabal, G. S. Higashi, and S. B. Christman, "Hydrogen chemisorption on Si(111)-(7x7) and -(1x1) surfaces. A comparative infrared study," *Phys. Rev. B*, vol. 28, no. 8, 1983.
 - [84] P. O. Hahn, "SPA-LEED Measurements on Etched and Polished Silicon (111) Surfaces," *Mater. Res. Soc. Symp. Proc.*, no. 54, p. 645, 1986.
 - [85] E. Yablonovitch, D. L. Allara, C. C. Chang, T. Gmitter, and T. B. Bright, "Unusually low surface-recombination velocity on silicon and germanium surfaces," *Phys. Rev. Lett.*, vol. 57, no. 2, p. 249, 1986.
 - [86] Y. J. Chabal, G. S. Higashi, and R. K., "Infrared spectroscopy of Si(111) and Si(100) surfaces after HF treatment: Hydrogen termination and surface morphology," *J. Vac. Sci. Technol. A Vacuum, Surfaces, Film.*, vol. 7, no. 3, p. 2104, 1989.

- [87] G. S. Higashi, Y. J. Chabal, G. W. Trucks, and K. Raghavachari, "Ideal hydrogen termination of the Si (111) surface," *Appl. Phys. Lett.*, vol. 56, no. 7, p. 656, 1990.
- [88] G. S. Higashi, R. S. Becker, Y. J. Chabal, and A. J. Becker, "Comparison of Si(111) surfaces prepared using aqueous solutions of NH_4F versus HF ," *Appl. Phys. Lett.*, vol. 58, no. 15, p. 1656, 1991.
- [89] P. van der Putte, W. J. P. van Enkevort, L. J. Giling, and J. Bloem, "Surface morphology of HCL etched silicon wafers," *J. Cryst. Growth*, vol. 43, p. 659, 1978.
- [90] P. Jakob and Y. J. Chabal, "Chemical etching of vicinal Si(111): Dependence of the surface structure and the hydrogen termination on the pH of the etching solutions," *J. Chem. Phys.*, vol. 95, no. 4, p. 2897, 1991.
- [91] W. Schmidt and J. Bernholc, "Step-induced optical anisotropy of Si(111):H surfaces," *Phys. Rev. B*, vol. 61, no. 11, p. 7604, 2000.
- [92] G. J. Pietsch, U. Köhler, and M. Henzler, "Anisotropic etching versus interaction of atomic steps: Scanning tunneling microscopy observations on $\text{HF}/\text{NH}_4\text{F}$ -treated Si(111)," *J. Appl. Phys.*, vol. 73, no. 10, p. 4797, 1993.
- [93] J. Flidr, Y. Huang, T. A. Newton, and M. A. Hines, "The formation of etch hillocks during step-flow etching of Si(111)," *Chem. Phys. Lett.*, no. 302, p. 85, 1999.
- [94] P. H. Hahn, W. G. Schmidt, F. Bechstedt, O. Pulci, and R. Del Sole, "P-rich GaP (001) $(2\times 1)/(2\times 2)$ surface: A hydrogen-adsorbate structure determined from first-principles calculations," *Phys. Rev. B*, vol. 68, no. 3, p. 033311, 2003.
- [95] H. Döscher, K. Möller, and T. Hannappel, "GaP(100) and InP(100) surface structures during preparation in a nitrogen ambient," *J. Cryst. Growth*, vol. 318, no. 1, p. 372, 2011.
- [96] T. Löben, T. Hannappel, K. Möller, H.-J. Crawack, C. Pettenkofer, and F. Willig, "RDS, LEED and STM of the P-rich and Ga-rich surfaces of GaP (100)," *Surf. Sci. Lett.*, vol. 494, no. 1, p. L755, 2001.
- [97] P. Vogt, T. Hannappel, S. Visbeck, K. Knorr, N. Esser, and W. Richter, "Atomic surface structure of the phosphorous-terminated InP(001) grown by MOVPE," *Phys. Rev. B*, vol. 60, no. 8, p. R5117, 1999.
- [98] T. Hannappel, W. E. McMahon, and J. M. Olson, "An RDS, LEED, and STM study of MOCVD-prepared Si(100) surfaces," *J. Cryst. Growth*, vol. 272, p. 24, 2004.
- [99] S. Zollner, M. Garriga, J. Kircher, J. Humlíček, M. Cardona, and G. Neuhold, "Temperature dependence of the dielectric function and the interband critical-point parameters of GaP," *Thin Solid Films*, vol. 233, p. 185, 1993.
- [100] O. Supplie, "GaPN-on-Si(100) and buried interfaces: In situ spectroscopy during MOVPE growth," Ph.D. thesis, Humboldt-Universität zu Berlin, 2015.
- [101] S. Visbeck, T. Hannappel, M. Zorn, J.-T. Zettler, and F. Willig, "Temperature dependence and origin of InP(100) reflectance anisotropy down to 20 K," *Phys. Rev. B*, vol. 63, no. 24, p. 245303, 2001.
- [102] M. Miyao, R. Goto, T. Sukegawa, and M. Hagino, "Cleaning of GaP surface by forming oxide film," *Surf. Sci.*, vol. 71, p. 148, 1978.
- [103] Y. R. Xing and W. Ranke, "UPS study of oxygen chemisorption on the GaP(ITT) surface," *Surf. Sci.*, vol. 167, no. 1, p. L171, 1986.
- [104] H. Y. Xiao, X. K. Lu, G. S. Dong, X. M. Ding, P. Chen, and X. Wang, "Surface adsorption properties of GaP (ITT) studied by XPS, UPS and HREELS," *Phys. Scr.*, vol. 41, no. 6, p. 1037, 1990.
- [105] A. J. van Bommel and J. E. Crombeen, "The adsorption and desorption of Cs on GaP and GaSb (001), (110), (111) and (ITT) surfaces, studied by leed, AES and photoemission,"

- Surf. Sci.*, vol. 93, no. 2–3, p. 383, 1980.
- [106] K. Hattori, K. Ishihara, Y. Miyatake, F. Matsui, S. Takeda, H. Daimon, and F. Komori, “GaP(111) reconstructed surface studied with STM and LEED,” *Surf. Sci.*, vol. 525, p. 57, 2003.
 - [107] G. Xu, W. Hu, M. Puga, S. Tong, J. Yeh, S. Wang, and B. Lee, “Atomic geometry of the 2×2 GaP(111) surface,” *Phys. Rev. B*, vol. 32, no. 12, p. 8473, 1985.
 - [108] S. Itagaki, M. Shimomura, N. Sanada, and Y. Fukuda, “Surface structures of clean and sulfur-treated GaP(111)A studied using AES, LEED, and STM,” *e-Journal Surf. Sci. Nanotechnol.*, vol. 7, no. April, p. 213, 2009.
 - [109] R. D. Bringans, D. K. Biegelsen, and L.-E. Swartz, “Atomic-step rearrangement on Si(100) by interaction with arsenic and the implication for GaAs-on-Si epitaxy,” *Phys. Rev. B*, vol. 44, no. 7, p. 3054, 1991.
 - [110] R. Kaplan, “LEED study of the stepped surface of vicinal Si (100),” *Surf. Sci.*, vol. 93, p. 145, 1980.
 - [111] O. L. Alerhand, A. N. Berker, J. D. Joannopoulos, D. Vanderbilt, R. J. Hamers, and J. E. Demuth, “Finite-temperature phase diagram of vicinal Si(100) surfaces,” *Phys. Rev. Lett.*, vol. 64, no. 20, p. 2406, 1990.
 - [112] T. Bork, W. E. McMahon, J. M. Olson, and T. Hannappel, “Surface science studies including low-temperature RDS on MOCVD-prepared, As-terminated Si(100) surfaces,” *J. Cryst. Growth*, vol. 298, p. 54, 2007.
 - [113] E. L. Warren, A. E. Kibbler, R. M. France, A. G. Norman, P. Stradins, and W. E. McMahon, “Growth of antiphase-domain-free GaP on Si substrates by metalorganic chemical vapor deposition using an in situ AsH₃ surface preparation,” *Appl. Phys. Lett.*, vol. 107, no. 8, p. 082109.1, 2015.
 - [114] M. A. Olmstead, R. D. Bringans, R. I. G. Uhrberg, and R. Z. Bachrach, “Arsenic overlayer on Si(111): Removal of surface reconstruction,” *Phys. Rev. B*, vol. 34, no. 8, p. 6041, 1986.
 - [115] J. Patel, P. Freeland, M. Hybertsen, D. Jacobson, and J. Golovchenko, “Location of atoms in the first monolayer of GaAs on Si,” *Phys. Rev. Lett.*, vol. 59, no. 19, p. 2180, 1987.
 - [116] J. Northrup, R. Bringans, R. Uhrberg, M. Olmstead, and R. Bachrach, “Electronic and atomic structure of GaAs epitaxial overlays on Si(111),” *Phys. Rev. Lett.*, vol. 61, no. 26, p. 2957, 1988.
 - [117] T. R. Ohno and E. D. Williams, “Step structure and interface morphology: Arsenic on vicinal silicon surfaces,” *J. Vac. Sci. Technol. B Microelectron. Nanom. Struct.*, vol. 8, no. 4, p. 874, 1990.
 - [118] A. Antons, R. Berger, K. Schroeder, and B. Voigtländer, “Structure of steps on As-passivated Si(111): Ab initio calculations and scanning tunneling microscopy,” *Phys. Rev. B*, vol. 73, no. 12, p. 125327, 2006.
 - [119] S. Brückner, “Atomic scale in situ control of Si (100) and Ge (100) surfaces in CVD ambient,” Ph. D. thesis, Humboldt-Universität zu Berlin / Helmholtz-Zentrum Berlin (Germany), 2014.
 - [120] K. W. Kolasinski, W. Nessler, A. De Meijere, and E. Hasselbrink, “Hydrogen adsorption on and desorption from Si: Considerations of the applicability of detailed balance,” *Phys. Rev. Lett.*, vol. 72, no. 9, p. 1356, 1994.
 - [121] V. Alberts, J. H. Neethling, and J. S. Vermaak, “Nucleation and growth of gallium arsenide on silicon (111),” *J. Mater. Sci.*, vol. 29, no. 1994, p. 2017, 1994.
 - [122] H. Suzuki, D. Ito, A. Fukuyama, and T. Ikari, “Reduction of rotational twin formation by

- indium pre-evaporation in epitaxially grown GaAs films on Si (111) substrate,” *J. Cryst. Growth*, vol. 380, p. 148, 2013.
- [123] H. Udono, A. Motogaito, M. Kimura, A. Tanaka, and T. Sukegawa, “Suppression of twins in GaAs layers grown on a GaP(111)B substrate by liquid phase epitaxy,” *J. Cryst. Growth*, vol. 169, no. 1, p. 181, 1996.
- [124] H. Suzuki, D. Ito, A. Haga, A. Fukuyama, and T. Ikari, “The effects of Indium Pre-Evaporation on Rotational Twin Formation in GaAs films on Si (111),” no. 111, p. 1830, 2014.
- [125] V. Narayanan, S. Mahajan, K. J. Bachmann, V. Woods, and N. Dietz, “Stacking faults and twins in gallium phosphide layers grown on silicon,” *Philos. Mag. A*, vol. 82, no. 4, p. 685, 2002.
- [126] D. Cohen, S. McKernan, and C. Carter, “Characterization of the absolute crystal polarity across twin boundaries in gallium phosphide using convergent-beam electron diffraction,” *Microsc. Microanal.*, vol. 5, no. 3, p. 173, 1999.
- [127] A. Proessdorf, F. Grosse, O. Romanyuk, W. Braun, B. Jenichen, A. Trampert, and H. Riechert, “Interface engineering for improved growth of GaSb on Si(111),” *J. Cryst. Growth*, vol. 323, no. 1, p. 401, 2011.
- [128] I. V. Markov, *Crystal growth for beginners. Fundamentals of nucleation, crystal growth and epitaxy*. World Scientific Publishing Co. Pte. Ltd., 1995.
- [129] J. E. Ayers, *Heteroepitaxy of Semiconductors: Theory, Growth, and Characterization*. CRC Press, 2007.
- [130] A. C. Jones and M. L. Hitchman, Eds., *Chemical Vapour Deposition: Precursors, Processes and Applications*. Royal Society of Chemistry, 2008.
- [131] D. E. Aspnes and A. A. Studna, “Anisotropies in the above-band-gap optical spectra of cubic semiconductors,” *Phys. Rev. Lett.*, vol. 54, no. 17, p. 1956, 1985.
- [132] J. T. Zettler, “Characterization of epitaxial semiconductor growth by reflectance anisotropy spectroscopy and ellipsometry,” *Prog. Cryst. growth charact.*, vol. 35, p. 27, 1997.
- [133] P. Weightman, D. S. Martin, R. J. Cole, and T. Farrell, “Reflection anisotropy spectroscopy,” *Reports Prog. Phys.*, vol. 68, no. 6, p. 1251, 2005.
- [134] M. S. Dresselhaus, *Solid state physics, part II: Optical properties of solids*. 2001.
- [135] P. Lautenschlager, M. Garriga, L. Vina, and M. Cardona, “Temperature dependence of the dielectric function and interband critical points in silicon,” *Phys. Rev. B*, vol. 36, no. 9, p. 4821, 1987.
- [136] D. E. Aspnes and A. A. Studna, “Dielectric functions and optical parameters of Si, Ge, GaP, GaAs, GaSb, InP, InAs, and InSb from 1.5 to 6.0 eV,” *Phys. Rev. B*, vol. 27, no. 2, p. 985, 1983.
- [137] J. Singh, *Semiconductor Devices: Basic Principles*, First. Wiley, 2000.
- [138] A. Selloni, P. Marsella, and R. Del Sole, “Microscopic calculation of the surface contribution to optical reflectivity: Application to Si,” *Phys. Rev. B*, vol. 33, no. 12, p. 8885, 1986.
- [139] P. Honenberg and W. Kohn, “Inhomogeneous Electron Gas,” *Phys. Rev.*, vol. 136, no. 3B, p. B864, 1964.
- [140] D. E. Aspnes, J. P. Harbison, A. A. Studna, and L. T. Florez, “Application of reflectance difference spectroscopy to molecular-beam epitaxy growth of GaAs and AlAs,” *J. Vac. Sci. Technol. A Vacuum, Surfaces, Film.*, vol. 6, no. 3, p. 1327, 1988.

- [141] K. Haberland, "Optical in-situ studies during metal-organic vapor phase epitaxy with respect to III-V device production," Ph.D. thesis, Technische Universität Berlin, 2002.
- [142] F. Reinert and S. Hüfner, "Photoemission spectroscopy—from early days to recent applications," *New J. Phys.*, vol. 7, p. 97, 2005.
- [143] C. J. Powell and A. Jablonski, *NIST Electron Effective-Absorption-Length Database, Version 1.3, SRD 82*. National Institute of Standards and Technology, Gaithersburg, 2011.
- [144] P. Marcus and F. B. Mansfeld, *Analytical Methods In Corrosion Science and Engineering*. CRC Press, 2005.
- [145] K. Oura, V. G. Lifshits, A. Saranin, A. V. Zotov, and M. Katayama, *Surface Science, an introduction*. Springer-Verlag Berlin Heidelberg, 2003.
- [146] B. H. Stuart, *Infrared Spectroscopy: Fundamentals and Applications*, vol. 8. Wiley, 2004.
- [147] P. R. Griffiths and J. A. De Haseth, *Fourier Transform Infrared Spectrometry*, 2nd ed. Wiley, 2007.
- [148] P. R. Griffiths and J. A. De Haseth, "Attenuated total reflection," in *Fourier Transform Infrared Spectrometry*, Wiley, 2007, p. 321.
- [149] J. Fahrenfort, "Attenuated total reflection: a new principle for the production of useful infra-red reflection spectra of organic compounds," *Spectrochim. Acta*, vol. 17, no. 7, p. 698, 1961.
- [150] N. J. Harrick, "Surface chemistry from spectral analysis of totally internally reflected radiation," *J. Phys. Chem.*, vol. 64, no. 9, p. 1110, 1960.
- [151] T. Letzig, "Wasserstoffbindungen auf rekonstruierten InP (100) Oberflächen," Ruhr-Universität Bochum, 2005.
- [152] I. Horcas, R. Fernández, J. M. Gómez-Rodríguez, J. Colchero, J. Gómez-Herrero, and A. M. Baro, "WSXM: A software for scanning probe microscopy and a tool for nanotechnology," *Rev. Sci. Instrum.*, vol. 78, no. 1, p. 013705, 2007.
- [153] E. S. Gadelmawla, M. M. Koura, T. M. A. Maksoud, I. M. Elewa, and H. H. Soliman, "Roughness parameters," *J. Mater. Process. Technol.*, vol. 123, p. 133, 2002.
- [154] T. Wolff, *Measurement theory for the Wafer Profiler CVP 21*. WEP, 203AD.
- [155] M. Palummo, N. Witkowski, O. Pluchery, R. Del Sole, and Y. Borenstein, "Reflectance-anisotropy spectroscopy and surface differential reflectance spectra at the Si(100) surface: Combined experimental and theoretical study," *Phys. Rev. B*, vol. 79, no. 3, p. 035327.1, 2009.
- [156] S. Brückner, P. Kleinschmidt, O. Supplie, H. Döscher, and T. Hannappel, "Domain-sensitive *in situ* observation of layer-by-layer removal at Si(100) in H₂ ambient," *New J. Phys.*, vol. 15, no. 11, p. 113049, 2013.
- [157] F. K. Men, A. R. Smith, K. Chao, Z. Zhang, and C. Shih, "Dimer-vacancy-dimer-vacancy interaction on the Si(001) surface: The nature of the 2x1 structure," *Phys. Rev. B Rapid Commun.*, vol. 52, no. 12, p. 8650, 1995.
- [158] N. Kitamura, M. G. Legally, and M. B. Webb, "Real-time observations of vacancy diffusion on Si(001)-(2x1) by scanning tunneling microscopy," *Phys. Rev. Lett.*, vol. 71, no. 13, p. 2082, 1993.
- [159] Z. Zhang, H. Chen, B. C. Bolding, and M. G. Legally, "Vacancy diffusion on Si(100)-(2x1)," *Phys. Rev. Lett.*, vol. 71, no. 22, p. 3677, 1993.
- [160] S. Swartzentruber, M. Matzke, L. Kendall, and J. E. Houston, "STM measurements of step-flow kinetics during atom removal by low-energy-ion bombardment of Si (001)," *Surf. Sci.*, vol. 329, p. 83, 1995.

- [161] P. Bedrossian and T. Klitsner, "Anisotropic vacancy kinetics and single-domain stabilization on Si(100)-2x1," *Phys. Rev. Lett.*, vol. 68, no. 5, p. 646, 1992.
- [162] S. Brückner, H. Döscher, P. Kleinschmidt, and T. Hannappel, "In situ investigation of hydrogen interacting with Si(100)," *Appl. Phys. Lett.*, vol. 98, no. 21, p. 98, 2011.
- [163] R. Shioda and J. Van Der Weide, "Observation of hydrogen adsorption on Si (001) by reflectance difference spectroscopy," *Appl. Surf. Sci.*, vol. 130–132, p. 266, 1998.
- [164] E. Barrigón, S. Brückner, O. Supplie, P. Kleinschmidt, I. Rey-Stolle, and T. Hannappel, "Optical in situ monitoring of hydrogen desorption from Ge(100) surfaces," *Appl. Phys. Lett.*, vol. 102, no. 11, 2013.
- [165] S. Brückner, O. Supplie, E. Barrigón, J. Luczak, P. Kleinschmidt, I. Rey-Stolle, H. Döscher, and T. Hannappel, "In situ control of As dimer orientation on Ge(100) surfaces," *Appl. Phys. Lett.*, vol. 101, no. 12, p. 121602, 2012.
- [166] C. Löbbel, "Fouriertransformierte Infrarotspektroskopie an MOVPE präparierten Si, Ge und GaP(100) Halbleiteroberflächen," Master thesis, Technische Universität Berlin / Helmholtz-Zentrum Berlin (Germany), 2012.
- [167] H. Döscher, A. Dobrich, S. Brückner, P. Kleinschmidt, and T. Hannappel, "Si(100) surfaces in a hydrogen-based process ambient," *Appl. Phys. Lett.*, vol. 97, no. 15, p. 151905, 2010.
- [168] Y. J. Chabal, "High-resolution infrared spectroscopy of adsorbates on semiconductor surfaces: Hydrogen on Si(100) and Ge(100)," *Surf. Sci.*, vol. 168, no. 1–3, p. 594, 1986.
- [169] H. Bender, S. Verhaverbeke, M. Caymax, O. Vatel, and M. M. Heyns, "Surface reconstruction of hydrogen annealed (100) silicon," *J. Appl. Phys.*, vol. 75, no. 2, p. 1207, 1994.
- [170] T. Aoyama, K. Goto, T. Yamazaki, and T. Ito, "Silicon (001) surface after annealing in hydrogen ambient," *J. Vac. Sci. Technol. A Vacuum, Surfaces, Film.*, vol. 14, no. 5, p. 2909, 1996.
- [171] J. S. Ha, K.-H. Park, Y.-J. Ko, and K. Park, "Role of surface steps in the arrangement of silicon nano-dots on a vicinal Si(111) surface: Scanning tunneling microscopy investigation," *J. Vac. Sci. Technol. B Microelectron. Nanom. Struct.*, vol. 20, no. 2, p. 747, 2002.
- [172] F. A. Reboredo, S. B. Zhang, and A. Zunger, "Hydrogen-induced instability on the flat Si(001) surface via steric repulsion," *Phys. Rev. B*, vol. 63, no. 12, p. 125316, 2001.
- [173] T. Yasuda, D. E. Aspens, D. R. Lee, C. H. Bjorkman, and G. Lucovsky, "Optical anisotropy of singular and vicinal Si–SiO₂ interfaces and H-terminated Si surfaces," *J. Vac. Sci. Technol. A Vacuum, Surfaces, Film.*, vol. 12, no. 4, p. 1152, 1994.
- [174] K. J. Bachmann, U. Rossow, N. Sukidi, H. Castleberry, and N. Dietz, "Heteroepitaxy of GaP on Si(100)," *J. Vac. Sci. Technol. B Microelectron. Nanom. Struct.*, vol. 14, no. 4, p. 3019, 1996.
- [175] K. Volz, A. Beyer, W. Witte, J. Ohlmann, I. Németh, B. Kunert, and W. Stolz, "GaP-nucleation on exact Si (001) substrates for III/V device integration," *J. Cryst. Growth*, vol. 315, no. 1, p. 37, 2011.
- [176] I. Regolin, C. Gutsche, A. Lysov, K. Blekker, Z.-A. Li, M. Spasova, W. Prost, and F.-J. Tegude, "Axial pn-junctions formed by MOVPE using DEZn and TESn in vapor–liquid–solid grown GaAs nanowires," *J. Cryst. Growth*, vol. 315, no. 1, p. 143, 2011.
- [177] S. Korte, M. Steidl, W. Prost, V. Cherepanov, B. Voigtländer, W. Zhao, P. Kleinschmidt, and T. Hannappel, "Resistance and dopant profiling along freestanding GaAs nanowires," *Appl. Phys. Lett.*, vol. 103, no. 14, p. 143104, 2013.

- [178] W. Zhao, M. Steidl, A. Paszuk, S. Brückner, A. Dobrich, O. Supplie, P. Kleinschmidt, and T. Hannappel, "Analysis of the Si(111) surface prepared in chemical vapor ambient for subsequent III-V heteroepitaxy," *Appl. Surf. Sci.*, vol. 392, p. 1043, 2017.
- [179] T. L. Barr, "An XPS study of Si as it occurs in adsorbents, catalysts, and thin films," *Applications of Surface Science*, vol. 15, no. 1–4, p. 1, 1983.
- [180] M. S. Hegde, R. Caracciolo, K. S. Hatton, and J. B. Wachtman, "Electronic structure and bonding in silicon oxynitride films: An XPS study," *Applied Surface Science*, vol. 37, no. 1, p. 16, 1989.
- [181] Z. H. Lu, M. J. Graham, D. T. Jiang, and K. H. Tan, "SiO₂/Si(100) interface studied by Al K α x-ray and synchrotron radiation photoelectron spectroscopy," *Appl. Phys. Lett.*, vol. 63, no. 21, p. 2941, 1993.
- [182] R. I. G. Uhrberg, E. Landemark, and Y. C. Chao, "High-resolution core-level studies of silicon surfaces," *J. Electron Spectros. Relat. Phenomena*, vol. 75, no. 95, p. 197, 1995.
- [183] J. F. Moulder, W. F. Stickle, P. E. Sobol, and K. D. Bomben, *Handbook of X-ray Photoelectron Spectroscopy*, 2nd ed. Eden Prairie: Physical Electronics, 1995.
- [184] S. Sato, I. Mizushima, K. Miyano, T. Sato, S. Nakamura, Y. Tsunashima, T. Arikado, and N. Uchitomi, "Defects induced by carbon contamination in low-temperature epitaxial silicon films grown with monosilane," *Japanese Journal of Applied Physics*, vol. 44, no. 3, p. 1169, 2005.
- [185] A. Ishizaka and Y. Shiraki, "Low temperature surface cleaning of silicon and its application to silicon MBE," *J. Electrochem. Soc.*, vol. 133, no. 11, p. 666, 1986.
- [186] G. J. Pietsch, "Hydrogen on Si: Ubiquitous surface termination after wet-chemical processing," *Appl. Phys. A*, vol. 60, p. 347, 1995.
- [187] W. G. Schmidt, F. Bechstedt, and J. Bernholc, "Understanding reflectance anisotropy: Surface-state signatures and bulk-related features," *J. Vac. Sci. Technol. B Microelectron. Nanom. Struct.*, vol. 18, no. 4, p. 2215, 2000.
- [188] L. Mantese, U. Rossow, and D. E. Aspnes, "Surface-induced optical anisotropy of oxidized, clean, and hydrogenated vicinal Si(001) surfaces," *Appl. Surf. Sci.*, vol. 32, no. 107, p. 35, 1996.
- [189] H. Döschner, P. Kleinschmidt, and T. Hannappel, "Atomic surface structure of Si(100) substrates prepared in a chemical vapor environment," *Appl. Surf. Sci.*, vol. 257, no. 2, p. 574, 2010.
- [190] M. Horn-von Hoegen and A. Golla, "Adsorbate induced change of equilibrium surface during crystal growth: Si on Si(111)/H," *Phys. Rev. Lett.*, vol. 76, no. 16, p. 2953, 1996.
- [191] U. Köhler, L. Andersohn, and H. Bethge, "The influence of hydrogen on CVD-growth on Si(111) surfaces," *Phys. Status Solidi*, vol. 159, no. 1, p. 39, 1997.
- [192] M. J.-P. Duchemin, M. M. Bonnet, and F. M. Koelsch, "Kinetics of silicon growth under low hydrogen pressure," *Journal of The Electrochemical Society*, vol. 125, no. 4, p. 637, 1978.
- [193] L. J. Giling, H. H. C. De Moor, W. P. J. H. Jacobs, and A. A. Saaman, "Adsorption on Si(111) during CVD of silicon from silane: The effect of temperature, bond strength, supersaturation and pressure," *Journal of Crystal Growth*, vol. 78, no. 2, p. 303, 1986.
- [194] R. N. Thomas and M. H. Francombe, "Influence of impurities on the surface structures and fault generation in homoepitaxial Si (111) films," *Surface Science*, vol. 25, no. 2, p. 357, 1971.
- [195] H. Minoda, Y. Takahashi, Y. Tanishiro, and K. Yagi, "In situ reflection electron microscopy study of Cu-induced step bunching on Si(111) vicinal surfaces," *Surf. Sci.*,

- vol. 438, no. 1–3, p. 68, 1999.
- [196] S. Watanabe, K. Horiuchi, and T. Ito, “Atomic step structure on vicinal H/Si(111) surface formed by hot water immersion,” *Jpn. J. Appl. Phys.*, vol. 32, no. 8, p. 3420, 1993.
- [197] A. Paszuk, S. Brückner, M. Steidl, W. Zhao, A. Dobrich, O. Supplie, P. Kleinschmidt, W. Prost, and T. Hannappel, “Controlling the polarity of metalorganic vapor phase epitaxy-grown GaP on Si(111) for subsequent III-V nanowire growth,” *Appl. Phys. Lett.*, vol. 106, no. 23, p. 231601, 2015.
- [198] R. Q. Zhang, Y. Lifshitz, D. D. D. Ma, Y. L. Zhao, T. Frauenheim, S. T. Lee, and S. Y. Tong, “Structures and energetics of hydrogen-terminated silicon nanowire surfaces,” *J. Chem. Phys.*, vol. 123, no. 14, p. 144703, 2005.
- [199] K. Hiruma, M. Yazawa, T. Katsuyama, K. Ogawa, K. Haraguchi, M. Koguchi, and H. Kakibayashi, “Growth and optical properties of nanometer-scale GaAs and InAs whiskers,” *J. Appl. Phys.*, vol. 77, no. 2, p. 447, 1995.
- [200] N. Chetty and R. M. Martin, “GaAs (111) and (111) surfaces and the GaAs/AlAs (111) heterojunction studied using a local energy density,” *Phys. Rev. B*, vol. 45, no. 11, p. 6089, 1992.
- [201] I. Miccoli, P. Prete, F. Marzo, D. Cannoletta, and N. Lovergine, “Synthesis of vertically-aligned GaAs nanowires on GaAs/(111)Si hetero-substrates by metalorganic vapour phase epitaxy,” *Cryst. Res. Technol.*, vol. 46, no. 8, p. 795, 2011.
- [202] A. U. M. Rae, “Low energy electron diffraction study of the polar {111} surfaces of GaAs and GaSb,” *Surf. Sci.*, vol. 4, no. 3, p. 247, 1966.
- [203] S. Y. Tong, G. Xu, and W. N. Mei, “Vacancy buckling model for the (111) surface of III–V compound semiconductors,” *physical review Lett.*, vol. 52, no. 19, p. 1693, 1984.
- [204] D. Chadi, “Vacancy-Induced 2×2 Reconstruction of the Ga(111) Surface of GaAs,” *Phys. Rev. Lett.*, vol. 52, no. 21, p. 1911, 1984.
- [205] H. A. Fonseka, H. H. Tan, J. Wong-Leung, J. H. Kang, P. Parkinson, and C. Jagadish, “High vertical yield InP nanowire growth on Si(111) using a thin buffer layer,” *Nanotechnology*, vol. 24, no. 46, p. 465602, 2013.
- [206] O. Romanyuk, T. Hannappel, and F. Grosse, “Atomic and electronic structure of GaP/Si(111), GaP/Si(110), and GaP/Si(113) interfaces and superlattices studied by density functional theory,” *Phys. Rev. B*, vol. 88, no. 11, p. 115312, 2013.
- [207] K. Werner, A. Beyer, J. O. Oelerich, S. D. Baranovskii, W. Stolz, and K. Volz, “Structural characteristics of gallium metal deposited on Si(001) by MOCVD,” *J. Cryst. Growth*, vol. 405, p. 102, 2014.
- [208] R. D. Bringans, M. A. Olmstead, R. I. G. Uhrberg, and R. Z. Bachrach, “Formation of the interface between GaAs and Si: Implications for GaAs-on-Si heteroepitaxy,” *Appl. Phys. Lett.*, vol. 51, no. 7, p. 523, 1987.
- [209] R. D. Bringans, “Arsenic passivation of Si and Ge surfaces,” *Crit. Rev. Solid State Mater. Sci.*, vol. 17, no. 4, p. 353, 1992.
- [210] C. Koppka, A. Paszuk, M. Steidl, O. Supplie, P. Kleinschmidt, and T. Hannappel, “Suppression of rotational twin formation in GaP/Si(111) quasi-substrates for III-V nanowire growth,” *Cryst. Growth Des.*, vol. 16, no. 11, p. 6208, 2016.
- [211] Y. Kohama, K. Uchida, T. Soga, T. Jimbo, and M. Umeno, “Quality improvement of metalorganic chemical vapor deposition grown GaP on Si by AsH₃ preflow,” *Appl. Phys. Lett.*, vol. 53, no. 10, p. 862, 1988.
- [212] R. S. Becker, T. Klitsner, and J. S. Vickers, “Arsenic-terminated silicon and germanium surfaces studied by scanning tunnelling microscopy,” *J. Microsc.*, vol. 152, no. August, p.

- 157, 1988.
- [213] R. Hull, A. Fischer-Colbrie, S. J. Rosner, S. M. Koch, and J. S. Harris, "Effect of substrate surface structure on nucleation of GaAs on Si(100)," *Appl. Phys. Lett.*, vol. 51, no. 21, p. 1723, 1987.
 - [214] M. Kawabe, T. Ueda, and H. Takasugi, "Initial stage and domain structure of GaAs grown on Si(100) by molecular beam epitaxy," *Jpn. J. Appl. Phys.*, vol. 26, no. 2, p. L114, 1987.
 - [215] E. García-Tabarés, D. Martín, I. García, J. F. Lelièvre, and I. Rey-Stolle, "Optimization of the silicon subcell for III-V on silicon multijunction solar cells: Key differences with conventional silicon technology," *AIP Conf. Proc.*, vol. 5, p. 1477, 2012.
 - [216] O. Supplie, M. M. May, P. Kleinschmidt, A. Nägelein, A. Paszuk, S. Brückner, and T. Hannappel, "In situ controlled heteroepitaxy of single-domain GaP on As-modified Si(100)," *APL Mater.*, vol. 3, no. 12, p. 126110.1, 2015.
 - [217] A. Paszuk, O. Supplie, M. Nandy, S. Brückner, A. Dobrich, P. Kleinschmidt, B. Kim, Y. Nakano, M. Sugiyama, and T. Hannappel, "Double-layer Stepped Arsenic-modified Si(100) Surfaces Prepared in As-rich CVD ambient," *Appl. Surf. Sci.*, *under review*, 2018.
 - [218] A. Paszuk, A. Dobrich, C. Koppka, S. Brückner, M. Duda, P. Kleinschmidt, O. Supplie, and T. Hannappel, "In situ preparation of Si p-n junctions and subsequent surface preparation for III-V heteroepitaxy in MOCVD ambient," *J. Cryst. Growth*, vol. 464, no. 4, p. 14, 2017.
 - [219] L. Kipp, D. K. Biegelsen, J. E. Northrup, L. Swartz, and R. D. Bringans, "Reflectance difference spectroscopy: Experiment and theory for the model system Si(001): As and application to Si(001)," *Phys. Rev. Lett.*, vol. 76, no. 15, p. 2810, 1996.
 - [220] C. H. Patterson and D. Herrendörfer, "Reflectance anisotropy of the Si(100)1×2-As surface: Discrete dipole calculation," *J. Vac. Sci. Technol. A Vacuum, Surfaces, Film.*, vol. 15, no. 6, p. 3036, 1997.
 - [221] W. G. Schmidt, F. Bechstedt, and J. Bernholc, "Terrace and step contributions to the optical anisotropy of Si(001) surfaces," *Phys. Rev. B*, vol. 63, no. 4, p. 045322, 2001.
 - [222] A. Müller, "In-Situ Massenspektrometrie bei der metallorganischen Gasphasenabscheidung," Master thesis, Fachhochschule Brandenburg / Helmholtz-Zentrum-Berlin, 2011.
 - [223] W. E. McMahon and J. M. Olson, "Atomic-resolution STM study of a structural phase transition of steps on vicinal As/Ge(100)," *Phys. Rev. B*, vol. 60, no. 23, p. 15999, 1999.
 - [224] W. E. McMahon and J. M. Olson, "Atomic-resolution study of steps and ridges on arsine-exposed vicinal Ge (100)," *Phys. Rev. B*, vol. 60, no. 4, p. 2480, 1999.
 - [225] O. Supplie, M. M. May, G. Steinbach, O. Romanyuk, F. Grosse, A. Nägelein, P. Kleinschmidt, S. Brückner, and T. Hannappel, "Time-resolved in situ spectroscopy during formation of the GaP/Si(100) heterointerface," *Phys. Chem. Lett.*, vol. 6, no. 3, p. 464, 2015.
 - [226] O. Supplie, M. M. May, C. Höhn, H. Stange, A. Müller, P. Kleinschmidt, S. Brückner, and T. Hannappel, "Formation of GaP/Si(100) Heterointerfaces in the Presence of Inherent Reactor Residuals," *ACS Appl. Mater. interfaces*, vol. 7, no. 18, p. 9323, 2015.
 - [227] H. Döscher and T. Hannappel, "In situ reflection anisotropy spectroscopy analysis of heteroepitaxial GaP films grown on Si(100)," *J. Appl. Phys.*, vol. 107, no. 12, p. 123523.1, 2010.
 - [228] P. H. Hahn, W. G. Schmidt, F. Bechstedt, O. Pulci, and R. Del Sole, "P-rich GaP(001) (2×1)/(1×2) surface: A hydrogen-adsorbate structure determined from first-principles calculations," *Phys. Rev. B*, vol. 68, no. 3, p. 033311, 2003.

- [229] P. Sippel, O. Supplie, M. M. May, R. Eichberger, and T. Hannappel, "Electronic structures of GaP(100) surface reconstructions probed with two-photon photoemission spectroscopy," *Phys. Rev. B*, vol. 89, no. 16, p. 165312, 2014.
- [230] I. Németh, B. Kunert, W. Stolz, and K. Volz, "Heteroepitaxy of GaP on Si: Correlation of morphology, anti-phase-domain structure and MOVPE growth conditions," *J. Cryst. Growth*, vol. 310, no. 7, p. 1595, 2008.
- [231] O. Supplie, T. Hannappel, M. Pristovsek, and H. Döscher, "In situ access to the dielectric anisotropy of buried III-V/Si(100) heterointerfaces," *Phys. Rev. B*, vol. 86, no. 3, p. 035308, 2012.
- [232] M. Lublow, T. Stempel, K. Skorupska, A. G. Muñoz, M. Kanis, and H. J. Lewerenz, "Morphological and chemical optimization of ex situ NH₄F (40%) conditioned Si(111)-(1×1):H," *Appl. Phys. Lett.*, vol. 93, no. 6, p. 062112, 2008.
- [233] E. García-Tabarés, I. García, D. Martín, and I. Rey-Stolle, "Influence of PH₃ exposure on silicon substrate morphology in the MOVPE growth of III-V on silicon multijunction solar cells," *J. Phys. D: Appl. Phys.*, vol. 46, no. 44, p. 445104, 2013.
- [234] T. C. Chan and C. C. Mai, "Diffusion of boron, phosphorus, arsenic, and antimony into (100) and (111) silicon slices," *Proc. IEEE*, vol. 58, no. 4, p. 588, 1970.
- [235] S. R. Schofield, N. J. Curson, M. Y. Simmons, F. J. Ruess, T. Hallam, L. Oberbeck, and R. G. Clark, "Atomically precise placement of single dopants in Si," *Phys. Rev. Lett.*, vol. 91, no. 13, p. 136104, 2003.
- [236] E. García-Tabarés, D. Martín, I. García, and I. Rey-Stolle, "Understanding phosphorus diffusion into silicon in a MOVPE environment for III-V on silicon solar cells," *Sol. Energy Mater. Sol. Cells*, vol. 116, p. 61, 2013.
- [237] H. M. Leedy and J. T. Neal, "Titanium tungsten-gold contacts for semiconductor devices," US patent No. 3601666 A1971.
- [238] J. W. Mayer, "Gold contacts to semiconductor devices," *Gold Bull.*, vol. 17, no. 1, p. 18, 1984.
- [239] R. Sinton and A. Cuevas, "A quasi-steady-state open-circuit voltage method for solar cell characterization," *16th Eur. Photovolt. Sol. Energy Conf.*, vol. Glasgow, U, p. 1152, 2000.
- [240] S. Schiefer, B. Zimmermann, S. W. Glunz, and U. Würfel, "Applicability of the suns-V_{OC} method on organic solar cells," *IEEE J. Photovoltaics*, vol. 4, no. 1, p. 271, 2014.
- [241] C. P. Wade and C. E. D. Chidsey, "Etch-pit initiation by dissolved oxygen on terraces of H-Si(111)," *Appl. Phys. Lett.*, vol. 71, no. 12, p. 1679, 1997.
- [242] M. Steidl, C. Koppka, L. Winterfeld, K. Peh, B. Galiana, O. Supplie, P. Kleinschmidt, E. Runge, and T. Hannappel, "Impact of Rotational Twin Boundaries and Lattice Mismatch on III-V Nanowire Growth," *ACS Nano*, vol. 11, no. 9, p. 8679, 2017.

Acknowledgements

This work would not have been possible without the advice, encouragement and support of many people. I owe especial gratitude to:

- Prof. Dr. Thomas Hannappel for presenting me with this great opportunity to join his excellent and talented research group, to learn, explore and also contribute to the great results;
- Prof. Dr. Gerhard Gobsch for taking an interest in this work and agreeing to review it, as well as for the opportunity to join the Thüringer Landesgraduiertenschule für Photovoltaik (PhotoGrad);
- Prof. Dr. Stefan Krischok for his concern in the progress of the work, and for the opportunity of the PhotoGrad;
- Prof. dr Regina Paszkiewicz for her willingness to be an external reviewer;
- Dr. Peter Kleinschmidt, Dr. Sebastian Brückner and Dr. Oliver Supplie for their help and endless knowledge about Si(100), Ge(100) and RAS, their supervision, guidance, for their patience in correcting my English, and mostly for their great support either at or after work;
- Dr. Anja Dobrich for her help with the FTIR, her support and great constant cooperation;
- Weihong Zhao and Matthias Steidl for starting this journey together, great collaboration, especially during many long hours in the laboratory, for their great, constant support, knowledge and friendship on and off work;
- Christian Koppka and Andreas Nägelein for the knowledge, help and support in experiments; and for extensive XRD and STM measurements, respectively, and to Andreas for fresh coffee every morning;
- Dr. Matthias M. May for introduction to XPS, for help at the Helmholtz-Zentrum-Berlin, and further consultations;
- Antonio Müller, Mathias Biester and Christian Höhn, for doing a great job in taking care of our experimental equipment, their help in “transfers” and for making the work a bit less serious;
- Simone Gutsche for reliable organizational and bureaucratic help, and for understanding my German;

Acknowledgements

- Marek Duda for the support with the p-n junction experiments and a great friendship beyond work;
- all friends and master's students not listed here, from TU Ilmenau and the Helmholtz-Zentrum-Berlin;
- all co-authors, not listed here, for their indispensable contribution to the papers;
- the German Federal Ministry of Education and Research (BMBF, projects no. 03SF0525B and 03SF0404A) and the PhotoGrad for the financial support;
- the Gleichstellungsrat for the "Promotionsabschlusstipendium" that supported me financially towards the last few months of my work;
- my family and all my friends who have supported me during this work, especially to Maria for having patience regarding my crazy work schedule and helping me to be a happy, positive person.

Erklärung

Ich versichere, dass ich die vorliegende Arbeit ohne unzulässige Hilfe Dritter und ohne Benutzung anderer als der angegebenen Hilfsmittel angefertigt habe. Die aus anderen Quellen direkt oder indirect übernommenen Daten und Konzepte sind unter Angabe der Quelle gekennzeichnet. Weitere Personen waren an der inhaltlich-materiellen Erstellung der vorliegenden Arbeit nicht beteiligt. Insbesondere habe ich hierfür nicht die entgeltliche Hilfe von Vermittlungs- bzw. Beratungsdiensten (Promotionsberater oder anderer Personen) in Anspruch genommen. Niemand hat von mir unmittelbar oder mittelbar geldwerte Leistungen für Arbeiten erhalten, die im Zusammenhang mit dem Inhalt der vorgelegten Dissertation stehen. Die Arbeit wurde bisher weder im In- noch im Ausland in gleicher oder ähnlicher Form einer Prüfungsbehörde vorgelegt. Ich bin darauf hingewiesen worden, dass die Unrichtigkeit der vorstehenden Erklärung als Täuschungsversuch angesehen wird und den erfolglosen Abbruch des Promotionsverfahrens zu Folge hat.

Ort, Datum

Unterschrift